Molecular tumour profiling of glioblastoma by mass spectrometry imaging

A thesis submitted to the University of Manchester for the Degree of Doctor of Philosophy in the Faculty of Biology, Medicine and Health

2022

Matthew C Gentry

School of Health Sciences

Division of Informatics, Imaging and Data Sciences

Table of contents

Contents

List of figures

List of tables

Abbreviations

2-HG	2-hydroxyglutarate
5-ALA	5-aminolevulinic acid
AMX	Abstract Model Builder
ATP	Adenosine tri-phosphate
AUC	Area under the curve
BBB	Blood brain barrier
CA-9	Carbonic anhydrase IX
CID	Collision induced dissociation
CPS	Counts per second
CPT-1	Carnitine palmityl transferase-1
CSF	Cerebral spinal fluid
CT	Computed Tomography
CV	Cresyl violet
DART	Direct Analysis in Real Time
DDA	Data dependant acquisition
DESI	Desorption Electrospray Ionisation
DPTA	Diethylenetriaminepentacetate
EASI	Easy ambient sonic-spray ionization
ECD	Electron capture dissociation
EGFR	Epidermal growth factor receptor
EOR	Extent of Resection
ESI	Electrospray ionisation
FA	fatty acid
FAO	Fatty acid oxidation
FASN	Fatty acid synthase
FGS	Fluorescence guided surgery
GBM	Glioblastoma
GM	Grey Matter
GTR	Gross Total Resection
H&E	Haematoxylin and Eosin
ICP	Inductively coupled plasma
ICP-MS	Inductively coupled plasma mass spectrometry
IDH	Isocitrate dehydrogenase
IHC	Immunohistochemical
iKnife	Intelligent Knife
IMMS	Ion mobility mass spectrometry
IMS	Industrial methylated spirits

IT MS/MS	Ion trap MS/MS
KED	Kinetic energy discrimination
LAESI	Laser ablation electrospray ionisation
LA-ICP-MS	Laser Ablation Inductively Coupled Mass Spectrometry
LOH	Loss of heterozygosity
LPL	Lysophopholipids
m/z	Mass to Charge
MALDI	Matrix Assisted Laser Desorption Ionisation
MB	Methylene Blue
MeOH	Methanol
MGMT	O-6-methylguanine-DNA methyltransferase
MRI	Magnetic Resonance Imaging
MRS	Magnetic Resonance Spectroscopy
MS	Mass Spectrometry
MS/MS	Tandem MS
MSI	Mass Spectrometry Imaging
NAA	N-acetyl aspartate
NFR	Nuclear Fast Red
NICE	National institute for health and care excellence
OTD	On-tissue digestion
OzID	Ozone identification
PA	Phosphatidic acid
PC	Principal component
PCA	Principal Component Analysis
PCho	Phosphatidylcholine
PDPA	Phase Doppler Particle Analysis
PE	Phosphatidylethanolamine
PESI	Probe electrospray ionisation
PFS	Progression free survival
PG	Phosphatidylglycerol
PI	Phosphatidylinositol
PI3-K	Phosphatidylinositol-3-kinase
PIP2	Phosphatidylinositol (4,5)-bisphosphate
PIP3	Phosphatidylinositol (3,4,5)-trisphosphate
PIRL	Picosecond infrared laser
pLSA	Probabilistic latent semantic analysis
PpIX	Protoporphyrin IX
PS	Phosphatidylserine
PTEN	Phosphatase and tensin homolog
QToF	Quadrupole time of flight
RAS	Renin-angiotensin system

RB	Retinoblastoma
REIMS	Rapid evaporation ionisation mass spectrometry
ROC	Receiver operator characteristics
ROI	Region of Interest
RTK	Receptor tyrosine kinase
SID	Surface induced dissociation
SIMS	Secondary Ion Mass Spectrometry
SOC	Standard of Care
SREBP	Sterol regulatory-element binding proteins
T2W	T2-Weighted
TAG	Triacylglycerides
TB	Toluidine Blue
TIC	Total ion current
TME	Tumour microenvironment
TMZ	Temozolomide
TQ	Triple quadrupole
UV	Ultraviolet
WALDI	Water assisted laser desorption ionisation
WHO	World Health Organisation
WM	White Matter

Abstract

Glioblastoma (GBM) is the most common and most aggressive primary brain tumour, with an extremely poor prognosis. Despite extensive research into this aggressive tumour, overall survival has been unaffected in the past 15 years with average survival at 12-15 months with optimal standard of care treatment. Glioblastoma tumour cells exhibit strong proliferative and infiltrative characteristics, which contributes to the infiltration of tumour cells into healthy brain. This feature means safe total resection of all tumour cells is impossible, which contributes to the poor survival and prognosis of GBM. Defining a safe tumour volume for resection and further understanding the underlying biochemistry of glioblastoma tumour cells at the molecular level, are therefore important aspects of research that can help to improve overall patient survival.

Investigation of the lipidomic changes associated with tumours is a rapidly growing field, with mass spectrometry imaging techniques widely used for molecular pathology applications. Lipidomic profiling provides downstream analysis of the proteomic and genomic changes that are also used to characterise tumours. Mass spectrometry imaging analysis by desorption electrospray ionisation mass spectrometry (DESI-MS) imaging provides an ideal toll to study investigate lipid profiles and small molecules pre-clinical model of GBM and human GBM biopsies. Laser ablation inductively coupled plasma mass spectrometry (LA-ICP-MS) imaging is highly specified for metal analysis and has also been used to study the metal ion distribution in the pre-clinical model of GBM, particularly that of gadolinium which was used as an MRI contrast agent alongside other endogenous metal species. The work outlined here has utilised DESI-MSI in the analysis of brain tumour samples to examine GBM at a molecular level. Overall survival in GBM has not improved for the last 15 years, so a full understanding of GBM at the molecular level is required in the hope to find new therapeutic strategies. Untargeted DESI-MS acquisition has allowed the generation of hundreds of lipid images, with subsequent multivariate statistical analysis revealing key molecular pathways implicated in GBM. Phosphatidylinositol lipid signalling molecules and overexpression of the PI3-K pathway as well as altered metabolism *via* β-oxidation of fatty acids and carnitines have been observed in the pre-clinical models. This altered metabolic activity of GBM utilising fatty acid oxidation

for energy production translated to human glioblastoma biopsies, where large number of acyl-carnitines were also detected.

The use of histology stains other than H&E have been investigated for compatibility with DESI-MS lipidomic analysis. Cresyl violet, toluidine blue, and methylene blue staining showing compatibility with DESI-MS imaging analysis which could provide an alternative data directed stream for targeted tissue analysis.

Declaration

No portion of the work referred to in the thesis has been submitted in support of an application for another degree or qualification of this or any other university or other institute of learning

Copyright statement

i. The author of this thesis (including any appendices and/or schedules to this thesis) owns certain copyright or related rights in it (the "Copyright") and s/he has given the University of Manchester certain rights to use such Copyright, including for administrative purposes.

ii. Copies of this thesis, either in full or in extracts and whether in hard or electronic copy, may be made only in accordance with the Copyright, Designs and Patents Act 1988 (as amended) and regulations issued under it or, where appropriate, in accordance with licensing agreements which the University has from time to time. This page must form part of any such copies made.

iii. The ownership of certain Copyright, patents, designs, trademarks and other intellectual property (the "Intellectual Property") and any reproductions of copyright works in the thesis, for example graphs and tables ("Reproductions"), which may be described in this thesis, may not be owned by the author and may be owned by third parties. Such Intellectual Property and Reproductions cannot and must not be made available for use without the prior written permission of the owner(s) of the relevant Intellectual Property and/or Reproductions.

iv. Further information on the conditions under which disclosure, publication and commercialisation of this thesis, the Copyright and any Intellectual Property and/or Reproductions described in it may take place is available in the University IP Policy (see http://documents.manchester.ac.uk/DocuInfo.aspx?DocID=24420), in any relevant Thesis restriction declarations deposited in the University Library, the University Library's regulations (see http://www.library.manchester.ac.uk/about/regulations/) and in the University's policy on Presentation of Theses

Disclaimer

This thesis is presented in the alternative format, and therefore it should be stated that no part of this thesis was written by any other author/collaborator, and the narrative put together was done so by the candidate alone. Author contributions will be stated at the end of each chapter.

Appreciation and Thanks

I’d like to dedicate this thesis to my Granny, Lady Bene Knox, who passed away in my second year. I love and miss you and I’m so sad to not have you around us anymore.

I would like to offer a massive thank you to Dr Adam McMahon and Professor Nick Lockyer, my supervisors, for their support from day one and the encouragement they have given me throughout my PhD. Special thanks must go to Adam for putting up with my stress in the last few weeks of writing up!

I would also like to thank the mass spectrometry imaging group members, particularly Irma Berrueta Razo who since she re-joined our group has had to put up with my countless questions about everything under the sun.

A massive thanks must go to my sponsors, Waters, and everyone who has helped me especially Dr Emrys Jones, Dr Emmanuelle Claude and Dr Mark Towers who training me and gave me my passion for DESI imaging. Special thanks to Emrys for all the help and time you have given me and my constant bombardment with messages!

Thank you, Chris, Luke and Charlie, my MRC cohort buddies who have got me through the hard times and helped motivate me throughout the PhD. You are all brilliant and smart people and I hope to be able to contribute something at the next pub quiz!

To my closest friends Dave and Mooly. You are the best. No further words required.

I also need to thank my family; Mum, Dad, Pip and Grandma. Thank you for everything you have done for me throughout my academic career and the support and love that you have given me. I forgive you all for moving so far away from me!

And last but not least to my fiancé, Dr Danielle McDougall. I can’t tell you how proud I am of you and everything you have achieved. Thank you for the volume of support you have given me in getting me over the finish line, I genuinely couldn’t have done it without you.

And to Doris. Thank you for being so cute.

Chapter 1: Introduction

1. Introduction to Glioblastoma

Glioblastoma (GBM) are classified by the World Health Organisation (WHO) as a grade IV astrocytoma [1]. GBMs are also the most common and malignant primary brain tumour in adults, accounting for 45.2% of all primary brain malignancies [2], as well as 60-70% [3] of all malignant glial tumours and occur in the UK with an incidence of 4.64 cases per 100,000 per year [4]. GBM arise in the glial cells of brain parenchyma and are most common in the supratentorial brain regions [1]. The WHO Grade IV covers all of GBM subcategory of glioma tumours and is assigned as a GBM to tumour masses that; show cytologic malignancy markers, signs of mitotic activity and display necrotic regions within the neoplasms [5]. GBM exhibits extensive micro-environmental heterogeneity as well as high genetic, epigenetic and molecular variability [6]. GBM is incurable: reflected by global median survival rate without treatment of between 6-9 months [7] and 6.1 months for the UK, and also makes GBM once of the most lethal cancer types [8]. Even following the Stupp protocol of optimal treatment Post diagnosis, prognosis is particularly poor and patients with GBM have an extremely bleak outlook with long term survival levels for 1,2 and 5 years standing at 28.4%, 11.5% and 3.4% respectively [4].

The 2016 update to the 'WHO Classification of tumours of the central nervous system', redefined GBM based on the Isocitrate Dehydrogenase (IDH) status [1], as to better define the heterogeneity of complex tumours [9], further with the potential to guide targeted therapies [10]. GBM is now classified as (1) Isocitrate Dehydrogenase (IDH)-wildtype (*wt*), closely linked to primary GBM; (2) IDH-mutant, corresponding closely to secondary GBM. Primary GBM account for roughly 90% of GBM cases and develop *de-novo*, whilst secondary GBM develop from lower grade gliomas. Histologically, GBM are characterised by microvascular proliferation (a hallmark of GBM histology), glial cell anaplasia, diminished apoptosis, nuclear pleomorphism, dense cellularity and grade IV defining hypoxic necrotic foci surrounding by pseudo-palisading cells [6].

Although GBM is a well-researched topic there has not been a significant change to overall patient survival in the last 15 years. It is therefore imperative that further research continues into this aggressive brain tumour to improve patient outcomes.

1.1. Detection methods

Computed tomography (CT) or magnetic resonance imaging (MRI) scans are used for the initial detection of tumour masses, as well as monitoring tumour progression. Initially if an abnormal mass is suspected, patients will undergo a CT scan. Once this abnormal mass is identified a contrast enhanced MRI will be performed, either T1 or T2. CT and MRI are both non-invasive, with MRI giving a high degree of confidence for GBM size and location. GBM show as hypointense on T1 and hyperintense on T2-weighted MRIs [11], Figure 1.

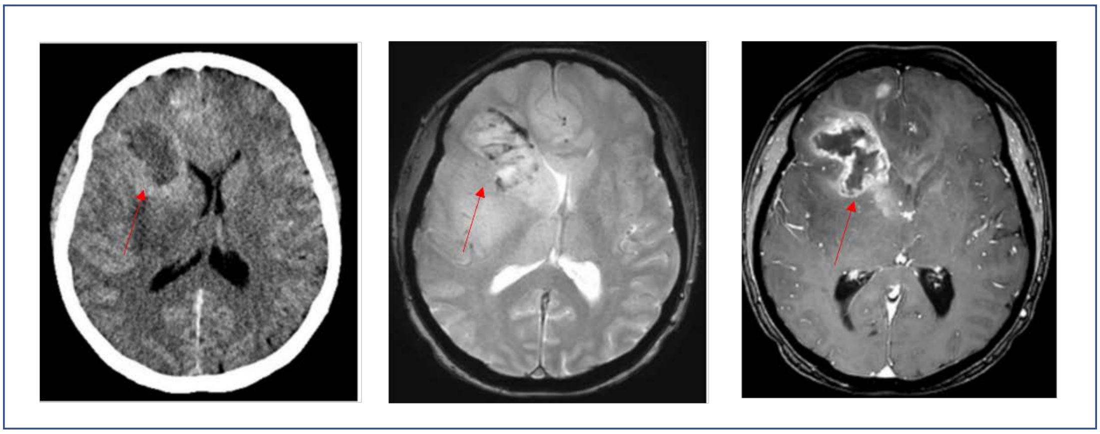

Figure 1 – An overview of imaging techniques use to determine the location of abnormal masses within the brain. The mass was identified as a glioblastoma tumour located in the right frontal lobe shown left to right in, an axial CT image, axial FLAIR T2 weighted MRI image and a T1 weighted axial image using gadolinium as a contrast enhance agent. In the T1 contrast enhanced image, additional areas of enhancement lie within the previously described region of 'FLAIR envelope'. Images extracted from [12]

Around half of all MRIs use gadolinium as a contrast agent to enhance visibility of the tumour masses. The addition of contrast enhancing agents enables the tumour mass to be exhibited in greater detail. Contrast enhancing agents are typically paramagnetic ion complexes, incorporating lanthanide elements such as gadolinium as Gd^{3+} ions [13]. Gadolinium complexes shorten the T1 relaxation time, causing increased signal intensity on the MRI image and brighten regions particularly in the tumour region. Upon administration, gadolinium contrast agents can cross the diseased blood brain barrier and are rapidly distributed between plasma and interstitial spaces found particularly in abnormal regions of the brain. This function allows gadolinium (III) ions to enhance tumour visibility, providing key location information that will be used for surgery [14].

1.2. Current treatment

The diffuse and invasive nature make GBM incurable by surgical resection [5, 15]. Breakthrough research in 2005, generated the Stupp Protocol [16], which remains the standard of care (SOC) today and involves maximum tumour removal, discussed in detail in section 1.4, followed by chemo-radiation using temozolomide (TMZ), further discussed in section 1.3. GBM is linked to poor prognosis and as such, treatment research has been widespread. A range of targeted therapies have appeared in clinical trials [17] including the promising use of bevacizumab for recurrent glioblastoma; a human monoclonal antibody acting as an antiangiogenic agent that inhibits VEGF [18]. Single agent bevacizumab was granted FDA approval based on the early results of a phase II clinical trial that shown improvements to progression free survival, but ultimately had no effect on overall survival. A further phase II trial comparing bevacizumab to placebo plus temozolomide for newly diagnosed GBM tumours, concluded similar results. Addition of bevacizumab to radiotherapy-temozolomide treatment did not improve overall survival and was associated with increased adverse events than in the placebo (66.8% vs 51.3%). Although the median progression free survival was longer in bevacizumab treatment group compared to placebo (10.6 months vs. 6.2 months), the increased adverse events were an issue and as such bevacizumab is not approved in Europe for treatment of GBM, but can be utilised for symptomatic patients with recurrent GBM as it likely improves quality of life [19].

Although targeted chemotherapy approaches provide exciting prospects for GBM treatment, many clinical trials, especially targeting epidermal growth factor receptor (EGFR) have shown no effect on overall survival [17]. Even though the extent of research into the underpinning molecular biology of GBM tumours has been significantly enhanced, advances to the therapeutic approaches have been insubstantial. As such the SOC treatment has not changed for over 15 years and a clear requirement for improved therapeutic strategies is demanded. Immunotherapy and precision oncology are two such areas that have been explored, which are both driven through the enhanced understanding of GBM at the molecular level. However, GBM tumours possess several challenges for novel therapies including the inaccessibility of the tumours, located beyond the blood brain barrier, as well as the unique tumour microenvironment and heterogeneity (within each tumour and between individual cases) associated with GBM tumours.

1.3. Stupp protocol

The Stupp protocol is the SOC for GBM treatment, incorporating the use of methylation agent TMZ in combination with maximal tumour resection & radiotherapy [16]. Work by Stupp *et al.* on a randomised population of 573 patients with newly diagnosed, histologically confirmed GBM, showed improved median survival with radiotherapy plus TMZ chemotherapy over radiotherapy alone, 14.6 months vs 12.1 months, as well as significantly increased two-year survival rate at 26.5% vs 10.4%[16]. TMZ is given at 75 mg/m^2 during radiotherapy, followed by adjuvant administration for 6 cycles of 28 days post radiotherapy at 150-200 mg/m^2 [20]. Radiotherapy is administered at a dose of 2 Gy per fraction given once daily, five days per week, over a six-week time period. Alongside 3-dimensional (3D) CT and 3D planning systems, radiotherapy was applied to the gross tumour volume (GTV) with a 2-3 cm margin [16]. GTV is defined as the visible enhancing brain tissue observed on CT or MRI scans at the primary tumour site [21].

1.4. Surgery

Surgery is the key to GBM treatment [20]. Excision of at least 98% of the tumour tissue is linked to increased overall survival of 5 months, compared to patients who reside with >2% residual tumour mass [22]. Two surgical options are commonly used for tumour treatment: intra-operative biopsy and gross total resection (GTR). Biopsy used in conjunction with an imaging modality, such as MRI, allows characterisation through histopathology analysis of resected tissue, whilst resection removes greater amount of tissue. Biopsies are typically undertaken for tumours located in eloquent brain regions; areas of the brain that control important motor functions such as primary motor, somatosensory, visual, and auditory cortex's, as well as in areas touching ventricles, which must receive less extent of resection (EOR), due to the chance of causing major neurological defects [23] [24].

GTR is used in roughly 40% of GBM patients [23, 25] and involves resection of ≥90% of the enhancing disease, designated where post operative MRI shows 90% or greater tumour resection [26]. Safe maximal tumour resection should be performed where this will benefit patient survival, as surgery provides both diagnostic and therapeutic benefits [27]. Another benefit of tumour resection is the ability to use the resected tissue for molecular testing, particularly amenable to this research in Chapter 3 where previously resected human tissue biopsies are analysed. However, patient related risk factors do arise such as GTR morbidity as well as problems affecting the functionally relevant areas in close proximity to the tumour mass [28]. Where potential risks outweigh the benefits of greater tumour removal, many patients still undergo incomplete surgical resection.

A recent multicentre study looked to compare the EOR and biopsy on their prognostic ability for newly diagnosed GBM following standard of care treatment; radio and chemotherapy in combination with GTR [29, 30]. A total of 345 newly diagnosed GBM patients were involved where 72 received biopsies and 273 underwent resection; of which 125 were classed as GTR (>90% of post-operative MRI tumour mass removed) and 148 were incomplete. Results showed post-surgery morbidity was lower after patient biopsy (1.4% v 12.1%, p=0.007), however the best overall median survival was observed in a group receiving GTR with radiotherapy and chemotherapy whose tumours exhibits O-6-methylguanine-DNA methyltransferase (MGMT) promoter methylation, at 33.2 months. An important study in 2005 revealed methylation to the MGMT protein is a significant favourable prognostic marker for GBM patients, with further survival benefits shown for those receiving SOC treatment of TMZ and radiotherapy treatment [31]. The results reported in the multicentre study assessing impact on EOR for GBM patients are in line with these earlier observed key findings of MGMT as a favourable prognostic marker.

Other prognostic factors observed from these findings and matched with reported literature included; patients aged ≤60 years [5], GTR [32, 33], MGMT promoter methylation [28], pre-operative Karnofsky performance score ≥80 [34] and radiotherapy plus chemotherapy. Overall results from this study suggest that resection or biopsy, rather than incomplete resection, where appropriate, should be used for surgical GBM removal [29] and that maximum tumour removal surgery alongside SOC adjuvant treatment is key to improving overall survival.

The goal of GTR is to remove 100% of the tumour enhanced region in post-operative MRI scans. However, this is not always possible due to imprecise correlation of pre-operative MRI images and intra-operative tissue anatomy as well as difficult differentiation between high grade glioma and parenchyma. As such tumour tissue often remains after surgery which can cause rapid disease recurrence [23, 35]. A novel key advancement in the visualisation of GBM tumours is the use of 5-ALA as an interoperative tumour visualisation guide, reviewed further in section 0.

Current surgical operating procedures utilise pre-operative MRI brain scans as a guide to the surgeon, with the goal to remove all non-contrasting tumour regions from the brain. However, the limiting factor for GTR is determining tumour margins. GBM is a heterogeneous (displaying both inter and intra tumour heterogeneity [15, 36]), invasive tumour and due to the infiltrating nature of GBM [9], intraoperative tumour margin determination is a difficult task with current imaging methods. Several other difficulties exist including differentiating tumour and healthy parenchyma under operating conditions. Steps towards enhanced visualisation of tumours during surgery have been undertaken, including the successful use of intra-operative MRI for glioma surgery [32]. A greater number of patients receiving interoperative MRI underwent a complete tumour resection (96% of 24 patients) compared to those in the control group (68% of 25 patients, p= 0.023). The control group received conventional microsurgery with pre-operative MRIs used for guidance.

However, there are certain limitations to intraoperative MRI, not limited to the cost, extension to surgical timings and limited availability of these devices. To assess the benefit of intraoperative MRI for glioblastoma resection a comprehensive was undertaken by Kubben et al.in 2011 to look at all papers published until this date [37]. Kubben et al. concluded that intraoperative MRI guided surgery for GBM tumours increases the extent of overall tumour resection which ultimately increases quality of life and prolongs overall survival. Intra-operative surgical procedures.

Aside from traditionally used imaging modalities, 5-aminolevulinic acid (5-ALA) as a fluorescent dye can be used to visualise GBM during tumour resection. The benefits of 5-ALA in fluorescence guided resection (FGS) were demonstrated in a phase III clinical trial, comprising multiple centres by the ALA research group in Germany [38]. Here, patients were randomly assigned to FGR with 5-ALA (n=161) or conventional microsurgery with white light (n=161). The utility of 5-ALA for FGR of Glioblastoma was showcased as the study reached both of its primary end points; complete resection of the contrast enhancing tumour on early MRIs as well as 6-month progression free survival. In the 5-ALA treatment group, 65% of patients received GTR of the contrast enhancing tumour compared to 36% with those in the white light group, whilst those patients in the study arm also had improved 6-month progression free survival at 41.0% (32.8 - 49.2) compared with 21.1% (14.0 – 28.2).

Recent guidelines set out by NICE to improve surgical resection of GBM, recommend the oral use of 5-ALA for all patients undergoing initial surgery for GBM. As an oral solution, Gliolan^{TM} or the 'pink drink' is a non-fluorescent pro-molecule, administered up to 2 hours before surgical intervention as an oral solution at 20 mg/kg body weight. As a naturally occurring biomolecule, 5-ALA acts as a precursor to the fluorescence molecule PpIX [39]. Upon administration, 5-ALA shows high efficacy in crossing the blood brain barrier, notably favouring areas of high-density malignant cells [39], [40] where it is metabolised in the mitochondria of proliferation cells to PpIX, as part of the heme synthesis pathway [39]. Many theories describe the mechanistic utility of 5-ALA for tumour imaging and reason 5-ALA and PpIX accumulates preferentially in tumour cells. PpIX conversion to heme is the rate limiting step, decreased ferrochelatase levels, increased proliferative activity by malignant cells, increased uptake of PpIX in ATP-binding cassette B6 and increased cellular density have all been implicated in increased fluorescence in gliomas [[40-43]. Although natural synthesis and conversion of 5-ALA to PpIX occurs, the synthesis and hence concentration of PpIX is controlled by a feedback system that avoids accumulation in healthy cells, as such natural PpIX will not interfere with the fluorescence from tumour cells [44].

PpIX is a photoactive compound, emitting light in the red region of the visible spectrum (705 nm), upon excitation of blue-violet light (410 nm). The red fluorescent signature is used as a guide to neurosurgeons during fluorescence guided surgery (FGS). FGS has shown great promise for treatment of GBM increasing the extent of resection, including GTR of MRI contrast enhancing tumour volume, as well as improvements to 6-month progression free survival achieved across a number of studies [38].

Although the use of FGR has shown great benefits to improve patient survival rates, there are still questions and problems surrounding PpIX distribution in tumours and sources of false results. GBM is a complex and heterogeneous tumour, comprising many different cell types and the distribution of PpIX within glioblastoma tumour material is understudied, although 5-ALA fluorescence is known to be dependent on tumour cell porphyrin metabolism [45]. There are many theories surrounding false-positive results of PpIX fluorescence including the possibility of PpIX secretion out of neoplastic cells into extracellular matrix [46] or even into surrounding tissue[47]. If these areas of leakage are located towards the tumour boundary, PpIX accumulation can occur in healthy parenchyma, thus putting the patient at risk to removal of healthy tissue. Whether specific tumour microenvironments fluorescence with comparable intensity to that of purely malignant tumour cells is also a possible problem, especially when the tumour can be largely comprised of necrotic or hypoxic areas or even contain high immune cell density. Problems also lie when visualising the fluorescent porphyrins intra-surgically. Due to the need for a specific wavelength of blue light, surgery would need to take place in a theatre equipped with a xenon lamp capable of switching between white and blue light. It is unlikely for a surgery to be solely performed with the blue light on, which leads to the surgery being paused whilst the tumour is visualised in the presence of blue light, before reverting to white for much of the procedure. A further problem with visualising the tumour is that lack of fluorescence can be introduced due to surgical obstacles. Often, GBM are surrounded by healthy parenchyma as well as blood, which can severely obstruct the surgical cavity and hence fluorescence visualisation.

Despite the concerns 5-ALA remains an optimal strategy alongside intraoperative MRI guided surgery for GBM resection and may be the best option available to neurosurgeons to visualise tumours.

1.5. Genetic landscape

GBM is a complex cancer containing numerous mutations tumour suppressor genes and oncogenes [48]. A 2008 study by Cancer Research Genome Atlas Project identified three key altered molecular pathways; (1) Receptor tyrosine kinase/RAS/ phosphatidylinositol-3 kinase (PI3K), (2) p53 & (3) Retinoblastoma (RB) [49], Figure 2. These affected pathways show many genetic alterations including the amplification and mutational activation of RTK, activation of PI3K pathway & inactivation of the p53 and RB tumour suppressor pathway [3].

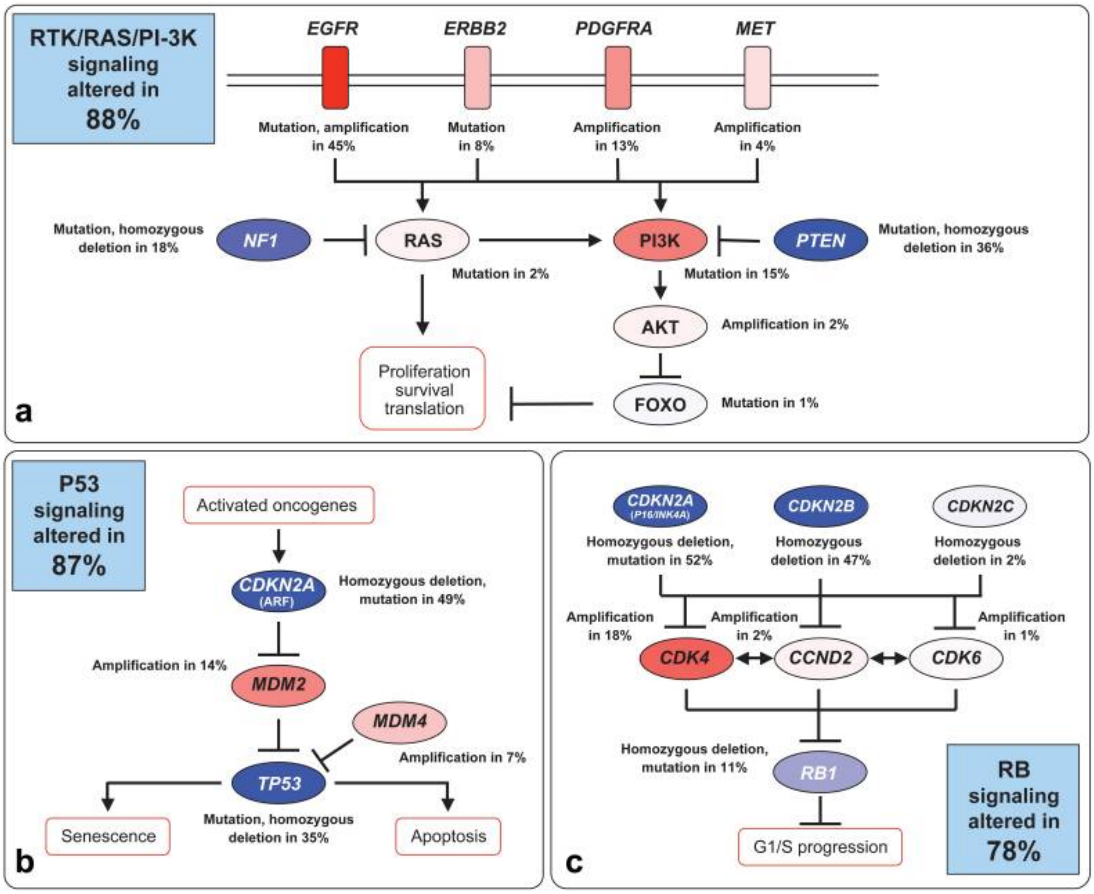

Figure 2 – Frequent genetic alterations in the three critical signalling pathways in GBM. (A) RTK/RAS/PI3K, (B) p53, (C) RB. Activating genetic alterations are highlighted in red. Inactivating genetic alterations are in blue. In each pathway, the altered components, the type of alteration, and the percentage of tumours carrying each alteration are shown. Blue boxes contain the total percentages of GBM with alterations in at least 1 known component gene of the designated pathway. Taken from [49].

Phosphatase and tensin homolog (PTEN) mutations are among the most common mutations in GBM with an occurrence of 24%-37% [50]. In normal functioning cells, PTEN is a dual protein and lipid phosphatase which predominantly dephosphorylates phosphatidylinositol-3, 4, 5-triphosphate (PIP3) [51]. PTEN mutation often occurs with loss of heterozygosity (LOH) on chromosome 10q23, which leads to loss of its tumour suppressor function and subsequently enables major cell growth and survival signalling pathways. PTEN deletion affects a number of key survival signalling pathways, including mitogen-activated protein kinase (MAPK) [52] and focal adhesion kinase (FAK) [53], but the PI3K and downstream AKT signalling pathway is considered to be one of the most important in GBM tumorigenesis due to its high prevalence [54]. PTEN acts directly on the PI3-K/ AKT signalling pathway as a negative regulator of many critical cellular functions including cell cycle progression, angiogenesis, migration/ invasion and cell survival and hence is a crucial prognostic determinant of malignant neoplasm [55].

Studies have shown that addition of PTEN into glial tumour cells results in a decreased intrinsic activity of AKT, suggesting the important role of PTEN in GBM tumour proliferation and progression. Further, this confirms the role that PTEN plays as a tumour suppressor gene [56]. Other studies have shown the deletion and loss of heterozygosity (LOH) of the PTEN gene acts as a progressive factor, driving tumours and cancers to highly malignant cancers[57], rather than initial formation. It is clear to see through the range of cell survival and proliferative mechanisms that are enhanced by dysregulation of the PI3K pathway, as to why PTEN mutation leads to such malignant neoplasms. Acting in a similar manner to PTEN mutations is that of EGFR. Found in around 35% of GBM [1], EGFR mutations activate PI3K, which as shown before activates downstream AKT signalling [58]. The most common EGFR mutation in GBM is EGFRvIII and is relevant to many dominant features of GBM including; high proliferative ability, invasion characteristics and low apoptotic levels, whilst also having the added effect of protection from conventional therapies [58].

Deregulation of the p53 signalling pathway is the second most altered pathway altered in glioblastoma, found in in 87% of GBM tumours and >90% TP53 mutations in co-occurrence with IDH1 mutations [59]. The TP53 gene encodes for p53 protein which plays a central role in maintaining cellular homeostasis. P53 activation can be triggered by several carcinogenesis events such as DNA damage, oncogene activation and hypoxia [60]. Although P53 mutations are oncogenic in GBM, it is the combination of other mutations such as those to PTEN that together that drive GBM progression [61].

GBM is shown to have a number of common genetic alterations, many of which have been selected for targeted therapy approaches, with however little overlay success. It is clear that multiple genetic alterations drive the formation and growth of tumours and as such targeting a single genetic alteration may not be enough to halt the growth of GBM tumours.

1.6. Molecular markers of Glioblastoma

A plethora of research exists at the genomic level to characterise GBM, but only in recent years has the metabolic activity of GBM been explored at the molecular level, with a view to further characterise this malignant tumour that displayed extremely poor prognosis for patients.

As mentioned previously, GBM is now classified based on its isocitrate dehydrogenase (IDH) mutation status with primary GBM closely related to IDH-*wt* and secondary GBM showing mutation in the IDH gene. Mutated IDH-1 proteins are able to convert α-ketoglutarate to 2-hydroxyglutarate (2-HG). Prescence of 2-HG is detected using mass spectrometry approaches (MS techniques discussed in section 4) providing rapid determination of IDH status [62] and is an excellent option for distinguishing primary and secondary GBM based on the metabolic species present.

Like many other tumours, GBM relies upon energy from ATP and has a high glycolytic activity [63], however recently a shift to metabolism using fatty acid oxidation (FAO) *via* β-oxidation has been shown with FAO emerging as a key metabolic feature of GBM providing metabolic plasticity [64]. Energy production *via* FAO requires carnitine to bind to free fatty acids forming acyl-carnitines, which can then provide transport into the mitochondria matrix. Carnitines and associated enzymes have been shown to be overexpressed in GBM tissue, further confirming this shift in metabolic activity [65, 66].

Aside to metabolic activity, lipid pathways severely altered in GBM include the PI3-K pathway; altered in over 80% of GBM tumours. Downstream signalling in this pathway is implemented *via* lipid signalling through phosphatidylinositol (PI) in the form of phosphatidylinositol (3,4,5)-trisphosphate (PIP_3) and phosphatidylinositol (4,5)-bisphosphate (PIP_2), reviewed in detail in [67] and further explored in this thesis.

The roles of fatty acids, carnitines and PIs are further explored in section 2.

2. Introduction to lipids

Lipids are non-polar biochemical species found at high abundance in mammalian cells. In mammalian cells lipids have many roles where they can; function as signalling molecules, provide cellular structure and also act as energy sources [68]. Although highly abundant, lipids are a diverse group of molecules that can be categorised into many different molecular classes including but not limited to fatty acids (FA), phospholipids, lyso-phospholipids (lyso-PL), triglycerides and sterol containing lipids such as cholesterol.

Fatty acids act as building blocks for more complex lipids of triacylglycerides (TAG) and phospholipids, but also have functions in the cells for energy produced via the β-oxidation pathway, explored further in 2.1. Fatty acids in mammals are comprised of an even number of carbon atoms either synthesised *de novo* from acetyl-CoA by FASN or taken up from the diet. Acetyl-CoA is a 2-carbon unit building block that mammalian cells use to produce only even chain length fatty acids and often contain unsaturated sites at position (Δ9), as well as other locations. Δ9-fatty acid desaturase is a commonly occurring enzyme in mammals responsible for the synthesis of oleic acid; an important monounsaturated fatty acid found in all human cells. In the synthesis of oleic acid, Δ9-fatty acid desaturase selectively adds a cis-double bond at the Δ9 position of acyl coA [69].

Fatty acid nomenclature is written as FA C:D; where C equals the total number of carbon atoms in the chain and D is the number of carbon carbon double bonds, or number of unsaturated bonds. For example, arachidonic acid containing 20 carbon atoms and 4 unsaturated double bonds is written as FA 20:4 or C20:4.

Lipid species make up around 50% of cell membranes, of which the class of phospholipid species are the most abundant, Figure 3. The brain is roughly 60% fat, making the brain the 'fattiest' organ. Brain lipids contribute to 25% of the brain's dry mass, making them highly abundant biomolecules of the brain of which the predominant role is to provide function and structure to cellular membranes [70].

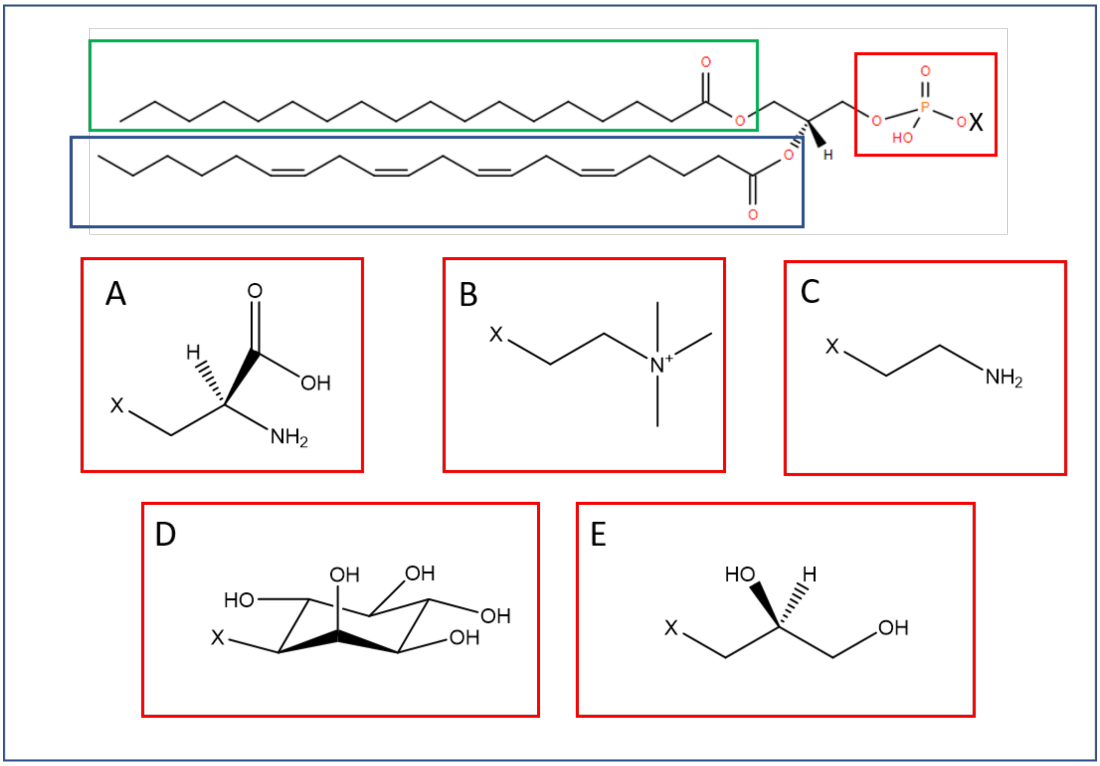

Figure 3 – An overview of the structure of various phospholipids. The top diagram is the structure of a phospholipid with three main areas of the molecule highlighted. The green region represents fatty acid side chain 1 (R1) equal to FA 18:0 in this case, the blue region represents fatty acid side chain 2 (R2) equal to FA 20:4 in this case and the red region is the phospholipid headgroup represented by structures A – E. X = Hydrogen represents phosphatidic acid (PA). A = serine headgroup in phosphatidylserine, B = choline headgroup in phosphatidylcholine (PCho), C = ethanolamine headgroup in phosphatidylethanolamine (PE), D = inositol headgroup in phosphatidylinositol (PI) and E = glycerol headgroup in phosphatidylglycerol (PG)

Phospholipids, alongside cholesterol, are key lipids involved in providing cell structure, forming the phospholipid bilayer. This double-layered phospholipid structure provides a barrier between the extracellular matrix of mammalian cells and their surroundings due to the hydrophobic and hydrophilic nature of the phospholipid tails (fatty acid R groups) and headgroup respectively.

Phospholipid nomenclature will state the parent class e.g., phosphatidylinositol (PI) and total number of carbon atoms and degree of unsaturation across both R groups. At a particular molecular weight there exists many phospholipid isotopomers with varying combinations of FA side chains. Isotopic phospholipids contain the same number of isotopes of each element; however, these elements will differ in position providing each lipid with a slight functional different. This feature is important for phospholipids within the phospholipid bilayer which contain varying fatty acid side chain length and providing the membrane with fluidity.

Throughout this thesis if the makeup of a phospholipid is known each contributing FA will be displayed. A PI made up of FA 18:0 and 20:4 would be shown as PI [38:4] or PI [18:0/20:4], further explained in Section 3.2.

The lipids addressed in this thesis will focus on fatty acids, carnitines, and phospholipids.

2.1. Lipids in cancer

Recently, research in the lipidomics field has increased, particularly in the field of cancer research where altered lipid metabolism has been shown in many cancers. Activation of lipid metabolism is an early trigger in tumours and altered metabolism is now recognised as a key hallmark of cancer. Many observations have been made for the changing lipid metabolism [71-73]. An emerging hallmark of cancer metabolism is the use of intermediates from glycolysis and the tricarboxylic acid (TCA) cycle for biosynthesis of further nutrients, one of which is acetyl CoA. As previously mentioned, acetyl CoA is the building block to longer chained fatty acids and the majority of the carbon required for FA synthesis comes from glucose. Mitochondrial acetyl- CoA is produced during glycolysis when pyruvate is converted into acetyl-coA by pyruvate dehydrogenase. Mitochondrial Acetyl CoA can however not be used for fatty acid production, so it enters the TCA, producing NADH (reduced nicotinamide adenine dinucleotide) and subsequent energy in the form of ATP molecules via oxidative phosphorylation. The citrate produced in the first step of the TCA from mitochondrial Acetyl CoA, initiates de novo lipid synthesis after shuttling to the cytosol. Here citrate is converted to cytosolic acetyl CoA by the enzyme ATP-citrate lyase, and 2 carbon units are available for fatty acid production [74]. The process of fatty acid metabolism, as well as the broader lipid metabolism is described in Figure 4.

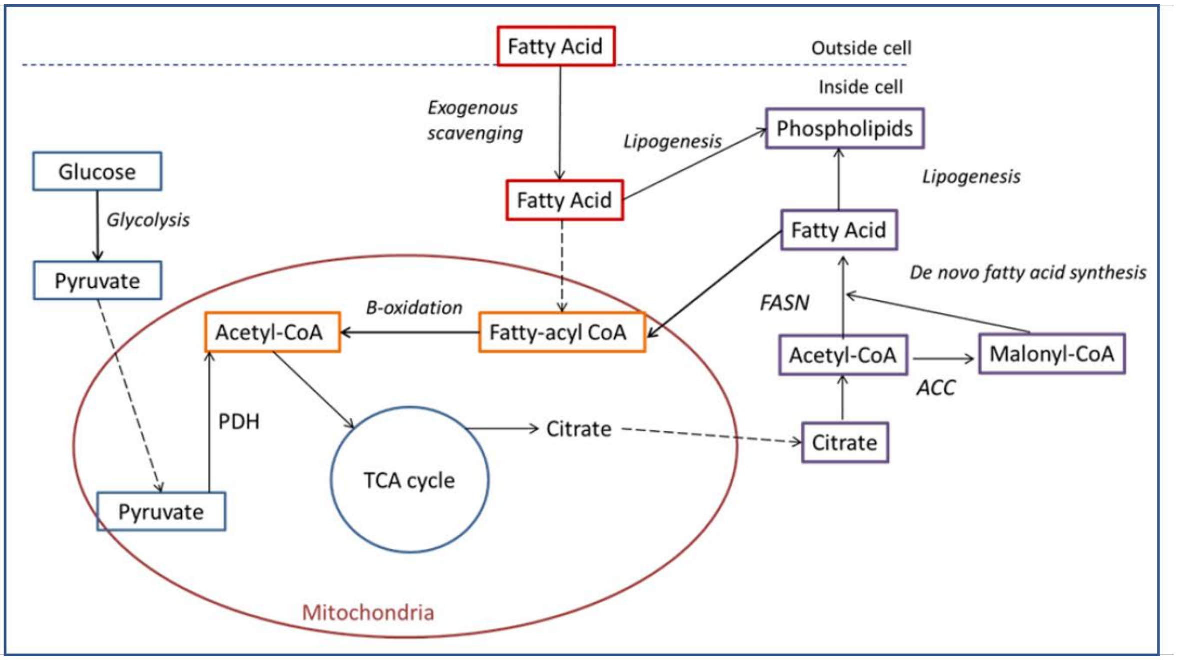

Figure 4 – A comprehensive overview of lipid metabolism in humans.

Fatty acids are the basic building blocks of more complex phospholipids and consist of long hydrocarbon chains with varying lengths and degrees of unsaturation. Recently, fatty acids have gained interest due to their metabolic activities in cancer as an energy source. FA are used in altered states of energy production via fatty acid oxidation (FAO) or β-oxidation in cancer cells. Under normoxic conditions with plenty of glucose availability, energy generation from glucose is preferred. However, as the production of ATP from fatty acids is a natural process, when there is a lack of available glucose or during fasting, cells can choose to switch to FAO. Rapidly proliferating tumour cell consume a lot of energy and as such alternative ATP production may be required via other metabolic pathways specifically exploited in cancer. β-oxidation breaks down FAs two carbon atoms at a time, back into acetyl-coA units, reusing the increasingly shortened chains for further oxidation and subsequent ATP production [75]. Fatty acid oxidation was shown in GBM as an efficient mechanisms to produce ATP in nutrient unfavourable conditions [64] and is reviewed in extensive detail in [76]. FAO occurs in the mitochondrial matrix where fatty acyl CoA is converted to β-ketoacyl-CoA and a unit of acetyl CoA that can be fed back into the TCA cycle for ATP production. The β-ketoacyl-CoA is now 2 carbon units shorter than it was, with the process repeating until the fatty acid has been completely consumed. Shortening of the fatty acid does not directly produce energy, but it does produce NADH that generates ATP from the electron transport chain as well as acetyl-CoA that can go back into the TCA.

Although FAO is important for GBM tumours, the preferred method of energy generation through ATP synthesis is via glycolysis. However, a recent study reports that glucose accounts for less than 50% of the acetyl CoA pool in human GBM as evidenced using radio-labelled glucose, suggesting FAO may play a bigger role in the energy needs of proliferating GBM tumours [63].

Carnitines play a key role in β-oxidation of fatty acids by transporting long chained FA into the mitochondria, known as the carnitine shuttle. Free fatty acids are not permeable to the mitochondrial membranes and cannot pass through without first forming acyl-carnitines. Free carnitine conjugation to FAs is controlled by carnitine palmityl transferase 1 (CPT-1), located in the mitochondrial membrane [78]. Carnitine palmityl transferase 1 are upregulated enzymes associated with GBM fatty acid oxidation and have been found in both pre-clinical and clinical cases [66, 79]. As well as FAO being prevalent in glioma cells of human origin, *Lin et al.* also showed that the fatty acid oxidation inhibitor etomoxir slowed tumour growth in a mouse model of glioma which subsequently increased survival. After transport of fatty acyl CoAs to the mitochondria for metabolism, carnitine is released. For any tumour cell to facilitate oxidation of fatty acid, carnitines must also be present and involved. As such a relationship exists between the fatty acids, fatty acyl carnitines and free carnitine within tumour cells.

Fatty acids are also key components of phospholipids, that contain two fatty acid groups bonded to a glycerol backbone. Phospholipids are major components of the cell membrane alongside cholesterol providing structure to cells as well as being involved in cell signalling processes. One such class of phospholipids involved in signalling are phosphatidylinositol’s (PI).

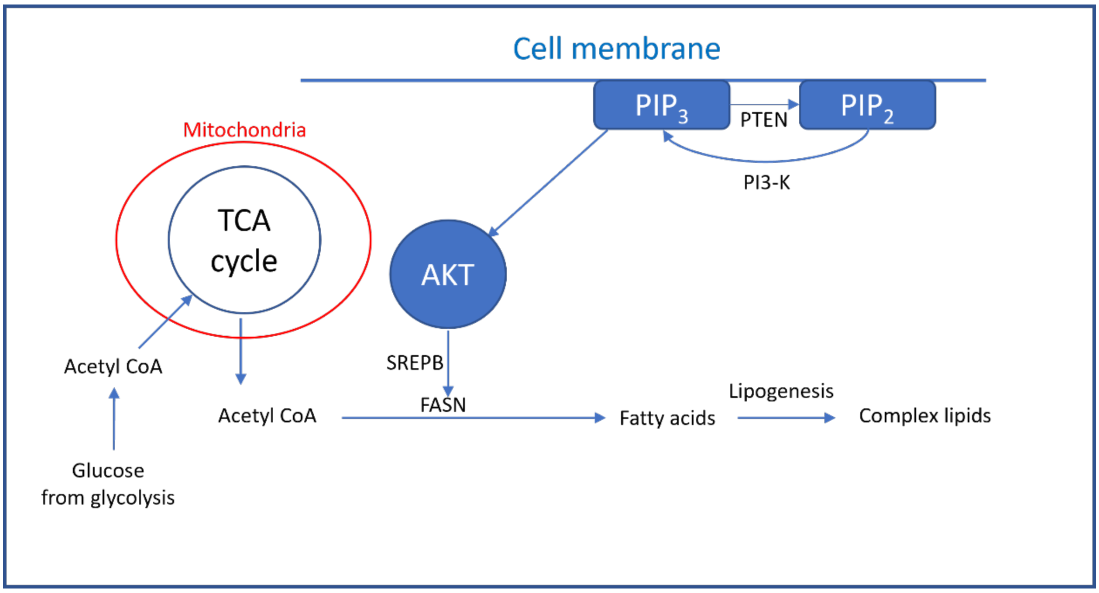

Figure 5 – Overview of phosphatidylinositol signalling pathway and downstream activation of AKT linked to fatty acid metabolism. Abbreviations: Protein Kinase B (AKT), phosphatidylinositol (3,4,5)-trisphosphate (PIP_3) and phosphatidylinositol (4,5)-bisphosphate (PIP_2), Fatty acid synthase (FASN), tricarboxylic acid cycle (TCA), Phosphatase and tensin homolog (PTEN), phosphatidylinositol-3 kinase (PI3-K).

Signalling PIs are controlled via the Phosphoinositide 3-kinase (PI3-K) pathway, which is shown to be one of the most altered pathways in cancer. PI3-K is a class of enzymes that catalytically converts PIP_3 to PIP_2 through the hydrolysis of a phosphate group on the inositol headgroup and as such signals via PI lipid species. PI3-K, and the associated pathways of Receptor tyrosine kinase (RTK) and (RAS) signalling, are the main genetically altered pathways in GBM, with 88% of all tumours found to harbour an alteration to this pathway [49]. Overexpressed PI3-K signalling affects downstream AKT (Protein Kinase B) acting as a regulator for many critical cellular functions including cell cycle progression, angiogenesis, migration/ invasion and cell survival and hence is a crucial prognostic determinant of malignant neoplasm [55]. On overview of the downstream AKT signalling pathway is shown in Figure 6.

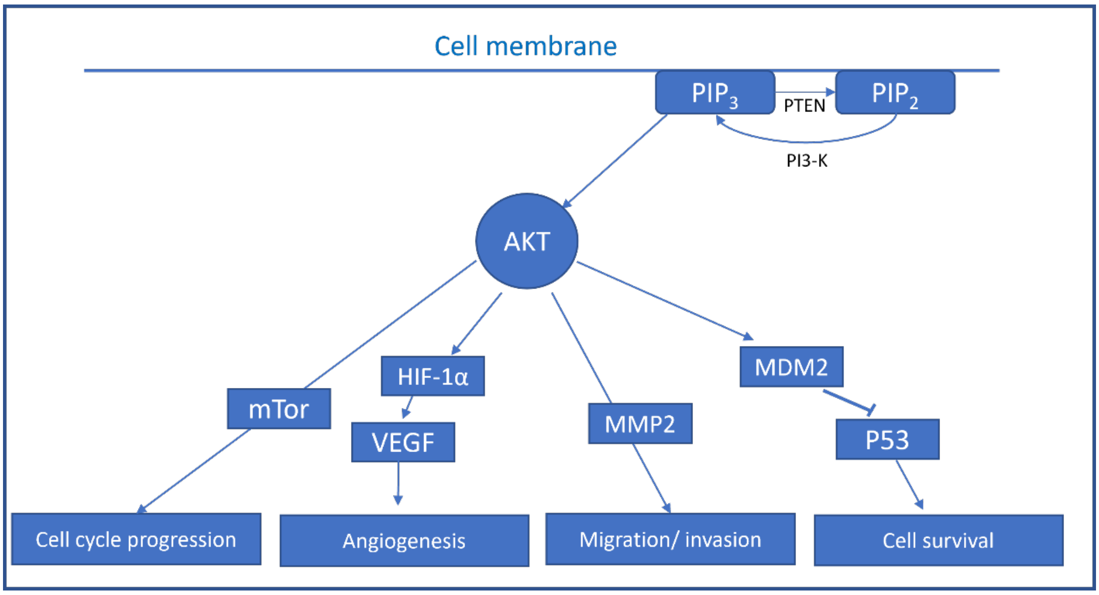

Figure 6 – Regulation of AKT and PI3-K signalling pathways by PTEN. PI3-K signalling pathway and downstream AKT signalling. Activation of PI3K generates PIP3, which recruits AKT to the membrane where it is phosphorylated and downstream acts as a regulator for many critical cellular functions. An example of a few downstream signalling molecules are shown The Example of abbreviations Protein Kinase B (AKT), phosphatidylinositol (3,4,5)-trisphosphate (PIP_3) and phosphatidylinositol (4,5)-bisphosphate (PIP_2), Fatty acid synthase (FASN), tricarboxylic acid cycle (TCA), Phosphatase and tensin homolog *(PTEN), phosphatidylinositol-3 kinase (PI3-K), Hypoxia-inducible factor 1-alpha (HIF-1α), Vascular endothelial growth factor (VEGF), Mechanistic target of rapamycin (mTor), Mouse double minute 2 homolog (MDM2), matrix metalloproteinase-2 (MMP2), protein 53 (P53).*

PI3-K and Akt also have a role in lipid metabolism whereby downstream signalling via SREBP regulates lipid metabolism via the production of fatty acids through FASN [80].

It is important to accurately determine the lipidomic profiles of GBM to evaluate the phospholipid makeup and the relationship between fatty acids and carnitine molecular species. Mass spectrometry imaging analysis of pre-clinical models and clinical biopsies of GBM can show high specificity and sensitivity to lipid species and as such will be used as the analytical technique in this thesis and is described in section 3.

3. Lipid identification by mass spectrometry

3.1. Tandem mass spectrometry

Tandem mass spectrometry (MS/MS) is a mass spectrometry method whereby molecular species ionised in the relative source are fragmented, producing a number of small fragment species that can be used to determine the structural makeup of the *m/z* species of interest.

There are many methods available to produce fragmentation in MS/MS. Collision induced dissociation (CID) introduces a high energy gas into the stream of ions, causing collisions between the neutral gas particles and the intact molecular species. Due to their high energy, fragmentation occurs of the intact species or parent ions, producing a number of smaller fragments or daughter ions. CID is the method of fragmentation in the Xevo G2-XS and used for MS/MS analysis of lipids in this work and is well documented [81].

Other types of MS/MS include in-source decay which is commonly used for electrospray ionisation (ESI) sources, whereby the energy of the source is increased, causing overload of charge on the molecular species, in turn causing fragmentation and the release of smaller charge molecules. Like in-source decay, Electron capture dissociation (ECD) uses electrons to increase the charge of the *m/z* species until they fragment into smaller molecular species.

Surface induced dissociation (SID) is an alternate fragmentation technique that used a surface to fragment the molecular species rather than a gas. Parent ions are accelerated towards a hard surface and upon impact cause fragmentation and release of fragment ions.

3.2. Lipid identification

Tandem MS/MS is used to determine the lipid class as well as the complete lipid makeup. Lipid identification is possible by fragmenting the intact parent ion to reveal a molecular fingerprint and multiple daughter ions. These daughter ions allow lipid identification through detection of the lipid species head group, alongside the two fatty acyl chains and associated mass fragments. Utilising the quadrupole feature of the Xevo G2-XS allows specific fragmentation at each *m/z* window, corresponding to an abundant molecular ion species, allowing precise MS/MS identification of the lipid species to be undertaken. In negative ion mode, the fatty acyl side chains of phospholipids are readily ionisable, often the most abundant species in the MS/MS spectra, so offer straight forward identification of the lipid species. Identification in positive ion is slightly trickier as these fatty acyl species do not analyse, so identification is based on the accurate molecular weight and head group fragment loss and detection from the parent ion.

MS/MS fragmentation by CID is sufficient to determine the molecular class of species and fatty acyl side groups but cannot fully determine the lipid structure and SN1/ SN2 orientation of the detected fatty acyl groups. To determine SN1 and SN2 location of the fatty acid species techniques utilising ion-trap technologies such as OzID can be utilised, whereby ozone is introduced across the carbon carbon double bonds to reveal further chemical information [82].

Shorthand nomenclature for lipid assignment states the class of phospholipid, number of carbon atoms and number of double bonds (unsaturation levels) for each fatty acid component, listed in the likely order of SN1 and SN2 position. In these cases, fatty acid positioning is undetermined, and this nomenclature uses a '_' to represent that either fatty acid could be in the SN1 or SN2 positions. A rule of thumb for MS/MS data shows SN1 or R_1 cleaves preferentially to SN2 or R_2, so typically the fatty acyl in R_1 position will be higher in abundance in the MS/MS spectra than R_2 [83]. Brain specific lipids also show polyunsaturated fatty acids to favour R_2 positioning, whilst saturated fatty acids preferentially occupy the R_1 position [84]. These points have been taken into account when labelling the lipid species in this document.

In this thesis where MS/MS has been undertaken and successfully identified lipid species, in text will outline the fatty acid groups of this molecule e.g., PI (18:0_20:4) with the fatty acid R groups in order of likely occurrence. Whereas if MS/MS cannot determine the exact lipid species, accurate mass will be used alongside METLIN [85] information to derive a likely lipid species, identified in text by PI (38:4), showing the phospholipid class and the total carbon atoms and number of carbon carbon double bonds across the two fatty acid sidechains.

To determine lipid species from firstly single MS data and then proceeding to the MS/MS experiments, METLIN™ (The Scripps Research Institute) [85] is first used to determine possible isomeric lipid species, from the instrument measure masses. This produces a series of possible lipid groups and isomers corresponding to this m/z mass. Upon lipid isomer & class determination, next Lipid Maps Product Ion Calculation Tool for Glycerophospholipids (negative ion mode) provides MS/MS fragmentation data for the lipid species covering phosphatidylcholine (PCho), phosphatidic acid (PA), phosphatidylserine (PS), phosphatidylethanolamine (PE), phosphatidylglycerol (PG) & PI. Isomeric lipid species at the same molecular weight vary in their MS/MS data, with key discriminating factors arising from the chain length of the R1 & R2 groups: fatty acid groups as well as head-group fragment masses and patterns.

4. Mass spectrometry imaging

Mass spectrometry (MS) is a powerful analytical technique whereby gaseous ionised chemical species are identified through sensitive detection and determination of their mass to charge ratios (*m/z*), allowing the analysis of the molecular makeup within a sample.

Since MS introduction in 1897, a wide variety of mass spectrometers have been developed with recent advances in MS imaging (MSI) used for tissue imaging and diagnostic approaches [86-89]. Many MS imaging methodologies are available to analyse a variety of biochemical species from large molecular weight proteins to low molecular weight metabolites and as such MS imaging has a key application in research. MS imaging is typically carried out on thin tissue sections between 10-20 µm thickness.

In a single MS imaging experiment, hundreds of mass spectra are acquired at pre-defined points across a sample surface known as pixels. Each pixel will contain a single mass spectrum, of which there will be many analytes of interest corresponding to an individual *m/z* value. In an MSI experiment a particular *m/z* value can be isolated, and the intensity of that *m/z* value mapped across the entire imaging dataset, producing ion intensity distribution maps, Figure 7.

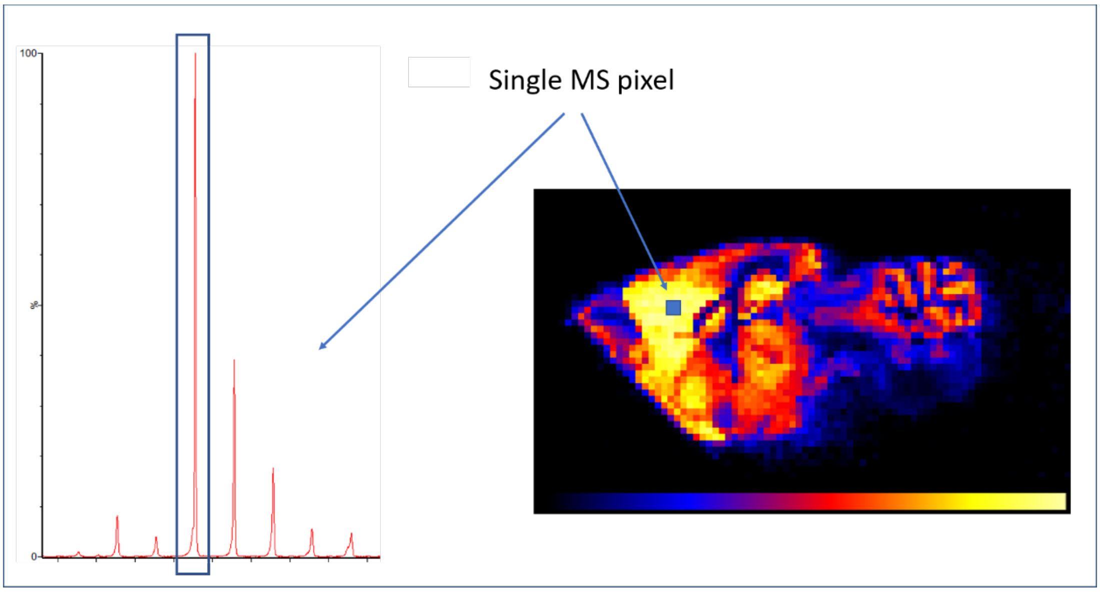

Figure 7 – An example of MS imaging in a control mouse brain section analysed by DESI-MS imaging. A single m/z peak can be selected, and the ion intensity mapped across the entire tissue section to reveal spatial information. This process can be repeated for every m/z species in the spectra and as such a plethora of data is available for MS imaging analysis

Combining MSI data with histology-stained sections is crucial to elucidate spatially resolved information about chemical species across a sample surface, providing key information on the distribution of analytes in relation to cellular features. The most commonly used MSI techniques are secondary ion mass spectrometry (SIMS), matrix assisted laser desorption ionisation (MALDI) MS, and desorption electrospray ionisation (DESI) MS. These label free, *ex-vivo* imaging techniques can map a wide range of biomolecular species.

SIMS and MALDI are traditional vacuum ionisation methods, but more recently a large number of ambient ionisation MS methods has entered the field, which has changed the way molecular information can be obtained, in near real time and under standard laboratory conditions. More than 30 ambient ionisation MS techniques have been developed [90] since DESI was introduced in 2004 [91], including laser ablation electrospray ionisation (LAESI) [92], easy ambient sonic-spray ionization (EASI) [93], direct analysis in real time (DART) [94], probe electrospray ionisation (PESI) [95], Touch Spray [96] amongst others which are described in Table 1.

Table 1 – An overview of mass spectrometry imaging techniques.

MS imaging technique	Ionisation and desorption source	Analytes analysed	Spatial resolution	Mass range	Ref
Matrix Assisted Laser Desorption Ionisation (MALDI)	UV laser beam	Metabolites, lipids, proteins, pharmaceuticals, and endogenous compounds	5 µm	Up to m/z 100,000	[97]
Secondary Ion Mass Spectrometry (SIMS)	Ion beam/ ion cluster gun	Small molecules, metabolites, and lipids	50 nm	Up to m/z 2000 with water cluster beam	[98]
Laser Ablation Inductively Coupled Plasma Mass Spectrometry (LA-ICP-MS)	UV lasers	Metal ions	Sub-micron range	Based on mass of metal ions of interest. Up to m/z 300	[99]

Desorption Electrospray Ionisation (DESI)	Charged droplet stream generated from ESI plume	Small molecules, metabolites, lipids, pharmaceuticals, and peptides	20 µm	Up to m/z 2000	[91]
Rapid Evaporation Ionisation Mass Spectrometry (REIMS)	Electrosurgical equipment	Lipids and metabolites	0.5 mm	Up to m/z 1000	[100]
Laser desorption ionisation (LDI)	Laser based electrosurgical equipment. CO$_2$, femtosecond lasers	Lipids and metabolites	10 µm using a femtosecond laser	Up to m/z 1000	[101]
Laser Ablation Electrospray Ionisation (LAESI)	IR laser	Proteins, lipids, and metabolites	55 µm	Up to m/z 2000	[102]
Easy Ambient sonic-spray ionization (EASI)	Charged droplet stream generated from sonic spray ionization	Small molecules, metabolites, lipids, pharmaceuticals, and peptides	150 µm	Up to m/z 2000	[103]
Direct Analysis in Real Time (DART)	Electrochemically charged gas particles	Small molecules including explosives and pharmaceuticals, lipids, amino acids and peptides	Dependant on instrument/ other source combined with for imaging	Dependant on MS instrument coupled to	[94]
Probe Electrospray Ionisation (PESI)	Charged electrospray	Metabolites, small molecules.	60 µm	Up to 1000 Da	[104]
Liquid extraction	Static solvent forming a liquid	Lipids, small molecules, and	1 mm	50-2000	[105]

surface analysis (LESA)	microjunction and nonspray ionsiation	metabolites and proteins.			

For the work presented in this thesis the mass spectrometry imaging techniques of DESI-MS and LA-ICP-MS were selected as to yield information on both the lipidomics and metallomics of the samples analysed.

Although many mass spectrometry imaging techniques exist DESI and LA-ICP-MS are well established and widely used for lipid and metal imaging respectively. Many ambient ionisation imaging methods are based on the principles of ESI and as such yield comparative data to that of DESI-MS and will also show high abundance of lipid species in the spectra. DESI-MS however has an excellent spatial resolution, pushing 20 µm with recent advances as well as a rapid analysis time that make it stand out compared to others.

The analysis of metals in clinical samples is limited particularly for mass spectrometry imaging methods. As such LA_ICP-MS is the standout technique to image metal ions at high spatial resolution as well as in a rapid and cost-efficient analysis time.

4.1. DESI-MS

DESI was the first ambient ionisation mass spectrometry technique to be described for surface analysis, and subsequently imaging [106], in 2004 by Cooks *et al*. [91]. DESI was developed from the principles evidenced in electrospray ionisation (ESI), whereby an electrically charged solvent produces gaseous ions. As an ambient ionisation technique, the introduction of DESI solved the problems associated with traditional feature of MS instruments whereby the sample for analysis must be introduced into a vacuum system [91], as in MALDI and SIMS. DESI-MS analysis occurs externally to the MS instrument at ambient temperatures and pressures. Analysis at atmospheric pressure also alleviates the problem that delicate samples can be damaged at high vacuums and increase the range of samples that can be analysed.

Basic principles of DESI involve the direct application of a stream of electrosprayed aqueous droplets to a specific location on the sample surface, located on a 2D moveable stage at atmospheric temperature and pressure. Upon contact, the aqueous droplets dissolve biochemical species from the sample producing ions via smaller, secondary, electrospray-like droplets, which are transferred to the mass spectrometer along a pressure gradient via a heated capillary, Figure 8. The heated capillary aids desolvation and ion droplet formation, typically set to 400-500 °C, powered at 12 V and 2.65 A for lipid analysis. Common mass analysers coupled to DESI sources include quadrupole Time of Flight (QToF), triple quadruple (QqQ or Q^3), ion traps and ion mobility mass spectrometry (IMS). In this thesis a Xevo G2-XS QToF is utilised for all DESI-MSI analysis.

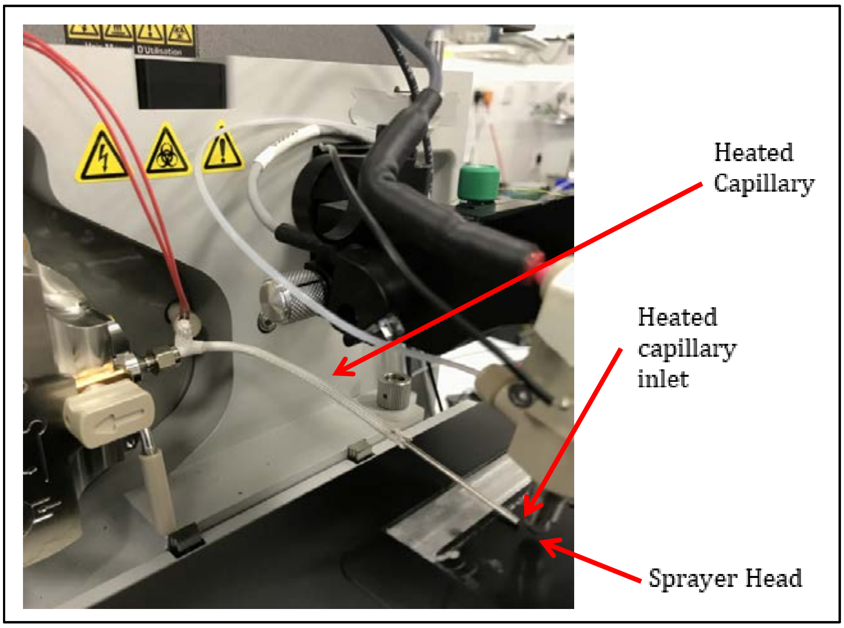

Figure 8 – A view of the heated capillary on the DESI-MSI setup on the Xevo G2-XS used throughout this work. The sample sits just below the sprayer head and heated capillary inlet which are both fixed in position above the 2D Prosolia stage. The 2D stage below can move and raster underneath the sprayer source to produce DESI-MS images.

DESI-MS has emerged as the most extensively-used ambient MS technique with applications in chemical imaging, analysis of tissue sections for imaging experiments [90], detection of explosives and forensics [107] amongst others.

One of the most widely used biological application of DESI is in analysing and characterising tissue samples. The different molecular species that can be detected via DESI includes proteins, peptides, lipids, drugs, and metabolites, making DESI an excellent choice of analytical tool to obtain large amounts of information from a single tissue section. The ability to raster the sample via the 2D stage located underneath the fixed spray nozzle, allows the distribution pattern of particular analytes of interest to be determined. The spatial resolution of the technique is defined as the distance between adjacent mass spectral points. True spatial resolution is determined by a number of factors that affect the solvent spray spot size, which itself is dependent on a range of different parameters available to the DESI system, such as MS scan time and stage velocity [108]. Spatial resolution of an imaging experiment is determined by several factors but must be considered carefully to determine the requirements of the scientific question being asked. Increasing spatial resolution is time consuming, so often DESI-MSI will be first performed at a large spatial resolution, such as 200 µm, before further high-resolution targeted acquisition which is made possible by the non-destructive nature of DESI-MSI. Typical spatial resolution of DESI-MS imaging is around 50-100 µm, however, recent advances to the DESI sprayer, alongside extensive optimisation of external parameters has allowed DESI-MSI experiments to be performed down as far as 20 µm spatial resolution [109]. Optimised parameters include solvent spray, scan time, step size and the optimisation of the DESI sprayer unit [110].

4.1.1. Sample Preparation

DESI & other ambient ionisation MS techniques are able to produce mass spectra from condensed phase samples with minimal or no sample preparation. A key advantage over other vacuum based methods is the sample analysis is carried out at atmospheric pressures and temperatures [86]. Atmospheric analysis via DESI-MS enable easy access to the sample and will be a key feature for many applications, particularly in allowing high throughput analysis [111]. In the analysis of biological tissues, no sample pre-treatment is needed whereas for samples analysed by MALDI-MS, samples must be coated with matrix prior to analysis which adds time and introduces an external substance and possible matrix affects associated with MALDI-MS. Typically, cryomicrotome cut sections of animal tissue are mounted onto histology glass slides and can be analysed directly by the solvent spray [112]. Importantly DESI-MS is a non-destructive MS imaging technique, and the sections can be used for further analysis such as histological staining. This is key to aligning DESI-MS imaging data with histology-stained images, providing key localisation data and assignment of MS data with histology features.

4.1.2. DESI Mechanisms

As DESI is based upon electrospray ionisation (ESI), the ionisation is well characterised. What is novel to DESI is the interaction of the electrosprayed droplets with a sample surface. A schematic of the DESI process, Figure 9, outlines how analytes are extracted from the sample surface by droplet pickup [112], which acts as the main mechanism of desorption and ionisation in DESI. Droplet pickup creates secondary micro-droplets which, if sufficient extraction has occurred, will contain the key biological information of the sample that is subsequently transferred to the MS [108]. This ionisation mechanism via a two-step liquid droplet pickup, has been validated using Phase Doppler Particle Analysis (PDPA) as well as computational fluid dynamics [113-115].

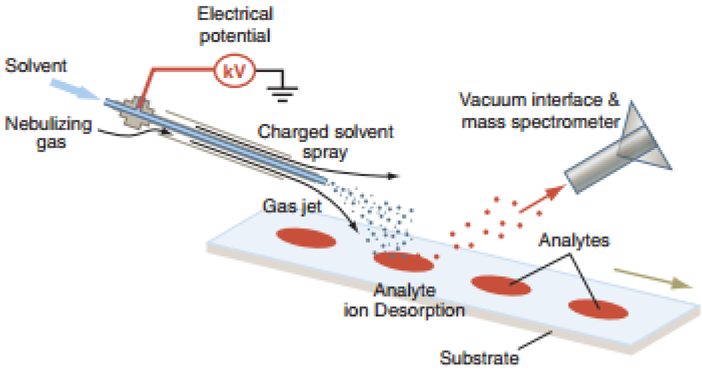

Figure 9 – A schematic of the DESI instrumentation and ionisation process, in the analysis of chemical samples. Taken from [41]

Similar to ESI, DESI produces both singularly charged and multiply charged ions of biological analytes [91], in a soft ionisation manner. Soft ionisation produces intact parent ions rather than molecular species with associated fragmentation patterns [116]. It is possible to obtain fragmentation of chemical ions in a DESI-MS setup, however fragmentation is introduced by collision induced dissociation (CID) using a high energy gas further along the mass spectrometry ion path, rather than ionising fragmentation as seen in MS techniques such as SIMS. Throughout this thesis, the DESI ion source is coupled to the Xevo G2-XS instrument that contains a quadrupole time of flight (QToF) mass filtering and detection system.

The key to a successful DESI-MS experiment is the extraction and ionisation of analytes from sample surface into charged droplets, a process greatly affected by the solvent spray. Changing solvent composition can be used to target specific classes of biomolecules [116], as well as increasing the sensitivity of analysis [117] [118]. DESI is able to detect many different classes of biomolecules including highly abundant lipids [119] [118] and proteins in liquid samples [120], [121], drug molecules [111, 122], metabolites [122] and hydrophobic solvents [108]. Recently, reactive DESI has allowed analysis of traditionally difficult to ionise substances including steroids [123], cholesterol [124] and saccharides [125]. Although a number of chemical classes can be analysed by DESI, it is particularly well suited to the analysis of lipids: covering fatty acids, phospholipids and glyceride molecules which is the major use in this work.

There are many parameters that must be optimised for successful experimental work with DESI-MS. There is a fine balance between the solvent spray, solvent flow rate, gas pressure and capillary voltage all of which must be optimised for imaging experiments. Traditional DESI solvent compositions use a combination of MeOH:H_2O [107] with a high MeOH % which fits in with the important solvent properties; electrical conductance, analyte extractability and volatility [116]. In this work MeOH:H_2O ratio of 98:2% is used which allows successful lipid extraction. Optimisation of the geometry of the DESI source, is vital for sufficient analyte extraction and must be optimised prior to analysis [112]. Optimised geometries used in this work are typically 1.5 mm spray tip to sample surface, 6 mm sprayer to heated capillary inlet, 80^o sprayer impact angle with a 5^o collection capillary angle.

DESI-MS is well suited for the analysis of lipids from biological samples and will provide an excellent technique to analyse the samples throughout this thesis. However, DESI-MS cannot provide any further information on the metal content of a sample and as such to probe metallomic information, LA-ICP-MS; a complimentary analysis technique will be required.

4.2. LA-ICP-MS

Laser ablation inductively coupled plasma mass spectrometry (LA-ICP-MS) is an elemental analytical technique able to image the metal ion distribution in samples. Combining a laser abaltion unit with a classical inductively coupld plasma mass spectrometry (ICP-MS) system allows for metal ion distirbution to be mapped across a solid sample surface and was first described in 1985 by Gray [99]. LA-ICP-MS has applications for the analysis of multiple samples including rocks and minerals to biological material, which is becoming more common in recent years. LA-ICP-MS imaging exhibits spatially resolved information of high precision elemental and stable isotope analysis, with a primary application for metal ion distribution on the low µm scale (10-100 µm).

As observed for DESI-MS imaging analysis, minimal sample preparation is required for LA-ICP-MS which typically analyses thin, flat solid sample surfaces. Laser ablation occurs using a powerful pulsed laser beam (typically nanosecond) to remove material from the sample surface. Shorter wavelength ultraviolet (UV) lasers, particularly the 193 nm ArF Excimer and 213 nm frequency coupled Nd:YAG lasers used in this thesis, provide excellent ablation conditions with subsequent efficient atomisation and ionisation of material in the inductively coupled plasma (ICP) torch [126]. The laser causes heating, evaporation and ionisation of the sample producing a plume of particles and ions, transferred to the inductively coupled plasma (ICP) torch by a constant flow of argon or helium. In the ICP torch, particles and ionic material is vaporised and converted to elemental ions and further transported to the MS unit where ions are separated and detected based on their *m/z*. Ion signals can be converted to concentrations by analysis with matrix matched standards [127]. An important aspect of LA-ICP-MS is the ability for quantitative analysis, which is not readily achievable with other MS imaging techniques due to matrix affects [128]. Matrix affects are commonly observed in mass spectrometry imaging analysis whereby the substrate being analysed influences the ionisation of endogenous molecules, or the molecules being analysed within a sample. This can cause the intensity of the analyte to be less than expected and cause issues in the analysis. Matrix affects from the substrate are less prevalent in LA-ICP-MS analysis of tissue samples as the entire region being imaging and analysed is ablated, leaving no tissue behind. The entire tissue is then atomised and ionisation occurs in the plasma gun.

4.3. Ambient ionisation methods for intraoperative tumour detection

Ambient ionisation mass spectrometry techniques are growing in popularity with a particular focus on the analysis and differentiation of biological tissue specimens. Acquiring MS profiles of multiple tissue types followed by subsequent multivariate analysis allows for tissue characterisation based on the MS spectra alone and makes these techniques useful for molecular pathology analysis over conventional histopathology. Tissue characterisation based solely on MS profiles is widely used for investigation of disease states, with particular relevance for rapid cancer and tumour analysis and determination in a surgical oncology situation. As such a number of ambient ionisation MS techniques have been developed and implemented in translational research for intraoperative analysis; DESI-MS imaging has been used for intraoperative assessment of tumour margins in gliomas [129], intelligent knife (iKnife) based on rapid evaporative ionisation mass spectrometry (REIMS) is an established technique utilising surgical devices for in vivo real time analysis of breast, ovary and cervical cancers [130-132], picosecond infrared laser (PIRL) for medulloblastoma analysis [133], the mass spec pen [134], and most recently SpiderMass utilising water assisted laser desorption ionisation (WALDI) [135].

5. Aims and objectives

The aim of this research project was to explore the use of mass spectrometry imaging (MSI) methods to study the lipid profiles in a range of biological samples of glioblastoma and to determine new lipid signatures of GBM. These data will then be compared to a plethora of multimodal techniques to highlight the potential of MSI in multimodal lipidomic research. The biological samples utilised will range from cellular materials through to human tissue samples, to examine how MSI can complement current gold standard techniques, in both clinical and preclinical settings.

Glioblastomas, like other tumours, are known to use free FA as an alternative energy source, aiding growth and proliferation, to that of glucose. To explore this phenomenon further, we aimed to utilise DESI-MSI to examine the distribution of lipid profiles in pre-clinical orthotopic glioblastoma tumour models. To confirm the location of the tumour, these samples will be imaged using MRI, which is the current industry gold standard. To further compare our findings to those of MRI, we aim to use LA-ICP-MS to explore the distribution of gadolinium within the MRI contrast agents as well as endogenous metal ions, to validate how MSI methods can completement these findings by providing an additional dimensionality to the data set.

Previous studies have highlighted the benefits of using 5-ALA as a fluorescent intra-operative visualisation guide of tumour margins. However, it is currently unknown how the tumour cells uptake this marker. This study aimed to correlate the pre-clinical MSI data collected and examine how these can be further expanded into clinical research. Using DESI-MS, human tissue samples will be imaged to examine the cellular molecular signature of 5-ALA to aid in understanding the uptake into tumour cells. Lipid profiles generated by DESI-MSI in clinical biopsies can also be linked to pre-clinical data to show the complementarity of pre-clinical orthotopic models.

Currently, histological staining with H&E is commonly used to aid in determining spatial distribution of cellular species within a biological section, be it clinical or pre-clinical. However, due to the harsh nature of the organic solvents used for washing, pre-stained tissue samples are unsuitable for MS imaging experiments. This study will aim to provide an alternative histology stain to that of H&E, by assessing the compatibility of stained tissue sections with lipid analysis and imaging quality acquired by DESI-MSI. This will offer the future potential to use directed MSI approaches, targeting areas of interest prior defined by histology.

Overall, this research aims to employ a wide variety of multivariate analysis technique to validate the findings, as well as highlight the benefit of using MSI methods alongside other more standard imaging techniques in a multimodal fashion.

6. References

1. Louis, D.N., et al., *The 2016 World Health Organization Classification of Tumors of the Central Nervous System: a summary.* Acta Neuropathologica, 2016. **131**(6): p. 803-820.
2. Thakkar, J.P., et al., *Epidemiologic and Molecular Prognostic Review of Glioblastoma.* Cancer Epidemiology Biomarkers & Prevention, 2014. **23**(10): p. 1985-1996.
3. Li, Q.J., J.Q. Cai, and C.Y. Liu, *Evolving Molecular Genetics of Glioblastoma.* Chinese Medical Journal, 2016. **129**(4): p. 464-471.
4. Brodbelt, A., et al., *Glioblastoma in England: 2007-2011.* European Journal of Cancer, 2015. **51**(4): p. 533-542.
5. Louis, D.N., et al., *The 2007 WHO classification of tumours of the central nervous system.* Acta Neuropathologica, 2007. **114**(2): p. 97-109.
6. Vartanian, A., et al., *GBM's multifaceted landscape: highlighting regional and microenvironmental heterogeneity.* Neuro-Oncology, 2014. **16**(9): p. 1167-1175.
7. Darefsky, A.S., J.T. King, and R. Dubrow, *Adult glioblastoma multiforme survival in the temozolomide era: A population-based analysis of Surveillance, Epidemiology, and End Results registries.* Cancer, 2012. **118**(8): p. 2163-2172.
8. Ostrom, Q.T., et al., *CBTRUS Statistical Report: Primary Brain and Central Nervous System Tumors Diagnosed in the United States in 2008-2012.* Neuro-Oncology, 2015. **17**: p. 1-62.
9. Aldape, K., et al., *Glioblastoma: pathology, molecular mechanisms and markers.* Acta Neuropathologica, 2015. **129**(6): p. 829-848.
10. Dimitrov, L., et al., *New Developments in the Pathogenesis and Therapeutic Targeting of the IDH1 Mutation in Glioma.* International Journal of Medical Sciences, 2015. **12**(3): p. 201-213.
11. Gutman, D.A., et al., *MR Imaging Predictors of Molecular Profile and Survival: Multi-institutional Study of the TCGA Glioblastoma Data Set.* Radiology, 2013. **267**(2): p. 560-569.
12. Shukla, G., et al., *Advanced magnetic resonance imaging in glioblastoma: a review.* Chin Clin Oncol, 2017. **6**(4): p. 40.

13. Xiao, Y.-D., et al., *MRI contrast agents: Classification and application.* International journal of molecular medicine, 2016. **38**(5): p. 1319-1326.
14. Zhou, Z. and Z.R. Lu, *Gadolinium-based contrast agents for magnetic resonance cancer imaging.* Wiley Interdisciplinary Reviews: Nanomedicine and Nanobiotechnology, 2013. **5**(1): p. 1-18.
15. Morokoff, A., et al., *Molecular subtypes, stem cells and heterogeneity: Implications for personalised therapy in glioma.* Journal of Clinical Neuroscience, 2015. **22**(8): p. 1219-1226.
16. Stupp, R., et al., *Radiotherapy plus concomitant and adjuvant temozolomide for glioblastoma.* New England Journal of Medicine, 2005. **352**(10): p. 987-996.
17. Wang, H.X., et al., *The Challenges and the Promise of Molecular Targeted Therapy in Malignant Gliomas.* Neoplasia, 2015. **17**(3): p. 239-255.
18. Raizer, J.J., et al., *A Phase 2 Trial of Single-Agent Bevacizumab Given in an Every-3-Week Schedule for Patients With Recurrent High-Grade Gliomas.* Cancer, 2010. **116**(22): p. 5297-5305.
19. Weller, M., et al., *How we treat glioblastoma.* ESMO open, 2019. **4**: p. e000520.
20. Weller, M., et al., *EANO guideline for the diagnosis and treatment of anaplastic gliomas and glioblastoma.* Lancet Oncology, 2014. **15**(9): p. E395-E403.
21. Ataman, F., et al., *Quality assurance of the EORTC 26981/22981; NCIC CE3 intergroup trial on radiotherapy with or without temozolomide for newly-diagnosed glioblastoma multiforme: the individual case review.* European Journal of Cancer, 2004. **40**(11): p. 1724-1730.
22. Kuhnt, D., et al., *Correlation of the extent of tumor volume resection and patient survival in surgery of glioblastoma multiforme with high-field intraoperative MRI guidance.* Neuro-Oncology, 2011. **13**(12): p. 1339-1348.
23. Orringer, D., et al., *Extent of resection in patients with glioblastoma: limiting factors, perception of resectability, and effect on survival Clinical article.* Journal of Neurosurgery, 2012. **117**(5): p. 851-859.
24. Duffau, H., et al., *Usefulness of intraoperative electrical subcortical mapping during surgery for low-grade gliomas located within eloquent brain regions: functional results in a consecutive series of 103 patients.* Journal of Neurosurgery, 2003. **98**(4): p. 764-778.
25. Chinot, O., et al., *PHASE III TRIAL OF BEVACIZUMAB ADDED TO STANDARD RADIOTHERAPY AND TEMOZOLOMIDE FOR NEWLY-DIAGNOSED GLIOBLASTOMA: MATURE PROGRESSION-FREE SURVIVAL AND PRELIMINARY OVERALL SURVIVAL RESULTS IN AVAGLIO.* Neuro-Oncology, 2012. **14**: p. 101-101.
26. Butowski, N., et al., *Historical controls for phase II surgically based trials requiring gross total resection of glioblastoma multiforme.* Journal of Neuro-oncology, 2007. **85**(1): p. 87-94.
27. Nam, J.Y. and J.F. De Groot, *Treatment of glioblastoma.* Journal of oncology practice, 2017. **13**(10): p. 629-638.
28. Thon, N., et al., *Predominant influence of MGMT methylation in non-resectable glioblastoma after radiotherapy plus temozolomide.* Journal of Neurology Neurosurgery and Psychiatry, 2011. **82**(4): p. 441-446.
29. Noorbakhsh, A., et al., *Gross-total resection outcomes in an elderly population with glioblastoma: a SEER-based analysis.* Journal of Neurosurgery, 2014. **120**(1): p. 31-39.

30. Kreth, F.-W., et al., *Gross total but not incomplete resection of glioblastoma prolongs survival in the era of radiochemotherapy.* Annals of oncology, 2013. **24**(12): p. 3117-3123.
31. Hegi, M.E., et al., *MGMT gene silencing and benefit from temozolomide in glioblastoma.* New England Journal of Medicine, 2005. **352**(10): p. 997-1003.
32. Senft, C., et al., *Intraoperative MRI guidance and extent of resection in glioma surgery: a randomised, controlled trial.* Lancet Oncology, 2011. **12**(11): p. 997-1003.
33. Stummer, W., et al., *Extent of resection and survival on glioblastoma multiforme-identification of and adiustment for bias.* Neurosurgery, 2008. **62**(3): p. 564-574.
34. Lacroix, M., et al., *A multivariate analysis of 416 patients with glioblastoma multiforme: prognosis, extent of resection, and survival.* Journal of Neurosurgery, 2001. **95**(2): p. 190-198.
35. Bloch, O., et al., *Impact of extent of resection for recurrent glioblastoma on overall survival Clinical article.* Journal of Neurosurgery, 2012. **117**(6): p. 1032-1038.
36. Parker, N.R., et al., *Molecular heterogeneity in glioblastoma: potential clinical implications.* Frontiers in Oncology, 2015. **5**.
37. Kubben, P.L., et al., *Intraoperative MRI-guided resection of glioblastoma multiforme: a systematic review.* Lancet Oncology, 2011. **12**(11): p. 1062-1070.
38. Stummer, W., et al., *Fluorescence-guided surgery with 5-aminolevulinic acid for resection of malignant glioma: a randomised controlled multicentre phase III trial.* Lancet Oncology, 2006. **7**(5): p. 392-401.
39. Regula, J., et al., *PHOTOSENSITIZATION AND PHOTODYNAMIC THERAPY OF ESOPHAGEAL, DUODENAL, AND COLORECTAL RUMORS USING 5-AMINOLEVULINIC ACID-INDUCED PROTOPORPHYRIN-IX - A PILOT-STUDY.* Gut, 1995. **36**(1): p. 67-75.
40. Ennis, S.R., et al., *Transport of 5-aminolevulinic acid between blood and brain.* Brain Research, 2003. **959**(2): p. 226-234.
41. Hadjipanayis, C.G., G. Widhalm, and W. Stummer, *What is the Surgical Benefit of Utilizing 5-Aminolevulinic Acid for Fluorescence-Guided Surgery of Malignant Gliomas?* Neurosurgery, 2015. **77**(5): p. 663-673.
42. Xia, Y.M., et al., *A comparative study on the enhancement efficacy of specific and non-specific iron chelators for protoporphyrin IX production and photosensitization in HaCat cells.* Journal of Huazhong University of Science and Technology-Medical Sciences, 2009. **29**(6): p. 765-770.
43. Zhao, S.G., et al., *Increased Expression of ABCB6 Enhances Protoporphyrin IX Accumulation and Photodynamic Effect in Human Glioma.* Annals of Surgical Oncology, 2013. **20**(13): p. 4379-4388.
44. Otake, M., et al., *Selective accumulation of ALA-induced PpIX and photodynamic effect in chemically induced hepatocellular carcinoma.* British Journal of Cancer, 2003. **89**(4): p. 730-736.
45. Yano, H., et al., *Pathological analysis of the surgical margins of resected glioblastomas excised using photodynamic visualization with both 5-aminolevulinic acid and fluorescein sodium.* Journal of Neuro-Oncology, 2017. **133**(2): p. 389-397.
46. Masubuchi, T., et al., *Experimental Study to Understand Nonspecific Protoporphyrin IX Fluorescence in Brain Tissues Near Tumors After 5-Aminolevulinic Acid Administration.* Photomedicine and Laser Surgery, 2013. **31**(9): p. 428-433.
47. Ferraro, N., et al., *The role of 5-aminolevulinic acid in brain tumor surgery: a systematic review.* Neurosurgical Review, 2016. **39**(4): p. 545-555.

48. Vogelstein, B. and K.W. Kinzler, *THE MULTISTEP NATURE OF CANCER.* Trends in Genetics, 1993. **9**(4): p. 138-141.
49. Chin, L., et al., *Comprehensive genomic characterization defines human glioblastoma genes and core pathways.* Nature, 2008. **455**(7216): p. 1061-1068.
50. Liu, A.Z., et al., *Genetics and Epigenetics of Glioblastoma: Applications and Overall Incidence of IDH1 Mutation.* Frontiers in Oncology, 2016. **6**.
51. Chen, C.-Y., et al., *PTEN: tumor suppressor and metabolic regulator.* Frontiers in endocrinology, 2018. **9**: p. 338.
52. Bouali, S., et al., *PTEN expression controls cellular response to cetuximab by mediating PI3K/AKT and RAS/RAF/MAPK downstream signaling in KRAS wild-type, hormone refractory prostate cancer cells.* Oncology Reports, 2009. **21**(3): p. 731-735.
53. Cheng, Z., et al., *[The role of PTEN-FAK signaling pathway in metastasis and invasive ability of leukemia cells].* Zhonghua xue ye xue za zhi= Zhonghua xueyexue zazhi, 2009. **30**(2): p. 115-120.
54. Testa, J.R. and A. Bellacosa, *Commentary - AKT plays a central role in tumorigenesis.* Proceedings of the National Academy of Sciences of the United States of America, 2001. **98**(20): p. 10983-10985.
55. Koul, D., *PTEN signaling pathways in glioblastoma.* Cancer Biology & Therapy, 2008. **7**(9): p. 1321-1325.
56. Cheng, J.Q. and S.V. Nicosia, *AKT signal transduction pathway in oncogenesis*, in *Encyclopedic reference of cancer*. 2001, Springer. p. 35-37.
57. Hollander, M.C., G.M. Blumenthal, and P.A. Dennis, *PTEN loss in the continuum of common cancers, rare syndromes and mouse models.* Nature Reviews Cancer, 2011. **11**(4): p. 289-301.
58. Gan, H.K., A.H. Kaye, and R.B. Luwor, *The EGFRvIII variant in glioblastoma multiforme.* Journal of Clinical Neuroscience, 2009. **16**(6): p. 748-754.
59. Brennan, C.W., et al., *The Somatic Genomic Landscape of Glioblastoma.* Cell, 2013. **155**(2): p. 462-477.
60. England, B., T. Huang, and M. Karsy, *Current understanding of the role and targeting of tumor suppressor p53 in glioblastoma multiforme.* Tumor Biology, 2013. **34**(4): p. 2063-2074.
61. Zheng, H., et al., *p53 and Pten control neural and glioma stem/progenitor cell renewal and differentiation.* Nature, 2008. **455**(7216): p. 1129-1133.
62. Santagata, S., et al., *Intraoperative mass spectrometry mapping of an onco-metabolite to guide brain tumor surgery.* Proceedings of the National Academy of Sciences of the United States of America, 2014. **111**(30): p. 11121-11126.
63. Maher, E.A., et al., *Metabolism of [U-13C] glucose in human brain tumors in vivo.* NMR in biomedicine, 2012. **25**(11): p. 1234-1244.
64. Kant, S., et al., *Enhanced fatty acid oxidation provides glioblastoma cells metabolic plasticity to accommodate to its dynamic nutrient microenvironment.* Cell death & disease, 2020. **11**(4): p. 1-13.
65. Fink, M.A., et al., *L-carnitine–mediated tumor cell protection and poor patient survival associated with OCTN2 overexpression in glioblastoma multiforme.* Clinical Cancer Research, 2019. **25**(9): p. 2874-2886.
66. Juraszek, B., J. Czarnecka-Herok, and K.A. Nałęcz, *Glioma cells survival depends both on fatty acid oxidation and on functional carnitine transport by SLC22A5.* Journal of Neurochemistry, 2020.

67. Gozzelino, L., et al., *PI (3, 4) P2 signaling in cancer and metabolism.* Frontiers in oncology, 2020. **10**.
68. *Biochemistry of Lipids, Lipoproteins and Membranes, 5th Edition*, in *Biochemistry of Lipids, Lipoproteins and Membranes, 5th Edition*, D.E. Vance and J.E. Vance, Editors. 2008. p. 1-640.
69. Guillou, H., et al., *The key roles of elongases and desaturases in mammalian fatty acid metabolism: Insights from transgenic mice.* Progress in lipid research, 2010. **49**(2): p. 186-199.
70. Veloso, A., et al., *Distribution of lipids in human brain.* Analytical and Bioanalytical Chemistry, 2011. **401**(1): p. 89-101.
71. Pavlova, N.N. and C.B. Thompson, *The emerging hallmarks of cancer metabolism.* Cell metabolism, 2016. **23**(1): p. 27-47.
72. Hanahan, D. and R.A. Weinberg, *Hallmarks of Cancer: The Next Generation.* Cell, 2011. **144**(5): p. 646-674.
73. Snaebjornsson, M.T., S. Janaki-Raman, and A. Schulze, *Greasing the wheels of the cancer machine: the role of lipid metabolism in cancer.* Cell metabolism, 2020. **31**(1): p. 62-76.
74. Raimundo, N., B.E. Baysal, and G.S. Shadel, *Revisiting the TCA cycle: signaling to tumor formation.* Trends in Molecular Medicine, 2011. **17**(11): p. 641-649.
75. Houten, S.M. and R.J. Wanders, *A general introduction to the biochemistry of mitochondrial fatty acid β-oxidation.* Journal of inherited metabolic disease, 2010. **33**(5): p. 469-477.
76. Caniglia, J.L., et al., *Beyond glucose: alternative sources of energy in glioblastoma.* Theranostics, 2021. **11**(5): p. 2048.
77. Warburg, O., *ORIGIN OF CANCER CELLS.* Science, 1956. **123**(3191): p. 309-314.
78. Stanley, C.A. and M.J. Bennett, *Disorders of mitochondrial fatty acid β-oxidation.* U: Robert M. Kliegman, 2007: p. 567-572.
79. Lin, H., et al., *Fatty acid oxidation is required for the respiration and proliferation of malignant glioma cells.* Neuro-oncology, 2017. **19**(1): p. 43-54.
80. Krycer, J.R., et al., *The Akt–SREBP nexus: cell signaling meets lipid metabolism.* Trends in Endocrinology & Metabolism, 2010. **21**(5): p. 268-276.
81. Williams, J.P., et al., *Collision-induced fragmentation pathways including odd-electron ion formation from desorption electrospray ionisation generated protonated and deprotonated drugs derived from tandem accurate mass spectrometry.* Journal of mass spectrometry, 2006. **41**(10): p. 1277-1286.
82. Poad, B.L., et al., *Ozone-induced dissociation on a modified tandem linear ion-trap: observations of different reactivity for isomeric lipids.* Journal of the American Society for Mass Spectrometry, 2010. **21**(12): p. 1989-1999.
83. Manicke, N.E., et al., *Desorption electrospray ionization (DESI) mass Spectrometry and tandem mass spectrometry (MS/MS) of phospholipids and sphingolipids: Ionization, adduct formation, and fragmentation.* Journal of the American Society for Mass Spectrometry, 2008. **19**(4): p. 531-543.
84. Sparvero, L.J., et al., *Mass-spectrometry based oxidative lipidomics and lipid imaging: applications in traumatic brain injury.* Journal of Neurochemistry, 2010. **115**(6): p. 1322-1336.
85. Smith, C.A., et al., *METLIN - A metabolite mass spectral database.* Therapeutic Drug Monitoring, 2005. **27**(6): p. 747-751.

86. Cooks, R.G., et al., *Ambient mass spectrometry.* Science, 2006. **311**(5767): p. 1566-1570.
87. McDonnell, L.A. and R.M.A. Heeren, *Imaging mass spectrometry.* Mass Spectrometry Reviews, 2007. **26**(4): p. 606-643.
88. Seeley, E.H. and R.M. Caprioli, *Molecular imaging of proteins in tissues by mass spectrometry.* Proceedings of the National Academy of Sciences of the United States of America, 2008. **105**(47): p. 18126-18131.
89. Walch, A., et al., *MALDI imaging mass spectrometry for direct tissue analysis: a new frontier for molecular histology.* Histochemistry and Cell Biology, 2008. **130**(3): p. 421-434.
90. Ifa, D.R. and L.S. Eberlin, *Ambient Ionization Mass Spectrometry for Cancer Diagnosis and Surgical Margin Evaluation.* Clinical Chemistry, 2016. **62**(1): p. 111-123.
91. Takats, Z., et al., *Mass spectrometry sampling under ambient conditions with desorption electrospray ionization.* Science, 2004. **306**(5695): p. 471-473.
92. Nemes, P. and A. Vertes, *Laser ablation electrospray ionization for atmospheric pressure, in vivo, and imaging mass spectrometry.* Analytical Chemistry, 2007. **79**(21): p. 8098-8106.
93. Santos, V.G., et al., *Venturi Easy Ambient Sonic-Spray Ionization.* Analytical Chemistry, 2011. **83**(4): p. 1375-1380.
94. Cody, R.B., J.A. Laramee, and H.D. Durst, *Versatile new ion source for the analysis of materials in open air under ambient conditions.* Analytical Chemistry, 2005. **77**(8): p. 2297-2302.
95. Hiraoka, K., et al., *Development of probe electrospray using a solid needle.* Rapid Communications in Mass Spectrometry, 2007. **21**(18): p. 3139-3144.
96. Kerian, K.S., A.K. Jarmusch, and R.G. Cooks, *Touch spray mass spectrometry for in situ analysis of complex samples.* Analyst, 2014. **139**(11): p. 2714-2720.
97. Hillenkamp, F. and J. Peter-Katalinic, *MALDI MS: a practical guide to instrumentation, methods and applications*. 2013: John Wiley & Sons.
98. Jones, E.A., et al., *Suppression and enhancement of secondary ion formation due to the chemical environment in static-secondary ion mass spectrometry.* Journal of the American Society for Mass Spectrometry, 2007. **18**(8): p. 1559-1567.
99. Gray, A.L., *Solid sample introduction by laser ablation for inductively coupled plasma source mass spectrometry.* Analyst, 1985. **110**(5): p. 551-556.
100. Balog, J., et al., *Identification of Biological Tissues by Rapid Evaporative Ionization Mass Spectrometry.* Analytical Chemistry, 2010. **82**(17): p. 7343-7350.
101. Schafer, K.C., et al., *In Situ, Real-Time Identification of Biological Tissues by Ultraviolet and Infrared Laser Desorption Ionization Mass Spectrometry.* Analytical Chemistry, 2011. **83**(5): p. 1632-1640.
102. Sripadi, P., et al., *Direct Detection of Diverse Metabolic Changes in Virally Transformed and Tax-Expressing Cells by Mass Spectrometry.* Plos One, 2010. **5**(9): p. 15.
103. Santos, V.G., et al., *Venturi easy ambient sonic-spray ionization.* Analytical chemistry, 2011. **83**(4): p. 1375-1380.
104. Mandal, M.K., et al., *Application of Probe Electrospray Ionization Mass Spectrometry (PESI-MS) to Clinical Diagnosis: Solvent Effect on Lipid Analysis.* Journal of the American Society for Mass Spectrometry, 2012. **23**(11): p. 2043-2047.

105. Kertesz, V. and G.J. Van Berkel, *Fully automated liquid extraction-based surface sampling and ionization using a chip-based robotic nanoelectrospray platform.* Journal of mass spectrometry, 2010. **45**(3): p. 252-260.
106. Wiseman, J.M., et al., *Mass spectrometric profiling of intact biological tissue by using desorption electrospray ionization.* Angewandte Chemie-International Edition, 2005. **44**(43): p. 7094-7097.
107. Takats, Z., et al., *Direct, trace level detection of explosives on ambient surfaces by desorption electrospray ionization mass spectrometry.* Chemical Communications, 2005(15): p. 1950-1952.
108. Badu-Tawiah, A.K., et al., *Chemical Aspects of the Extractive Methods of Ambient Ionization Mass Spectrometry*, in *Annual Review of Physical Chemistry, Vol 64*, M.A. Johnson and T.J. Martinez, Editors. 2013. p. 481-505.
109. Tillner, J., et al., *Faster, more reproducible DESI-MS for biological tissue imaging.* Journal of the American Society for Mass Spectrometry, 2017. **28**(10): p. 2090-2098.
110. Campbell, D.I., et al., *Improved spatial resolution in the imaging of biological tissue using desorption electrospray ionization.* Analytical and Bioanalytical Chemistry, 2012. **404**(2): p. 389-398.
111. Chen, H.W., et al., *Desorption electrospray ionization mass spectrometry for high-throughput analysis of pharmaceutical samples in the ambient environment.* Analytical Chemistry, 2005. **77**(21): p. 6915-6927.
112. Takats, Z., J.M. Wiseman, and R.G. Cooks, *Ambient mass spectrometry using desorption electrospray ionization (DESI): instrumentation, mechanisms and applications in forensics, chemistry, and biology.* Journal of Mass Spectrometry, 2005. **40**(10): p. 1261-1275.
113. Venter, A., P.E. Sojka, and R.G. Cooks, *Droplet dynamics and ionization mechanisms in desorption electrospray ionization mass spectrometry.* Analytical Chemistry, 2006. **78**(24): p. 8549-8555.
114. Costa, A.B. and R.G. Cooks, *Simulation of atmospheric transport and droplet-thin film collisions in desorption electrospray ionization.* Chemical Communications, 2007(38): p. 3915-3917.
115. Costa, A.B. and R.G. Cooks, *Simulated splashes: Elucidating the mechanism of desorption electrospray ionization mass spectrometry.* Chemical Physics Letters, 2008. **464**(1-3): p. 1-8.
116. Domin, M. and R. Cody, *Ambient ionization mass spectrometry*. 2014: Royal Society of Chemistry.
117. Eberlin, L.S., et al., *Discrimination of Human Astrocytoma Subtypes by Lipid Analysis Using Desorption Electrospray Ionization Imaging Mass Spectrometry.* Angewandte Chemie-International Edition, 2010. **49**(34): p. 5953-5956.
118. Eberlin, L.S., et al., *Desorption Electrospray Ionization then MALDI Mass Spectrometry Imaging of Lipid and Protein Distributions in Single Tissue Sections.* Analytical Chemistry, 2011. **83**(22): p. 8366-8371.
119. Eberlin, L.S., et al., *Desorption electrospray ionization mass spectrometry for lipid characterization and biological tissue imaging.* Biochimica Et Biophysica Acta-Molecular and Cell Biology of Lipids, 2011. **1811**(11): p. 946-960.
120. Ferguson, C.N., et al., *Direct Ionization of Large Proteins and Protein Complexes by Desorption Electrospray Ionization-Mass Spectrometry.* Analytical Chemistry, 2011. **83**(17): p. 6468-6473.

121. Miao, Z.X., S.Y. Wu, and H. Chen, *The Study of Protein Conformation in Solution Via Direct Sampling by Desorption Electrospray Ionization Mass Spectrometry.* Journal of the American Society for Mass Spectrometry, 2010. **21**(10): p. 1730-1736.
122. Wiseman, J.M., et al., *Desorption electrospray ionization mass spectrometry: Imaging drugs and metabolites in tissues.* Proceedings of the National Academy of Sciences of the United States of America, 2008. **105**(47): p. 18120-18125.
123. Huang, G., et al., *Rapid screening of anabolic steroids in urine by reactive Desorption Electrospray ionization.* Analytical Chemistry, 2007. **79**(21): p. 8327-8332.
124. Wu, C.P., et al., *Rapid, Direct Analysis of Cholesterol by Charge Labeling in Reactive Desorption Electrospray Ionization.* Analytical Chemistry, 2009. **81**(18): p. 7618-7624.
125. Zhang, Y. and H. Chen, *Detection of saccharides by reactive desorption electrospray ionization (DESI) using modified phenylboronic acids.* International Journal of Mass Spectrometry, 2010. **289**(2-3): p. 98-107.
126. Guillong, M. and D. Günther, *Effect of particle size distribution on ICP-induced elemental fractionation in laser ablation-inductively coupled plasma-mass spectrometry.* Journal of Analytical Atomic Spectrometry, 2002. **17**(8): p. 831-837.
127. Sylvester, P.J. and S.E. Jackson, *A brief history of laser ablation inductively coupled plasma mass spectrometry (LA–ICP–MS).* Elements, 2016. **12**(5): p. 307-310.
128. Limbeck, A., et al., *Recent advances in quantitative LA-ICP-MS analysis: challenges and solutions in the life sciences and environmental chemistry.* Analytical and bioanalytical chemistry, 2015. **407**(22): p. 6593-6617.
129. Pirro, V., et al., *Intraoperative assessment of tumor margins during glioma resection by desorption electrospray ionization-mass spectrometry.* Proceedings of the National Academy of Sciences of the United States of America, 2017. **114**(26): p. 6700-6705.
130. St John, E.R., et al., *Rapid evaporative ionisation mass spectrometry of electrosurgical vapours for the identification of breast pathology: towards an intelligent knife for breast cancer surgery.* Breast Cancer Research, 2017. **19**(1): p. 1-14.
131. Alexander, J., et al., *A novel methodology for in vivo endoscopic phenotyping of colorectal cancer based on real-time analysis of the mucosal lipidome: a prospective observational study of the iKnife.* Surgical endoscopy, 2017. **31**(3): p. 1361-1370.
132. Phelps, D.L., et al., *The surgical intelligent knife distinguishes normal, borderline and malignant gynaecological tissues using rapid evaporative ionisation mass spectrometry (REIMS).* British journal of cancer, 2018. **118**(10): p. 1349-1358.
133. Woolman, M., et al., *Rapid determination of medulloblastoma subgroup affiliation with mass spectrometry using a handheld picosecond infrared laser desorption probe.* Chemical science, 2017. **8**(9): p. 6508-6519.
134. Zhang, J., et al., *Nondestructive tissue analysis for ex vivo and in vivo cancer diagnosis using a handheld mass spectrometry system.* Science translational medicine, 2017. **9**(406).
135. Ogrinc, N., et al., *Water-assisted laser desorption/ionization mass spectrometry for minimally invasive in vivo and real-time surface analysis using SpiderMass.* Nature protocols, 2019. **14**(11): p. 3162-3182.

Chapter 2: A multi-modal investigation into the lipidomic and metallomic profiles of an invasive glioblastoma orthotopic murine tumour model

Matthew C. Gentry[1], Emrys A. Jones[2], Joe Ready[3], Romain Tartese[4] Catherine C. Duckett[3], Joanna L. Birch[5], Antoine Vallatos[5, 6], Jamie Gilmour[4], Malcolm R. Clench[3], Anthony J. Chalmers[5], Nicholas P. Lockyer[7], Adam McMahon[1]

[1]Wolfson Molecular Imaging Centre, Division of Informatics, Imaging and Data Sciences, University of Manchester, United Kingdom

[2]Waters Corporation, Wilmslow, United Kingdom

[3]Centre for Mass Spectrometry Imaging, Biomedical Research Centre, Sheffield Hallam University, United Kingdom

[4]Earth Sciences, University of Manchester, United Kingdom

[5]Wolfson Wohl Translational Cancer Research Centre, Institute of Cancer Sciences, University of Glasgow, United Kingdom

[6]Centre for Clinical Brain Sciences, University of Edinburgh, United Kingdom

[7]Photon Science Institute, Depart of Chemistry, University of Manchester, United Kingdom

1. Abstract

Glioblastoma (GBM) are the most common, grade IV, primary brain tumours, with an average life expectancy of 12–15 months following standard of care (SOC) treatment. Glioblastoma malignancies are characterised by heterogeneity, high proliferation, and infiltration into surrounding healthy tissue parenchyma, meaning removal of 100% of the tumour cells is near impossible. Despite a plethora of research into GBM, survival rates have not improved in the last 15 years. Further research is required, particularly targeting the biochemical makeup of these malignancies.

The main contributing factor to poor prognosis, is the invasive characteristics of the GBM tumour. This is an important attribute, and thus is essential pre-clinical models to ensure any research is representative of real-life. Orthotopic models involve implantation patient derived cell lines into animal models, allowing for the tumour to be cultured in a more disease-appropriate environment, thus more accurately

representing the real-life biology. As a result, these models will be used in this research.

Mass spectrometry imaging (MSI) is a technique capable of elucidating spatial information about analytes of a sample. Due to the invasive nature of the GMB, exploring the biological changes with respect to the spatial location is of great value. Thus, a multi-modal, multi-omic, MSI approach to profile an invasive G7 orthotopic tumour model was applied. Using desorption electrospray ionization mass spectrometry imaging (DESI-MSI), revealed a number of upregulated and overexpressed lipids species were identified within the tumour mass. An overall increase in phosphatidylinositol lipid species, was linked to an overexpressed PI3-K pathway, highlighting altered GMB fatty acid metabolism *via* the β-oxidation pathway. This was further supported by the presence of acyl carnitine species.

Currently, an MRI approach for initial tumour localisation is standard. To further complement these data, laser ablation inductively coupled plasma mass spectrometry (LA-ICP-MS) was employed to investigate the distribution of metal-based MRI contrast agents, to demonstrate how MSI approaches can complement standard methodologies. As a result, LA-ICP-MS accurately detected gadolinium within the tumour regions, alongside other metals including zinc and manganese, whilst copper was demonstrated to be in low abundance. These data demonstrate the benefits of using a multi-modal MSI approach, allowing for spatial information to complement standard clinical methods.

2. Introduction

2.1. Glioblastoma introduction

A glioblastoma (GBM) is defined by the World Health Organisation (WHO) as a grade IV astrocytoma, and is the most common primary adult brain tumour [1]. These malignancies are associated with extremely poor prognosis and life expectancy. Following SOC treatment, average life expectancy is between 12–15 months. Typical patient treatment follows the Stupp protocol, introduced in 2005. This which uses adjuvant temozolomide chemotherapy in combination with radiotherapy, followed by complete resection of the tumour mass [2]. Despite the

SOC protocol, prognosis is poor and heavily relies upon successful total resection to remove more than 95% of the tumour tissue without disrupting surrounding healthy tissue [3, 4]. As a result, removing as much of the tumour mass as possible is currently the most effective option for improving life expectancy.

As a result, defining tumour boundaries is imperative to allow safe resection of the tumour [5, 6]. The current standard for defining abnormal brain masses, is a MRI scan and is used intraoperatively to guide surgeons [7]. An MRI scan involves the use of a contrast enhancing agent to improve visualisation of any masses, many of which contain gadolinium [8]. Intraoperative guided surgery uses 3D MRI scans generated prior to surgery as guidance for the neurosurgeon [9]. Glioblastoma malignancies are highly invasive by nature, and as such infiltrate into surrounding tissue parenchyma in the brain [1, 10]. Thus, determining a safe tumour margin using an MRI scan is crucial for a successful surgery. Nonetheless, there are several associated problems using this method, including brain shift, the deformation of the brain during surgery, which can make it difficult to establish a safe surgical resection boundary. Additionally, the low availability of such imaging facilities and high associated costs, creates additional drawbacks. [9].

An extensive micro-environmental heterogeneity is exhibited in the biological structure of a GBM. This, combined with a high genetic, epigenetic, and molecular variability can cause large problems for chemotherapy and radiotherapy treatment. [11] Over the years, research into GBM has been extensive and although many new genetic mutations have been discovered, there has been little impact on the prognosis and overall patient survival status [12].

Pre-clinical GBM models based on patient derived cell lines are becoming more frequently used to answer questions about clinical GBM. The G7 GBM tumours, from Colin Watts (Cambridge), are derived from patient derived cells lines that have been shown to mimic clinical cases in *ex vivo* models. Research by Chalmers *et al* show that post treatment with temozolomide, bevacizumab and erlotinib in 2D and 3D models of G7 cultured cells, can accurately reflect the results observed in the clinic. G7 GBM tumours are invasive along white matter tracts in the mouse brain [13]. As such, this clinically relevant model was selected to investigate the biochemical species present in orthotopic GBM tumour.

2.2. Mass spectrometry imaging analysis

Mass spectrometry imaging (MSI) is a growing field of analytical methods that allow spatially resolved analysis of endogenous and exogenous chemical species in a single experiment.

Desorption electrospray ionisation mass spectrometry imaging (DESI-MSI) is an ambient ionisation imaging method with high sensitivity to lipid species. Due to the high lipid content of the brain, this method was selected to allow for a thorough examination of the changing lipid species within the GBM model.

Laser ablation inductively coupled mass spectrometry (LA-ICP-MS) is an analytical technique used for the detection of metals. There are many essential metals that provide a range of cellular functions. Gadolinium, a paramagnetic metal species, is also used in MRI contrast agents to improve visualisation of brain abnormalities. Mapping the distribution of gadolinium alongside lipid profiles of tumour regions, will further assess how gadolinium aids tumour visualisation in MRIs. Combining LA-ICP-MS with DESI-MS will allow for high spatial resolution imaging of both lipids and metal cations observed for analysis of the selected GBM model.

In this work, a multi-modal MSI approach was utilised to investigate the molecular profiles of lipids and metals in a clinically relevant GBM model. DESI-MSI and LA-ICP-MS have been applied to investigate the lipidomic and metallomic profiles of GBM aiming to elucidate spatially resolved information about the differing chemical species of the tumour and surrounding tissue, as well as further investigate the metabolic features of this tumour model.

2.3. Phosphatidylinositol introduction

Phosphatidylinositol lipids form an important part of the plasma membrane, but also act as key signalling molecules, with the ability to bind to cell receptors. Phosphoinositide 3-kinase (PI3-K) is a class of enzymes that catalytically converts Phosphatidylinositol (3,4,5)-trisphosphate PIP3 to Phosphatidylinositol (4,5)-

bisphosphate (PIP2) through the hydrolysis of a phosphate group on the inositol headgroup and as such signals *via* PI lipid species. The main genetically altered pathways in GBM are PI3-K, the associated pathways of Receptor tyrosine kinase (RTK) and renin-angiotensin system (RAS) signalling, with 88% of all tumours found to harbour an alteration to this pathway [14]. Overexpressed PI3-K signalling affects downstream Akt (Protein Kinase B) signalling, which is responsible for several cancer cell like traits. PI3-K and Akt also have a role in lipid metabolism, whereby downstream signalling *via* SREBP regulates lipid metabolism *via* the production of fatty acids, whose distribution will be assessed later on in section 4.2.2 [15].

The G7 GBM was obtained from patient anonymised clinical GBM cases and has shown to correlate the results of clinical GBM *in vivo* [13, 16, 17]. As such, the G7 cell line is expected to match clinical GBM, showing alterations to the PI3-K signalling pathway which may explain these results.

3. Methods

3.1. Materials

All solvents, unless otherwise stated were purchased from Sigma Aldrich.

3.2. G7 orthotopic mouse model

G7 GBM cell lines were obtained from Colin Watts (Cambridge) and were derived from anonymized patient resection specimens as previously described [17]. Cell lines were routinely cultured on Matrigel-coated plates (0.23 mg/L in AdDMEM, Life Technologies) in serum-free AdDMEM supplemented with 20 ng/mL EGF, 10 ng/mL FGF, 0.5% B27 supplement, and 0.5% N2 supplement (all Life Technologies).

A subculture of 1 x 10^5 cells were orthotopically injected into the subventricular zone of female CD1 nude mice, and allowed to develop tumours with regular health monitoring. The mice were maintained in individually ventilated cages with environmental enrichment and ARRIVE guidelines followed.

In total, 10 mice were used, with tumour cells implanted into 9 of them. The 9 tumour bearing mice were split into three groups, each containing 3 mice with tumours grown for 9, 11 and 13 weeks. The final mouse was not injected with tumour cells and sustained for 13 weeks to act as a biological control. The mice in each group are labelled mouse 1 (M1), mouse 2 (M2) and mouse 3 (M3), and for the week 13 group only mouse 4 (M4). The control mouse in week 13 is labelled M2. After 9, 11, and 13 weeks following MRI scans the mice were culled using CO_2 and cervical dislocation. The brains from each mouse were collected and snap-frozen in isopentane and dry ice before sectioning.

In this paper, sample IDs will be given in the form of the week, the mouse number, and the corresponding section number, WkX, MX, SX. For example, section 3 from week 13 Mouse 2 will be annotated as Wk13 M2 S3.

3.3. MRI

Once each mouse had reached the desired age for tumour growth, MRI experiments were performed on a Bruker Pharmascan 7T imaging system with a 30 cm horizontal bore (Bruker, Ettlingen, Germany). Homogeneous radiofrequency excitation was achieved using a birdcage volume resonator (diameter=72 mm, length=110 mm) and an actively decoupled 4-channel phased array receive-only head surface coil was used for signal detection (Rapid Biomedical, Wurzburg, Germany).

The animals were anaesthetized using 5% isoflurane and a 30:70 O_2/N_2O ratio before being positioned prone on an MRI animal cradle. A hot water circulation jacket was used to regulate physiological temperature (37±1 °C). The mouse head was secured laterally by conical ear rods and longitudinally by the nose cone used for anaesthetic gas delivery. The animals breathed spontaneously through a facemask, with isoflurane delivered at a constant flow mixed with a 40:60 ratio of O_2/N_2O (1 L min^{-1}). Isoflurane concentration varied (1.5–3 %) to maintain stable respiration rates within normal physiological ranges (40–70 bpm). Respiration was monitored using a pressure sensor connected to an air-filled balloon placed under the animal abdomen (Biotrig software, Bruker, Ettlingen, Germany).

Following a geometry-correction sequence, a series of MRI experiments were performed (field of view 1.76×1.76 cm, imaging slices centred at 4 mm posterior from rhinal fissure). T2-weighted imaging (T2) was performed using a rapid acquisition with relaxation enhancement (RARE) sequence (TE=47 ms, TR=4,300 ms, matrix=176×176, 14* 0.5 mm coronal slices). Perfusion weighted imaging (PW) was performed using an optimized multiple boli Arterial Spin Labeling sequence (mbASL) [18], labelling with a train of twenty hyperbolic-secant inversion pulses (duration=3.3 ms, dimensionless amplitude parameter μ=8, angular modulation β=760 s-1) evenly distributed over 5 s (post-labelling delay=50 ms). The inversion slice width was 8.5 mm and the offset from the imaging slice was 15 mm. PW image acquisition was achieved with a 4-shot EPI module (TE=12 ms, TR=7 s, matrix=96×96, partial FT=1.4, 10 averages, 7*1 mm coronal slices). Finally, contrast-enhanced T1 imaging (cT1) was performed using RARE acquisition (TE=12.3 ms, TR=800 ms, matrix = 176×176, 14* 0.5 mm coronal imaging slices centered at 4 mm posterior from rhinal fissure). Images were acquired before and 5 min after Gadolinium-DTPA injection (Magnevist, Bayer).

3.4. Sample preparation and selection

Sections for analysis were determined from a 1mm^2 region selected from the T2W MRI images of all brains, Figure 34. A section was cut at 20 µm thickness on LEICA CM 3050 S cryostat (Leica, UK) for DESI-MSI, H&E and LA-ICP-MS. Each section was thaw mounted onto a labelled glass slide. In total, 5 sections were cut for each method, spaced at 200 µm distance from each other, covering a 1 mm thickness to provide a clear overview of the tumour from each mouse. Sectioning was guided by MRI data to allow for comparison between the MRI and MS data generated.

3.5. H&E

Haematoxylin and eosin (H&E) staining was carried out on an adjacent tissue section to those taken for DESI-MS and LA-ICP-MS imaging. Sections mounted onto glass slides were fixed in 10% formal saline for 5 minutes and washed in running water for 3 minutes. The slides were de-fatted in a series of ethanol washes at 70%, 90%, 100%, 100% and then rehydrated in ethanol washes at 90% and 70% (2 mins each). Sections were then washed in running water and stained in haematoxylin for 4–5 minutes, followed by a further water wash. Slides were then differentiated by a few dips in acid alcohol and washed again in running water. The now blue stained sections are washed in Scotts Tap Water Substitute (STWS) for 2 mins and dip washed in water. Sections were then dehydrated in 70% and 90% ethanol for 2 mins at a time before staining with alcoholic eosin for 2 mins. Lastly, each slide was dehydrated in ethanol, (3 x 4 mins), followed by clearing in histoclear (3 x 4 mins) and left to dry. Sections were mounted with a cover slip using an aqueous mounting media and scanned using the Zeiss Axioimager upright fluorescence microscopes.

3.6. DESI MS

3.6.1. DESI-MS Imaging

DESI-MS imaging experiments were carried out on a modified 2D DESI stage (Prosolia, Indianapolis USA) mounted onto a Xevo G2-XS quadrupole time of flight (QtoF) (Waters, Wilmslow, UK) in negative and positive ion mode. The DESI slide plate was modified to allow the automated PL200 microscope slide loader (Prior Scientific, Cambridge) to load a sample onto the stage and then remove it after acquisition. A camera, mounted to a fixed position on the slide loading set-up, acquired an image of the glass slide and determined the region for analysis, allowing fully automated DESI-MS imaging of all sections in negative ion mode.

MATLAB and C# executables (Waters, UK) automated the co-registration of the glass slide snapshot with the stage coordinates, using object definition algorithms, to identify the tissue location on the slide. These co-ordinates were subsequently written into the MassLynx (Waters, UK) experiment file and imaging undertaken on all sections.

In total 50 sections (5 sections from each of the 10 brains) were analysed in negative ion mode over two batches each running for around 16 hours.

Subsequent positive ion mode analysis was carried out on a typical DESI-MSI set-up, imaging one section at a time. Images were acquired at a spatial resolution of 100 µm, over a mass range of 50-1200, at 10 scans/second with the aid of a heated collection capillary at 12kV, giving an inlet temperature of 450 ^{o}C (Waters Research Centre, Budapest, Hungary) and a source temperature of 100 ^{o}C. Spray conditions used 98:2% methanol:water solvent composition at a flow rate of 1.5 µL/min delivered using a syringe pump (Harvard Apparatus Inc, Holliston, USA) with nitrogen nebulising gas at 25 PSI. DESI source geometry positions were optimised prior to all imaging experiments, determining maximal lipid signal extraction on control liver sections. Optimised parameter used in this work are 1.5 mm spray tip to sample surface, 6 mm sprayer to heated capillary inlet, 80^{o} sprayer impact angle with a 5^{o} collection capillary angle. Capillary voltages of 1.06 kV and 1 kV were used for negative and positive ion mode respectively, with spectra acquired in sensitivity mode on the Xevo G2-XS.

3.6.2. MS/MS analysis

DESI MS/MS experiments were performed on the Waters Xevo G2-XS QtoF using collision induced dissociation (CID) through fast data dependent acquisition (Fast DDA). Collision energy ramps of 12 – 15 kV for the low molecular mass and 50 – 70 kV for the high molecular weight masses were employed to ensure successful fragmentation of all molecular species between 50 and 1200 Da.

3.7. LA-ICP-MS

3.7.1. LA-ICP-MS imaging

Mapping of trace element abundances in brain tissue sections was carried out on two LA-ICP-MS instruments; one at Sheffield Hallam University, and one at The University of Manchester. As a result, elemental maps of carbon-13, silicon-29 (UoM only), manganese-55, iron-57, copper 63, zinc-66, gadolinium 157 and 158, were created.

Initial LA-ICP-MS imaging was performed at Sheffield Hallam University on a Perkin Elmer NexION 350X coupled to a UP213 Universal Platform Laser Ablation System (New Wave, Freemont, CA) utilising a frequency quintupled NdYAG deep UV laser with the resulting wavelength of 213 nm. The parameters used for each imaging run are as follows; laser power 28%, laser fluence 0.07 J/cm^2, spot size 100 µm, and a laser repetition rate of 20 Hz. Each image was acquired at 100 µm spatial resolution using a raster spacing of 100 µm and a scan speed of 100 µm/second, equating to 1 scan per second acquired in kinetic energy discrimination (KED) mode. This ensured the full tissue section was analysed.

Further high-resolution LA-ICP-MS imaging was carried out at the University of Manchester using a Teledyne Photon Machines Analyte Excite+ 193 nm ArF Excimer laser ablation system with a HelEx II active 2-volume ablation cell, coupled to an Agilent 8900 ICP-MS.

Samples were ablated along linear scans of 0.9 to 2.5 mm using a 20 µm square laser beam ablating over a stage moving at a continuous speed 20 µm/s, corresponding to 45 to 125 s of data acquisition per line. Rectangular images were produced by stacking vertically linear scans every 20 µm with no gap or overlap between lines. The number of stacked lines ranged between 75 and 189, corresponding to 1.5 to 3.8 mm vertically. A fluence of ~0.18-0.27 J.cm-2 and a repetition rate of 6 Hz was used.

Matrix matched standards with known element concentrations were prepared to allow quantitative, elemental concentration maps to be obtained. Sheep brain, purchased from a local butcher, was dosed with various quantities of the ICP-MS standard elements solutions (SPEX CertiPrep, Stanmore, UK). Standard solutions of the elements of interest (gadolinium (1000 ng/mL) and copper, iron, manganese, nickel, and zinc (all 100 ng/mL)) were added to known amounts of homogenised brain and further homogenised using a handheld PowerGen 125 homogeniser at 6000 rpm (Fischer Scientific, Loughborough, UK). The final concentrations of elements in brain tissue were 50, 20 and 10 µg/g prepared in triplicate for sectioning (LA-ICP-MS imaging).

Compacted homogenates were snap frozen in isopentane and stored at -80 ^{o}C until sectioning. Following this, each homogenate was removed from the sample falcon tubes and mounted onto 30 mm specimen discs using 2% CMC. All homogenates were sectioned at 20 µm thickness, to match that of the brain sections and analysed before and after LA-ICP-MS imaging of tissue sections for quantitative mapping across tissue sections.

3.8. Data analysis

3.8.1. DESI-MSI

SciLS lab software (Version 2021a / Release 9.00 (Bruker Daltonik GmbH, Bremen, Germany, www.scils.de) was used for DESI-MS imaging data analysis. All DESI-MS imaging data files were converted into the vendor neutral .imzML format through HDImaging software. The resulting .imzML files were converted to SciLS lab compatible files for data analysis (SciLS Lab, Version 2021a / Release 9.00 (Bruker Daltonik GmbH, Bremen, Germany, www.scils.de)). The 50 DESI-MS imaging data files were loaded into SciLS lab simultaneously and combined into a single dataset to allow comparison between all analysed sections. Spectra were normalised to the total ion current (TIC) and regions of interest (ROIs) annotated on each section.

Bisecting k-means segmentation was applied to the entire dataset and extracted areas of; grey matter (GM), white matter (WM), and tumour spectra were extracted for discriminative analysis. Using receiver operator characteristics (ROC) a random subset of the data was selected due to the large differences between the numbers of non-tumour (~160,000) and tumour (~11,000) spectra. The resultant ROC analysis assessed the discriminative qualities of *m/z* values found in different regions of the sections. Unless stated discriminative values reported are from the ROC analysis of tumour (class 1) versus surrounding non-tumour tissue and healthy sections (GM and WM combined spectra – class 2). The produced plots display true positive rate (sensitivity) against false positive rate (specificity) and the area under the curve is assigned to each *m/z* value as the discriminative value. These values range from 0 to 1, values greater than 0.5 are higher in abundance in the tumour spectra and less than 0.5 is higher in abundance in non-tumour spectra. Discrimination values greater than 0.9 are considering outstanding matches to that class, 0.8-0.9 is an excellent match and 0.7-0.8 would be acceptable for a diagnosis test [19]. For this paper, the corresponding *m/z* values in the top and bottom 20% were investigated.

Bisecting k-means results in SciLS lab produce interactive labelled maps that allow for interactive exploration. This method is useful where there are a large number of samples in the dataset that show common features [20].DESI-MS spectra were viewed and extracted from MassLynx v4.1 (Waters, Milford, USA) and DESI-MSI overlays were performed in HDImaging v1.5 (Waters, UK).

3.8.2. LA-ICP-MS

LA-ICP-MS imaging datasets were analysis in Iolite 3 or Iolite 4 and the Trace Element data reduction scheme was used [21].

4. Results and Discussion

4.1. Negative ion mode DESI-MS Imaging

Negative ion DESI-MSI of each brain section were viewed and analysed in SciLS Lab (Bruker Daltonik GmbH, Bremen). The bisecting k-means segmentation pipeline, available on the SciLS lab software, was used to find areas of similar biochemical signature across the whole data set. Comparing the results of the bisecting k-means segmentation maps to the H&E-stained tissue sections, demonstrated that the regions of interest highlighted in the stained tissue are also observed in the MSI data. In all cases, MSI was able to accurately differentiate tumour from the surrounding tissues as well as distinguishing tumour from the healthy brain tissue sections, Figure 10.

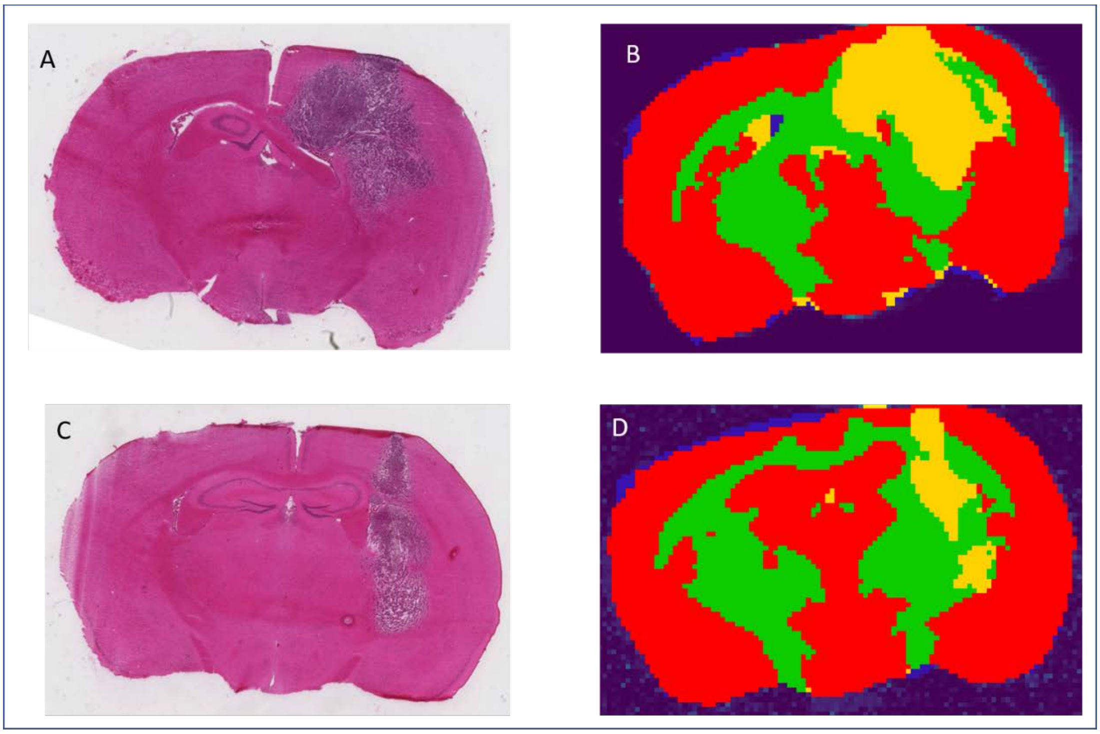

Figure 10 – Section A – H&E Week 13 M1 Section 4; B – Week 13 M1 Section 4 bisecting k-means segmentation map; C – H&E Week 11 M2 Section 5; D – Week 11 M2 Section 5 bisecting k-means segmentation map. Sections B and D show the bisecting k-means segmentation of the DESI-MSI data, splitting the brain sections into grey matter (red), white matter (green) and tumour regions (yellow), highlighting distinct biochemical signals from the tumour area. This correlates to the known location of the tumour volume from the H&E images show in panels A and C. The tumour volume is observed in the right hemisphere of the brain sections, shown as darker purple masses in the H&E images.

The tumour masses are easily observed in the H&E sections due to the high cell density, showing as darker masses in the left hemispheres of all mice brain. This directly correlates to the regions of yellow produced from the k-means segmentation image maps, Figure 10. The tumour regions are observed in the right hemispheres of the brain sections due to orientation of the brain during sectioning. Initial k-means segmentation (Supplementary Figure 36) splits the entire MS dataset into two distinct regions. From observing the H&E images and known structures within the mouse brain, the most chemically distinct regions correspond to the white matter (WM) (yellow) and the grey matter (GM) combined with the tumour regions (red). Initial segmentation suggests the associated *m/z* values found in the tumour region are most chemically related to the grey matter *m/z* species over the white matter *m/z*.

Segmenting the grey matter region to provide a full overview of the tissue sections, produces the three distinct brain regions, Figure 10, to represent the GM (red), WM (green) and the tumour volume (yellow). DESI mass spectra are extracted from these regions to observe differences between the chemical distinct regions produced from the bisecting k-means segmentation, Figure 11 and Figure 12.

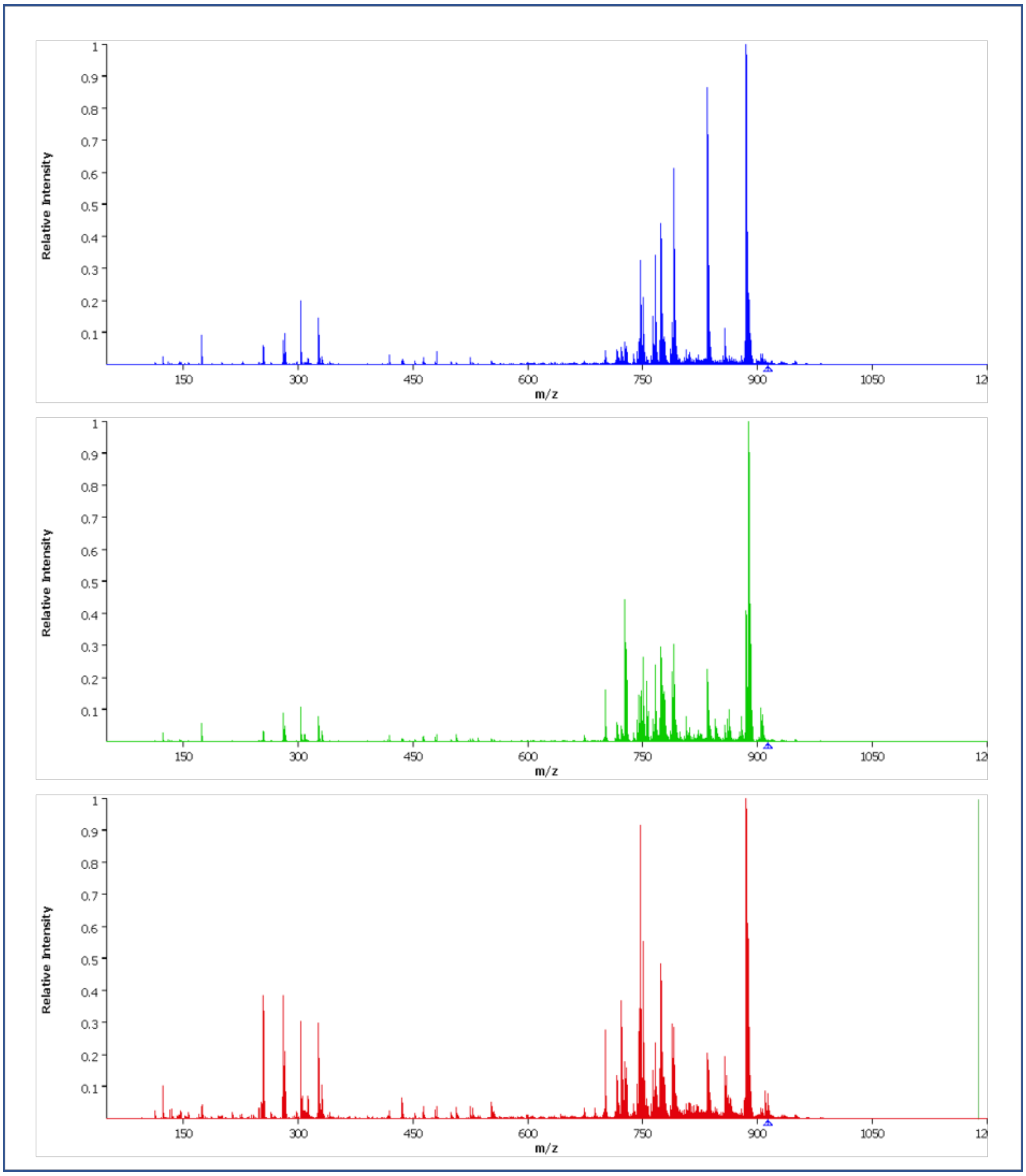

Figure 11 – Extracted DESI-MS spectra from the three distinct regions in the bisecting k-means segmented DESI maps Figure 10 Top = average grey matter spectra (red k-means regions), middle = average white matter spectra (green k-means regions), bottom = average tumour spectra (yellow k-means regions)

The extracted spectra from each distinct region in the orthotopic brain tumour sections show spectra differences between the different groups. The differences in m/z values will be used to assess which molecular species are at high abundance in the tumour regions compared to the surrounding tissue. The extracted DESI-MS spectra are overlaid in Figure 12 to give a greater representation of the differences between GM, WM, and tumour regions.

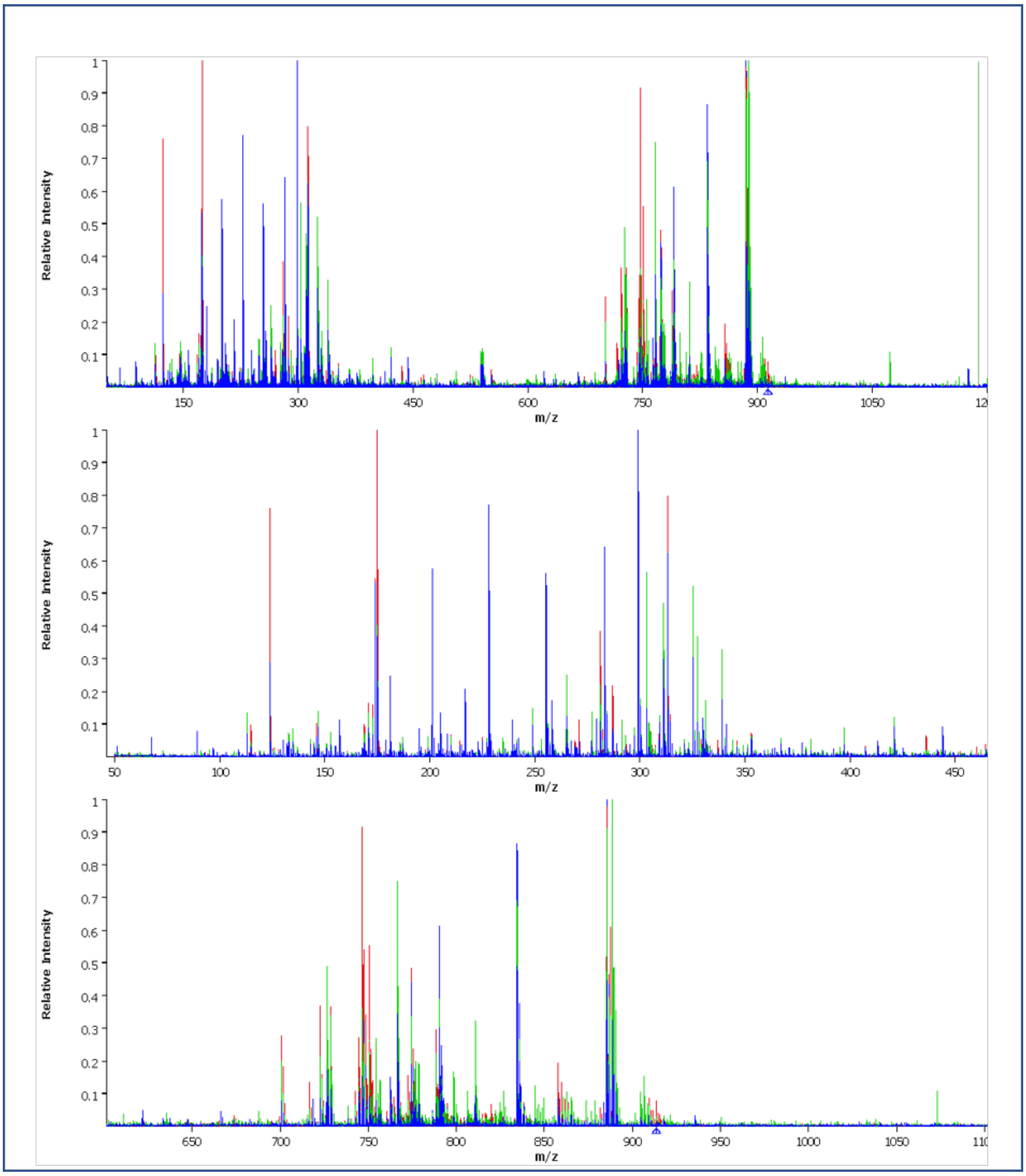

Figure 12 – Skyline overlaid extracted DESI-MS spectra for each of the three distinct chemical regions GM, WM, and tumour, display the most abundant species within each region at a relative intensity of 1, highlighting differences in m/z values between the three regions. Differences can be observed throughout the DESI-MS spectra's mass range suggesting changes to metabolites (100-350 m/z) and lipids (600-1000 m/z). D = overlay GM, WM, Tumour across full mass range (50-1200 m/z), E = overlay 0 – 450 m/z, F = overlay 600 – 1100 m/z.

Skyline spectra of GM, WM and tumour overlayed in Figure 12 reveal many common molecular species between the regions, an observation seen previously in the DESI-MSI analysis of GBM samples [22]. There are also many spectral differences observed between 600 – 900 *m/z* and 100 – 350 *m/z* regions. To determine differences between the tumour and surrounding tissue, the MSI were examined.

4.2. Tumour lipidomic analysis by negative and positive ion DESI-MS imaging to reveal high abundant tumour species

In this section images showing the distribution of certain *m/z* values are shown from a single section from each timepoint; Wk 9 M3 section 5, Week 11 M2 section 5, Week 13 M4 section 5, and Week 13 M2 section 5 (control). By comparing the *m/z* distributions obtained over these 4 sections between one another and to the adjacently stained H&E section, any biological differences between the samples can be elucidated and to assess whether there are differences in the lipid profiles as tumours develop.

Lipid species with ROC values over 0.8 show high relative intensity and overexpression in the tumour region compared to the surrounding healthy tissue. Whilst species with a discriminative value less than 0.2 are more abundant in the surrounding tissue. The chemical species of resultant *m/z* values were determined where possible by accurate mass and MS/MS analysis. The tentative assignment for each *m/z* value to a lipid species shown in supplementary Table 5 and the corresponding ROC discriminative values are shown in supplementary Table 3 . Three main categories of lipids were observed; phosphatidylinositol’s (PI), fatty acids (FA) and short single chained phospholipids termed lyso-phospholipids (LPL). This is the first instance of these molecular groups being observed in orthotopic tumour models and build upon the analysis by Henderson *et al.* in the DESI-MS analysis of a glioma xenograft model [23].

4.2.1. Phosphatidylinositol’s overexpressed in the G7 tumour

The molecular species showing the highest degree of difference between the tumour volume and the healthy surrounding tissue is *m/z* 913.55 with a discriminative value of 0.9748. The area under the curve (AUC) graph that correlates all *m/z* values to a discriminative value, as well as the ion intensity box plot that depicts the intensity of *m/z* 913.55 in the tumour region and surrounding tissue, Figure 13.

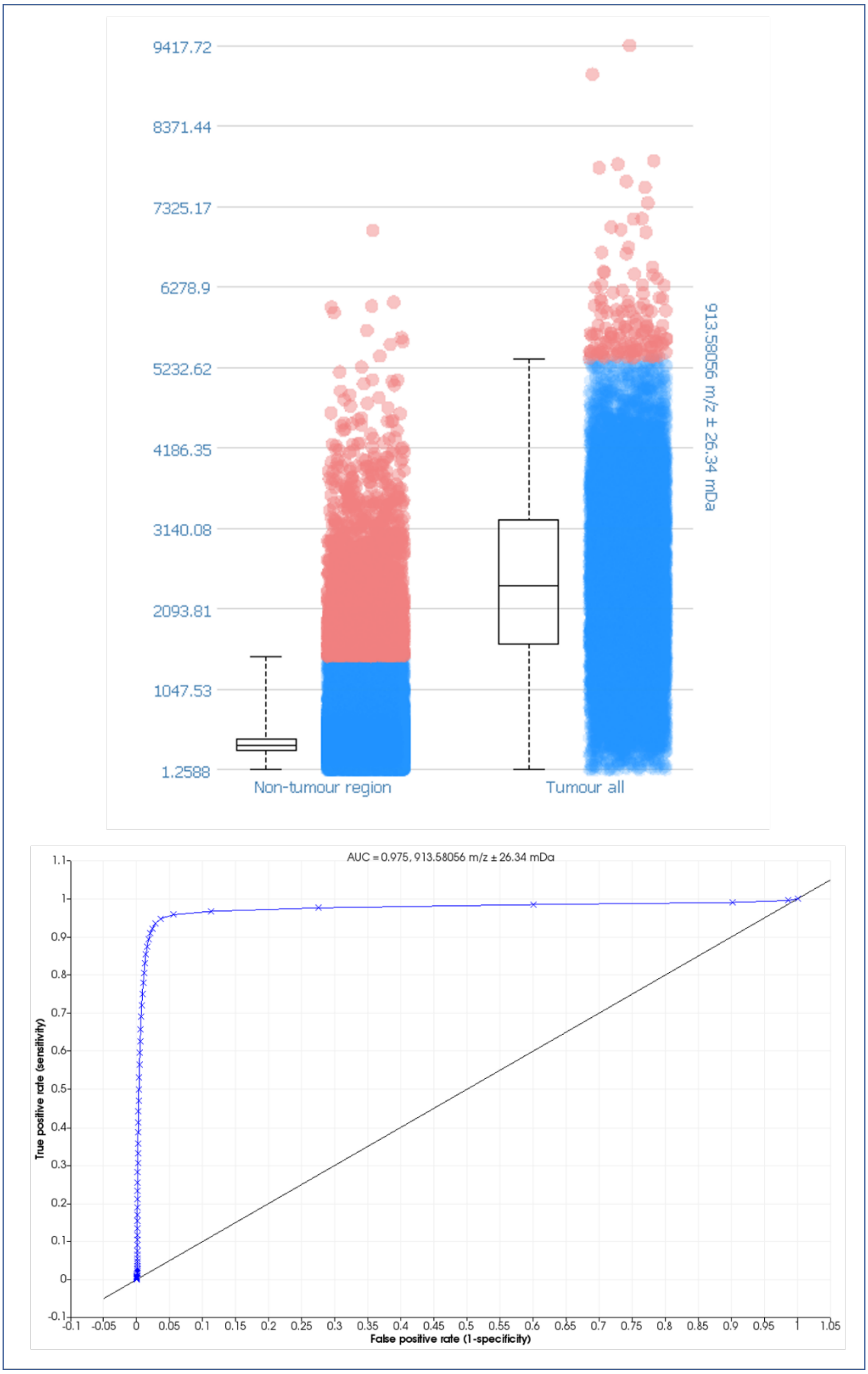

Figure 13 – Box and whisker intensity plot and ROC curve for m/z 913.55 PI (18:0/22:4); the molecular marker that discriminates between the tumour region and the surrounding tissue with the highest sensitivity, ROC = 0.975. The signal intensity of m/z 913.55 in 99% of the non-tumour regions is less than the lowest 25% in the tumour regions, highlighting the increased abundance in tumour regions. The box and whiskers show the spread of 99% of the data. The middle line of the box represents the median and the two edges of the middle box represent the 1st and 3rd quartile. The lower extremity of the whisker to the upper whisker show the data from 0% to 99% and encompass the blue dots, whilst the red dots are termed outliers and only correspond to 1% of the data.

An AUC of 1 would represent complete correlation to the tumour region, as a result, *m/z* 913.55 is highly specific to the tumour region. Putative MS/MS assignment corelates *m/z* 913.55 to PI [18:0/22:4], Figure 14.

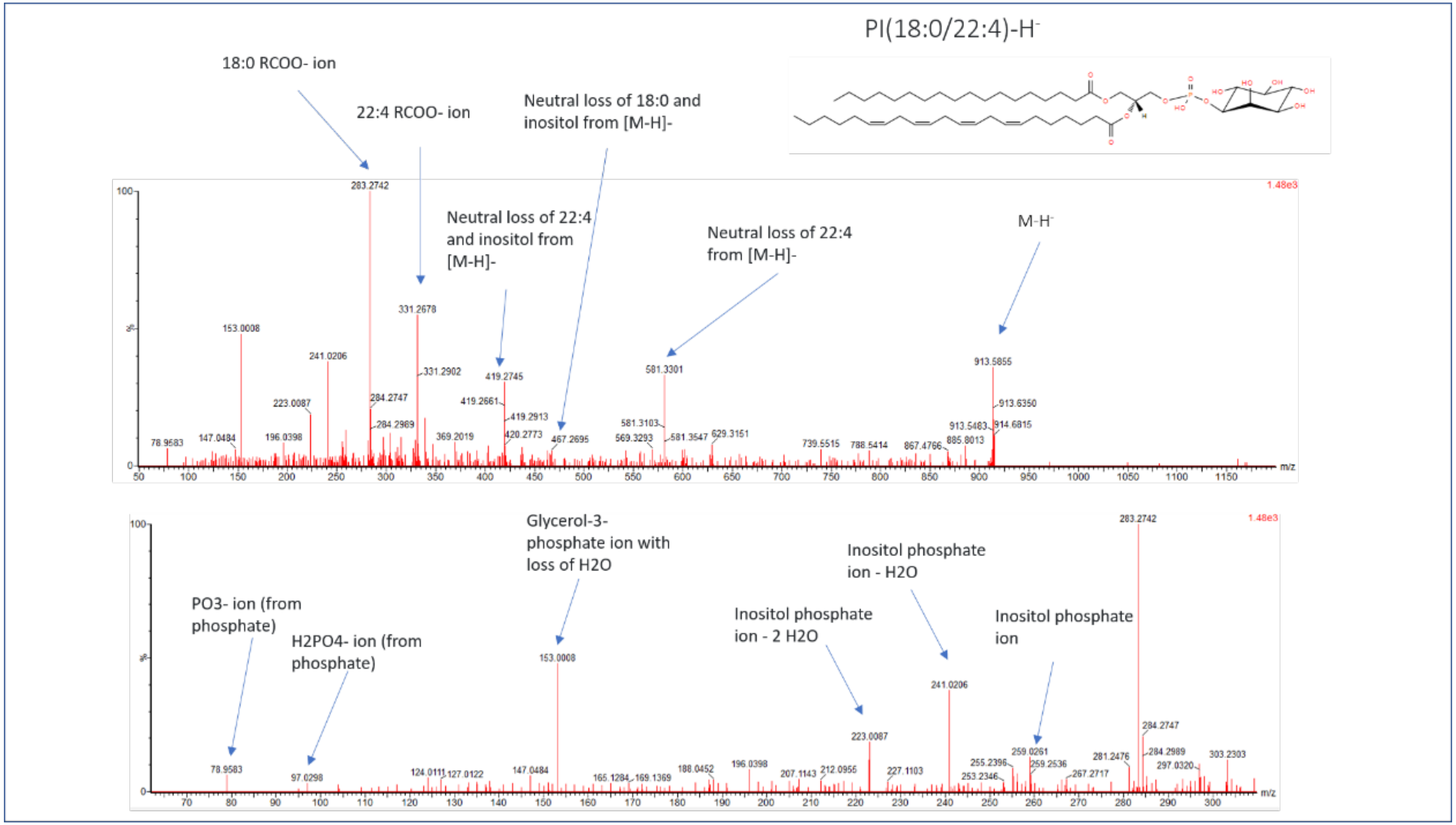

Figure 14 – DESI-MS/MS spectra of m/z 913.55 PI (40:4), determines this molecular ion as PI (18:0/22:4). m/z 913.55 is the most abundant molecular marker for the tumour region. MS/MS ion peaks at 223.01, 241.02 and 259.03 all confirm the presence of the inositol functionality, m/z 283.23 and 331.27 confirm the fatty acid makeup of this phospholipid

Fragments at *m/z* 259.02, 241.02 and 223.08 are key determining species of phosphatidylinositol's (PIs) and the FA side chains, R1 and R2, are readily ionised and determined by accurate mass to determine the overall structure. Multiple PI lipids are observed at high abundance in the tumour region with discriminative values greater than 0.8, supplementary Table 3. This suggests high abundance of this lipid class are found in the tumour environment. The distribution of each m/z associated with a PI species is shown, Figure 15.

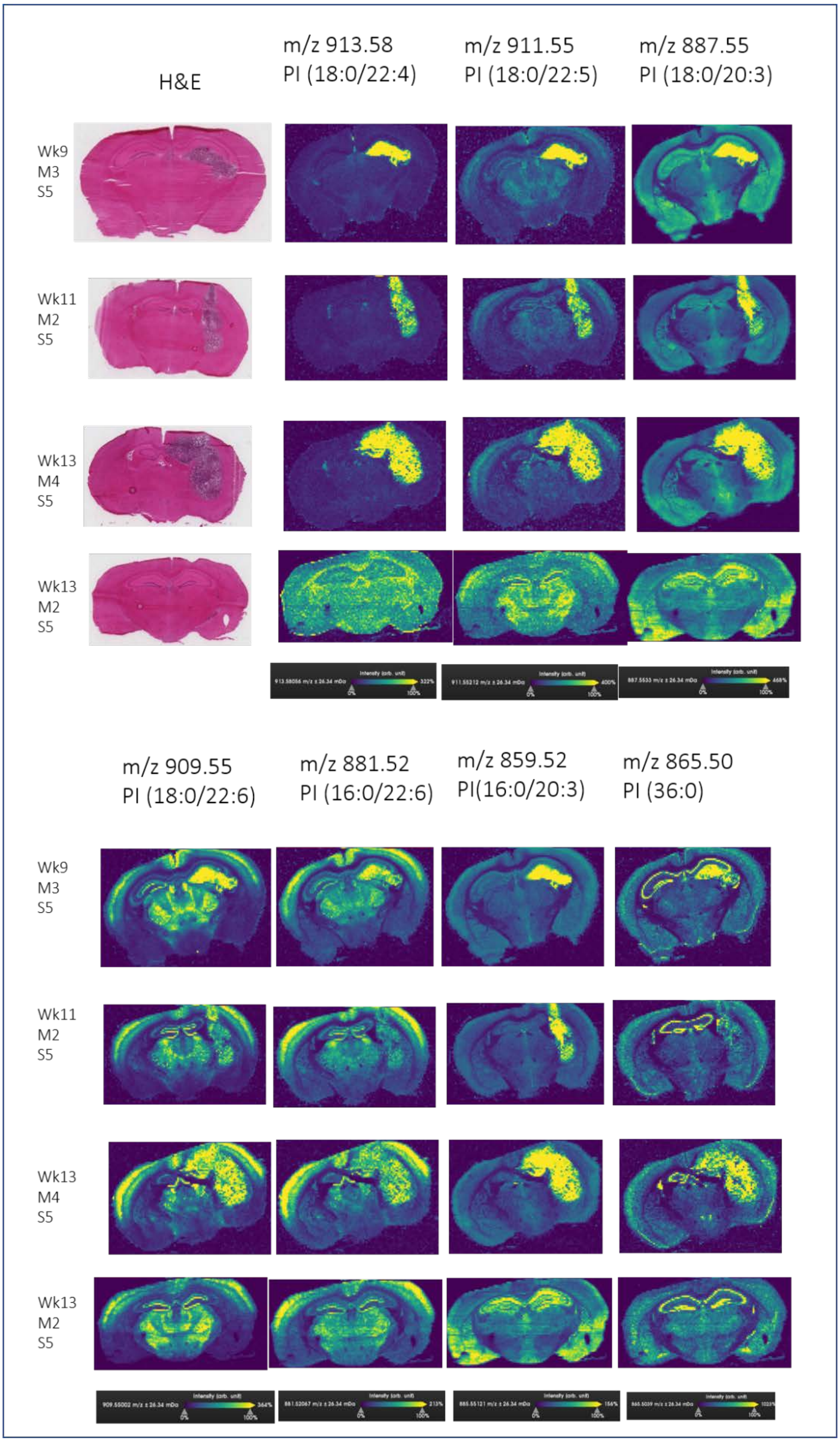

Figure 15 – DESI-MS images of PI species found at high abundance (ROC AUC > 0.8) in the tumour regions across all timepoints. The PI molecular species distribution in healthy brain (Wk13 M2 Section 5) are located to GM regions. In tumour bearing brains PI species are higher in abundance in the tumours compared to the surrounding GM tissue, in all samples. Distributions of PI species; m/z 913.58 (PI (18:0/22:4)), m/z 911.55 (PI(18:0/22:5)), m/z 887.55 (PI(18:0/20:3), m/z 909.55 (PI(18:0/22:6), m/z 881.52 (PI(16:0/22:6), m/z 859.52 (PI(16:0/20:3) & m/z 865.50

(PI(36:0) are shown in Wk9 M3, S5, Wk11 M2 S5 and Wk13 M4 S5, alongside the adjacent H&E section. Results from the control brain Wk13 M2 S5 are also shown for comparison. Lipid identification is made based on accurate mass and MS/MS data shown in Supplementary table 4, Table 5 .

The PIs species observed at *m/z* 913.58 ([18:0/22:4]), 911.55 ([18:0/22:5]), G887.55 ([18:0/20:3]), 909.55 ([18:0/22:6]), 881.52 ([16:0/22:6]), 859.52 ([16:0/20:3]) and 865.50 ([36:0]) are all shown to be highly abundant in the tumour area matching closely to the tumour region observed in the adjacent H&E sections, Figure 15. In the normal healthy tissue, demonstrated by section 5 of M2 Week 13, the PI species are abundant in the GM. These lipids are localised predominantly in the isocortex, hypothalamic and midbrain grey matter regions. With the spatial resolution of DESI-MS imaging at 100 µm the PIs appear homogenously distributed throughout the tumour volumes at high abundance, confirming these species to be key components of G7 GBM tissue and thus, crucial differentiators to surrounding tissue. These species are excellent examples of high correlating molecular species with this G7 glioblastoma tissue, particularly PI [18:0/ 22:6] at *m/z* 913.55 which shows the highest abundance in the tumour compared to healthy tissue.

The PI species with the highest discriminative values; *m/z* 913.58 (PI [18:0/22:4]), *m/z* 911.55 (PI [18:0/22:5]) and *m/z* 887.55 (PI [18:0/20:3]), appear at low abundance in the DESI-MSI plots of the healthy tissue sections, suggesting low natural abundance of these PI molecules in a control tissue, Figure 15. To explore this further, extracted mass spectra from healthy brain and contralateral non-tumour regions are compared to the tumour spectra, Figure 16.

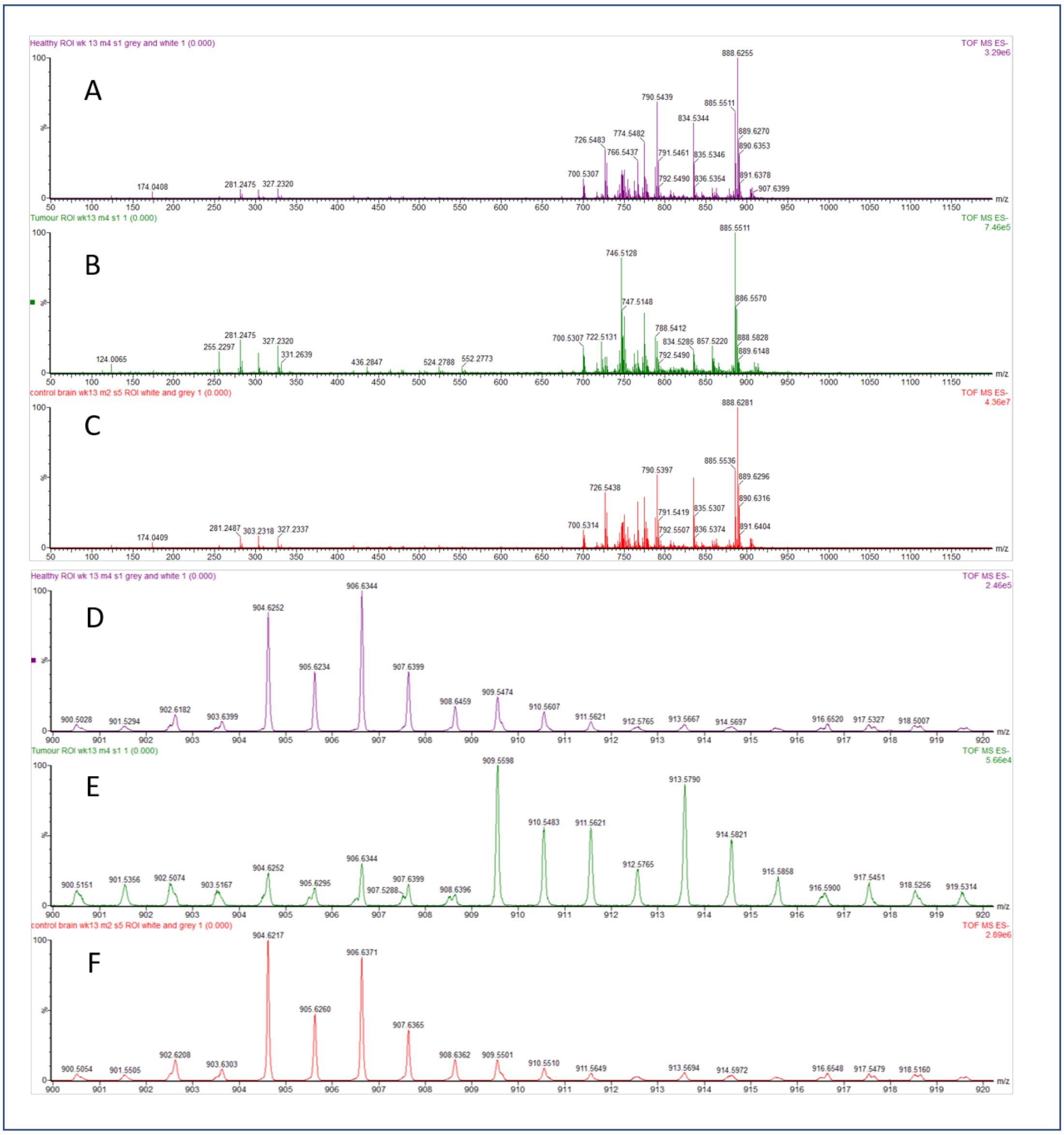

Figure 16 – Differences in lipid composition between an un-diseased brain hemisphere, tumour bearing brain hemisphere and healthy brain hemisphere as shown in extracted DESI-MS negative ion spectra. m/z 909.56 and 913.58 are highlighted as only abundant in the DESI-MS spectra of the tumour bearing brain hemisphere. A – mass spectrum extracted from the contralateral non-tumour containing brain area Week 13 M4 S1, B – mass spectrum extracted from tumour region Week 13 M4 S1, C – mass spectrum extracted from healthy control brain week 13 M2 S5. D, E and F – corresponding mass spectrum from A-C zoomed into m/z 900 – 920 to highlight the PI region of the DESI-MS spectrum––

Over the full mass range the overall MS spectra appear similar, however analysing the mass range greater than *m/z* 900 reveals *m/z* 913.58 and *m/z* 909.55 are abundant in the tumour spectra (Figure 16 E) and relatively low in intensity in the healthy and non-tumour containing spectra (Figure 16 D and F).

The majority of PI species shown in Figure 15 are highly abundant in the tumour region, however the same distribution is not observed for *m/z* 885.55. This *m/z* value is putatively assigned to PI [18:0/20:4] by MS/MS, and is one of the most abundant

PI species observed in mammalian tissue, with up to 85% of mammalian PIs accounted for by this species [24]. The DESI-MSI distribution for *m/z* 885.55 is shown for all tumour growth periods, Figure 17.

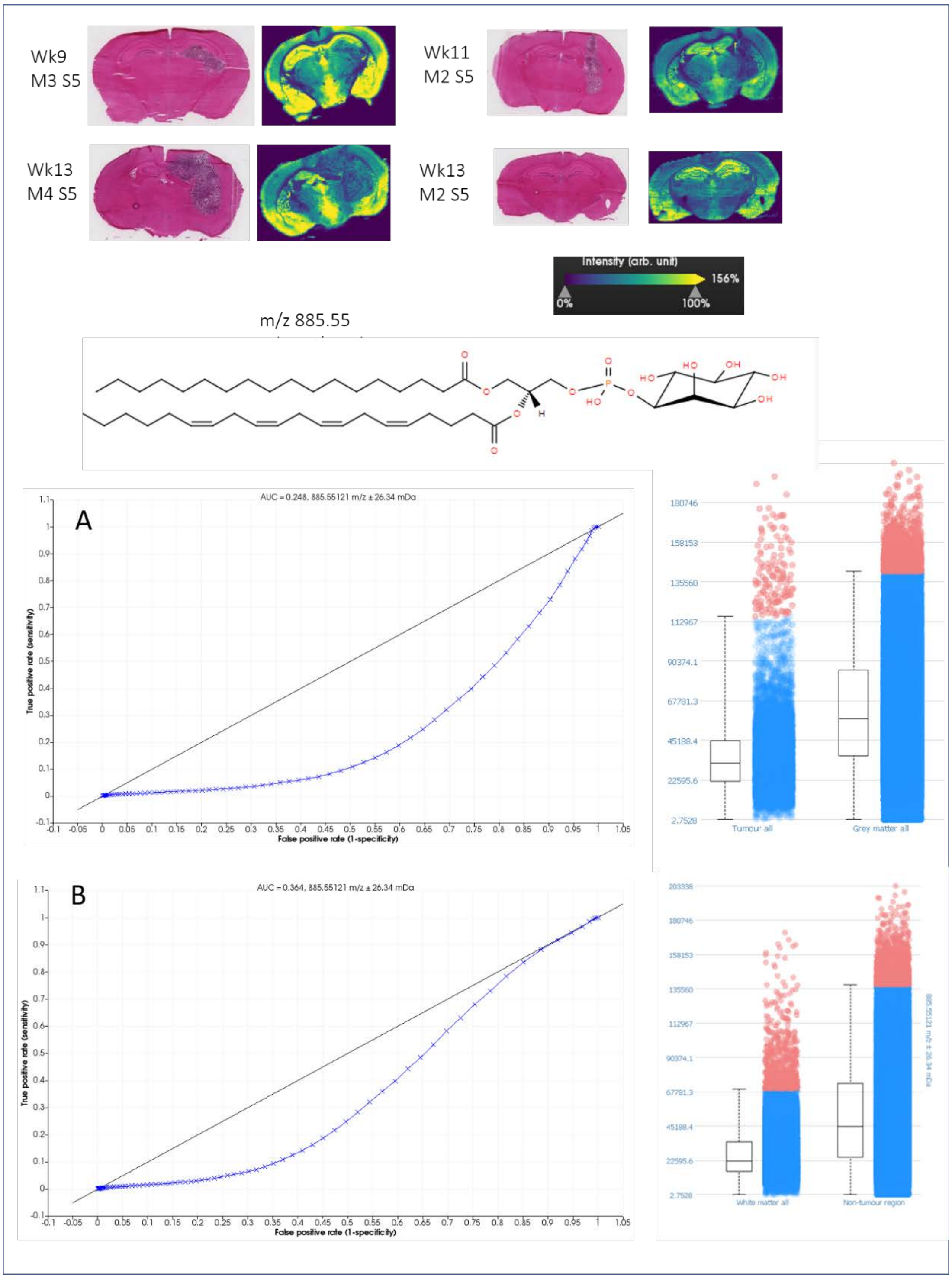

Figure 17 – Distribution of m/z 885.55, PI 38:4 in diseased brain across all 3 timepoints and control brain sections as observed in the negative ion DESI-MS images. m/z 885.55 is confirmed as PI (18:0/20:4) by MS/MS, a common PI found in all mammalian cells that is the precursor phospholipid to PIP2 and PIP3 signalling molecules. PI (38:4) is distributed throughout the grey matter of the brain sections, predominantly in the isocortex and hypothalamic regions and is at lower concentration in the tumour region compared to the grey matter in the contralateral

hemisphere, as confirmed by the ROC analysis (A: Tumour v Grey matter and B: Tumour v healthy brain, AUC = 0.248 and 0.364 respectively) and the accompanying intensity box plots..

The ROC analysis of PI (18:0/20:4), demonstrates the species is highly abundant in the GM regions. This is supported by the DESI-MS imaging distribution of this *m/z* to multiple GM regions including the cerebral cortex (olfactory areas), hippocampus and hypothalamic regions. PI (18:0/20:4) is at low abundance in the tumour region whereas all other PI molecules shown in Figure 15 are at high abundance. This suggests a differing function of PI (18:0/20:4) to the rest of the PI species found in the orthotopic tumour sections.

ROC analysis comparing tumour and GM, returns a discriminative value of 0.248 (Figure 17 A), whilst comparing tumour and surrounding brain regions (WM and GM spectra combined) increased the value to 0.364 (Figure 17B). The intensity box plot shows WM levels of PI (18:0/20:4) to be at lower than those in the tumour, suggesting *m/z* 885.55 (PI [18:0/20:4]) is highly abundant in the GM region. PI (18:0/20:4) is the unphosphorylated form of Phosphatidylinositol-4,5-bisphosphate, PI(4,5)P (PIP2), and Phosphatidylinositol-3,4,5-triphosphate (PI(3,4,5)P (PIP3), which differ by the number of phosphorylated groups on the inositol headgroups, supplementary Figure 38.

As an unphosphorylated species, PI (18:0/20:4) is highly abundant in mammalian tissue as seen in this model and observed in literature [24], however detecting the phosphorylated PIs by DESI wasn’t achieved in this study. Phosphorylated PIs are at low concentrations within cells and the phosphate moieties are also extremely labile. Currently, phosphorylated PI analysis is limited to radioisotope labelling of phosphorous in ATP and hydrogen in myo-inositol [25], which due to the low abundances, aren’t suited for DESI-MS imaging analysis. However, 3D MALDI analysis of medulloblastoma metastasis have imaged PIP and PIP_2 species and shown these to co-locate to PI (18:0/20:4) in metastasising medulloblastoma tumours [26].

The results from the G7 GBM tumour shows many overexpressed PI lipid species that could be indicative of an altered PI3-K metabolic pathway. All PIs (shown in Figure 16) overexpressed in the tumour, apart from PI [16:0/22:6], all contain FA 18:0 at the SN1 position of the inositol lipid and the unsaturated FA moiety present in position 2. This observation matches known PI synthesis in the endoplasmic reticulum, with mammalian cells enriched with PIs containing stearic acid (C18:0) at the SN1 position. Typically SN2 would be highly enriched with arachidonic acid (C20:4), with up to 85% of all PIs accounted for by PI (18:0/20:4) [24, 27].

Mutations to LPIAT1 can disrupt the arachidonic acid content of PIs with shifts to greater unsaturated FA containing PIs [28]. Lee *et al.* have shown a significant decrease in the arachidonic acid (C20:4) component of PI [18:0/20:4], with significant changes to incorporating other common fatty acids C16:0, C18:0 and C22:6 into PIs, whilst also increasing 38:5, 40:6 and 40:7 PI lipids in mice without the enzyme LPIAT1. This may provide insight into the changes we have seen here. Mutation to p53 in colorectal cancer cells (HCT116) showed a decrease in PI (38:4) but to shorter chained PI species C38:3, C36:2 and C34:1, with a higher amount of mono and di-unsaturated FAs [29], whereas an overexpression in p53 in a subsequent study, using the same cell line, also saw a shift to mono or saturated FAs in PIs [30]. These results appear to counter our results where we are seeing an increase in the polyunsaturated FAs incorporated at the SN2 position in PI species over the typical C20:4. The incorporation of FAs may be driven by the availability of FA within the tumour and not simply a shift to mono or saturated FA.

4.2.2. Fatty acids at high abundance in tumour regions revealed by DESI-MS imaging

As mentioned previously, multiple FA species have ROC discriminative values greater than 0.8 (Supplementary Table 3) suggesting high abundance in the tumour regions. Tumour cells are highly metabolic requiring large amount of energy for growth. The preference for normal functioning cells to produce energy is *via* glycolysis, however, cancer cells require a more rapid turnover of energy sources and as such use altered metabolic processes including the use of FAs *via* β-oxidation [31]. Several FA species are shown to be highly abundant in the G7 tumour, observed across all tumours by DESI-MS imaging, Figure 18.

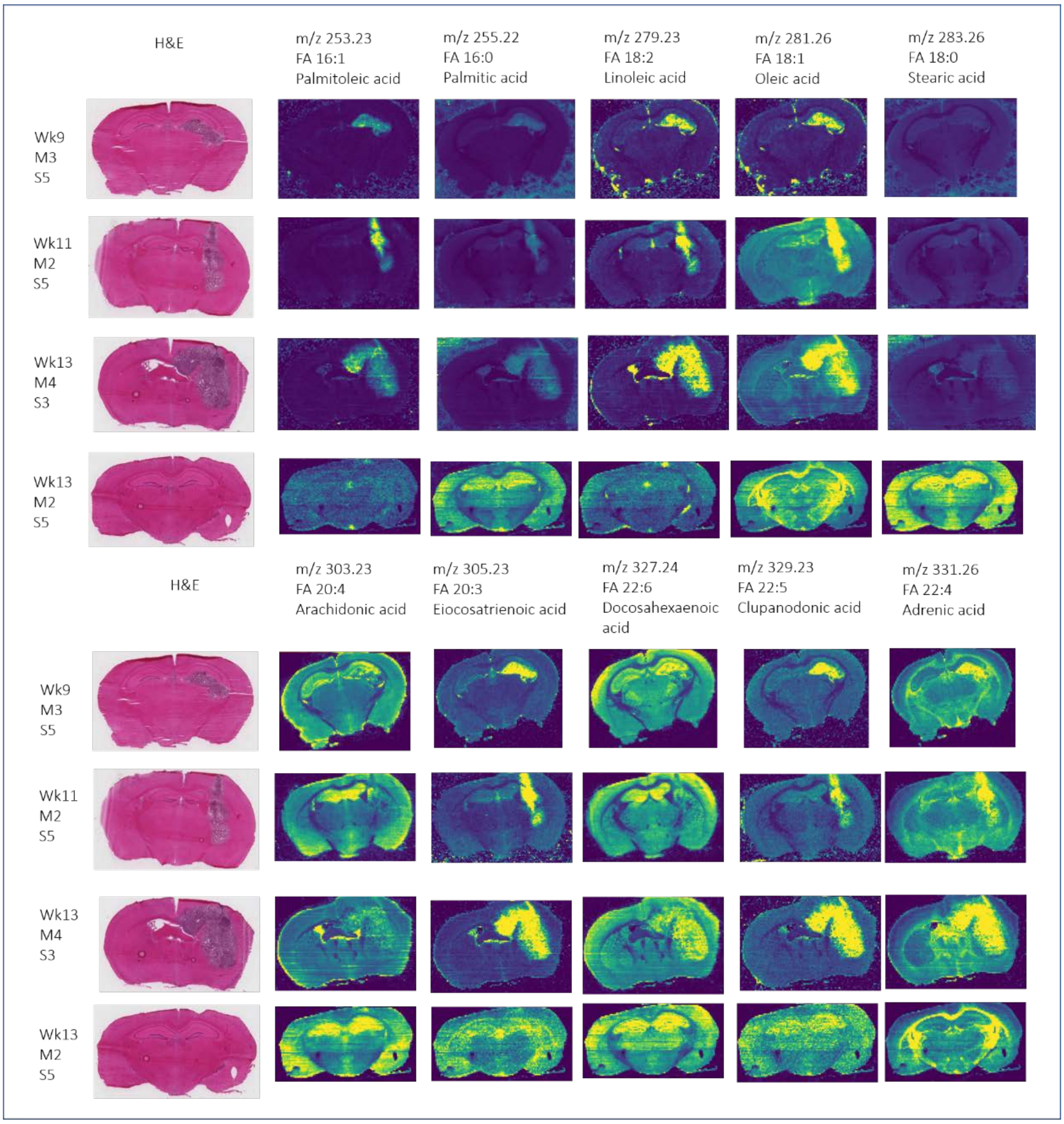

Figure 18 – DESI-MS imagines showing the distribution of fatty acid species observed at high abundance in the tumours. All fatty acids shown have an ROC discriminative value of greater than 0.8 (supplementary table 2). DESI-MS images of; m/z 255.23 (FA 16:1), m/z 255.22 (FA 16:0), m/z 279.23 (FA 18:2), m/z 281.26 (FA 18:1), m/z 283.26 (FA 18:0), m/z 303.23 (FA 20:4), m/z 305.23 (FA 20:3), m/z 327.24 (FA 22:6), m/z 329.23 (FA 22:5) and m/z 331.26 (FA 22:4) are shown for one tumour baring section from each timepoint; Wk9 M3, S5, Wk11 M2 S5 and Wk13 M4 S5. The control brain Wk13 M2 S5 are also shown for comparison, alongside the adjacent H&E section, highlighting the tumour location within each section. Each m/z value identified as a fatty acid species is accompanied by the carbon atom composition and the universal name. All fatty acids shown here are at high abundance in the tumour region and are often only abundant in the tumour compared to surrounding tissue. FA distribution in Wk13 M2 S5 is grainy suggesting low natural abundance of these molecular species .

Fatty acids are building blocks for more complex phospholipids, and as a result, do not readily fragment in MS/MS analysis. As such, accurate mass was used to determine the identity of *m/z* values in 250 – 350 mass range, supplementary Table 4. Palmitic (C16:0), Palmitoleic (C16:1), linoleic (C18:2), eicosatrienoic (C20:3), clupanodonic (22:5) and oleic (C18:1) acid are all observed at high abundance in the defined tumour areas. In healthy control brains, the free FA content is low. For normal metabolic tissue, this is expected as at sufficiently high concentrations, free FA exhibit toxic effects [32]. No FA species detected in the healthy region show a discriminative value of less than 0.5, suggesting each of these is at least at the same abundance in the tumour as the healthy tissue.

Arachidonic acid (C20:4), shown to be low abundance in tumour related PIs, has the lowest ROC discriminative value of any FA species detected (0.5125). The DESI-MSI distribution arachidonic acid, Figure 18, appears throughout the section, matching that observed for *m/z* 885.55 (PI [18:0/20:4]) in Figure 17.

The large number of FA species observed at high abundance in the tumour compared to the surrounding tissue and healthy brain sections, is consistent with an altered metabolic state of these GBM tumours. Metabolic changes in tumours are regarded as key hallmarks of cancer [33, 34]. Recent literature, has demonstrated altered metabolism from glycolysis to β-oxidation of FA lipids in GBM [31] providing metabolic plasticity and adaptational properties of GBM tumour cells. A recent study by Lin *et al.* indicated that inhibiting this pathway using the fatty acid oxidation inhibitor etomoxir impacts the proliferative nature of these tumours [35].

FA are building blocks for more complex phospholipids. The FA observed by DESI-MSI at high abundance are also those seen in the overexpressed PIs in the tumour tissue, which may suggest these FAs are being incorporated into new phospholipids, required for tumour proliferation and growth [24].

4.2.3. Lyso-phospholids at high abundance in the tumour mass

Lyso-phospholipids (LPLs) of both phosphatidylethanolamine (PE) and phosphatidylcholine (Pcho) species are observed and confirmed by MS/MS at *m/z* 436.29 (Lyso-phosphatidylethanolamine (lyso-PE) [P-16:0]), 528.28 (lyso-PE [22:4]) and 552.28 (lyso -phosphatidylcholine (lyso-PC) [18:3]). The DESI-MS imaging results of these three species are compared to the H&E sections, Figure 19.

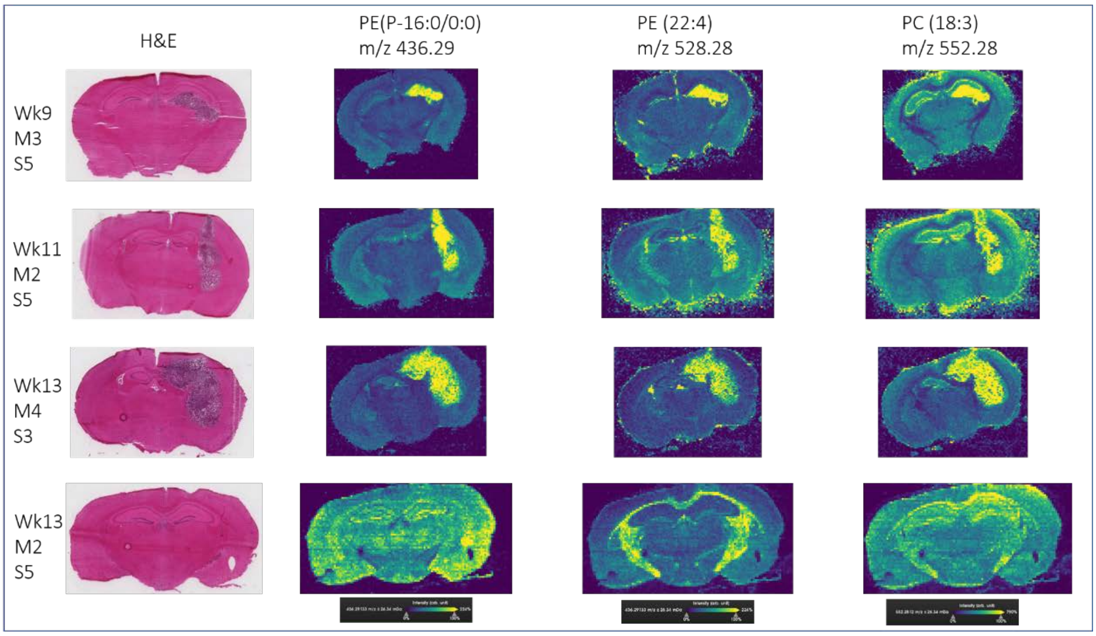

Figure 19 – Distribution of lyso-phospholipid (LPL) species of phosphatidylethanolamine (lyso-PE) and phosphatidylcholine (lyso-Pcho) detected at high abundance in the tumour regions as shown in the above DESI-MS images. DESI-MS images of; m/z 436.29 (PE(P-16:0/0:0)), m/z 528.28 (PE (22:4)) and m/z 552.28 (PC (18:3)) are shown in one tumour baring section from each timepoint, Wk9 M3, S5, Wk11 M2 S5 and Wk13 M4 S5, alongside the adjacent H&E section. Results from the control brain Wk13 M2 S5 are also shown for comparison. Lipid identification is made based on accurate mass and MS/MS data

Unlike many commonly occurring and detected phospholipid species in the DESI-MS spectra, LPLs only contain a single FA side chain rather than the usual double. Fragmentation patterns following MS/MS of PE [P-16:0] is presented, Figure 20.

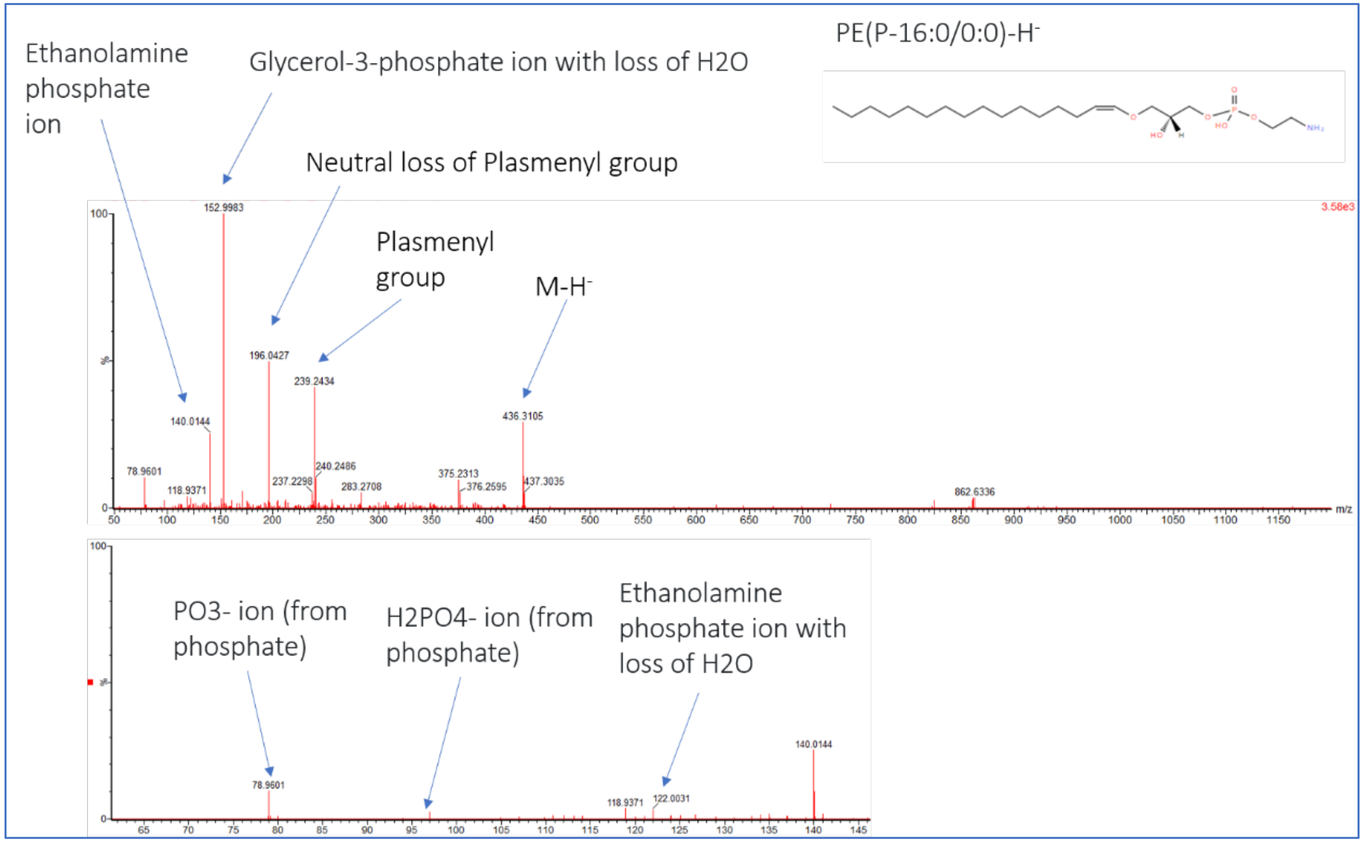

Figure 20 – DESI-MS/MS spectra of m/z 436.31, determines this molecular ion as lyso-PE(P-16:0/0:0). m/z 436.29 is an abundant molecular marker for the tumour region. MS/MS ion peaks at 122.00 and 140.01 confirming the presence of the ethanolamine functionality, m/z 196.04 and 239.24 confirm the fatty acid makeup of this single fatty acid containing phospholipid.

The lyso-lipids, Figure 19, present in the control section Week 13 M2 S5, are mainly confined to the white matter tracts and the corpus callosum. The LPLs are highly abundant in all tumour masses and appear to be homogenously distributed throughout the tumour volume when compared to the H&E map.

Unlike other phospholipids that are key constituents of the phospholipid bilayer, LPLs are thought to have a greater role in cancer. LPLs play important roles in the immune system through the development and activation of immune cells including M1 macrophages [36]. Immune cells are important features of the tumour microenvironment (TME), associated immunosuppressive properties and poor prognosis of GBMs [37, 38]. A link between lyso-phosphatidic acid and sphingosine 1-phosphate has also been shown to be involved in the progression of cancer by regulating tumour cell growth, proliferation, migration and survival acting on specific G-protein coupled receptors to stimulate these key characteristics of cancer cells [39, 40]. To assess the role LPLs play in G7 GBM IHC, staining for macrophages and subsequent correlation to the LPL distribution should be assessed.

4.3. Low abundant tumour phospholipids and metabolites can distinguish surrounding tissue from tumour regions

4.3.1. Phospholipids at high abundance in surrounding tissue

As well as lipid species that are observed at high abundance, and in some cases overexpressed in the tumour region, there are also multiple species specific to the healthy brain tissue and as such are not detected in the G7 tumours. Low abundant tumour lipid species are shown with ROC discriminative values less than 0.15, Figure 21.

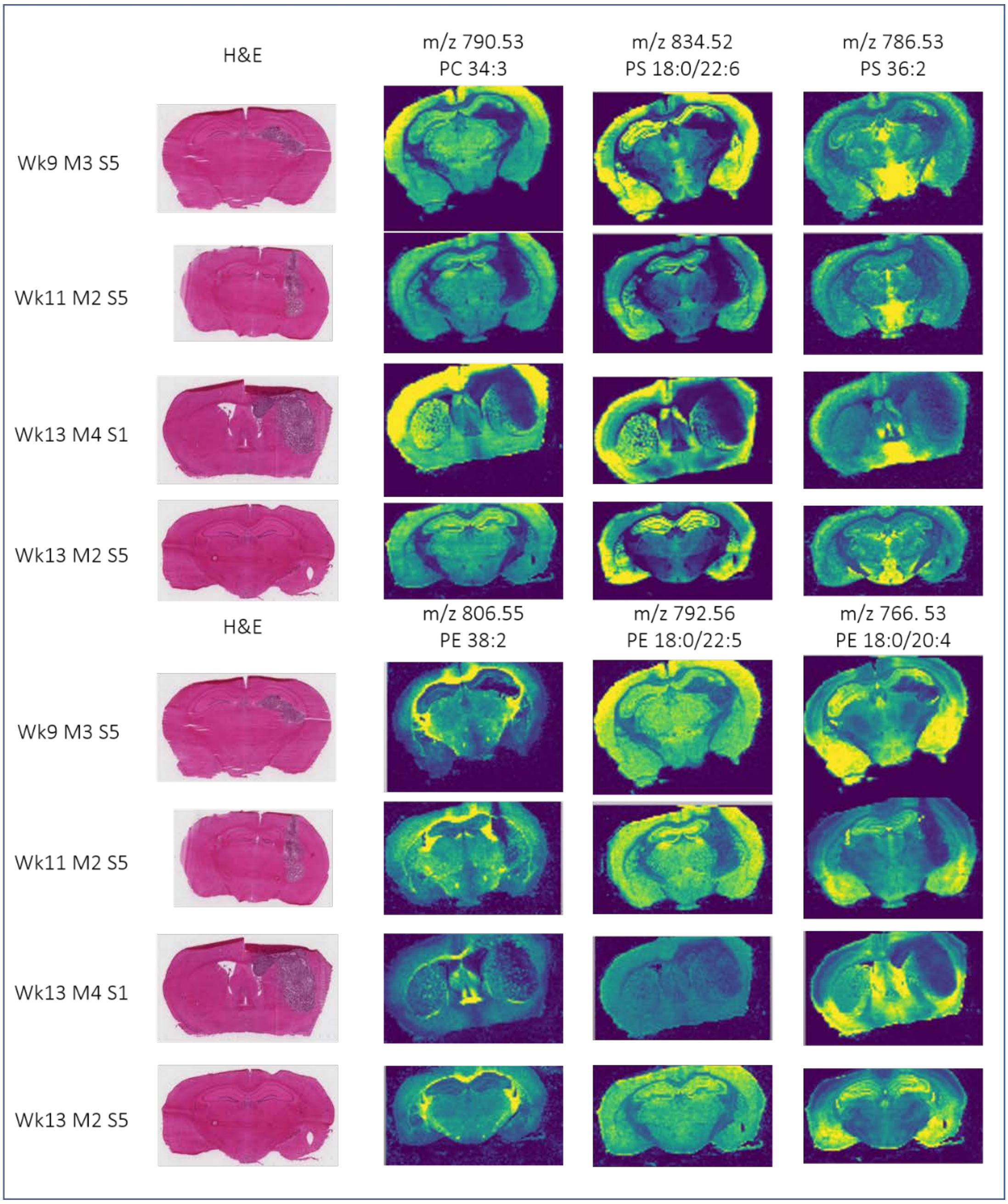

Figure 21 – Distribution of lipid species observed at low abundance in the tumour regions of the DESI-MS images. All species have an ROC discriminative value less than 0.15 (Supplementary table 2). Multiple phospholipid groups are observed at low abundance in the tumour compared to surrounding tissue, of which the least abundant are shown here. DESI-MS images of m/z 790.53 (PC 34:3), m/z 834.52 (PS 18:0/22:6), m/z 786.53 (PS 36:2), m/z 806.55 (PE 38:2), m/z 792.56 (PE 18;0/22:5), m/z 766.53 (PE 18:0/20:4) are shown in one tumour baring section from each timepoint, Wk9 M3, S5, Wk11 M2 S5 and Wk13 M4 S1, alongside the adjacent H&E section. Results from the control brain Wk13 M2 S5 are also shown for comparison. Phospholipids from PC, PS and PE are all shown at low abundance in the tumour regions of tumour bearing sections. .

Phospholipids from a range of lipid classes, including Pcho, phosphatidylserine (PS) and PE are all observed at low abundance in the G7 tumours. These lipids are localised to either the GM or WM, with very few observed in both. GM and WM are made up of different cells and as such contain specific lipids which are subsequently extracted and analysed by DESI-MS. White matter structures apparent in these sections comprise the corpus callosum and the WM associated nerve tracts, whereas GM regions comprise areas within the cerebrum, mainly the isocortex, and the midbrain containing hypothalamic, thalamus and hippocampal brain regions.

Molecular species that show low abundance in the tumour can be useful for tissue differentiation and used as markers for healthy versus tumour tissue. The range of phospholipids observed here have not been previously discussed. However, using a molecular species as a negative marker has implications, particularly if that molecular species is suppressed for unknown reasons, such as ion suppression. Ion suppression is less evident in DESI-MSI due to low matrix affects but may be issues in other MSI approaches such as MALDI [41]. As such caution must be observed if using the lack of a particular molecular species as a marker to signify the absence of tumour.

4.3.2. N-acetyl aspartate as a marker of neuronal health

The molecular species discussed above that differentiate the tumour and surrounding brain regions have been assigned to complex phospholipids or FA species. One of the key discriminating low molecular species (ROC value of 0.1083) that is not observed in the tumour region is *m/z* 174.04, assigned to N-acetyl aspartate (NAA), Figure 22.

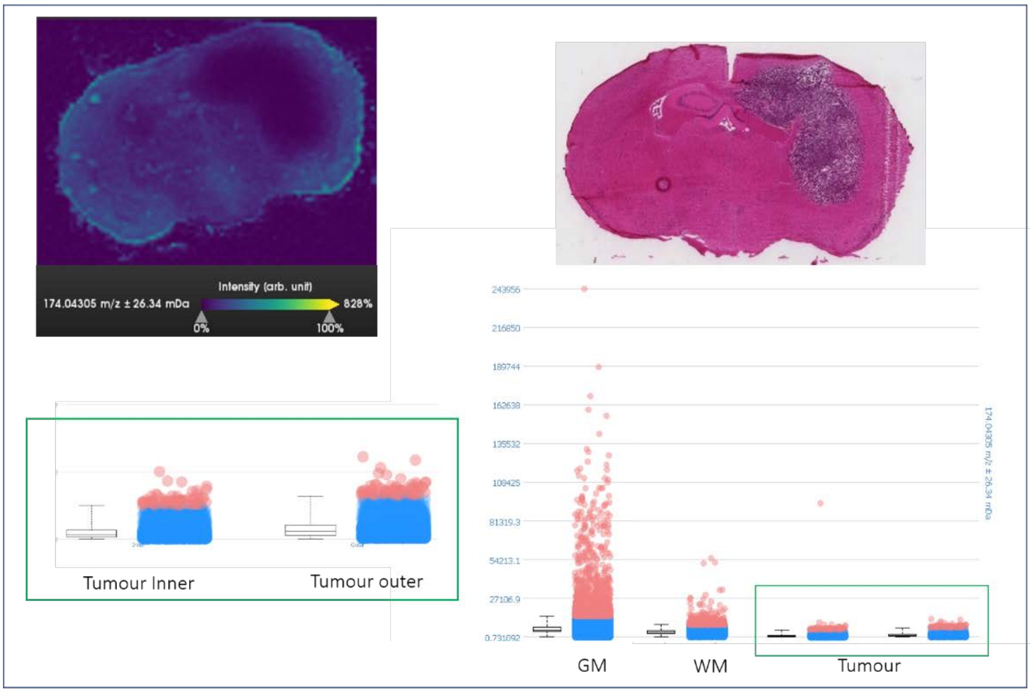

Figure 22 – Distribution of N-acetyl aspartate (NAA) observed in a tumour containing brain as assessed by DESI-MS imaging. Negative ion mode DESI-MS image of NAA (m/z 174.04) in Wk 13 M4 S5 alongside adjacent H&E-stained

image. Intensity box plots from extracted GM, WM, and tumour regions of the tissue section. NAA is not observed in the tumour region on the DESI-MS image, matching the low intensity of m/z 174.04 in the intensity box plots. Intensity of NAA further decreases towards the inner tumour region (significance un-tested).

NAA has been observed previously in the analysis of brain tumour biopsies by Cooks *et al.* and is a key component used in the analysis of GBM biopsies to distinguish tumour from healthy tissue [42]. NAA is a marker of neuronal health and as such is suspected to be at much higher abundance in the healthy tissue versus the tumour tissue [43]. In this model, NAA is observed at higher abundance in the GM compared to WM and much lower in the tumour volumes, as evidenced by the ion intensity box plots. Although less apparent due to the low abundance in the tumour region, NAA is also decreased in the inner region of the tumour compared to the outer region. This further confirms NAA as a good negative marker of GBM tumours.

4.4. Complimentary positive ion mode DESI-MS imaging to reveal further tumour regions

Alongside the comprehensive negative ion mode data, sections from each time point were analysed in positive ion mode to provide complimentary information to that of the negative ion mode data. The bisecting k-means segmentation of WK13 M3 S1, Figure 23, highlights comparative distribution to those observed in negative ion mode images.

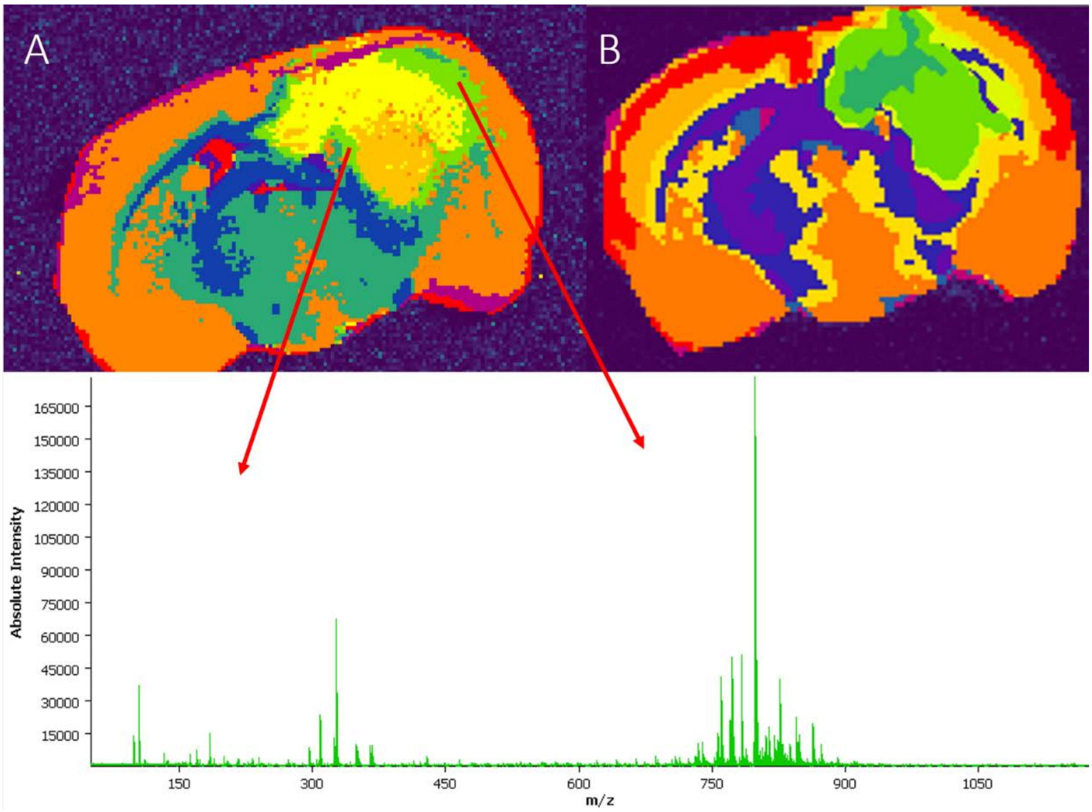

Figure 23 – Bisecting k-means segmentation analysis of positive ion mode DESI-MSI to discriminate further tumour regions. A – bisecting k-means results of positive ion mode DESI-MSI Wk13 M1 Section 3, B - bisecting k-means results of negative ion mode DESI-MSI Wk13 M1 Section 4. Bottom -representative positive ion mode DESI mass spectrum from the light green bisecting k-means region of wk13 M1 Section 3. Segmenting both the positive and negative ion mode date from the same tissue section reveal a further tumour region only found in the positive ion DESI-MS data.

The light green region surrounding the tumour in the DESI-MSI positive ion mode segmentation, does not appear in the DESI-MS negative ion mode and suggests further information can be extracted about the tumour by investigating the positive ion mode data. Many lipid species are only readily ionised in positive ion mode, and as such it is common for many lipidomic experiments to focus on this polarity. However, there are still many lipid species that are ionised in negative polarity, thus, analysing sections in both polarities allow further molecular species to be found, providing a more comprehensive overview of the GBM tissue.

Table 2 – Observed m/z species in positive ion mode DESI-MS imaging data that are assigned to carnitines by accurate mass. No MS/MS analysis was carried out on these sections; thus, lipid assignment is based on accurate mass measurements.

Observed *m/z*	Carnitine assignment	Fatty acyl component	Theoretical mass	ppm error
400.3413	Palmitoylcarnitine	C16:0	400.3421	2.00
428.3692	Stearoylcarnitine	C18:0	428.3734	9.80
162.1109	L-carnitine	-	162.1125	9.87

Many of the *m/z* values observed in this region are abundant in the total tumour region, however, *m/z* 400.34 and *m/z* 428.36 (tentatively assigned as palmitoylcarnitine C16:0 and stearoylcarnitine C18:0 by accurate mass) are observed at higher abundance in this band of the tumour, Figure 24. These *m/z* values, 400.34 and 428.36, are at low abundance in the tissue and thus MS/MS confirmation was not possible, however, the use of accurate mass has been used to aid assignment, Table 2.

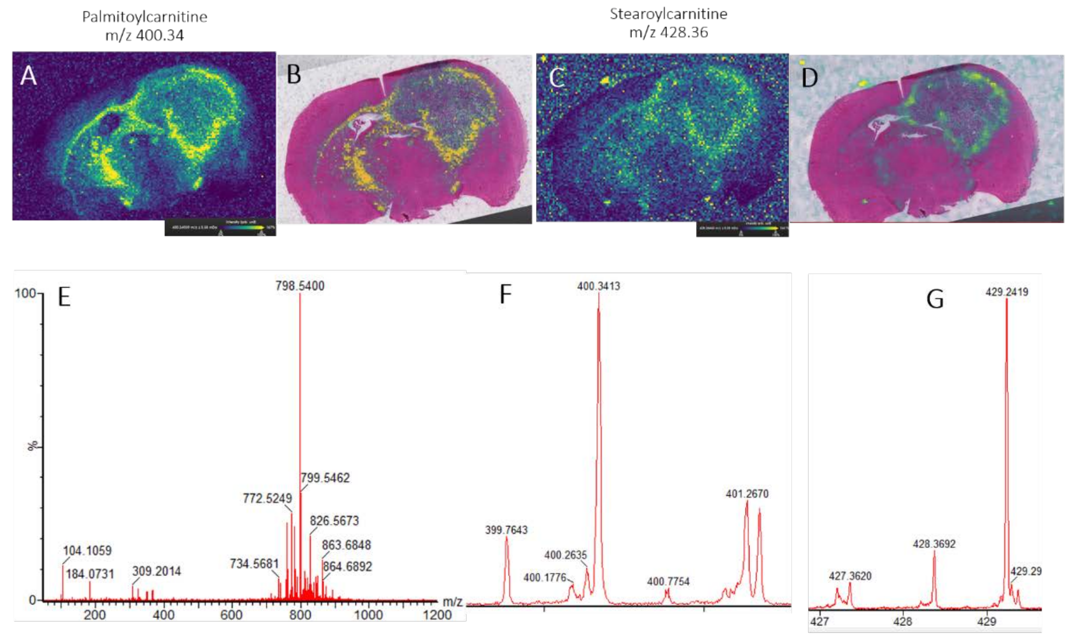

Figure 24 – Distribution of carnitines in tumour containing brain as assessed by positive ion mode DESI-MS imaging. Ion mapping locates the carnitines to the extremity of the tumour mass in Wk13 M1 S3. A & B – distributipon of palmitoylcarnitine single ion image & single ion image overlayed with H&E image, C & D – stearoylcarnitine single ion image & single ion image overlayed with H&E image. E – full DESI-MS positive spectrum from the tumour region, F & G – zoomed in spectrum to highlight carnitine molecular peaks at m/z 400.34 and m/z 428.37 for palmitoylcarnitine and stearoylcarnitine respectively.

Overlaying the carnitine distributions with the H&E image shows *m/z* 400.34 and 428.36 located towards the tumour edge, rather than being located throughout the whole tumour as has been shown prior for other tumour lipids. The molecules also appear in the WM region in this section. Another peak, *m/z* 162.11 was observed in the positive ion DESI-MS imaging of wk13 M1 S3 and putatively assigned by accurate mass as L-carnitine, Figure 25.

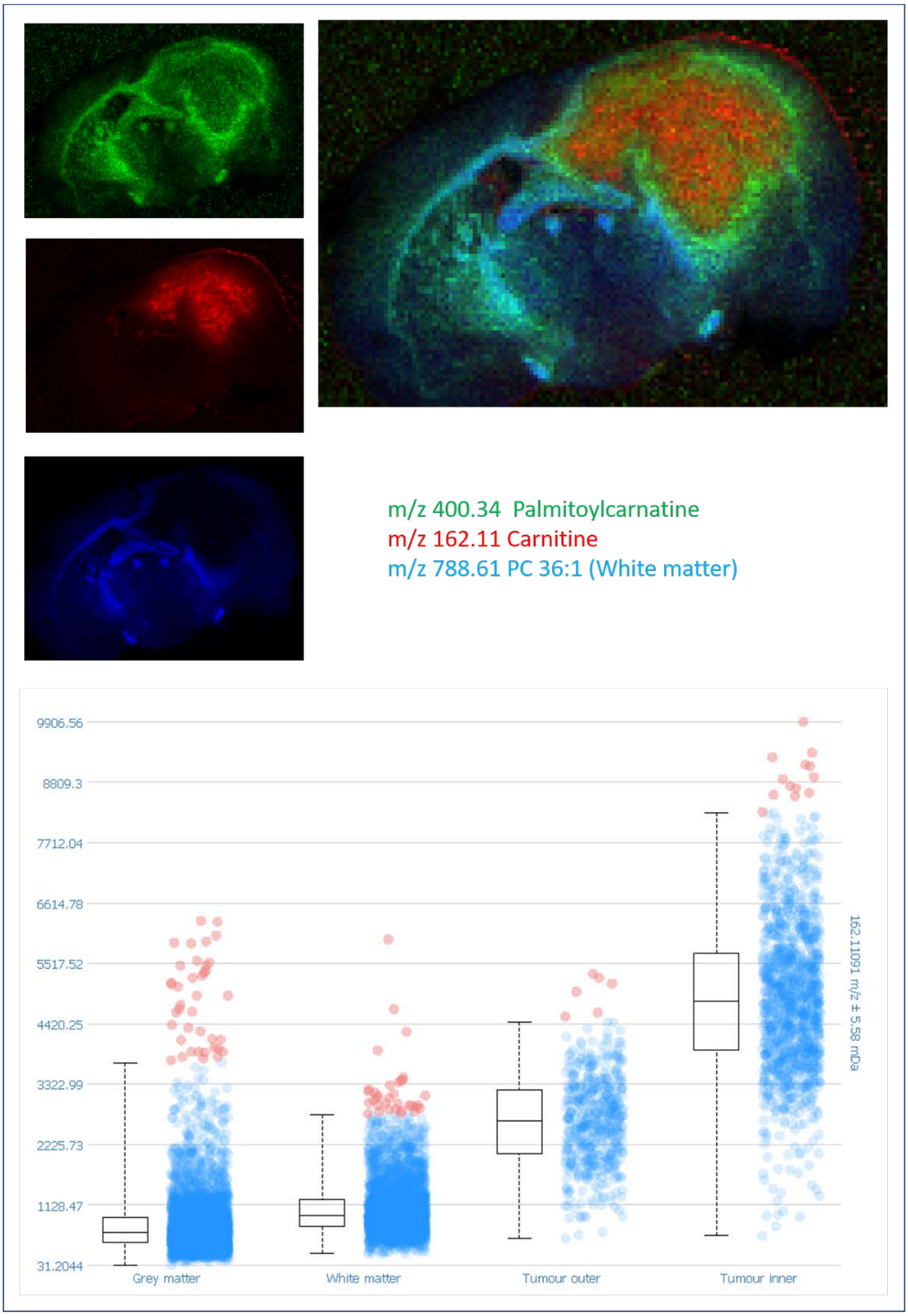

Figure 25 – Assessing the relationship between fatty acids and carnitines by multi-polarity DESI-MSI. Single ion images and overlayed DESI-MS distribution of m/z 400.34 palmitoylcarnitine (green), m/z 162.11 L-carnitine (red) and m/z 788.61 PC 36:1 (blue) in Wk13 M1 S3 shows the distribution throughout the tissue sections. Palmitoylcarnitine forms a band around the L-carnitine at the edge of the tumour with L-carnitine located within the tumour region. m/z 788.61 is a WM marker to highlight the tissue morphology. Ion intensity boxplot shows the abundance of m/z 162.11 assigned to carnitine throughout the tissue section highest in the middle of the tumour.

L-carnitine is overlayed with its acyl counterpart (*m/z* 400.34) and reveals contrasting distributions. *m/z* 162.11 is abundant in the tumour core whilst *m/z* 400.34 is shown in a band surrounding *m/z* 162.11. The intensity box plots, Figure 25, show the intensity of L-carnitine (*m/z* 162.11) to be higher in the inner tumour region compared to the outer region, the opposite to that observed from the acyl-carnitines.

Overlaying palmitoylcarnitine *m/z* 400.34 with a known marker of WM in mice brain PC 36:1, *m/z* 788.61, further highlights that *m/z* 400.34 is forming a separate ring at the tumour edge as well as locating in the WM region of the corpus callosum. The green and blue regions corresponding to palmitoylcarnitine and PC [36:1] in the WM are not observed in the same pattern, Figure 25. L-carnitine and acyl L-carnitines, primarily palmitoylcarnitine, are recruited by astrocytes in the brain, which are key components of the white matter [44] and may explain these results.

Carnitines are involved in the transport of long chained fatty acids into the mitochondria for fatty acid oxidation (FAO) where β-oxidation occurs [45]. Fatty acids are first converted into fatty acyl-CoAs, which are subsequently converted into the acyl-carnitines by incorporation with L-carnitine [45]. Previous DESI-MSI results observed carnitines in hypoxic bands of a U87 GBM xenograft, correlating with CA9 immunohistochemical staining [23]. If the results in the orthotopic tumour matches those from U87 xenograft the carnitine band observed in wk13 M1 S1 at the tumour periphery may also be due to hypoxic conditions. CA-9 IHC staining could confirm this result and further explain the distribution. MALDI-MS imaging has also previously shown palmitoyl and stearoyl carnitine to locate to the tumour edges in patient derived GBM xenografts [46]. Randall *et al.* has shown fatty acid metabolism enzymes to be highly expressed in tumours with high acyl carnitine content which may corroborate the DESI-MS images [46].

To investigate the relationship between FA and carnitines in all tumours, Wk11 M2 S5 and Wk9 M2 S4 were also analysed in positive ion mode by DESI-MS imaging. DESI-MSI positive ion mode highlights the distribution of these carnitine species across all tumours, Figure 26.

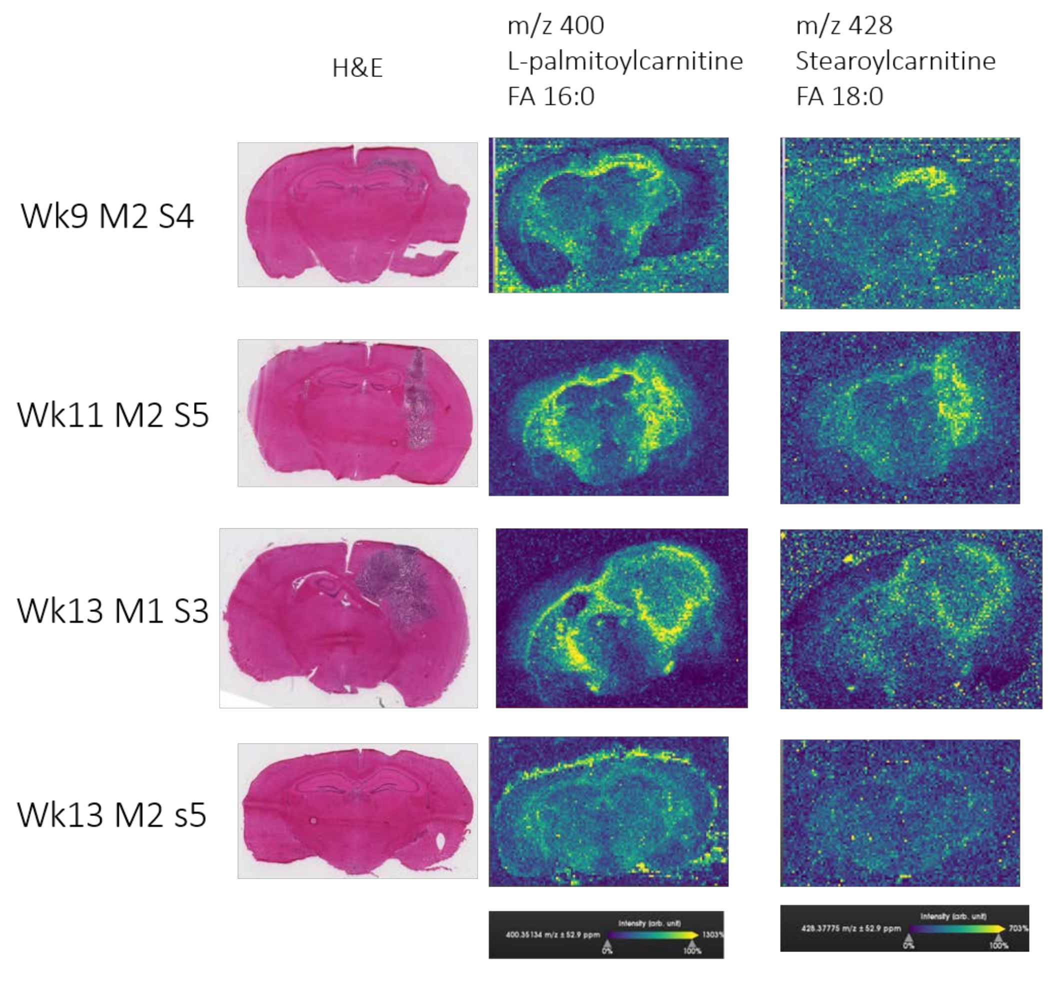

Figure 26 – The presence of carnitines only occurring in tumour containing brain sections is achieved by plotting the distributions of multiple lipids across all tumour timepoints, alongside control brain section. Results from the control brain Wk13 M2 S5 show no or very low abundance of carnitines. The carnitines are labelled with their corresponding fatty acyl component. DESI-MS positive ion images of m/z 400 (palmitoylcarnitine) and m/z 428 (stearoylcarnitine) in Wk9 M2 S4, Wk11 M2 S5 and Wk13 M4 S1 are shown alongside H&E image of the adjacent section.

In the healthy brain, *m/z* 400.34 and 428.36 are observed in the WM at low abundance. The distribution of *m/z* 400.34 and 428.36 in all sections containing tumours is not located to the entire tumour region, rather showing abundance to the extremity of the tumour. The carnitines in Wk9 M2 S4 are more difficult to accurately assign to the extremity of the tumour due to the small size of the tumour mass in this section.

Fatty acids and carnitines are shown to be related in cancers where β-oxidation is used for energy production [45]. The distributions of FA of the same chain length to the acyl component in the carnitines for Wk11 M2 S5 and W13 M1 S3 are compared to the carnitine distributions, Figure 27 and Figure 28. FAs are ionised preferentially in negative ion mode and carnitines in positive ion mode, so data from both polarities is shown.

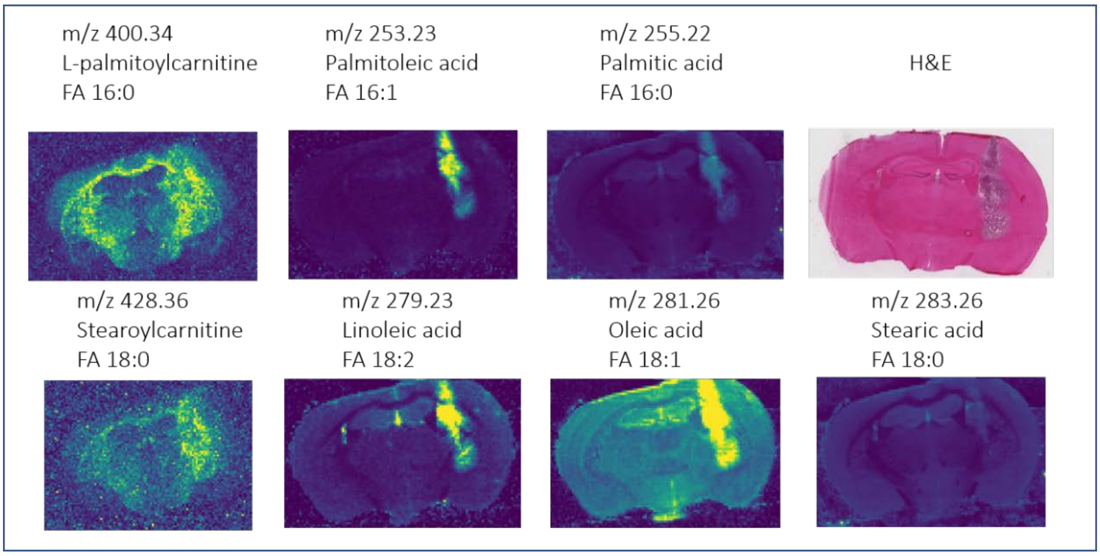

Figure 27 – The relationship between fatty acyl carnitines and the corresponding free fatty acids by comparing the DESI-MS distribution in week 11 M2 S5. The fatty acids selected are those that contain the same number of carbon atoms as those found in the acyl chain in the carnitines. Fatty acid species are detected in the negative ion mode and carnitines in the positive ion mode from the same section. The carnitines and fatty acids appear to locate to differing parts of the tumour mass.

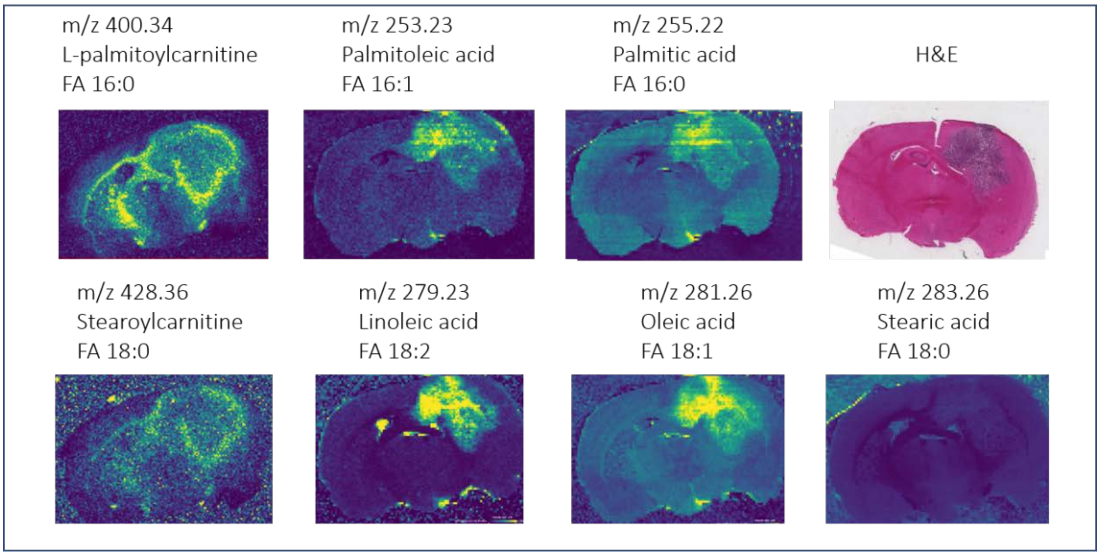

Figure 28 – The relationship between fatty acyl carnitines and the corresponding free fatty acids by comparing the DESI-MS distribution in week 13 M1 S3. The fatty acids selected are those that contain the same number of carbon atoms as those found in the acyl chain in the carnitines. Fatty acid species are detected in the negative ion mode and carnitines in the positive ion mode from the same section. The carnitines and fatty acids appear to locate to differing parts of the tumour mass.

The distributions of carnitines and FA are comparative for week 11 and week 13 tumour sections. Palmitoylcarnitine and stearoylcarnitine, containing the acyl counterparts of FA 16:0 and FA 18:0 respectively, are distributed towards the boundary of the tumour whilst their FA counterparts are located at high abundance within the tumour region. The molecular species assigned to FA 18:0 and FA 16:0 are low abundant in the tumour compared to other the unsaturated version, which may be explained by the detection of their respective carnitines. Carnitines containing FA 16:1 and 18:1 acyl derivatives are not detected in the positive ion spectra, whilst their respective FAs are highly abundant in the tumour. Observing both FA and carnitines in the tumour, although in contrasting locations, may further confirm the altered metabolic activity of these tumours.

4.5. Elemental analysis using LA-ICP-MS

Laser ablation inductively coupled plasma mass spectrometry (LA-ICP-MS) images were acquired from serial sections to those used for DESI-MS imaging. Samples from each timepoint were imaged for trace element analysis of carbon, gadolinium, zinc, manganese, iron, nickel, and copper. Gadolinium is contained with the MRI contrast agent used in this study, whilst zinc, manganese, iron, nickel, and copper are all endogenous compounds with varying cellular roles.

Section 5 from the control brain (Wk13 M2) was imaged to determine metal ion distribution in a non-tumour containing brain and as such has an intact blood brain barrier (BBB) Figure 29.

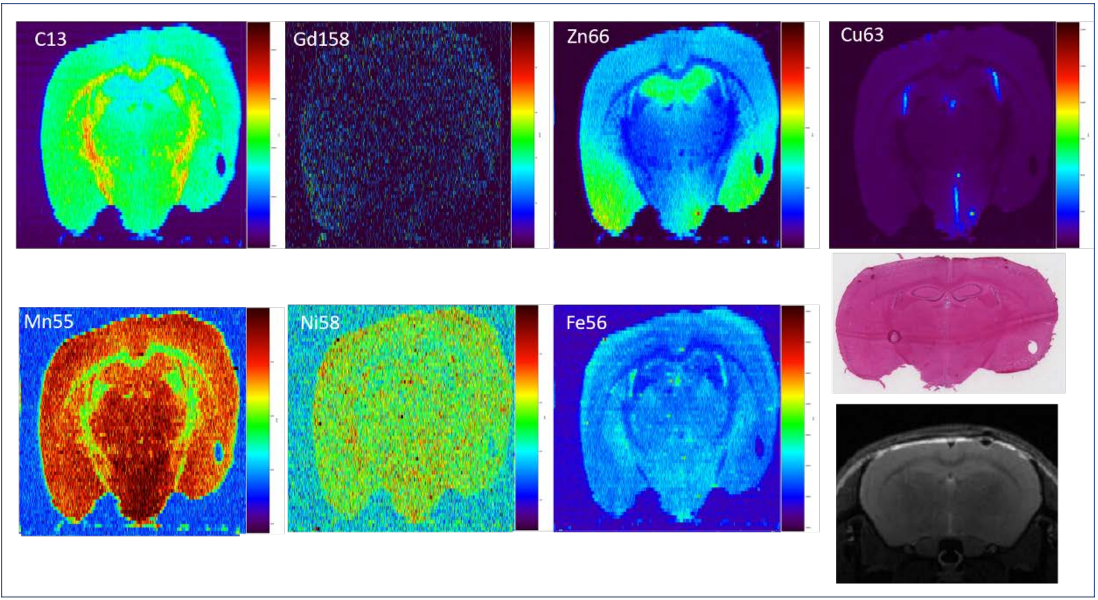

Figure 29 – Distribution of all metal ions analysed in a control brain section Wk 13 M2 S2 analysed by LA-ICP-MS. The intensity scale bars range from red to violet. Red regions show high intensity whilst blue/ purple show low abundance. Distributions of carbon-13, gadolinium-158, zinc-66, copper-63, manganese-55, nickel-58 and iron-56 are mapped as ion density distribution maps to show the overall distribution expected for each in a non-diseased brain. Gadolinium shows no distribution in non-tumour bearing brains as indicated by the grainy blue pixelated

image. H&E image of the adjacent section is also shown, alongside the T2W MRI slice closely representing the section imaged.

Gadolinium is not observed in the control brain, imaged as isotope 158. There are four main gadolinium isotopes, 156, 157, 158 and 160, all with similar relative abundances. Mapping each isotope yielded complementary results, so mass 158 was selected due to its highest natural abundance at 24.84% (data not shown). Zinc-66 is located in the GM regions of the brain, with the highest abundance in the hippocampus and the isocortex, primarily the olfactory areas. Copper is localised to a portion of the brain stem attributed to the hypothalamus as well as the ventricular regions, containing the choroid plexus, which also contains zinc-66 and iron-56. Manganese-55 and nickel-58 are not observed at high abundance but altering the manganese-55 counts per second CPS scale, Figure 29, shows higher abundance in the grey matter regions vs white matter. Iron-56 appears in the grey matter and not the white matter, likely locating within haem found in red blood cells. The distributions of copper, zinc and iron match those reported for LA-ICP-MS atlas in mice brains [47].

Elemental distributions in Wk11 M2 S5 from a single 100 µm resolution LA-ICP-MS imaging experiment reveal the distribution of all metals across the entire tumour containing brain section, Figure 30.

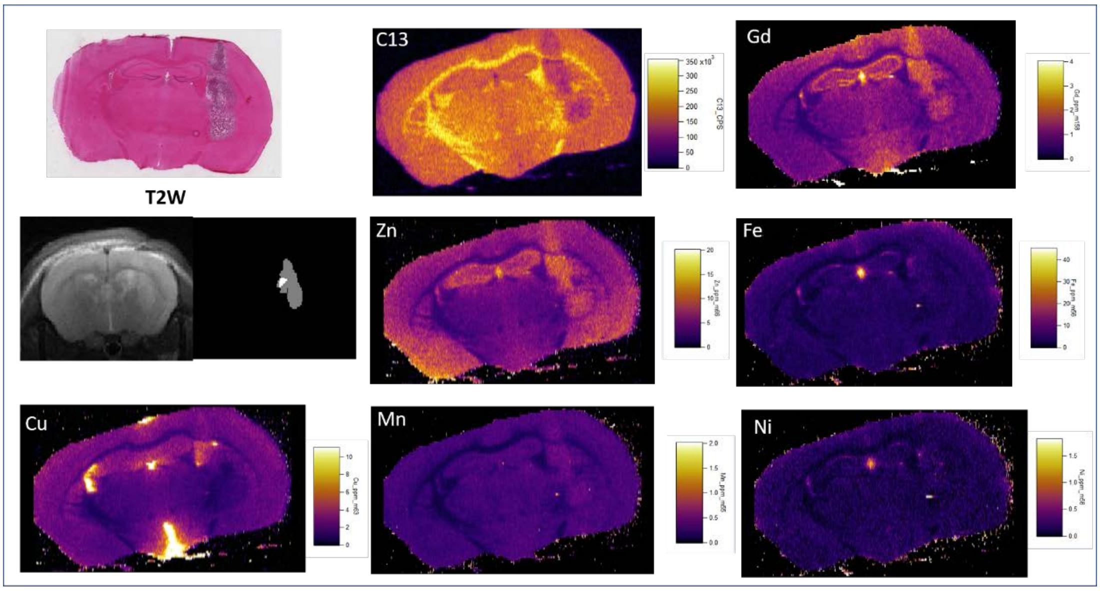

Figure 30 – Distribution of all metal ions analysed in a tumour containing section Wk 11 M2 S5 analysed by LA-ICP-MS. The distribution of each metal can be compared to the tumour volume, highlighted in the H&E image and the T2W MRI image, and extracted tumour voxels. Zinc and gadolinium are observed at higher abundance in the tumour

region whereas the abundance of all other ions appears unaffected. Carbon-13 is at low abundance in the tumour region. .

The T2W MRI and extracted abnormal volume shown in Figure 30 appears to match closely to the tumour volume observed in the H&E section. Carbon-13 appears at low abundance throughout the tumour region versus the rest of the brain, with high abundance in white matter as matching to the control section. Carbon appears to inversely map to the tumour region and at lower abundance versus the rest of the brain section. Gadolinium distribution correlates closely to the tumour region, also at high abundance in GM structures, but not present in the WM. Zinc also maps closely to the tumour volume, and GM structures shown in the control section. Manganese, observed at low abundance in the control section shows increased abundance in the tumour volume and surrounding grey matter. Copper matches the distribution observed in the control section, whilst Nickel and Iron both appear in similar locations. A hotspot in the central ventricle contains gadolinium, zinc, iron, copper and nickel suggesting abundance also in cerebral spinal fluid (CSF).

Of the chemical maps, zinc and gadolinium locate to the entirety of tumour region. A recent literature review of trace metal concentration changes in brain tumours showed gadolinium and zinc, as well as manganese to be high in high malignant tumour, which corroborate the results shown in our LA-ICP-MS images [48].

Gadolinium exists as Gd (III) ions in MRI contrast agents, chelated to a ligand to minimise the toxic properties and to prevent the accumulation in tissue. Free Gd is known to accumulate in a number of tissues including the liver, spleen, bones and the kidneys in mice and has been shown to be retained in clinical biopsies of gliomas and glioblastomas using ICP-MS analysis [49]. Zinc is highly abundant in mammalian cells and in blood and urine analysis has been shown to transmetallate with the chelating species associated with Gadolinium contrast agents, in particular pentetic acid or diethylenetriaminepentacetate (DPTA) [50, 51].

Zinc and gadolinium distributions in multiple tumour section map closely to the entire tumour volume, Figure 31.

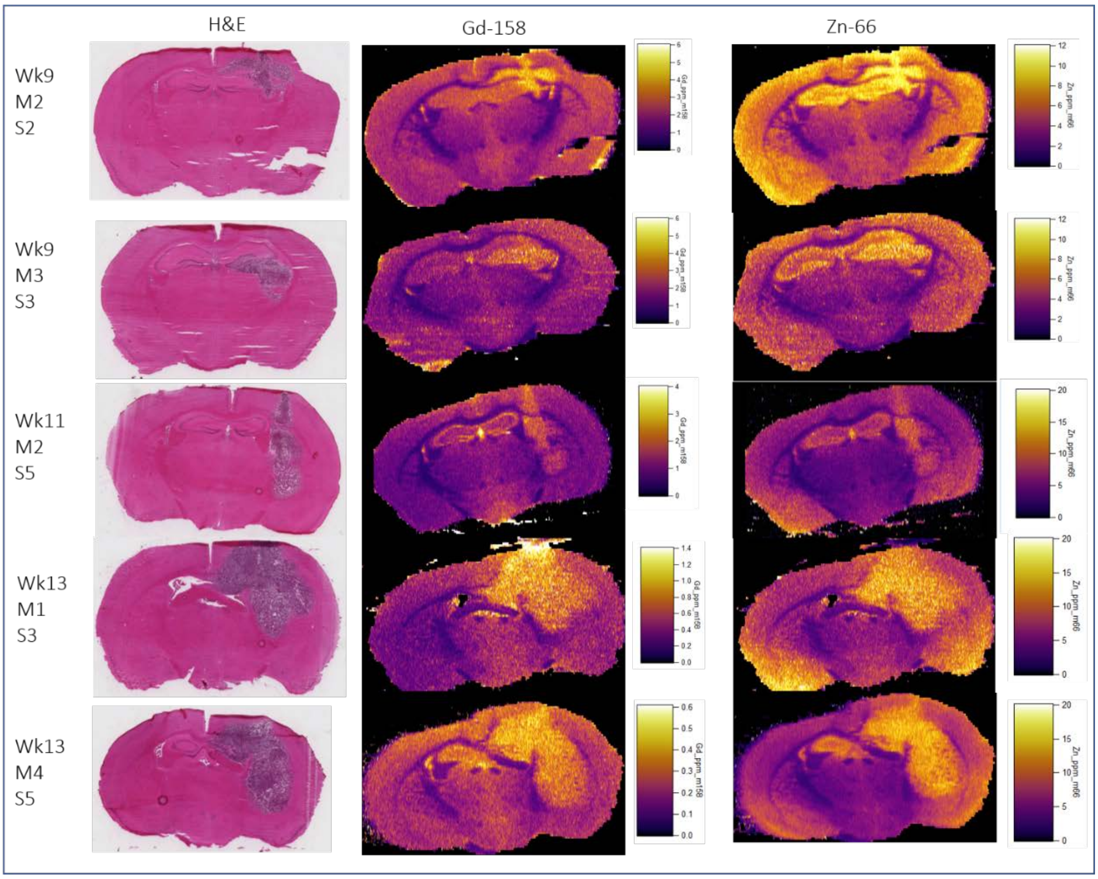

Figure 31 – Determining the relationship between gadolinium and zinc by mapping their distribution from LA-ICP-MS imaging experiments, across all timepoints. Across all tumours Gd and Zn are observed at high abundance in the tumour mass and match closely together, although Gd is at much lower concentrations than endogenous zinc

In the tumour containing brain sections, gadolinium distribution matches very closely with the tumour volumes. In the Wk9 sections, gadolinium has a maximum concentration of 6 ppm and a tumour concentration between 4 - 6 ppm as represented by the yellow region on the scale. The tumours are small in these sections and as such there is a smaller volume for the gadolinium to occupy. As tumour size increases in Wk11 and Wk13 tumours, the observed gadolinium ppm decreases to 4 and 0.6 & 1.4 ppm respectively. This result is likely due to the size of tumours and where these are largest in Wk13 M1 and M4 sections, the gadolinium has to distribution throughout a larger region, hence decreasing the observed highest abundance.

Zinc and gadolinium distributions map closely to the entire tumour volume and as such are excellent markers of the tumour region. However, a conflicting biological role and abundance of zinc is observed for GBM tumours and in this instance, the high abundance of zinc in the tumours may be associated with a chelating exchange effect with the gadolinium MRI contrast agent [50, 52].

Zinc is an essential element with a plethora of cell functions and has shown to be critical for cell proliferation in C6 gliomas, with a large uptake in tumours after 1 hour versus 6 days as shown using autoradiography [53]. Zinc's role in cancer and disease is complicated with ambiguous results at the serum and tissue level for a number of cancer types [54, 55]. Clinical GBM metallothionein's are associated with poor prognosis, which can bind zinc [56], and recently zinc has been proposed as an epigenetic modulator of GBM [57]. As such accurately determining the distribution of zinc is important.

To further investigate the distribution of zinc alongside gadolinium, LA-ICP-MS imaging was carried out at a higher spatial resolution of 20 µm on an Agilent TQ instrument. The elemental mapping of gadolinium and zinc are shown in Figure 32. Due to the long experiments time of images at 20 µm pixel size, smaller regions for analysis were selected from the H&E tissue to represent distinct regions of the tumour, including some surrounding non-tumour regions. High resolution area 1 was acquired at the top of the tumour, including part of the hippocampus and highlights white matter tract associated with the corpus callosum that passes through the tumour volume. High resolution area 2 is at the bottom of the tumour where cellular density appears reduced compared to the top region.

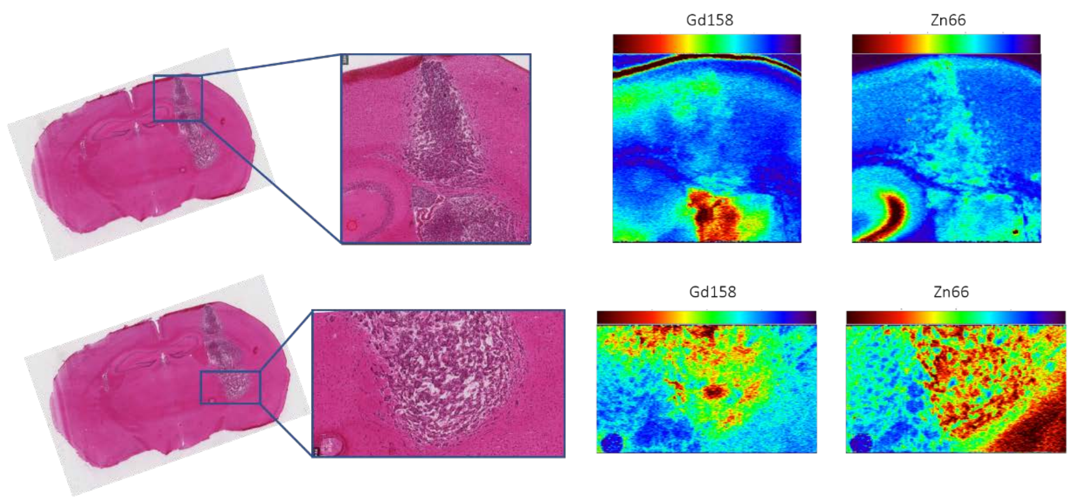

Figure 32 – Determining the distribution of zinc and gadolinium through high resolution LA-ICP-MS imaging at 20 µm resolution. Two regions were selected for high resolution MS imaging as shown on the H&E images, alongside the mapped distributions for both Gadolinium-158 and Zinc-66. An adjacent section was analysed to those at 100 µm. At 20 µm spatial resolution zinc and gadolinium appear to have specific but differing distribution within the tumour.

Within these regions we can clearly see a difference in the distributions of gadolinium and zinc in both regions of the high-resolution LA-ICP-MS data. More apparent in the bottom high-resolution image, the gadolinium still matches that of the tumour area but has a clear hotspot in the central region, whereas zinc is observed more uniformly through the tissue.

This would suggest the zinc is not binding to the gadolinium chelate in the MRI contrast agent Magnevist and that there may be a biological reasoning for its distribution in the tumour volumes. Zinc is the most abundant essential element in the cell, providing key biological functions for hundreds of enzymes, but is also linked to proteins and enzymes upregulated in GBM. These results provide evidence that zinc is highly abundant in the tumour volume and a potential biological reasoning in GBM.

The 20 µm and 100 µm spatial resolution images acquired on separate sections of Wk11 M2 section 5 are shown in Figure 33. As LA-ICP-MS is a destructive technique an adjacent spare section was analysed at 20 µm spatial resolution. As such these sections are 60 µm apart. However, we would still expect a comparable distribution between the images.

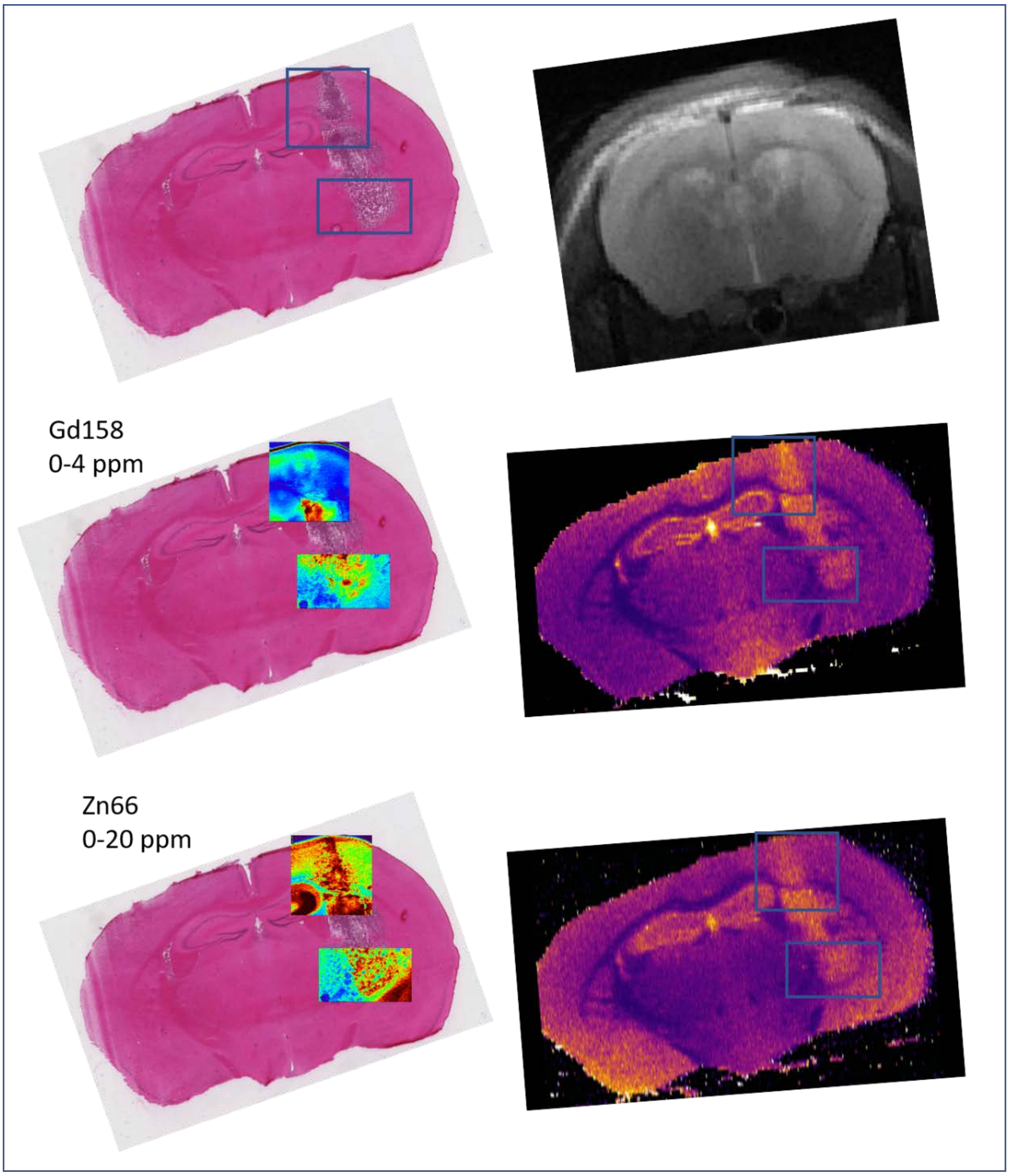

Figure 33 – Comparison between LA-ICP-MS images acquired at 20 µm and 100 µm pixel size images from Wk11 M2 S5. The small regions analysed at 20 µm pixel size are overlayed with the H&E images from adjacent sections and the corresponding regions are highlighted on the 100 µm images. Top left and right are the blank H&E and corresponding T2W MRI slice.

The distribution of gadolinium and zinc in the 20 µm and 100 µm spatial resolution LA-ICP-MS elemental maps show that in both cases these species are highly abundant in the tumour volume. The 100 µm spatial resolution analysis reveals a comparative distribution of gadolinium and zinc in the section, defining the tumour volume. At 20 µm we can clearly see a difference in the zinc and gadolinium distributions in both the top and bottom regions of the tumour.

This observation further corroborates the high-resolution data that shows different distributions of these two species.

5. Conclusions

This study used a combination of DESI-MSI and LA-ICP-MS methods to analyse the lipidomic, and metallomic profiles of a clinically relevant G7 glioblastoma orthotopic tumour model. This analysis has provided a rich insight into the metabolic processes within this model, as well as determining multiple molecular species to define the tumour volume in comparison to surrounding brain tissue. The results found following this study, will provide an additional perspective and data set, to that current available in this field, as no information on the metabolomics, lipidomics, and metallomics of this model has been previously provided using mass spectrometry analysis. The orthotopic model selected, allowed for healthy and tumorous tissue to be simultaneously analysed. This shows the benefit of using such a pre-clinical model, as this is not attainable for human biopsies where healthy tissue cannot be removed, and hence analysed.

5.1. DESI results highlight several upregulated lipid species

DESI-MS imaging experiments have highlighted several lipid species that are upregulated and overexpressed in the G7 tumour region of the sections. From these species detected and identified; PI's, FA's and carnitine species were of particular interest, with respect to the signalling and metabolic activities observed within glioblastoma tumours. As well as these lipid classes, multiple other lipids moieties, and some smaller molecular weight species provide additional information into the biology of these tumours. Many lipid species identified, were not observed in the tumour but were at much higher abundance in the surrounding healthy brain. This further highlights the use of MSI in the detection and differentiation of disease states in these biological tumour models, and further paves the way for the use of DESI-MS imaging as a classification platform.

The detection of multiple PIs in the tumour region suggests an overexpression of the PI3-K signalling pathway and the requirement for these molecules within the GBM tumour. PIs act as signalling lipids *via* the PI3-K pathway, a key pathway altered in cancer and GBM, which provide proliferation mechanisms and cell survival features of tumour cells. Downstream PI3-K signalling, *via* AKT, also regulates lipid metabolism *via* fatty acid synthesis which corroborates our results revealing high abundance of FA species in the tumours. Signalling of PI3-K *via* downstream AKT may also explain the increased FA species observed in the G7 tumour, which is known to stimulate energy production *via* fatty acid oxidation. The high abundance and specificity of PI [18:0/22:6] to the tumour, compared to the surrounding tissue could indicate the use of this as a marker of the G7 GBM tissue.

The detection of carnitines and fatty acids in our samples reflect clinical data that the GBM tumours are utilising FA metabolism for energy consumption. Palmitoyl carnitine and stearoyl carnitine are shown to locate at the periphery of the tumour region, whereas free carnitine or L-carnitine, as well as the FA species, are abundant throughout the entire tumour mass. These results suggest the tumour mass is highly metabolic, using FA for β-oxidation, and hence carnitine and fatty acids are unconjugated in the mitochondrial membrane. Whereas, the tumour periphery may be the site of FA recruitment, and hence incorporation into acyl-carnitines. Further investigation into the FA and carnitine distribution, using techniques such as IHC staining will help to reveal further biochemical and metabolism information in this clinically relevant model of glioblastoma, as well as providing potential insight into the chemical properties at the tumour boundary.

5.2. LA-ICP-MS reveals the location of gadolinium and endogenous metallo-species

Data from the LA-ICP-MS imaging experiment revealed that the distribution of gadolinium and zinc closely map the tumour regions and appear to have comparative distributions at 100 µm spatial resolution. High resolution imaging at 20 µm spatial resolution determined a different distribution of these two molecules, suggesting a potential biological feature of zinc within GBM. Further experiments investigating the proteomic profiles of G7 tumour would be required to confirm this potential role of zinc. MALDI-MS analysis was attempted to image the distribution of the chelating agent, pentetic acid, to determine if zinc or gadolinium is bound to the molecule. However, this did not pass the feasibility stage of experimental work. A standard of Magnevist was spotted onto control tissue samples but was not detected on tissue at 10 µg/mL (10 ppm), and such would be an insufficient concentration for detection within the of the brain sections (Data not shown).

Further work linking the metallomic and lipidomic profiles to proteomic and IHC data will be of key interest to fully understand the metabolic activity of this G7 GBM model, as well as determining the zinc and gadolinium metal ion distributions and link to biological pathways.

6. Acknowledgements

Thanks to MRC and Waters who funded this research. Special thanks to Malcolm Clench at Sheffield Hallam University and Anthony Chalmers at The University of Glasgow who collaborated on this project.

7. Author contributions

Matthew Gentry carried out all the DESI-MSI negative and positive ion mode analysis. Additionally, Matthew Gentry carried out all analysis, MS/MS analysis, lipid identification and data analysis. Emrys Jones helped set up the DESI-MS imaging runs using the robotic slide loader at Waters, Wilmslow.

Matthew Gentry collect and analysed the LA-ICP-MS data at Sheffield Hallam University under the supervision of Joe Ready, who both helped to design the study with Catherine Duckett. Romain Tartese collected the LA-ICP-MS data at The University of Manchester and provided data analysis help as Matthew Gentry was not able to enter the building due to COVID-19 safety features.

Malcolm Clench and Catherine Duckett facilitated the collaboration with Sheffield Hallam University.

Antoine Vallatos collected and provided all the MRI data including data analysis and interpretation. Joanna Birch, Anthony Chalmers, Antoine Vallatos and Adam McMahon assisted with the study design, further Joanna Birch handled the mice husbandry and co-ordinated the MRI scans with Antoine Vallatos, as well as providing the H&E staining.

Adam McMahon, Nicholas Lockyer and Emrys Jones were Matthew Gentry's supervisory team, providing support and guidance throughout this project.

8. Ethical considerations

All animal experiments were performed under the relevant UK Home Office Project Licence and carried out with ethical approval from the University of Glasgow under the Animal (Scientific Procedures) Act 1986 and the EU directive 2010.

9. Supplementary figures

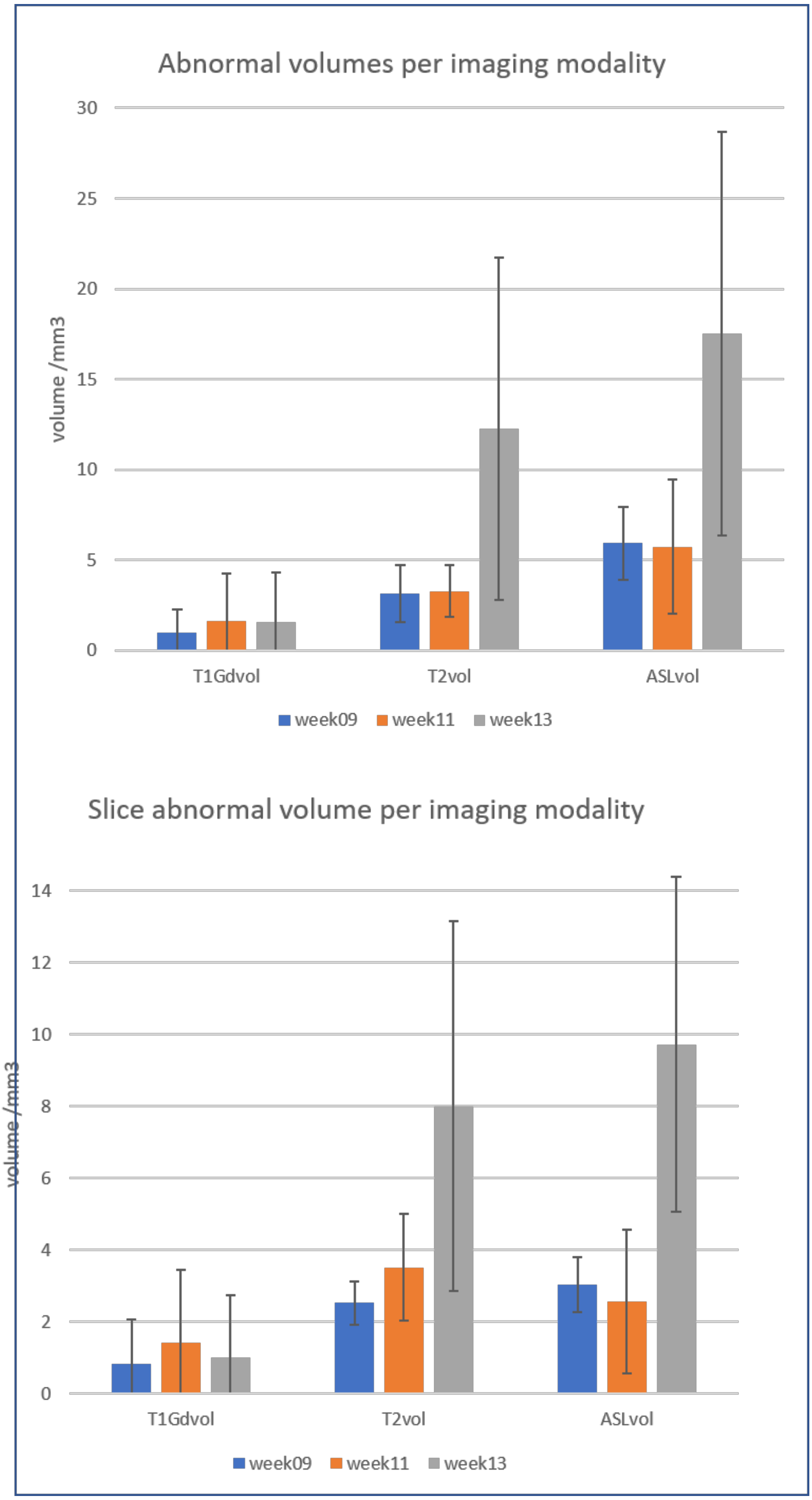

Figure 34 – average MRI tumour volume for all brains separated out into each timepoint

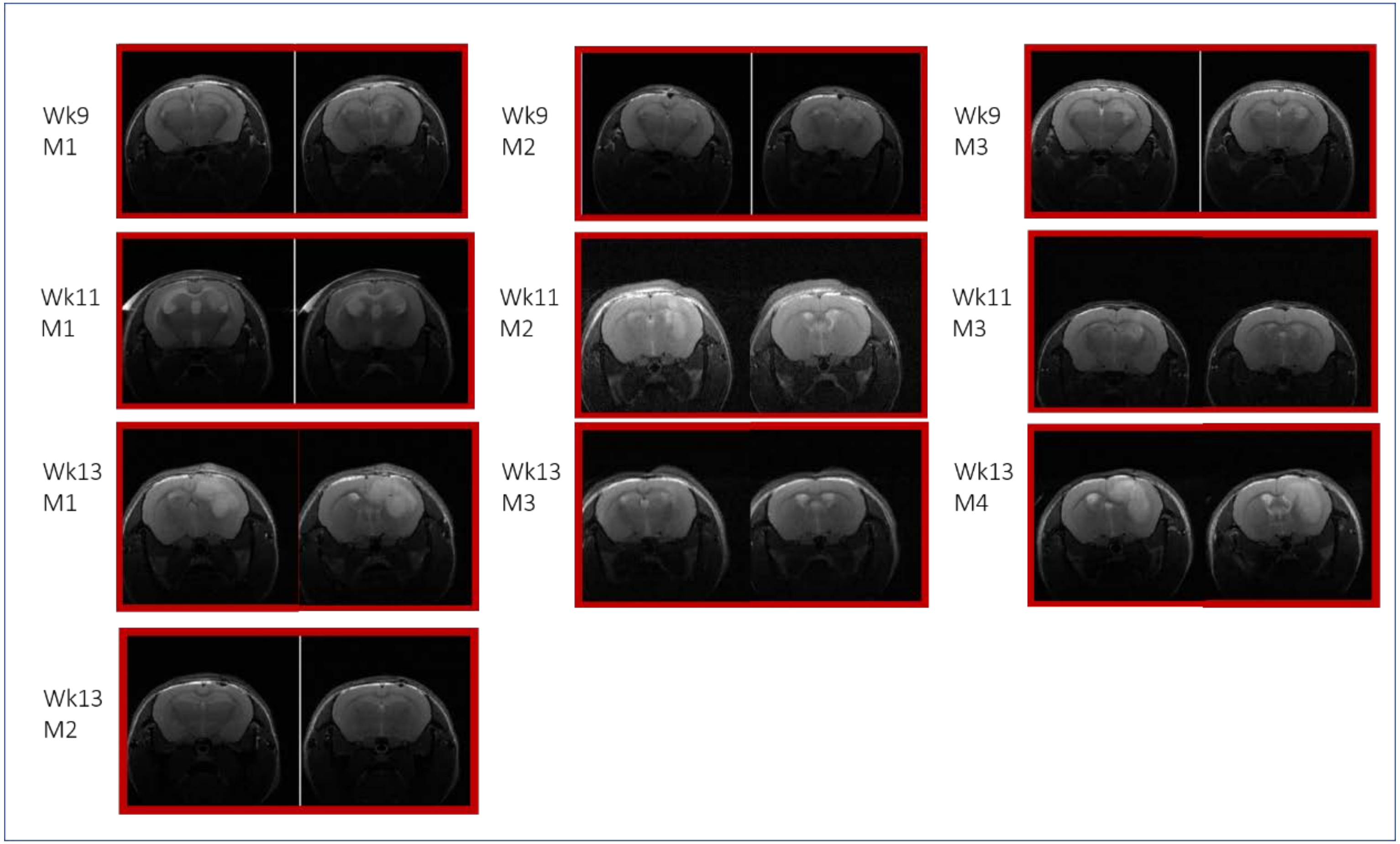

Figure 35 – regions selected for sectioning from the T2W MRI areas. The areas selected cover >50% of the total tumour volume over a 1mm distance. Sectioning was undertaken following MRI guided histology

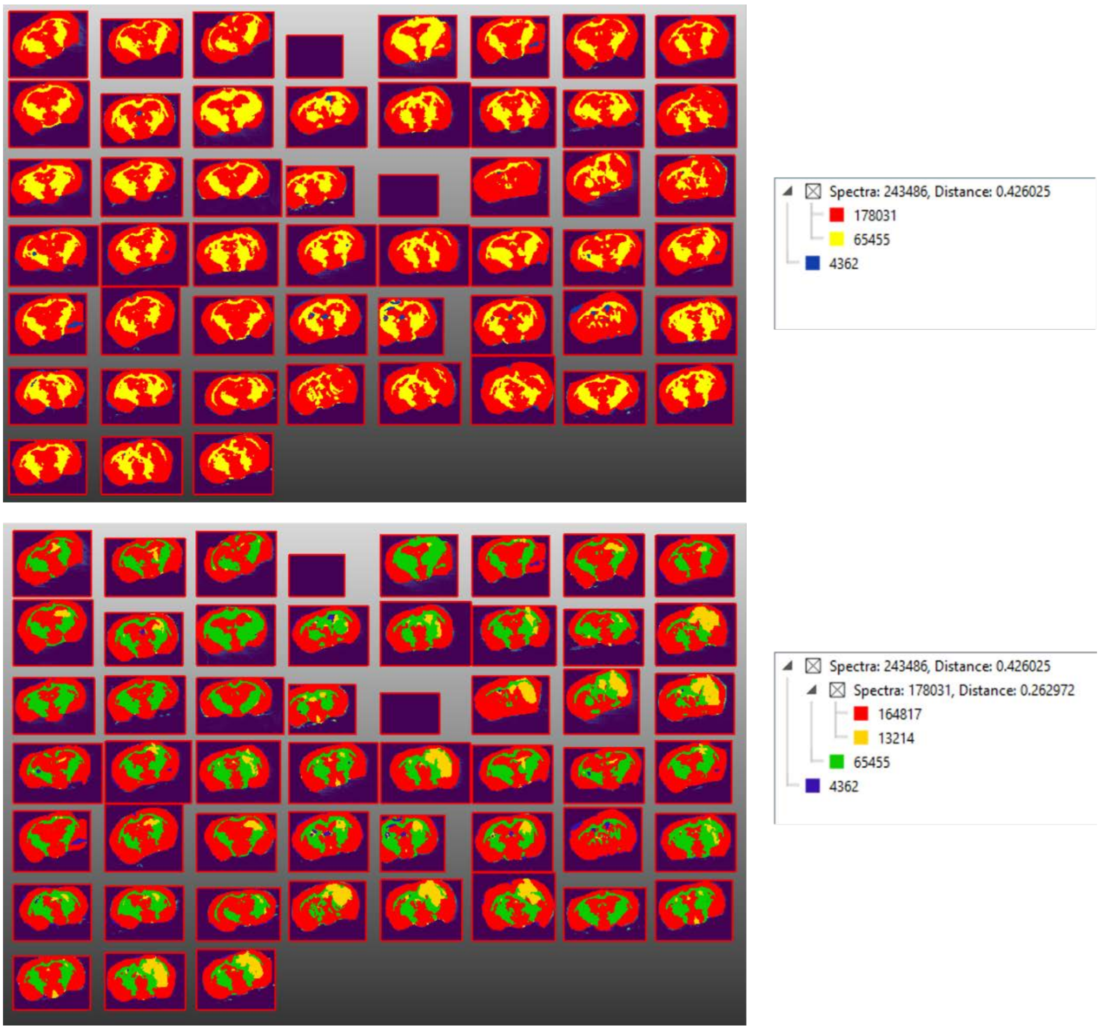

◢ ☒ Spectra: 243486, Distance: 0.426025
🟥 178031
🟨 65455
🟦 4362

◢ ☒ Spectra: 243486, Distance: 0.426025
◢ ☒ Spectra: 178031, Distance: 0.262972
🟥 164817
🟨 13214
🟩 65455
🟦 4362

Figure 36 – Top: bisecting k-means segmentation of all brain sections in DESI-MSI negative ion mode to show white matter (yellow map) and grey matter (red map) of all images loaded into SCiLS lab. Bottom: bisecting k-means segmentation with the grey matter further segmented to show grey matter (red), white matter (green) and tumour regions (yellow).

Figure 37 – overview of DESI-MSI negative ion mode MS images loaded in SCiLS lab for data analysis alongside the sample ID

Table 3 – list of m/z values with discriminative values less than 0.2 and greater than 0.8 from the analysis between tumour spectra and healthy brain (white and grey matter) when analysed by ROC, alongside possible lipid ID and where confirmed by MS/MS full lipid characterisation is input

m/z	Discriminative mz values Tumour v GM & WM	Possible lipid from accurate mass METLIN	Confirmed by MS/MS
790.5307	0.080358387	PC (34:3)	PC(16:0/18:3)
834.5241	0.082466435	PS (40:6)	PS(18:0/22:6)
791.5317	0.085659085	Isotopologue PC 34:3	-
419.2472	0.102873455	Unconfirmed	-
174.0431	0.108295719	N-Acetyl Aspartate	-
786.5265	0.113644498	PS (36:2)	-
806.5474	0.115224942	PE (38:1)	-
792.5591	0.12787302	PE (40:5)	PE(18:0/22:5)
787.5275	0.150047689	Isotopologue of PS (36:2)	-
835.5251	0.151019369	Isotopologue of PS (40:6)	-
807.5485	0.158064287	Isotopologue of PE (38:1)	-
766.5318	0.16252516	PE (38:4)	PE(18:0/20:4)

822.5379	0.163841561	C19-OH Sulfatide	-
838.5546	0.169454807	PS(40:4)	PS(18:0/22:4)
767.5329	0.170772165	Isotopologue PE (38:4)	-
808.5495	0.171451517	Unconfirmed	-
839.5557	0.193982904	Isotopologue PS(18:0/22:4)	-
836.5262	0.194832652	PS (40:5)	Unconfirmed
906.6259	0.205423415	C24-OH Sulfatide	C24-OH Sulfatide
884.5238	0.211821268	Unconfirmed	-
907.627	0.212393054	Unconfirmed	-
904.6238	0.214310269	C24:1-OH sulfatide	C24:1-OH sulfatide
878.5966	0.215678034	PI (36:2) or sulfatide C22-OH	Unconfirmed
297.251	0.817422277	Unconfirmed	-
241.2187	0.823737939	Unconfirmed	-
136.8726	0.826826906	Unconfirmed	-
746.5109	0.827946365	PE(P-16:0/22:6)	PE(P-16:0/22:6)
313.1887	0.829739487	C20:1	-
910.5511	0.839121252	Isotopologue PI(40:6)	-
909.55	0.842259878	PI(40:6)	PI(18:0/22:6)
124.017	0.856086013	Unconfirmed	-
331.2603	0.856148836	C22:4	-
227.204	0.85778408	Unconfirmed	-
552.2812	0.864889881	Lyso-PC (18:3)	Lyso-PC (18:3)
132.8684	0.873660935	Unconfirmed	-

819.5347	0.875267204	Unconfirmed	-
865.5039	0.87604861	PI (36:0)	PI (18:0/18:0)
134.8705	0.880098549	Unconfirmed	-
724.5142	0.880512096	PE (O-16:0/20:4)	Unconfirmed
528.2824	0.900885684	PE (22:4)	Lyso-PE (22:4)
282.2616	0.916915623	Isotopologue of Oleic acid	-
723.5131	0.917535383	Isotopologue 722.5121	-
887.5533	0.917776535	PI (38:3)	PI(18:0/20:3)
281.2606	0.922465238	Oleic acid C18:1)	-
329.2319	0.933891762	Docosapentaenoic acid C22:5	-
911.5521	0.938099874	PI (40:5)	PI(18:0/22:5)
722.5121	0.941104131	PE (P-36:4)	PE(P-16:0/20:4)
859.524	0.943252054	PI (36:3)	PI(16:0/20:3)
436.2913	0.95251267	PE (P-16:0/0:0)	PE(P-16:0/0:0)
305.233	0.958460811	Eicosatrienoic acid C20:3	-
279.2321	0.961807281	Linoleic acid C18:2	-
256.2344	0.963463351	Isotopologue Palmitic acid	-
253.2049	0.967406564	Palmitoleic acid C16:1	-
255.2333	0.969396275	Palmitic acid C16:0	-
913.5806	0.974869075	PI(40:4) (18:0/22:4)	PI(18:0/22:4)

Table 4 – Fatty acids observed in negative ion mode DESI-MS imaging data. The observed mass is assigned to the respective fatty acid with the ppm error from the imaging datasets shown. The number of carbon atoms (C) and number of unsaturated carbon carbon double bonds (D) is shown.

Observed *m/z*	Fatty Acid assignment	C:D	Theoretical mass [M-H-]	ppm error

253.2150	Palmitoleic acid	16:1	253.2168	7.11
255.2297	Palmitic acid	16:0	255.233	12.93
279.2316	Linoleic acid	18:2	279.2324	2.86
281.2475	Oleic acid	18:1	281.2481	2.13
283.2638	Stearic acid	18:0	283.2643	1.77
303.2303	Arachidonic acid	20:4	303.233	8.90
305.2486	Eicosatrienoic acid	20:3	305.2481	1.64
329.2430	Clupanodonic acid	22:5	329.2486	17.01
331.2639	Adrenic acid	22:4	331.2643	1.21

Table 5 – MS/MS fragment details and their assignments and theoretical masses for selected lipids acquired in DESI-MSI negative ion mode

Parent ion *m/z*	Fragment ion *m/z*	Fragment theoretical mass	Fragment assignment	Putative lipid assignment
913.5806	152.9983	152.9958	Glycerol-3-phosphate ion with loss of H2O	PI(18:0/22:4)
	222.9964	223.0013	Inositol phosphate ion - 2 H2O	
	241.0111	241.0119	Inositol phosphate ion - H2O	
	283.2708	283.2643	FA 18:0 sn1 RCOO- ion	
	331.6243	331.2643	FA 22:4 sn2 RCOO- ion	
	419.2703	419.2568	Neutral loss of FA 22:4 sn2 RCOOH group and inositol from [M-H]-	
	581.3005	581.3096	Neutral loss of FA 22:4 sn2 RCOOH group from [M-H]-	
436.285	140.0144	140.0118	Ethanolamine phosphate ion	PE(P-16:0/0:0)
	152.9983	152.9958	Glycerol-3-phosphate ion with loss of H2O	
	196.0427	196.038	Neutral loss of plasmenyl group RCH=CHOH) from [M-H]-	
722.5121	140.0144	140.0118	Ethanolamine phosphate ion	PE(P-16:0/20:4)
	153.0008	152.9958	Glycerol-3-phosphate ion with loss of H2O	
	259.2503	259.2431	Loss of CO2 from FA 20:4 sn2 RCOO- ion (PUFA)	
	303.2446	303.233	FA 20:4sn2 RCOO- ion	
	418.277	418.2728	Neutral loss of FA 20:4 sn2 RCOOH group from [M-H]-	
	436.2934	436.2834	Loss of FA 20:4 sn2 acyl chain as ketene (RCH=C=O) from [M-H]-	
859.52	153.0008	152.9958	Glycerol-3-phosphate ion with loss of H2O	PI(16:0/20:3)
	241.0174	241.0119	Inositol phosphate ion - H2O	
	255.2363	255.233	FA 16:0 sn1 RCOO- ion	
	305.2594	305.2486	FA 20:3 sn2 RCOO- ion	
	391.2353	391.2255	Neutral loss of sn2 RCOOH group and inositol from [M-H]-	
	553.2982	553.2783	Neutral loss of sn2 RCOOH group from [M-H]-	

911.5521	153.0008	152.9958	Glycerol-3-phosphate ion with loss of H2O	PI(18:0/22:5)
	241.0238	241.0119	Inositol phosphate ion - H2O	
	283.2708	283.2643	FA 18:0 sn1 RCOO- ion	
	329.2505	329.2486	FA 22:5 sn2 RCOO- ion	
	419.2661	419.2568	Neutral loss of sn2 RCOOH group and inositol from [M-H]-	
	437.2735	437.2674	Loss of sn2 acyl chain as ketene (RCH=C=O) and inositol from [M-H]-	
887.5533	152.9983	152.9958	Glycerol-3-phosphate ion with loss of H2O	PI(18:0/20:3)
	223.0056	223.0013	Inositol phosphate ion - 2 H2O	
	241.0143	241.0119	Inositol phosphate ion - H2O	
	283.2708	283.2643	FA 18:0 sn1 RCOO- ion	
	305.2558	305	FA 20:3 sn2 RCOO- ion	
	315.0552	315.0487	Glycerophosphoinositol -H2O	
	419.2619	419.2568	Neutral loss of FA 20:3 sn2 RCOOH group and inositol from [M-H]-	
	581.34	581.3096	Neutral loss of FA 20:3 sn2 RCOOH group from [M-H]-	
528.2824	140.0144	140.0118	Ethanolamine phosphate ion	Lyso-PE (22:4)
	153.0008	152.9958	Glycerol-3-phosphate ion with loss of H2O	
	196.0306	196.038	Neutral loss of FA 22:4 sn1 RCOOH group from [M-H]-	
	214.0686	214.0486	Loss of FA 22:4 sn1 acyl chain as ketene (RCH=C=O) from [M-H]-	
	331.2752	331.2643	FA 22:4 sn1 RCOO- ion	
865.5039	152.9958	152.9958	Glycerol-3-phosphate ion with loss of H2O	PI(18:0/18:0)
	241.0174	241.0119	Inositol phosphate ion - H2O	
	283.2742	283.2643	FA 18:0 sn1 RCOO- ion	
	419.2577	419.2568	Neutral loss of FA 18:0 sn1 RCOOH group and inositol from [M-H]-	
909.55	152.9958	152.9958	Glycerol-3-phosphate ion with loss of H2O	PI (18:0/22:6)
	223.0056	223.0013	Inositol phosphate ion - 2 H2O	
	241.0206	241.0119	Inositol phosphate ion - H2O	

	283.2742	283.2643	FA 18:0 sn1 RCOO- ion	
	327.2395	327.233	FA 22:6 sn2 RCOO- ion	
	419.2619	419.2568	Neutral loss of FA 22:6 sn2 RCOOH group and inositol from [M-H]	
	581.3202	581.3096	Neutral loss of sn2 RCOOH group from [M-H]-	
746.5109	140.0168	140.0118	Ethanolamine phosphate ion	PE(P-16:0/22:6)
	152.9983	152.9958	Glycerol-3-phosphate ion with loss of H2O	
	283.2708	283.2643	FA 18:0 sn1 RCOO- ion	
	327.2432	327.233	FA 22:6 sn2 RCOO- ion	
	418.2854	418.2728	Neutral loss of FA 22:6 sn2 RCOOH group from [M-H]-	
	436.2977	436.2834	Loss of FA 22:6 sn2 acyl chain as ketene (RCH=C=O) from [M-H]-	
744.5615	140.0144	140.0118	Ethanolamine phosphate ion	PE(18:1/18:0)
	153.0008	152.9958	Glycerol-3-phosphate ion with loss of H2O	
	281.2544	281.2486	FA 18:1 sn1 RCOO- ion	
	283.2708	283.2643	FA 18:0 sn2 RCOO- ion	
	460.3054	460.2834	Neutral loss of sn2 RCOOH group from [M-H]-	
	462.3156	462.299	Neutral loss of sn1 RCOOH group from [M-H]-	
	480.3218	480.3096	Loss of sn1 acyl chain as ketene (RCH=C=O) from [M-H]-	
716.5321	140.0119	140.0118	Ethanolamine phosphate ion	PE (16:0/18:1)
		152.9958	Glycerol-3-phosphate ion with loss of H2O	
	255.233	255.233	FA 16:0 sn2 RCOO- ion	
	281.2486	281.2486	FA 18:1 sn1 RCOO- ion	
	452.2909	452.2783	Loss of sn2 acyl chain as ketene (RCH=C=O) from [M-H]-	
834.5241	152.993	152.9958	Glycerol-3-phosphate ion with loss of H2O	PS (18:0/22:6)
	283.2742	283.2643	FA18:0 sn1 RCOO- ion	
	327.2432	327.233	FA 22:6 sn2 RCOO- ion	
	419.2703	419.2568	Neutral loss of sn2 RCOOH group and serine from [M-H]-	

	437.2821	437.2674	Loss of sn2 acyl chain as ketene (RCH=C=O) and serine from [M-H]-	
		747.497	Loss of serine from precursor ion	
766.318	140.0144	140.0118	Ethanolamine phosphate ion	PE (20:4/18:0)
		152.9958	Glycerol-3-phosphate ion with loss of H2O	
	283.2742	283.2643	FA 18:0 sn2 RCOO- ion	
	303.2446	303.233	FA 20:4 sn1 RCOO- ion	
	480.3173	480.3096	Loss of sn2 acyl chain as ketene (RCH=C=O) from [M-H]-	
838.5546	153.0008	152.9958	Glycerol-3-phosphate ion with loss of H2O	PS(18:0/22:4)
	283.2673	283.2643	FA 18:0 sn1 RCOO- ion	
	331.2678	331.2643	FA 22:4 sn2 RCOO- ion	
	419.2703	419.2568	Neutral loss of sn2 RCOOH group and serine from [M-H]-	
	751.5407	751.5283	Loss of serine from precursor ion	
480.3111	140.119	140.0118	Ethanolamine phosphate ion	Lyso-PE 18:0
	196.0427	196.038	Neutral loss of sn1 RCOOH group from [M-H]-	
	283.2673	283.2643	FA 18:0 sn1 RCOO- ion	
810.529	152.983	152.9958	Glycerol-3-phosphate ion with loss of H2O	PS(18:0/20:4)
	283.2708	283.2643	FA 18:0 sn1 RCOO- ion	
	303.2411	303.233	FA 20:4 sn2 RCOO- ion	
	419.2661	419.2568	Neutral loss of sn2 RCOOH group and serine from [M-H]-	
	437.2778	437.2674	Loss of sn2 acyl chain as ketene (RCH=C=O) and serine from [M-H]-	
	723.5209	723.497	Loss of serine from precursor ion	

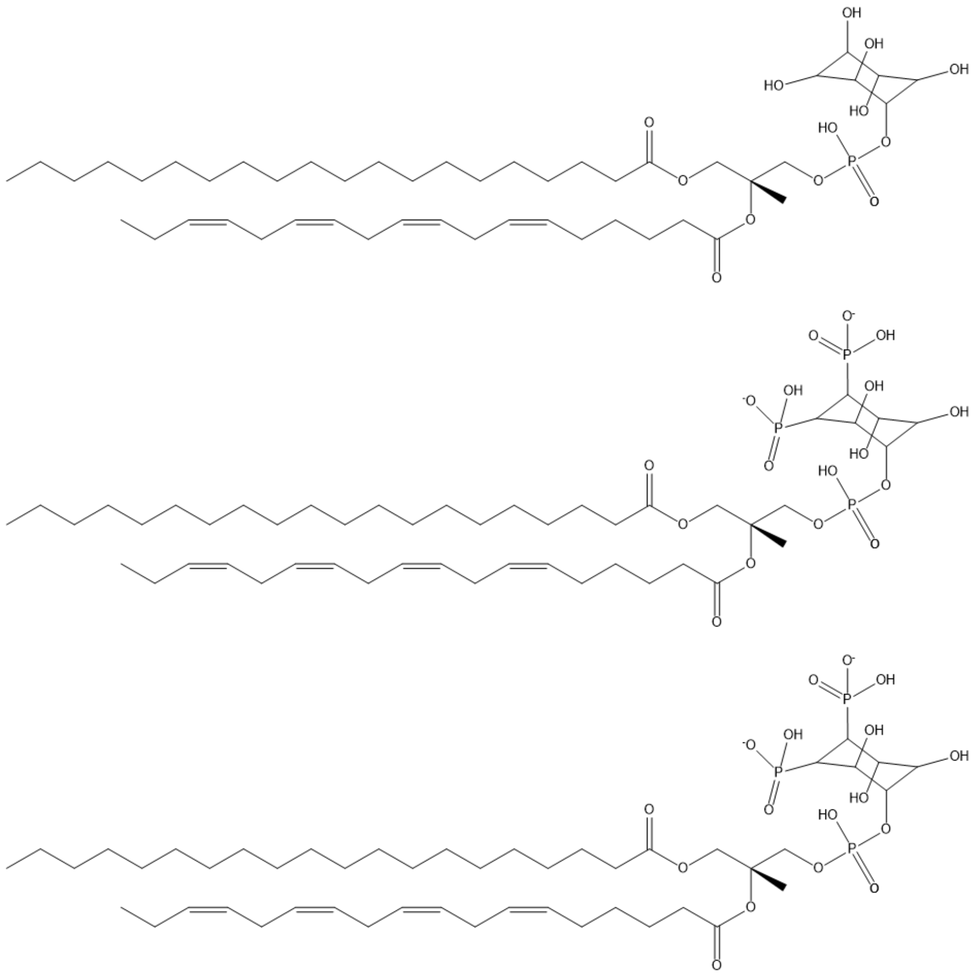

Figure 38 – Structures of the lipid species involved in the PI3-K signalling pathway Top: PI (18:0/20:4), middle: phosphatidylinositol (4,5)-bisphosphate (PIP2), bottom: phosphatidylinositol (3,4,5)-trisphosphate (PIP3)

10. References

1. Louis, D.N., et al., *The 2016 World Health Organization Classification of Tumors of the Central Nervous System: a summary.* Acta Neuropathologica, 2016. **131**(6): p. 803-820.
2. Stupp, R., et al., *Radiotherapy plus concomitant and adjuvant temozolomide for glioblastoma.* New England Journal of Medicine, 2005. **352**(10): p. 987-996.
3. Brodbelt, A., et al., *Glioblastoma in England: 2007-2011.* European Journal of Cancer, 2015. **51**(4): p. 533-542.
4. Weller, M., et al., *EANO guideline for the diagnosis and treatment of anaplastic gliomas and glioblastoma.* Lancet Oncology, 2014. **15**(9): p. E395-E403.

5. Kuhnt, D., et al., *Correlation of the extent of tumor volume resection and patient survival in surgery of glioblastoma multiforme with high-field intraoperative MRI guidance.* Neuro-Oncology, 2011. **13**(12): p. 1339-1348.
6. Orringer, D., et al., *Extent of resection in patients with glioblastoma: limiting factors, perception of resectability, and effect on survival Clinical article.* Journal of Neurosurgery, 2012. **117**(5): p. 851-859.
7. Gutman, D.A., et al., *MR Imaging Predictors of Molecular Profile and Survival: Multi-institutional Study of the TCGA Glioblastoma Data Set.* Radiology, 2013. **267**(2): p. 560-569.
8. Zhou, Z. and Z.R. Lu, *Gadolinium-based contrast agents for magnetic resonance cancer imaging.* Wiley Interdisciplinary Reviews: Nanomedicine and Nanobiotechnology, 2013. **5**(1): p. 1-18.
9. Garzon-Muvdi, T., et al., *Intraoperative imaging techniques for glioma surgery.* Future Oncology, 2017. **13**(19): p. 1731-1745.
10. Morokoff, A., et al., *Molecular subtypes, stem cells and heterogeneity: Implications for personalised therapy in glioma.* Journal of Clinical Neuroscience, 2015. **22**(8): p. 1219-1226.
11. Vartanian, A., et al., *GBM's multifaceted landscape: highlighting regional and microenvironmental heterogeneity.* Neuro-Oncology, 2014. **16**(9): p. 1167-1175.
12. Louis, D.N., et al., *International Society of Neuropathology-Haarlem Consensus Guidelines for Nervous System Tumor Classification and Grading.* Brain Pathology, 2014. **24**(5): p. 429-435.
13. Gomez-Roman, N., et al., *A novel 3D human glioblastoma cell culture system for modeling drug and radiation responses.* Neuro-oncology, 2016: p. now164.
14. Chin, L., et al., *Comprehensive genomic characterization defines human glioblastoma genes and core pathways.* Nature, 2008. **455**(7216): p. 1061-1068.
15. Krycer, J.R., et al., *The Akt–SREBP nexus: cell signaling meets lipid metabolism.* Trends in Endocrinology & Metabolism, 2010. **21**(5): p. 268-276.
16. Gomez-Roman, N., et al., *Radiation responses of 2D and 3D glioblastoma cells: a novel, 3D-specific radioprotective role of VEGF/Akt signaling through functional activation of NHEJ.* Molecular cancer therapeutics, 2020. **19**(2): p. 575-589.
17. Al-Mayhani, T.M.F., et al., *An efficient method for derivation and propagation of glioblastoma cell lines that conserves the molecular profile of their original tumours.* Journal of neuroscience methods, 2009. **176**(2): p. 192-199.
18. Vallatos, A., et al., *Multiple boli arterial spin labeling for high signal-to-noise rodent brain perfusion imaging.* Magnetic resonance in medicine, 2018. **79**(2): p. 1020-1030.
19. Mandrekar, J.N., *Receiver operating characteristic curve in diagnostic test assessment.* Journal of Thoracic Oncology, 2010. **5**(9): p. 1315-1316.
20. Trede, D., et al., *Exploring three-dimensional matrix-assisted laser desorption/ionization imaging mass spectrometry data: three-dimensional*

spatial segmentation of mouse kidney. Analytical chemistry, 2012. **84**(14): p. 6079-6087.

21. Paton, C., et al., *Iolite: Freeware for the visualisation and processing of mass spectrometric data.* Journal of Analytical Atomic Spectrometry, 2011. **26**(12): p. 2508-2518.
22. Jarmusch, A.K., et al., *Differential Lipid Profiles of Normal Human Brain Matter and Gliomas by Positive and Negative Mode Desorption Electrospray Ionization - Mass Spectrometry Imaging.* Plos One, 2016. **11**(9): p. 15.
23. Henderson, F., et al., *3D DESI-MS lipid imaging in a xenograft model of glioblastoma: a proof of principle.* Scientific Reports, 2020. **10**(1): p. 1-7.
24. Blunsom, N.J. and S. Cockcroft, *Phosphatidylinositol synthesis at the endoplasmic reticulum.* Biochimica Et Biophysica Acta (BBA)-Molecular and Cell Biology of Lipids, 2020. **1865**(1): p. 158471.
25. Guillou, H., L.R. Stephens, and P.T. Hawkins, *Quantitative measurement of phosphatidylinositol 3, 4, 5-trisphosphate.* Methods in enzymology, 2007. **434**: p. 117-130.
26. Paine, M.R., et al., *Three-dimensional mass spectrometry imaging identifies lipid markers of medulloblastoma metastasis.* Scientific reports, 2019. **9**(1): p. 1-10.
27. Anderson, K.E., et al., *Lysophosphatidylinositol-acyltransferase-1 (LPIAT1) is required to maintain physiological levels of PtdIns and PtdInsP 2 in the mouse.* PLoS One, 2013. **8**(3): p. e58425.
28. Lee, H.-C., et al., *LPIAT1 regulates arachidonic acid content in phosphatidylinositol and is required for cortical lamination in mice.* Molecular biology of the cell, 2012. **23**(24): p. 4689-4700.
29. Naguib, A., et al., *p53 mutations change phosphatidylinositol acyl chain composition.* Cell reports, 2015. **10**(1): p. 8-19.
30. Rueda-Rincon, N., et al., *p53 attenuates AKT signaling by modulating membrane phospholipid composition.* Oncotarget, 2015. **6**(25): p. 21240.
31. Kant, S., et al., *Enhanced fatty acid oxidation provides glioblastoma cells metabolic plasticity to accommodate to its dynamic nutrient microenvironment.* Cell death & disease, 2020. **11**(4): p. 1-13.
32. Gordon, G.B., *Saturated free fatty acid toxicity: II. Lipid accumulation, ultrastructural alterations, and toxicity in mammalian cells in culture.* Experimental and molecular pathology, 1977. **27**(2): p. 262-276.
33. Pavlova, N.N. and C.B. Thompson, *The emerging hallmarks of cancer metabolism.* Cell metabolism, 2016. **23**(1): p. 27-47.
34. Hanahan, D. and R.A. Weinberg, *Hallmarks of Cancer: The Next Generation.* Cell, 2011. **144**(5): p. 646-674.
35. Lin, H., et al., *Fatty acid oxidation is required for the respiration and proliferation of malignant glioma cells.* Neuro-oncology, 2017. **19**(1): p. 43-54.
36. Qin, X., C. Qiu, and L. Zhao, *Lysophosphatidylcholine perpetuates macrophage polarization toward classically activated phenotype in inflammation.* Cellular immunology, 2014. **289**(1-2): p. 185-190.

37. Tomaszewski, W., et al., *Brain tumor microenvironment and host state: implications for immunotherapy.* Clinical Cancer Research, 2019. **25**(14): p. 4202-4210.
38. Huang, S., et al., *Identification of immune cell infiltration and immune-related genes in the tumor microenvironment of glioblastomas.* Frontiers in Immunology, 2020. **11**.
39. Mills, G.B. and W.H. Moolenaar, *The emerging role of lysophosphatidic acid in cancer.* Nature Reviews Cancer, 2003. **3**(8): p. 582-591.
40. Makide, K., et al., *Emerging lysophospholipid mediators, lysophosphatidylserine, lysophosphatidylthreonine, lysophosphatidylethanolamine and lysophosphatidylglycerol.* Prostaglandins & other lipid mediators, 2009. **89**(3-4): p. 135-139.
41. Taylor, A.J., A. Dexter, and J. Bunch, *Exploring ion suppression in mass spectrometry imaging of a heterogeneous tissue.* Analytical chemistry, 2018. **90**(9): p. 5637-5645.
42. Pirro, V., et al., *Intraoperative assessment of tumor margins during glioma resection by desorption electrospray ionization-mass spectrometry.* Proceedings of the National Academy of Sciences of the United States of America, 2017. **114**(26): p. 6700-6705.
43. Moffett, J.R., et al., *N-acetylaspartate in the CNS: From neurodiagnostics to neurobiology.* Progress in Neurobiology, 2007. **81**(2): p. 89-131.
44. Nałęcz, K.A., et al., *Carnitine: transport and physiological functions in the brain.* Molecular aspects of medicine, 2004. **25**(5-6): p. 551-567.
45. Longo, N., M. Frigeni, and M. Pasquali, *Carnitine transport and fatty acid oxidation.* Biochimica et biophysica acta (BBA)-molecular cell research, 2016. **1863**(10): p. 2422-2435.
46. Randall, E.C., et al., *Localized metabolomic gradients in patient-derived xenograft models of glioblastoma.* Cancer research, 2020. **80**(6): p. 1258-1267.
47. Hare, D.J., et al., *Three-dimensional atlas of iron, copper, and zinc in the mouse cerebrum and brainstem.* Analytical chemistry, 2012. **84**(9): p. 3990-3997.
48. Cilliers, K., C.J. Muller, and B.J. Page, *Trace Element Concentration Changes in Brain Tumors: A Review.* The Anatomical Record, 2020. **303**(5): p. 1293-1299.
49. Kiviniemi, A., et al., *Gadolinium retention in gliomas and adjacent normal brain tissue: association with tumor contrast enhancement and linear/macrocyclic agents.* Neuroradiology, 2019. **61**(5): p. 535-544.
50. Tweedle, M., et al., *Reaction of gadolinium chelates with endogenously available ions.* Magnetic resonance imaging, 1991. **9**(3): p. 409-415.
51. Puttagunta, N.R., W.A. Gibby, and G.T. Smith, *Human in vivo comparative study of zinc and copper transmetallation after administration of magnetic resonance imaging contrast agents.* Investigative radiology, 1996. **31**(12): p. 739-742.
52. Greenberg, S.A., *Zinc transmetallation and gadolinium retention after MR imaging: case report.* Radiology, 2010. **257**(3): p. 670-673.

53. Takeda, A., H. Tamano, and N. Oku, *Alteration of zinc concentrations in the brain implanted with C6 glioma.* Brain research, 2003. **965**(1-2): p. 170-173.
54. Gumulec, J., et al., *Serum and tissue zinc in epithelial malignancies: a meta-analysis.* PLoS One, 2014. **9**(6): p. e99790.
55. Anyz, J., et al., *Spatial mapping of metals in tissue-sections using combination of mass-spectrometry and histology through image registration.* Scientific reports, 2017. **7**(1): p. 1-13.
56. Mehrian-Shai, R., et al., *High metallothionein predicts poor survival in glioblastoma multiforme.* BMC medical genomics, 2015. **8**(1): p. 1-9.
57. Kumar, N., S. Satarker, and M. Nampoothiri, *Zinc as a plausible epigenetic modulator of glioblastoma multiforme.* European Journal of Pharmacology, 2020: p. 173549.

Chapter 3: Mass spectrometry imaging of malignant glioblastoma brain tumour biopsies

Matthew C. Gentry[1], Emrys A. Jones[2], Erjon Agushi[1], Federico Roncaroli[3], David J Coope[1], Adam McMahon[1]

[1]Wolfson Molecular Imaging Centre, Division of Informatics, Imaging and Data Sciences, University of Manchester, United Kingdom

[2]Waters Corporation, Wilmslow, United Kingdom

[3]Division of Neuroscience & Experimental Psychology, University of Manchester, United Kingdom

1. Abstract

Glioblastoma (GBM) are the most common primary brain tumour, grade IV, with an average life expectancy of 12-15 months following standard of care (SOC) treatment. Altered lipid metabolism is observed in glioblastoma tumours, with metabolic energy production occurring at increased rates *via* fatty acid oxidation. Previously, desorption electrospray ionisation mass spectrometry imaging (DESI-MSI) has been able to visualise the changes associated with increased FAO, co-localising fatty acids, and acyl carnitine molecular species in pre-clinical models. Although useful information can be obtained from pre-clinical models, it is important to determine if these are translatable to clinical samples. In this study, DESI-MSI was used to analyse human tissue biopsies, detecting multiple acyl-carnitines at high abundance with very specific tissue distributions, locating to the borders of hypoxia. These results corroborate previously seen pre-clinical analysis of orthotopic and xenograft GBM samples.

A novel key advancement in the visualisation of GBM tumours is the use of 5-amino levulinic acid (5-ALA) as an interoperative tumour visualisation guide. 5-ALA is taken up by tumour cells and converted to protoporphyrin IX (PpIX) which fluoresces red under blue light at 412 nm. The patients, from whom the clinical biopsies analysed in

this study are from, were all given 5-ALA prior to surgery to allow intraoperative tumour assessment. It is unsure where within the tumour mass PpIX is expressed, thus mapping the distribution of the molecular ion at m/z 563.24 is desired. The molecular ion of PpIX was not detected in any clinical biopsy, however the feasibility study of PpIX analysis by DESI-MSI is presented.

2. Introduction

Glioblastomas (GBM), defined as grade IV astrocytoma by the World health Organisation (WHO), are the most common primary malignant brain tumour in adults, accounting for 45.2% of all primary brain neoplasms [1, 2], and 60-70% [3] of all malignant glial tumours. Prognosis of this disease is extremely poor, with average life expectancy between 12–15 months with standard of care (SOC) treatment; maximal tumour resection, followed by radiation and adjuvant chemotherapy with temozolomide [4]. The most important aspect of treatment is that of maximal tumour resection, which has an important impact on increasing overall survival. Gross total resection (GTR) has shown to increase median survival by 5 months vs incomplete resection, as well as improving progression free survival (PFS) [5]. However, GTR is not always possible due to imprecise correlation of pre-operative MRI images and intra-operative tissue anatomy as well as difficult differentiation between high grade glioma and parenchyma. As such tumour tissue often remains after surgery which can cause rapid disease recurrence [6, 7].

GBM is a heterogeneous, invasive tumour displaying both inter and intra tumour heterogeneity [8, 9]. An extensive micro-environmental heterogeneity is exhibited in the biological structure of a GBM. This, combined with a high genetic, epigenetic and molecular variability within GBM tumours can cause problems for chemotherapy and radiotherapy treatment. [10] Over the years, research into GBM is extensive and although many new genetic mutations have been discovered, there has been little impact on the prognosis and overall patient survival status [11].

It is well understood that tumours exhibit altered lipid metabolism and research into the lipidome is current of great interest [12]. Lipids provide a number of functions in cells providing cellular structure, providing energy sources and being involved in signalling properties [13]. Pre-clinical analysis of GBM tumour models has revealed extensive lipid heterogeneity, with altered metabolism to fatty acid oxidation (FAO) observed previous DESI-MS imaging [14] as well as in the G7 tumour model described in detail in chapter 2.

Mass spectrometry imaging (MSI) is a growing field of analytical methods that allow spatially resolved analysis of endogenous and exogenous chemical species in a single experiment of which desorption electrospray ionisation mass spectrometry imaging (DESI-MSI) is a popular technique for lipid imaging. DESI-MSI is an ambient ionisation imaging method that allows rapid analysis of tissue sections and comprehensive analysis of the lipids in biological specimens through untargeted analysis.

In this study, human tissue biopsies from 5-ALA guided surgeries were examined to explore the lipidomic segmentation of the tissue sections to find signals that reveal tumour heterogeneity, as well as corroborating findings from lipid imaging of preclinical glioma models to the lipid signatures found in human tissues and thereby partially validate these models in the lipidomic context.

2.1. Fluorescence guided surgery using 5-ALA

The infiltrating nature of GBM [15] requires intraoperative tumour margin determination, which is now commonly enhanced using the fluorescent probe 5-aminolevulinic acid (5-ALA) [16]. Recent guidelines set out by NICE to improve surgical resection of high-grade gliomas (HGG), recommend the oral use of 5-ALA for all patients undergoing initial surgery for GBM. As an oral solution, Gliolan^{TM} or the ‘pink drink’ is given to a patient up to 2 hours before surgical intervention. 5-ALA is a naturally occurring biomolecule acting as a precursor to the fluorescence molecule protoporphyrin IX (PpIX) [17] *via* the heme biosynthesis pathway where PpIX accumulates in high density malignant cells [18, 19], whose fluorescent signature is used as a guide to neurosurgeons during fluorescence guided surgery (FGS). FGS has enhanced the intraoperative visualisation of GBM tumours, with studies showing that patients undergoing FGS have increases to the extent of resection, including GTR of MRI contrast enhancing tumour volume, as well as improvements to 6-month progression free survival achieved across a number of studies [16].

DESI-MSI was also used to determine whether the fluorescent agent PpIX can be detected, and its distribution mapped and correlated to the lipid signatures observed. Matching lipid signatures to the molecular marker of PpIX fluorescence will determine a specific signature of the tumour where PpIX is located. Future analysis of clinical biopsies can draw upon this known signature to distinguish tumour containing biopsies, even in the absence of fluorescence or PpIX molecular signature.

3. Materials and Methods

3.1. Materials

All solvents were purchased from Sigma-Aldrich, UK.

Protoporphyrin IX was purchased from Sigma-Aldrich, UK as the disodium salt and dissolved in MQ water to make the standard concentrations.

3.2. Sample preparation

Specimens from frozen human biopsies were obtained from the Royal Salford biobank from patients receiving 5-aminolevulinic acid (5-ALA) prior to surgery. Biopsies were sectioned at 12 µm thickness on a cryostat (LEICA CM3050 S) for DESI-MS imaging and H&E analysis). Sections thaw-mounted onto SuperFrost Plus adhesion slides (Thermo Scientific, UK) for all mass spectrometry imaging applications. All slides were stored at -80 ^{o}C until use. Sections were allowed to equilibrate to room temperature before analysis.

3.3. PpIX feasibility study on control liver tissue

For feasibility study, PpIX was dissolved in water at a concentration of 1 mg/mL and subsequently diluted to concentrations of 500, 250, 125, 60, 30 and 15 ng/µL. Control liver was sectioned at 12 µm on a cryostat (LEICA CM3050 S) and 1 µL of each concentration of PpIX was spotted directly onto the surface. Spots were left to dry prior to fluorescence or DESI-MS imaging.

3.4. DESI-MS imaging

Tumour biopsy sections were analysed by DESI-MS imaging in both positive and negative ionisation modes on a modified 2D DESI stage (Prosolia, Indianapolis USA) mounted onto a Xevo G2-XS quadrupole time of flight (QToF) (Waters, Wilmslow, UK). A modified slide loading plate (Prior Scientific, Cambridge) was used to hold a single slide on the plate for analysis. Images were acquired at a pixel size of 50 µm at 20 scans per second for negative ion mode and 10 scans per second in positive ion mode. Full scan MS data was acquired over the mass range m/z 50-1200. The solvent spray consisted of 98% Methanol: 2% Water at a flow rate of 2 µL/min and a nebulising gas of nitrogen at 20 PSI. A heated collection capillary at 12kV was used, giving an inlet temperature of 500 ^{o}C (Waters Research Centre, Budapest, Hungary) and a source temperature of 100 ^{o}C.

DESI source geometry positions were optimised prior to all imaging experiments determining maximal lipid signal extraction on control liver sections. Optimised parameter used in this work are 1.5 mm spray tip to sample surface, 6 mm sprayer to heated capillary inlet, 80^{o} sprayer impact angle with a 5^{o} collection capillary angle. Capillary voltages of 1 kV and 0.7 kV were used for positive and negative ion mode respectively, with spectra acquired in sensitivity mode on the Xevo G2-XS.

3.5. DESI-MS/MS and imaging

MS/MS experiments were carried out using the same spray setup as used for DESI-MS imaging including spray settings on a modified 2D DESI stage (Prosolia, Indianapolis USA) mounted onto a Xevo G2-XS quadrupole time of flight (QToF) (Waters, Wilmslow, UK). MS/MS images for the feasibility study of PpIX on liver tissue were acquired at 2 scans per second. PpIX fragmentation used an isolation window of 563.25 and a collision gas of argon at 50 V.

3.6. Data analysis

SCiLS lab software (Version 2021a / Release 9.00 (Bruker Daltonik GmbH, Bremen, Germany, www.scils.de) was used for DESI-MS imaging data analysis. All DESI-MS imaging data files were converted into the vendor neutral .imzML format through HDImaging software. The resulting .imzML files were converted to SCiLS lab compatible files for data analysis (SCiLS Lab, Version 2021a / Release 9.00 (Bruker Daltonik GmbH, Bremen, Germany, www.scils.de). Spectra were normalised to the total ion current (TIC) and regions of interest (ROIs) annotated on each section.

Probabilistic latent semantic analysis (pLSA) was applied to the whole tissue sections across the full mass range, using 5 components with random initialisation.

Individual MS spectra were extracted from ROIs using HDimaging v1.4 (Waters Corporation, Wilmslow, UK) and viewed in MassLynx v4.1 (Waters, Milford, USA)

3.7. Histology staining

Haematoxylin and eosin (H&E) staining was carried out on adjacent tissue sections to those analysed by DESI-MS imaging. Sections mounted onto glass slides were de-fatted in ethanol washes at 70%, 90%, 100%, 100%, 90% and 70% (2 minutes each). The samples were washed in running water and stained in haematoxylin (2 mins) , followed by another water wash. The sections were then differentiated by a few dips in 1% HCl in 70% IMS and washed again in running water before eosin staining (5 mins) . Lastly, each slide was dehydrated in a series of IMS washes at 95% and 100% (2 x 2 mins of separate washes), followed by xylene washes (2 x 5 mins) and left to dry. Sections were mounted with a cover slip using an aqueous mounting media and scanned using the Zeiss Axioimager upright fluorescence microscopes.

3.8. Fluorescence imaging

To assess the concentration at which PpIX fluoresces, control liver tissue was spotted with varying concentrations of PpIX in dH_2O between 500 ng/µL and 15 ng/µL. Blue light at 410 nm was used to excite PpIX which was visually observed on the control tissue. Images were acquired on Olympus BX51 fluorescence microscope (Olympus Corporation, Japan) with QImaging Retiga 6000 snapshot CCD camera (QImaging, British Columbia, Canada). Images were acquired using yellow light excitation 560 nm with red absorbance of PpIX at 705 nm. An exposure time of 2000 ms, gain of 2.5 and γ of 1 on QCapture Pro 7.

4. Results and Discussion

4.1. DESI-MSI human biopsies

Positive and negative ion mode DESI-MS imaging analysis was carried out on several GBM biopsies from 5-ALA positive cases, to investigate lipid heterogeneity across tumour samples. Initial DESI-MS imaging results were carried out across the full mass range from 50-1200 *m/z* to profile the lipid constituent of the human tissue biopsies.

Many lipid species in the DESI-MS spectra, as well as areas of heterogeneity within the DESI-MS images, are observed in the single biopsy samples. Probabilistic latent semantic analysis (pLSA) of 6 tissue biopsies analysed by DESI-MS imaging positive ion mode, revealed stark differences in the lipid profiles throughout the tissue sections. Component 1, 3 and 4 from the positive ion mode DESI-MSI pLSA define regions within the tumour biopsy sections, Supplementary Figure 53.

The main multivariate analysis tool used to determine heterogeneity in tumour samples was pLSA, which provides at alternative to principal component analysis (PCA). An important advantage of using pLSA to determine heterogeneity in these samples is that the scores and loadings are non-negative and can be visualised as images. The *m/z* values for each component can be interpreted by their mass spectral intensities, meaning molecular species with higher weighting are more abundant in that particular region as denoted by the component images distribution [20].

Of the samples that showed interesting heterogeneity, NP19120T was further investigated. The pLSA results from positive and subsequent negative ion mode DESI-MS imaging analysis of an adjacent section are compared, Figure 39.

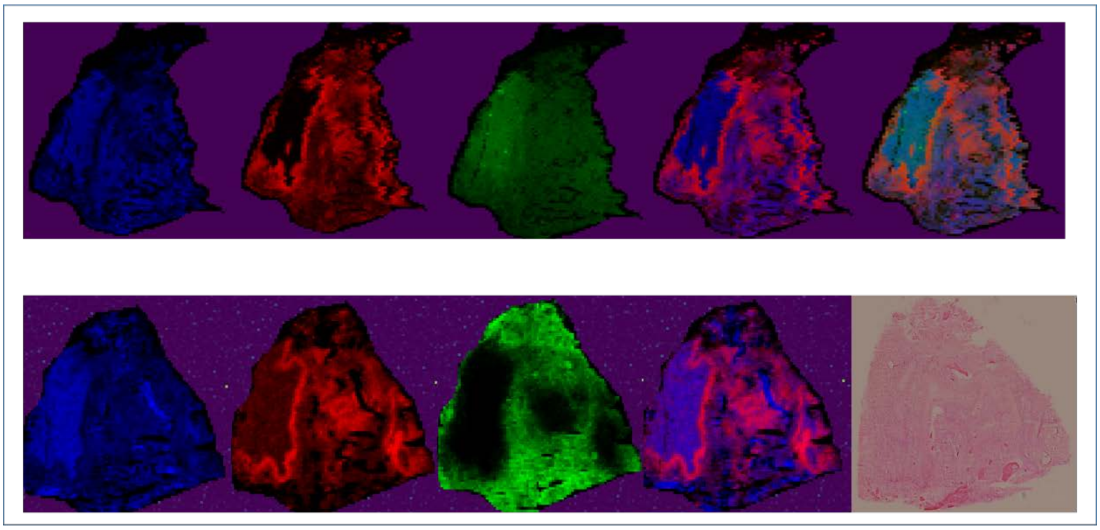

Figure 39 – pLSA analysis from DESI-MSI analysis of human GBM biopsy NP19120T. The pLSA analysis was undertaken on the positive and negative ion mode data, acquired on adjacent tissue sections, revealing corresponding regions from each of the DESI-MS imaging datasets. Each pLSA component is produced from a combination of m/z ion intensities and reveals spatial tissue components based on the mass spectral data. Overlayed pLSA components in positive and negative DESI-MS imaging data reveal the same tissue features.

The pLSA results from NP19120T show each individual component represented as a single colour map across the tissue section. Areas with similar biomolecular properties linked to the DESI-MS imaging results are grouped into a single image. Components in both polarities reveal clear and corresponding biochemical heterogeneity in the tumour biopsy. Component 3 from the pLSA positive ion mode data (top row Figure 39) and component 5 from the negative ion mode data (bottom row Figure 39), both highlighted in red, reveal an interesting distribution on the left side of the section, with chemical species appearing to locate to the border of a chemical feature in this region. The major species contributing to these two components, Table 8 & Table 9, reveal a number of lipid species between 400 – 500 m/z in the positive ion mode data and in the 250 - 330 *m/z* region in negative ion mode.

Spectra from ROIs in the red band and the tumour region that is confined within this band, were extracted for each polarity and the major lipid species in each of the pLSA components corresponding to these regions are mapped across the tissue section, Figure 40 & Figure 42. The location of the ROIs is shown overlayed with the pLSA data.

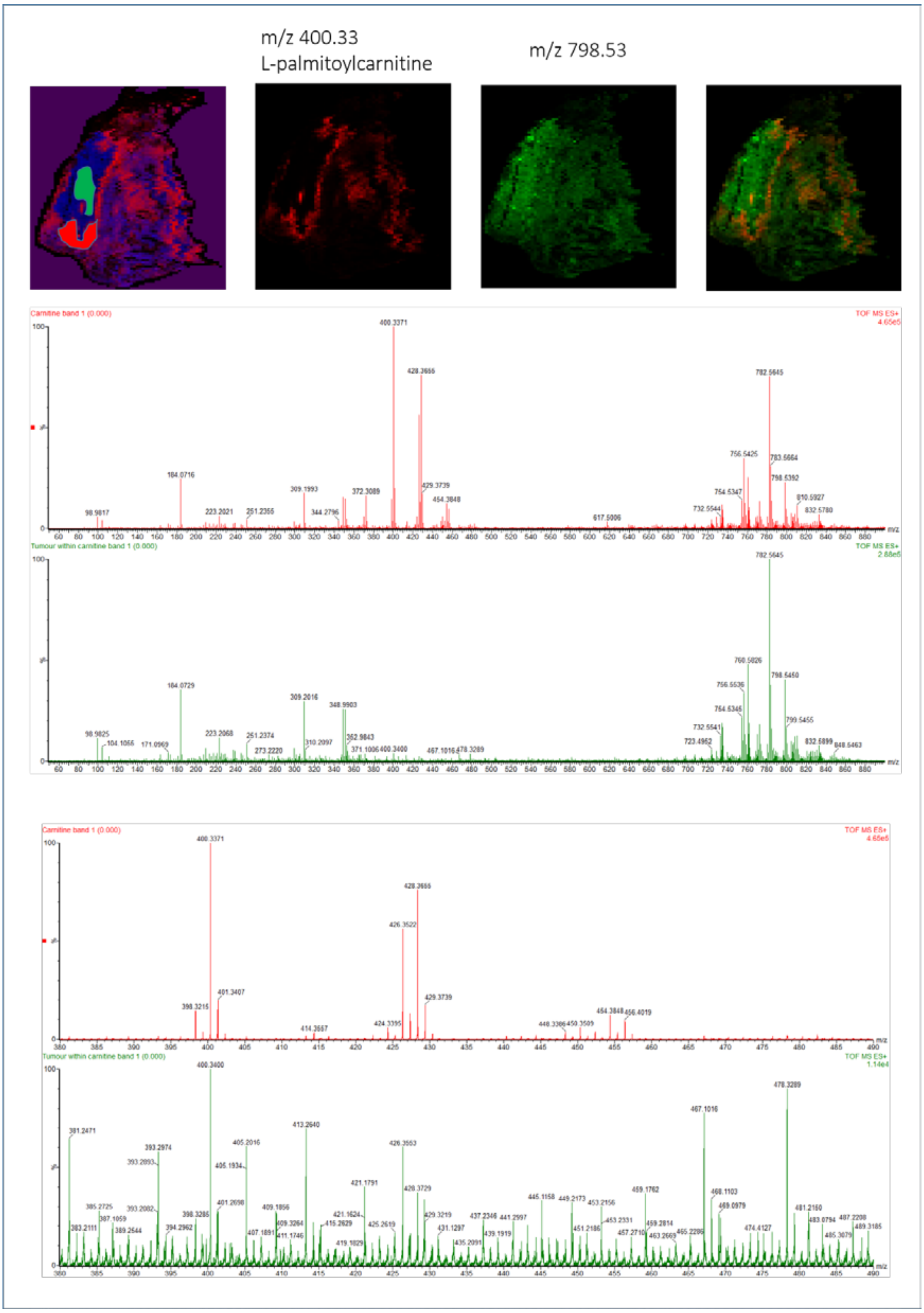

Figure 40 – Lipid distribution in human tissue biopsy human GBM biopsy NP19120T from DESI-MSI analysis. The overlayed image of m/z 400.33 and m/z 798.53 closely matches the overlayed pLSA components 1 & 3 (right hand image). MS spectra extracted from two corresponding regions on the DESI-MS images revealed clear biochemical differences between the two regions.

The pLSA components 3 and 4, overlayed in Figure 39 & Figure 40, show this red band is chemically distinct to the adjacent tumour regions. Mapping and overlaying the two highest weighted species for pLSA component 3 and 4, *m/z* 400.33 and 798.53, show high correlation to the regions defined in the pLSA data. The molecular species are tentatively assigned to palmitoyl carnitine (*m/z* 400.33*)* and PC 34:1 (*m/z* 798.53), with PC 34:1 being the most abundant molecular species observed in the GBM biopsies. The $M+H^+$, *m/z* 760, and $M+Na^+$, *m/z* 782, of PC 34:1 are also detected at high abundance in the tumour regions and correlate to *m/z* 798 ($M+K^+$) being highly weighted in pLSA component 4 that shows abundance across the entire tissue section.

The two spectra extracted from the red band and the inner tumour area show very similar *m/z* chemical species suggesting underlying similarities, however the red spectra revealed a large number of chemical species between m*/z* 400 and 500, Figure 41.

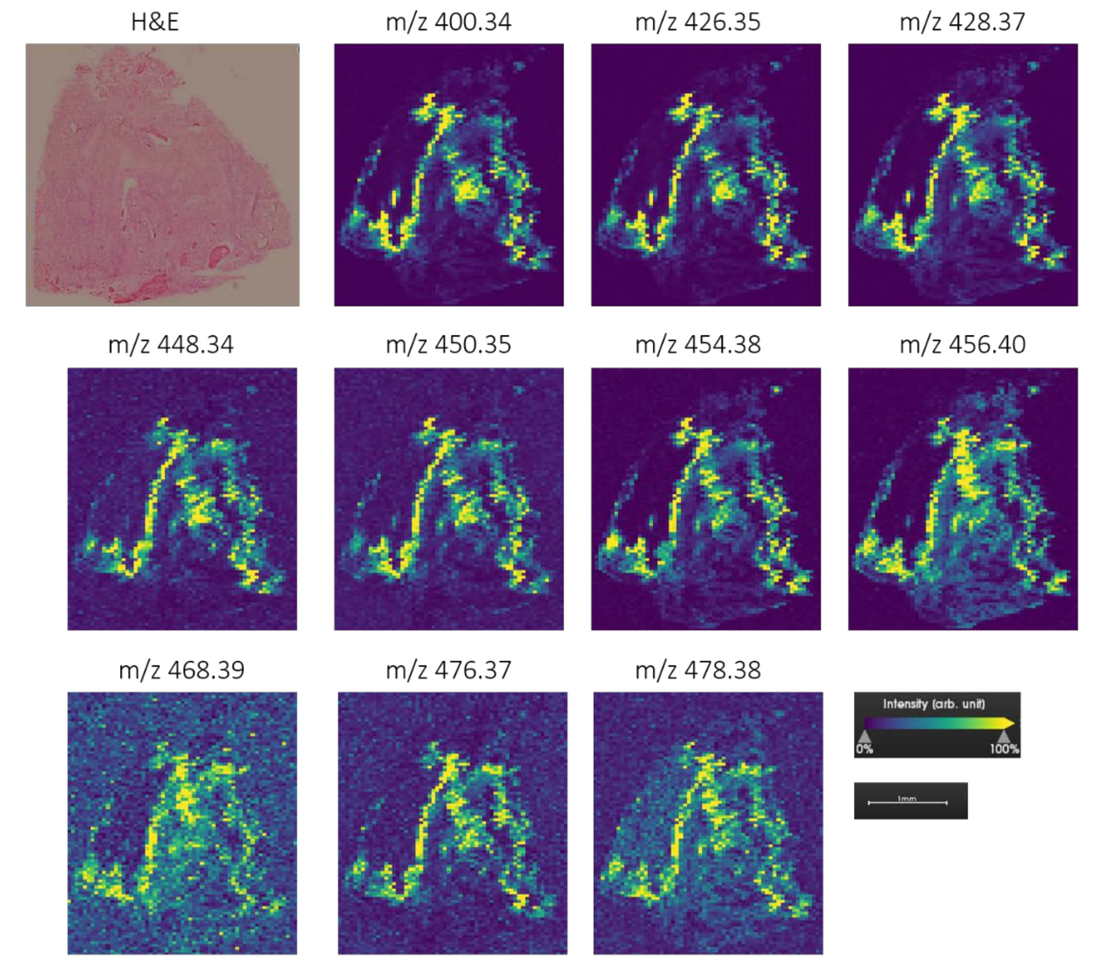

Figure 41 – Positive ion mode DESI-MS imaging analysis of human GBM biopsy NP19120T to show all observed molecular masses observed in the 400 – 500 m/z range assigned as carnitines. DESI-MS images of these molecular species reveal identical distribution within the tumour.

The DESI-MS imaging distributions of these molecules all show comparable distributions, defining the band seen in the biopsy. These chemical species are tentatively assigned to carnitines by accurate mass with single fatty acid side chains ranging from 16 to 22 carbon atoms in length, Table 5.

Table 6 – A list of molecular species tentatively assigned to acyl-carnitines shown in the DESI-MS imaging positive ion mode data of NP19120T, Figure 41. Carnitine assignment based on accurate mass using METLIN and Lipidmaps databases. The carnitines contain a single fatty acid species denoted as the number of carbon atoms and the number of unsaturated double bonds.

Observed m/z	Theoretical m/z	ppm error	Carnitine assignment	Fatty acid component	Ion adduct
400.3371	400.3421	12	Palmitoyl carnitine	16:0	H+
426.3522	426.3578	13	Elaidic carnitine	18:1	H+
428.3655	428.3734	18	Stearoylcarnitine	18:0	H+
448.3386	448.3397	2	Elaidic carnitine	16:0	Na+
450.3509	450.3554	10	Stearoylcarnitine	18:0	Na+
454.3848	454.3896	11	Eicoseneoylcarnitine	20:1	H+
456.4019	456.4053	7	Arachidyl carnitine	20:0	H+
468.3902			Unassigned		
476.3676	476.374	13	Docosatetraenoylcarnitine	22:4	H+
478.3882	478.3872	2	Arachidyl carnitine	20:0	Na
480.404	480.4053	3	Docosadienoylcarnitine	22:2	H+

Histological analysis of the H&E stained section of NP19120T reveals the region within the band of carnitines to contain features of hypoxia with a necrotic core, supplementary Figure 54 A & B. The band containing carnitines appears to be localised to the border of the hypoxic region within this tissue biopsy, a feature also observed in a U87 xenograft model of GBM analysed by DESI-MS imaging [14]. The band of carnitines surrounding the suspected hypoxic tissue, also matches to an area of microvascular proliferation, a key hallmark of GBM tissue [21], supplementary Figure 54 C & D. To confirm the histological analysis of NP19120T, CA-9 immunohistochemical (IHC) staining should be used to determine hypoxia regions within the tissue.

As seen in Chapter 2 positive ion mode DESI-MSI data, a number of species in the m/z 400 – 500 mass range were detected and tentatively assigned to carnitine chemical species. Carnitines, are heavily involved in GBMs and other tumours with altered metabolism, utilising fatty acids as energy via the beta-oxidation pathway.

L-carnitine is well established as having neuroprotective roles such as scavenging free radicals, enhancing antioxidative resources and promoting antiapoptotic pathways in the brain and as such is a target for many neurodegenerative diseases [22, 23]. Reactive oxygen species are common in the brain, particularly associated with hypoxic regions. The localisation of many acyl carnitines to suspected hypoxic regions in the tumour biopsy may confirm the neuroprotective role of carnitines in GBM.

Recently, L-carnitine has been associated as a prognostic marker in human GBM alongside the Na^+ dependent transporter OCTN2 [24]. Compared to healthy brain the OCTN2 expression was upregulated in primary and recurrent GBM, which ties in with our results where a large number of acyl-carnitines have been detected.

The band feature occupied by many carnitine species is also observed in the negative ion mode DESI-MS imaging analysis, Figure 42.

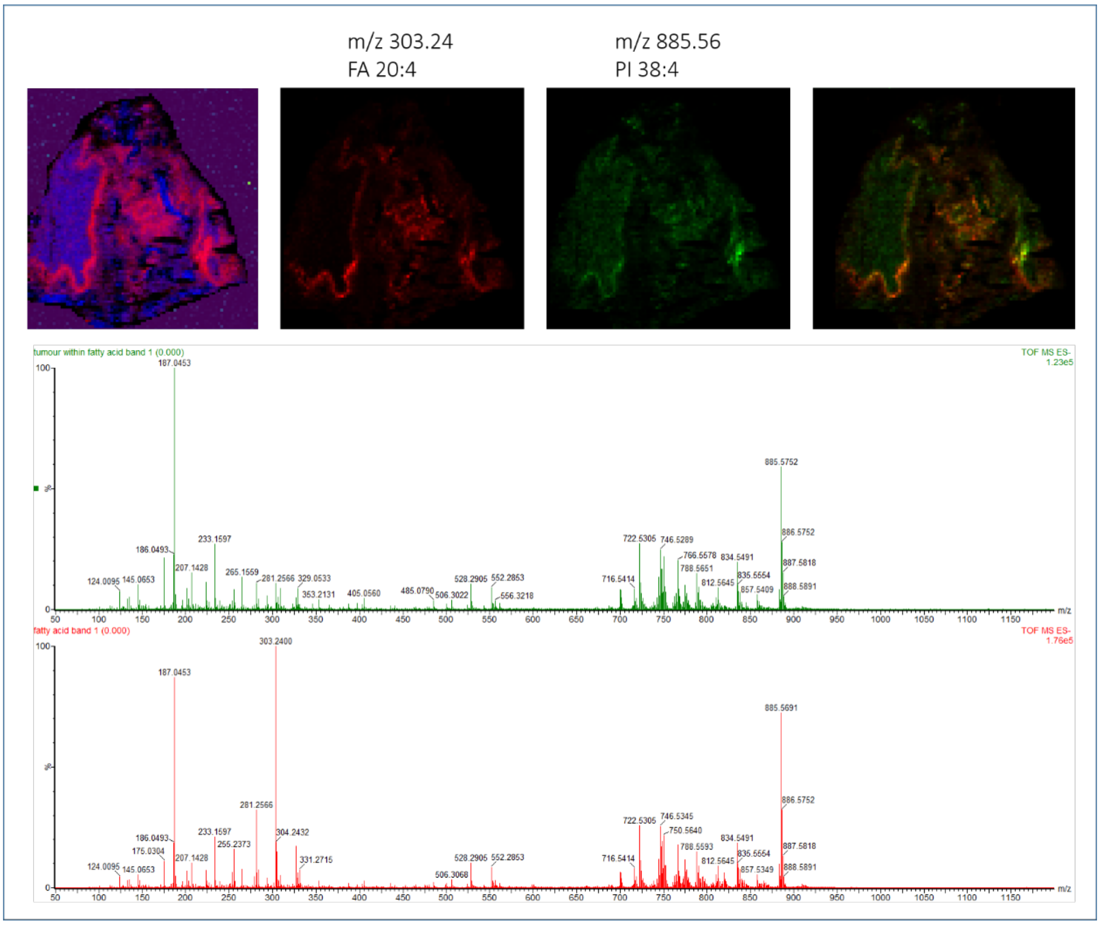

Figure 42 – Negative ion mode DESI-MS spectra from imaging analysis of human GBM biopsy NP19120T. m/z 303.24 and m/z 885.56 have complimentary distributions within the tissue, when overlayed map closely to the pLSA components. MS spectra extracted from two corresponding regions on the DESI-MS images revealed clear biochemical differences between the two regions.

As seen for the positive ion mode data, the spectra extracted from the region containing the carnitine band and the encased tumour region show comparable molecular species, but a higher abundance of low molecular weight species in the 250-330 *m/z* range is observed in the spectra extracted from the carnitine band. pLSA component 5 maps to the corresponding carnitine band in negative ion mode and several high weighted species to this component are assigned to fatty acids, Figure 43.

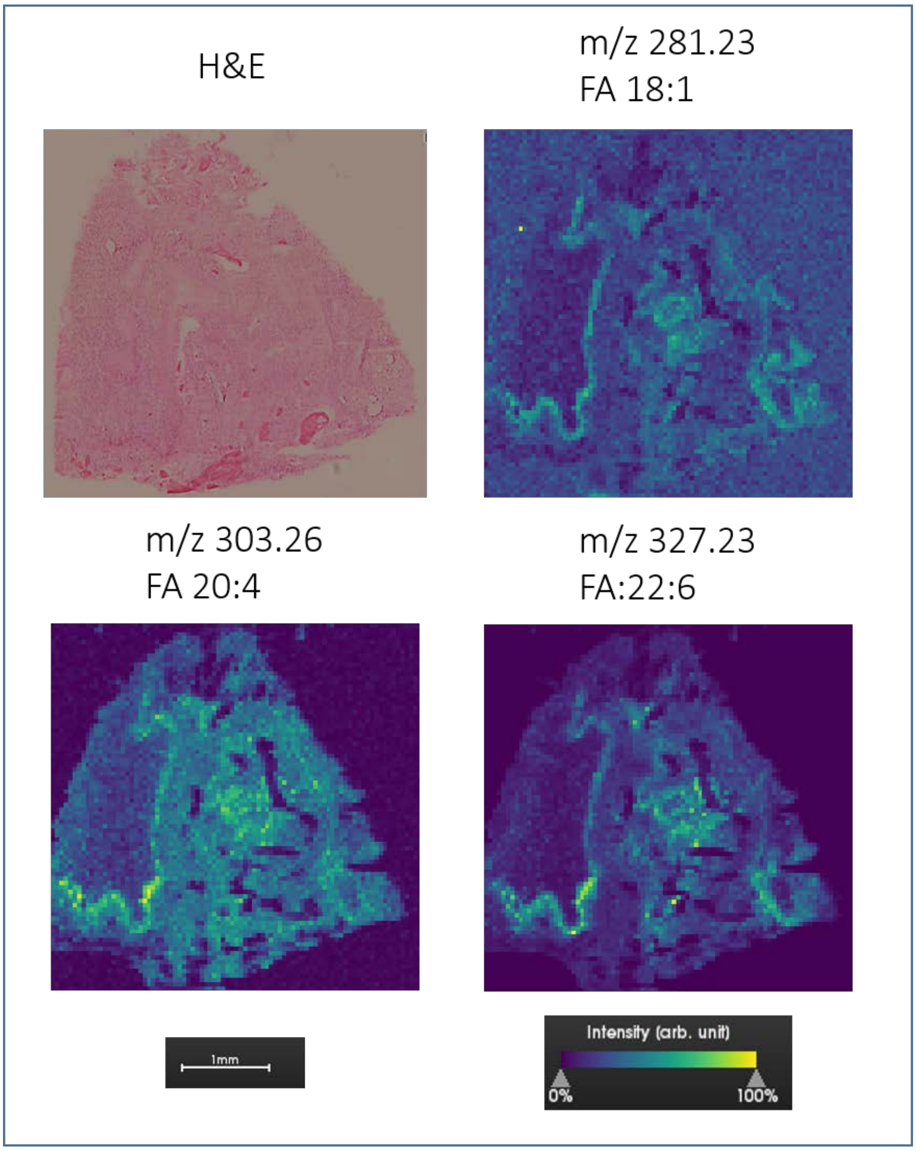

Figure 43 – Negative ion mode DESI-MS imaging of human GBM biopsy NP19120T. Fatty acid species observed in the carnitine band are shown with associated m/z and carbon atom composition of the fatty acid species alongside H&E of an adjacent biopsy section..

The fatty acids detected in this tumour biopsy assigned as oleic acid (C18:1 *m/z* 281.23), arachidonic acid (C20:4 *m/z* 303.26) and docosahexanoic acid (C22:6 *m/z*

327.23) all match the specific distributions observed for the carnitines suggesting these species may be chemically linked, Figure 41. Carnitines are known to play a key role in energy metabolism. They provide transport of fatty acids to the mitochondria, known as the carnitine shuttle, for beta-oxidation which is a key energy pathway aiding the proliferative nature of GBM cells [25, 26] and likely explain the presence of carnitines and fatty acids in the same vicinity. Energy metabolism in GBMs is known to be provided by multiple sources, with glucose providing less than 50% of the pool of acetyl-CoA used in glycolysis [27].

The location of carnitines and fatty acids is also shown in biopsy NP19057T, supplementary Figure 55. Although no regions of hypoxia are observed in this tumour section molecular heterogeneity is evidenced by the DESI-MS images in both positive and negative ion mode as further shown in the pLSA. Three distinct molecular regions are observed in the pLSA image highlighting regions of differing tumour cell density. The carnitines are abundant in region 2 showing lower tumour cell density than regions 1 and 3 on the H&E image, but no further molecular analysis could be determined by H&E alone. As observed in NP19120T, the fatty acid distributions in NP19057T correlate to the distribution of carnitines and are also shown in high abundance in region 1 of the H&E image.

Molecular species with high abundance in the hypoxic region, surrounded by the carnitine and fatty acid band, can act as markers for this feature in GBM and be of importance to investigate GBM heterogeneity, Figure 44.

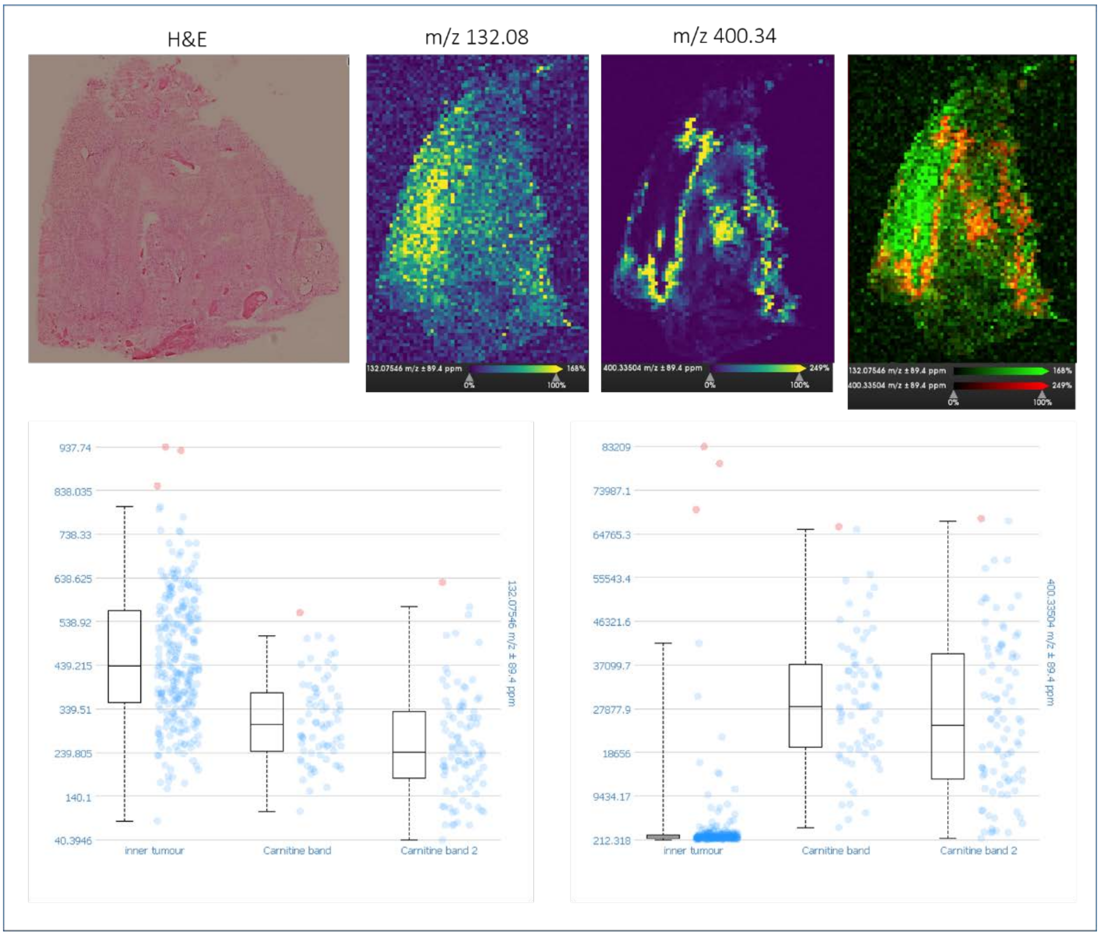

Figure 44 – Positive ion mode DESI-MS imaging of human GBM biopsy NP19120T showing the location of m/z 132.08 (creatine) and m/z 400.33 (palmitoyl carnitine). Intensity box plots of extracted ROIs from inner tumour region and the carnitine band highlight m/z 132.08 at high abundance in the inner tumour region and m/z 400.33 at a much lower intensity. Overlayed single ion DESI-MS images reveals the differing location of the two molecules..

Abundant to the hypoxic region of tumour biopsy NP19120T is *m/z* 132.08, tentatively assigned to creatine. Overlaying creatine with palmitoyl carnitine (*m/z* 400.34), shows this molecular species to be abundant to the region within the carnitine band. Intensity plots of these molecular species confirm creatine to be higher abundance within the hypoxic region, whereas palmitoyl carnitine is observed at extremely low abundance in this region, further confirming the acyl-carnitines location within a band surrounding a necrotic/ hypoxic region of the tumour biopsy.

Creatine and palmitoyl carnitine are further shown to occupy differing regions in NP19081T, supplementary Figure 56. No hypoxic regions were observed based on the histopathology analysis of this section, but the molecular ions assigned to carnitine and creatine appear mutually exclusive, as evidenced by the intensity box plots of ROIs extracted from the carnitine distributions.

Creatine is one of the key molecular signatures used in magnetic resonance spectroscopy (MRS) imaging and is found in metabolically active tissue including the brain [28]. Creatine is often used in conjunction with choline, with a high ratio of choline:creatine a marker of neoplastic tissue in MRS [29]. Elevated choline concentration in gliomas is linked to cellular proliferation and Choline:Creatine correlates to Ki-67 signal, a cellular marker of proliferation [30]. Elevated choline levels in tumour are linked to several choline containing species including phosphatidylcholines thought to be involved in the altered lipid synthesis and requirement for new membrane lipids in proliferative tissue [31]. This observation of increased choline in MRS of gliomas ties into *m/z* 798.53 [PC 34:1 + K^+] being the most abundant molecule in spectra of the GBM tissue biopsies analysed by positive ion mode DESI-MS imaging.

Creatine levels in gliomas are inversely correlated with Ki-67 which is a known marker of proliferative tissue [30]. Creatine is detected at higher abundance in the hypoxic region of the tumour biopsy in NP19120T which correlates this finding, as hypoxic tissue is known to show low signal for Ki-67.

4.2. PpIX feasibility test with DESI-MSI

All human tissue biopsies were obtained from 5-ALA surgeries with positive 5-ALA fluorescence and as such probing the PpIX distribution in relation to the lipid signatures already observed was investigated.

The detection of fluorescence in tumour tissue is a targeted analysis and as such the compatibility of PpIX with DESI-MS imaging was carried out. Standards of PpIX were spotted onto glass slides for MS and MS/MS analysis. Protoporphyrin IX was detected at *m/z 563.25* as the [$M+H^+$] ion, with MS/MS undertaken to determine the fragmentation pattern, Figure 45.

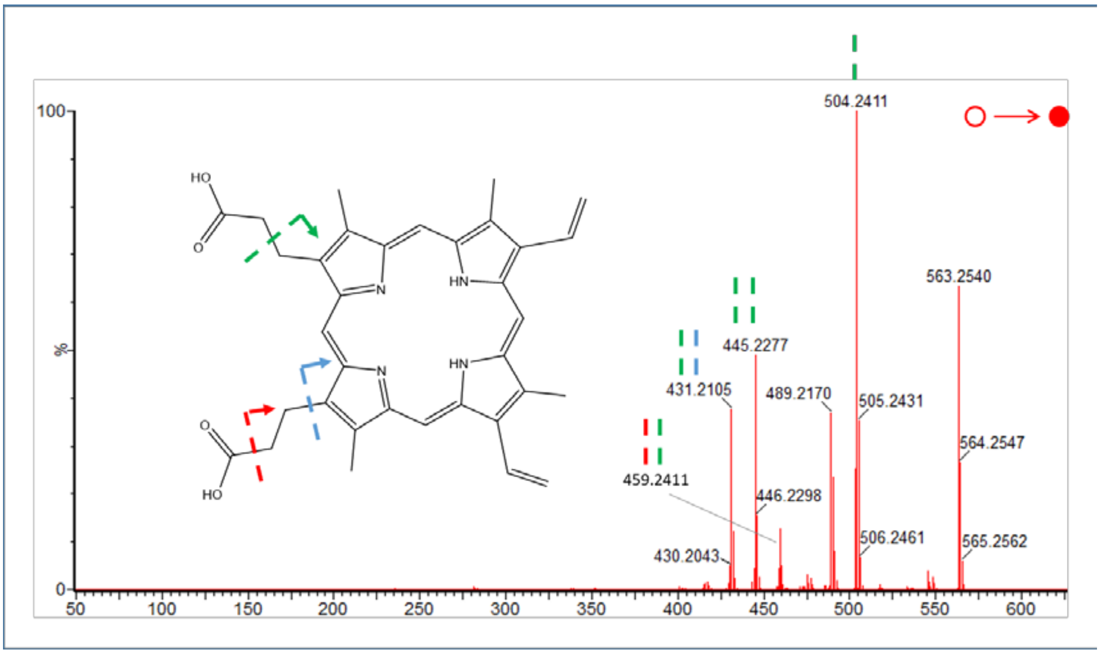

Figure 45 – DESI-MS positive ion mode MS/MS fragmentation of a standard of Protoporphyrin IX (m/z 563.25). m/z ion peaks on the MS/MS spectra are assigned with coloured lines to represent the masses loss from parent to daughter ion. Fragmentation at the red, green, and blue bond caused a loss of mass 45, 59 and 73 respectively. Collision energy of 50 V was used to fragment PpIX molecule.

The MS/MS spectra show several abundant daughter ions from the fragmentation of PpIX. The main cyclic ring of the molecule remains intact whilst the side chains fragment at varying positions as observed previously in the analysis of serum and blood from GBM patients using ESI [32], as well as by MALDI-MS imaging analysis of GBM biopsies [33]. Three main areas on the carboxylic acid side chains are observed to fragment, with various combinations of these fragmentation positions observed in the main daughter ions. The major daughter ion at *m/z* 504.24 occurs with loss of ethanoic acid (*m/z* 59). Fragmentation MS/MS conditions were optimised for the detection of this daughter ion resulting in a collision energy of 50 V used. This fragmentation is also observed in the analysis of heme, the final product of the biosynthetic pathway from 5-ALA to PpIX [34].

Daughter ions have been assigned to a fragmentation pattern based on a combination of each side chain fragmenting at one of three positions, Figure 45, with the resultant fragment ions shown in Supplementary Figure 52.

After assessing the fragmentation patterns, PpIX was spotted at varying concentrations onto control liver sections to determine the feasibility of analysing PpIX by DESI-MSI, which would be utilised in the analysis of the human tissue biopsies. Subsequent images of the same tissue section were acquired in MS and MS/MS mode allowing data collection across the whole mass range of interest (50 – 1200 Da) and fragmentation of parent ion and simultaneous DESI-MS imaging of all fragments ions to be mapped, Figure 46.

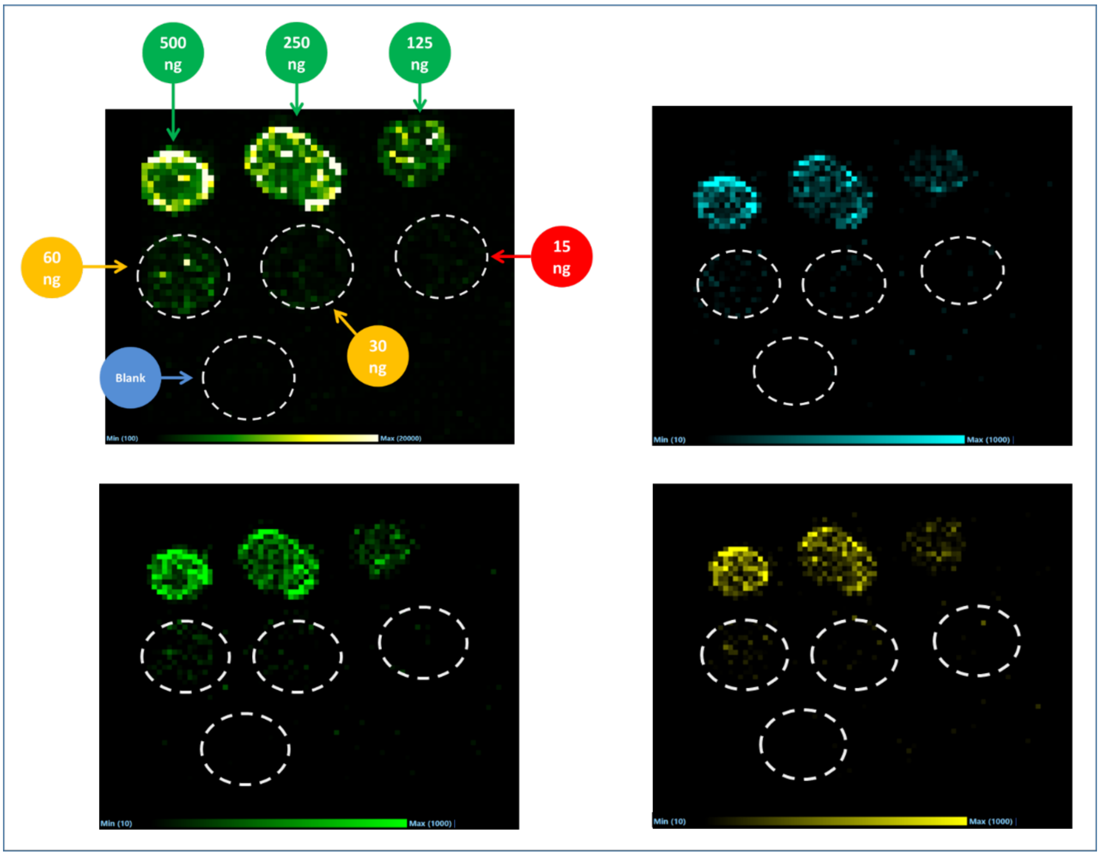

Figure 46 – Determining the detectable concentration of PpIX onto control liver sections by DESI-MS and MS/MS positive ion imaging. Each spot represents 1 µL of PpIX standard spotted at the accompanying concentrations (ng/ µL). Ion intensity distribution maps of parent ion (top left) and fragments previously observed; m/z 431.21 (blue), 445.23 (green) and 504.24 (yellow), reveal detection of PpIX at 30 ng/ µL concentration

The parent ion of PpIX (*m/z* 563.25) and the most abundant daughter ions (*m/z* 431.21, 445.23 and 504.24) after the fragmentation of *m/z* 563.3 are mapped across the concentration range from 500 to 15 ng/µL, Figure 46. The parent ion, in full MS mode, was detected at the 30 ng/µL concentration spot, whereas in MS/MS analysis daughter ions were detected at the 60 ng/µL spot. The full mass range MS spectra were extracted from each concentration from 500 – 30 ng/µL, Figure 47, and MS/MS spectra also extracted from the concentrations between 500 and 60 ng/µL spots, Figure 48.

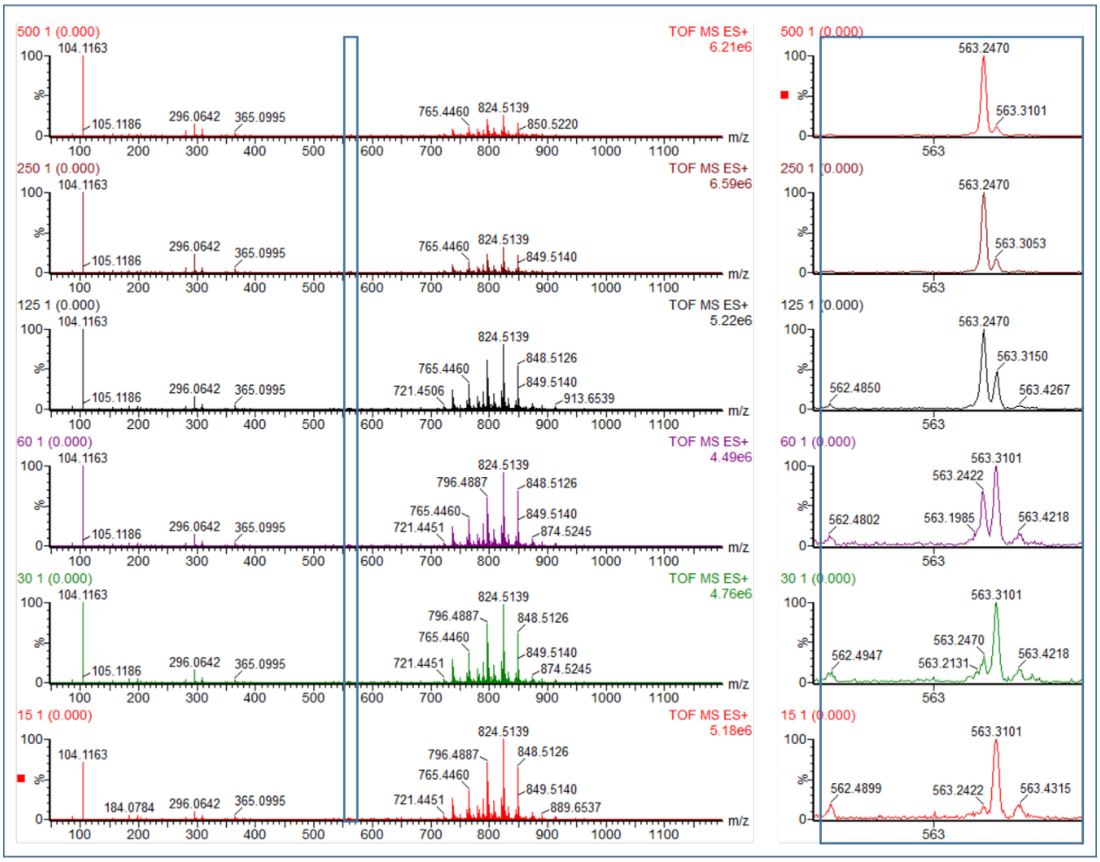

Figure 47 – Extracted DESI-MS positive ion spectra across all concentrations of PpIX standard spotted onto control liver sections. MS spectra from top to bottom show the DESI-MS data at 500, 250, 125, 60, 30 and 15 ng/µL. Zoomed spectra at m/z 563 show clearly resolved MS peaks for PpIX at m/z 563.24 and an endogenous species at m/z 563.31 (undetermined). No peak is found for PpIX at 15 ng/ µL..

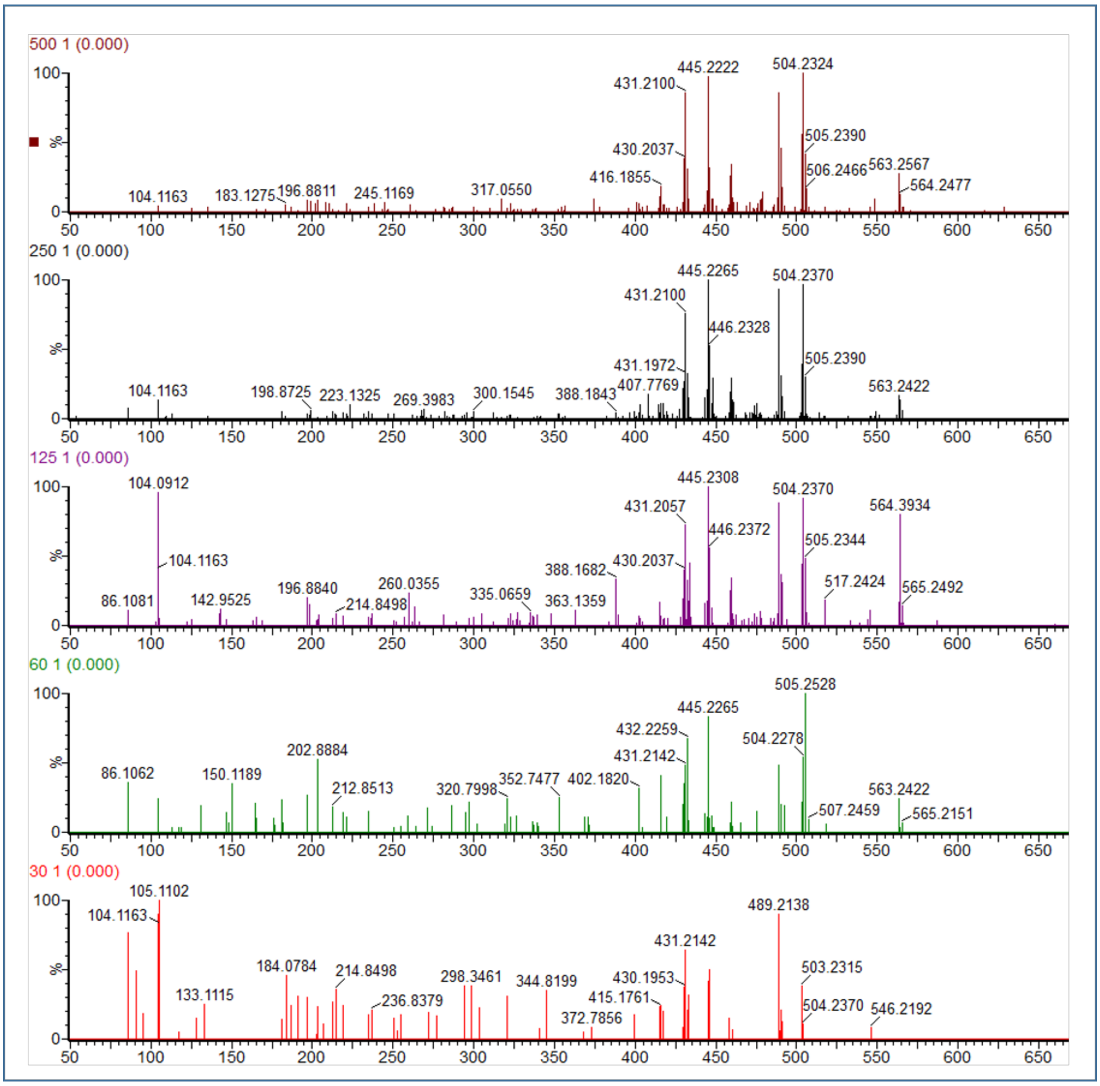

Figure 48 – Extracted DESI-MS/MS positive ion spectra across all concentrations of PpIX standard spotted onto control liver sections. MS/MS spectra highlight parent ion peak at m/z 563.24 and daughter fragment ions: top to bottom show the DESI-MS data at 500, 250, 125, 60 and 30 ng/µL. No molecular ion, or daughter peaks are found for PpIX at 30 ng/µL.

Although a range of concentrations were investigated, the signal for PpIX at the highest concentration of 500 ng/µL is not visible at first in the full scan MS data. The parent ion mass at *m/z* 563.24 is much lower abundance than those for the lipid species simultaneously detected in the DESI-MS imaging data in the 600 – 900 *m/z* mass range. There appears to be no interfering molecular species, with *m/z* 563.31 observed in the full mass range MS spectra but clearly resolved as a separate peak on the Xevo G2-XS, Figure 47. The full mass range MS spectra corroborate the imaging results, with no peak for PpIX [M+H$^+$] detected at 15 ng/µL spot.

The imaging distributions of the major fragment ions of PpIX all show complementary distributions, with detection of the fragments down to the 60 ng/µL spot. The extracted MS/MS spectra from each spot further highlight this result with the fragment of PpIX observed in the spectra to 60 ng/µL, although at relative low abundance. Fragment ions of PpIX are not visible in the spectra extracted from the 30 ng/µL spot.

Following DESI-MS and MS/MS imaging analysis fluorescence microscopy was used to determine the concentration at which PpIX standard fluoresces, Figure 49.

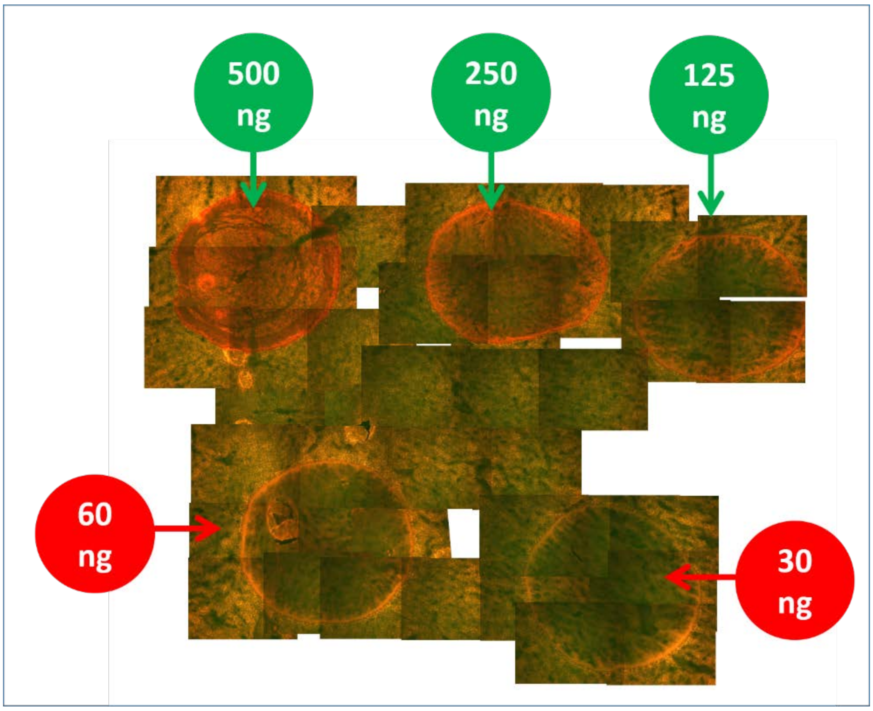

Figure 49 – Fluorescence imaging of PpIX standard spotted onto control liver tissue. PpIX excited using yellow light at 560 nm and visualised as red fluorescence at 705 nm. Multiple images acquired on Olympus BX51 fluorescent microscope are stitched together to show tissue makeup. PpIX fluorescence is visualised in the 125 ng/µL spot. Below this concentration at 60 and 30 ng/µL only background fluorescence is observed.

Excitation of PpIX with blue 410 nm light produced red fluorescence in the 500, 250 and 125 ng/µL concentration spots of PpIX visible to the naked eye. At concentrations below 125 ng/µL no fluorescent signature was observed. Fluorescence-guided surgery (FGS) uses the red fluorescence of PpIX upon excitation with blue 410 nm light, however it was not possible to capture this image using the fluorescence microscopes. The fluorescence image shows application of yellow light at 560 nm and excitation of PpIX at 705 nm and subsequent red fluorescence.

The feasibility results suggest that the molecular signature of PpIX in both MS and MS/MS DESI imaging analysis can be detected at concentrations lower than the fluorescent limit of PpIX. This result may mean that PpIX molecular species can be detected in tissue that does not observe fluorescence and as such, still be quantifiable.

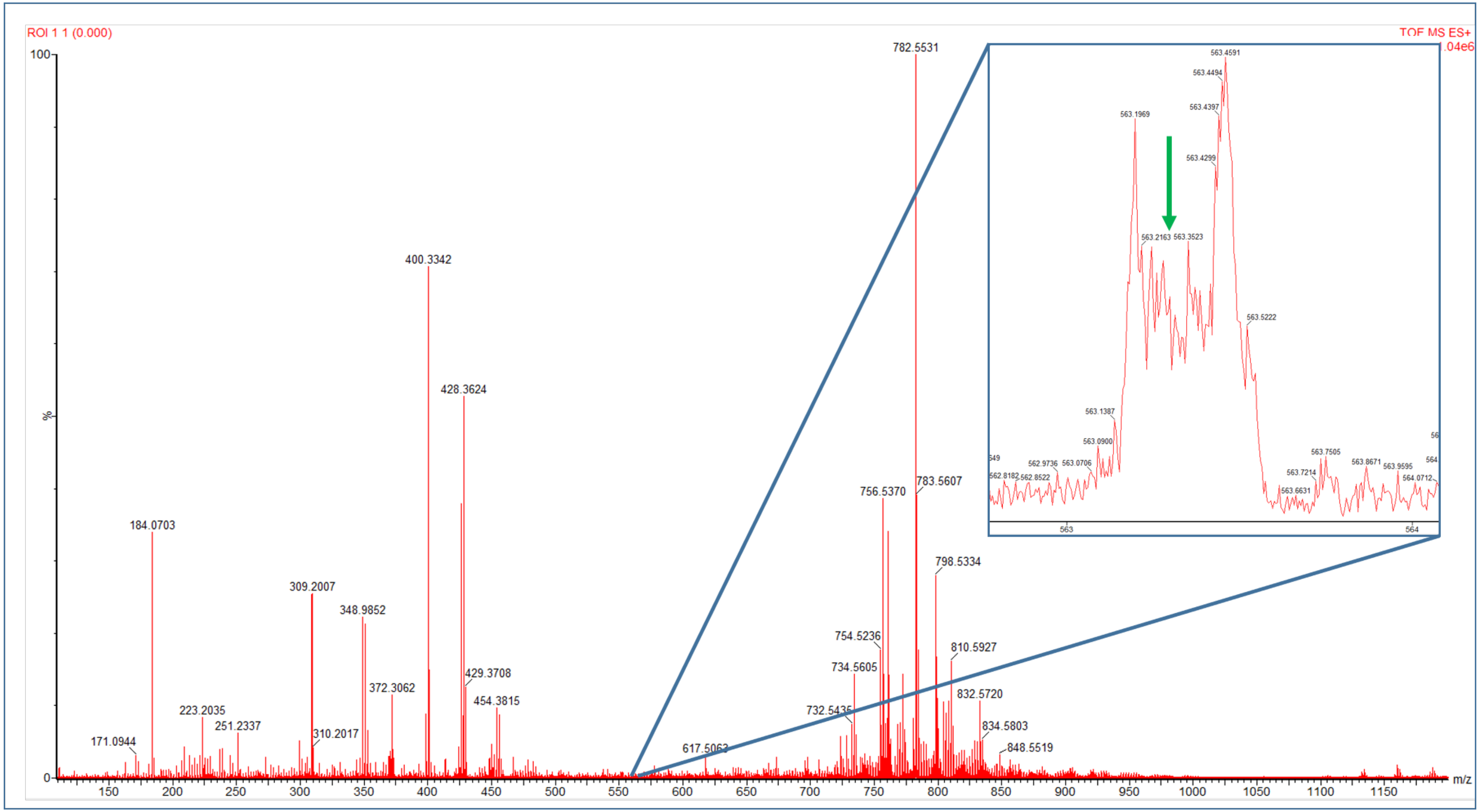

Figure 50 – DESI-MS positive ion mass spectra extracted from NP19120T; 5-ALA positive fluorescent GBM biopsy. MS data was acquired over the mass range 50-1200 Da with the zoomed in area showing the mass expected for PpIX at m/z 563.25. The peak for PpIX is not observed in the tissue spectra, implying that the concentration is below the limit of detection in the tumour biopsy

All human tissue biopsies were obtained from fluorescent regions of GBM tumour masses and have been histologically graded and confirmed as from GBM tumours, supplementary Table 7. However, the fluorescent porphyrin at m/z 563.25 was not detected in full scan mode and subsequent MS/MS analysis did not ascertain the detection of PpIX by DESI-MS imaging analysis, Figure 50.

Although DESI-MS imaging was not able to detect and map PpIX in tumour tissues, a recent study utilising matrix assisted laser desorption ionsiation mass spectrometry imaging (MALDI-MSI) was successfully used to investigate the distribution of PpIX in human GBM tissue samples [33]. Data from; three glioblastomas after 5-ALA administration, two glioblastomas without 5-ALA administration, one gliosarcoma, one low-grade glioma, and two reactive brains were analysed. PpIX was only detected in the GBM with 5-ALA administration. In this study only PpIX, heme and 5-ALA were analysed, but MALDI-MSI revealed increased PpIX accumulation in areas of high tumour-cell density and localisation of heme only to regions of haemorrhage and regions containing blood vessels. These results suggests that PpIX is detectable by MS imaging methods, but the higher sensitivity and extraction capabilities of MALDI-MSI are better suited to this targeted analysis.

5. Conclusions

These results have successfully demonstrated the use of DESI-MS imaging in the analysis of GBM biopsies with several biologically relevant lipid species detected across positive and negative ion mode. Many acyl-carnitines are shown to be abundant molecules in the tumour tissue with very specific tissue distributions, locating to the borders of hypoxia in NP19120T. A number of acyl-carnitines have been observed in the mass range 400 – 500 *m/z,* also correlating with multiple fatty acids species detected in negative ion mode analysis. The detection of carnitines in biopsies, with and without hypoxic regions, suggests a neuroprotective role of carnitines in the vicinity of hypoxia, as well as links to altered metabolism *via* fatty acid oxidation as evidenced by the correlation of fatty acids and the acyl-carnitines. These observation matches clinical data where L-carnitines are observed as prognostic markers of malignant GBM tissue and represents the first mass spectrometry imaging study of carnitines in clinical biopsies. Future work will look to confirm the lipid signatures observed here using CA-9 or HIF-1α IHC staining to determine hypoxic regions and further correlating these features with DESI-MS images. Full MS/MS analysis will be undertaken to determine the molecular ions presented match their assignment in text.

The distribution of PpIX, the fluorescence marker used in 5-ALA surgery from which these samples were obtained, was also investigated. Feasibility studies of PpIX spotted onto control tissue sections suggested DESI-MS imaging to be able to detect PpIX below the fluorescent level which would allow the cross-correlation of PpIX and corresponding lipid signatures of heterogeneity in the tissue. However, the molecular species corresponding to PpIX at *m/z* 563.25 was not detected in GBM biopsies when analysed by DESI-MS imaging in positive ionisation mode. Future work to accurately determine PpIX distribution in these tumours will be of key importance and work by Stummer *et al.* suggests this is possible using MALDI-MSI [33]. Correlating PpIX distribution with the lipid signatures would further enhance this work as to provide a correlation between the fluorescent signal observed during FGS and the molecular species of GBM tissue, with a further link to cell types and features by histopathology.

6. Ethical considerations

Tumour biopsies were collected by the Salford Royal Foundation Trust Brain Tumour Biobank from surgeries at Salford Royal Hospital in accordance to Ethics: 16/NW/0548, IRAS reference: 194361, ARSAC reference: RPC 595 / 3586 / 35328, Study Title: Imaging of the 18kDa Translocator Protein in Primary and Recurrent High-Grade Glioma using PET. Tissue samples were obtained from Royal Salford Biobank in accordance to NCA001-004.

7. Acknowledgements

The author acknowledges and gives thanks to the MRC and Water's for funding the studentship.

8. Author contributions

Matthew Gentry carried out all DESI-MS imaging acquisition and Matthew Gentry carried out subsequent data analysis.

Federico Roncaroli provided all histopathology analysis and acquired the H&E images.

Erjon Agushi and David Coope were part of the neurosurgical teams who collected the tissue samples and provided guidance alongside Federico Roncaroli and Adam McMahon on the study design and tissue acquisition.

Adam McMahon and Emrys Jones were Matthew Gentry's supervisory team, providing support and guidance throughout this project.

9. Supplementary information

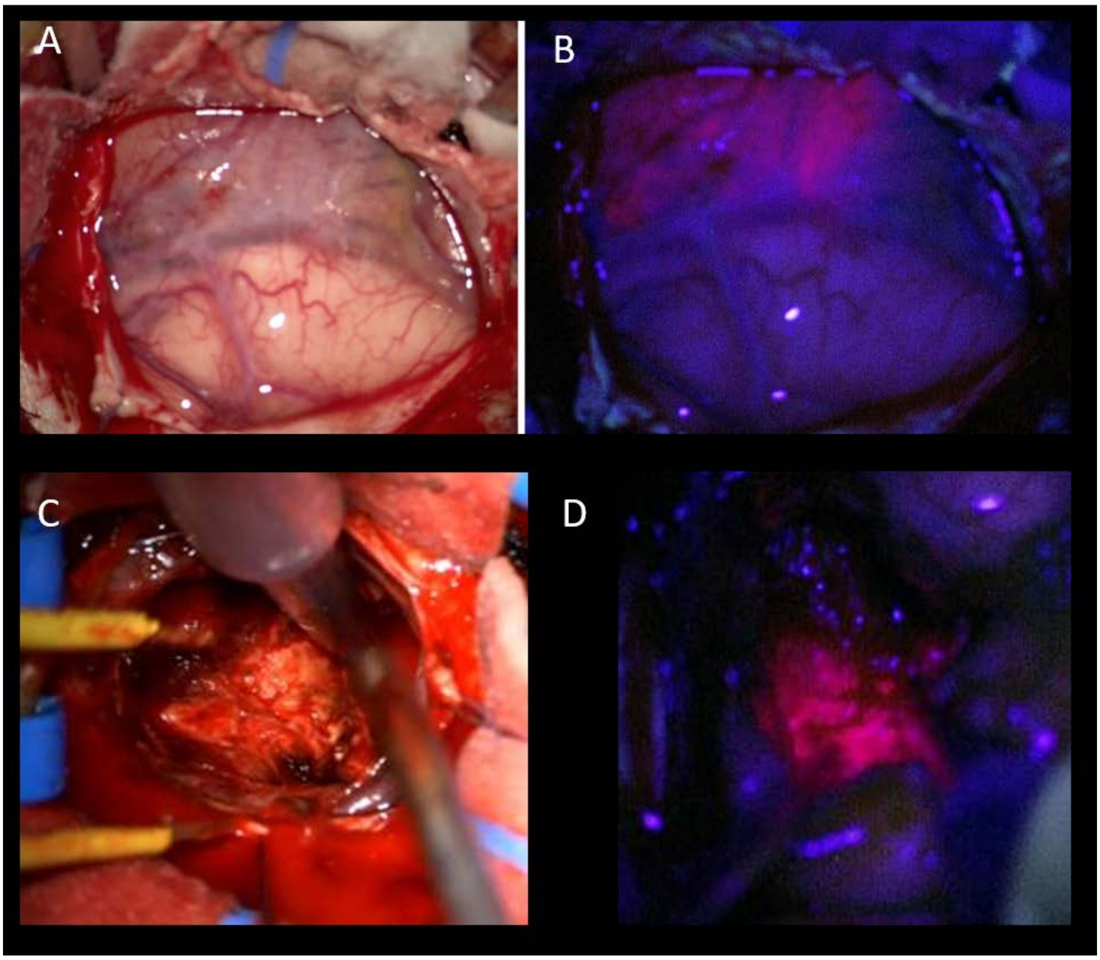

Figure 51 – example of an intraoperative field of view of GBM surgery using 5-ALA as an intraoperative guidance tool. A & C – show two areas under normal light conditions, B & D – show the same region but under blue fluorescent light at 412 nm with the GBM tumour observed by the red fluorescence associated with PpIX

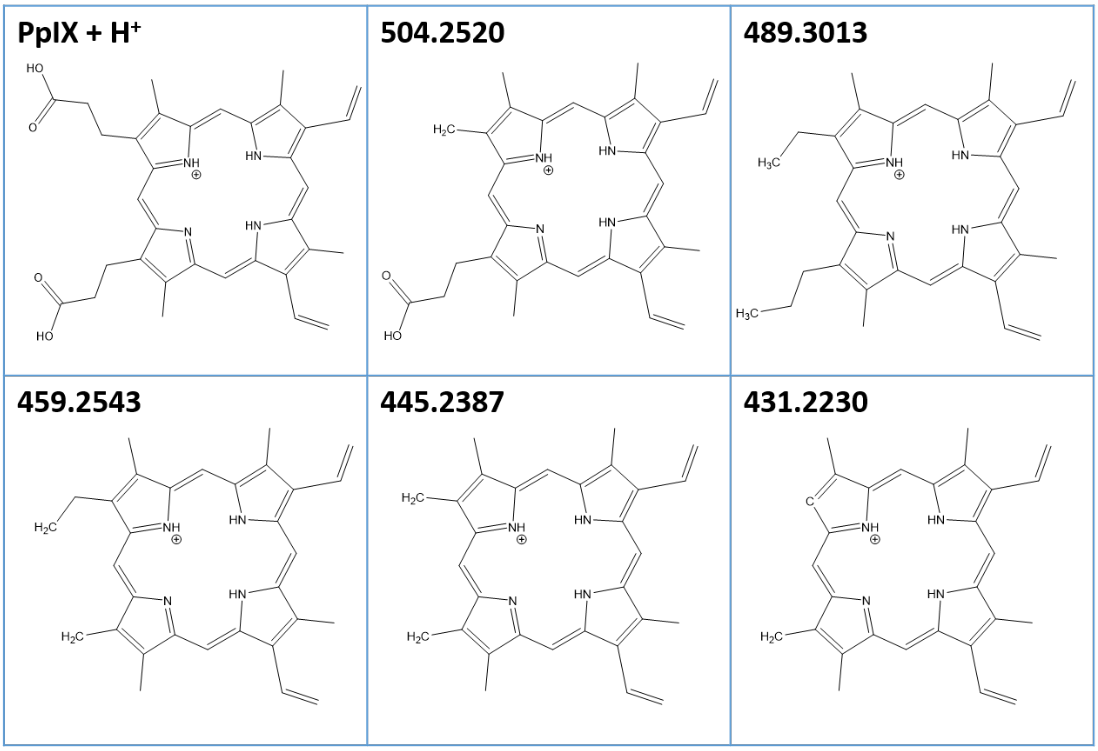

Figure 52 – the major daughter ions detected by the fragmentation of PpIX (m/z 563.25) and observed in the MS/MS spectra in Figure 45.

*Table 7 – details of the GBM biopsies analysed by DESI-MS imaging to detect PpIX. Sections with images shown in this chapter are denoted by a *. All GBM biopsies analysed were from primary GBMs showing positive for intraoperative 5-ALA fluorescence*

Sample ID	5-ALA	Diagnosis	MGMT status	IDH-1	Site
NP19017T	Yes	de novo GBM	hypermethylated	wild-type	right parietal
NP19057T*	Yes	de novo GBM	equivocal	wild-type	left temporal
NP19081T*	Yes	recurrence GBM	not tested	wild-type	left temporal
NP19093T	Yes	de novo GBM	unmethylated	wild-type	left thalamus
NP19104T	Yes	de novo GBM	hypermethylated	wild-type	left frontal
NP19109T	Yes	de novo GBM	unmethylated	wild-type	left parietal
NP19120T*	Yes	de novo GBM	pending	wild-type	left frontal
NP19168T	Yes	recurrence GBM	unmethylated	wild-type	right temporal
NP19186T	Yes	de novo GBM	pending	wild-type	left parietal

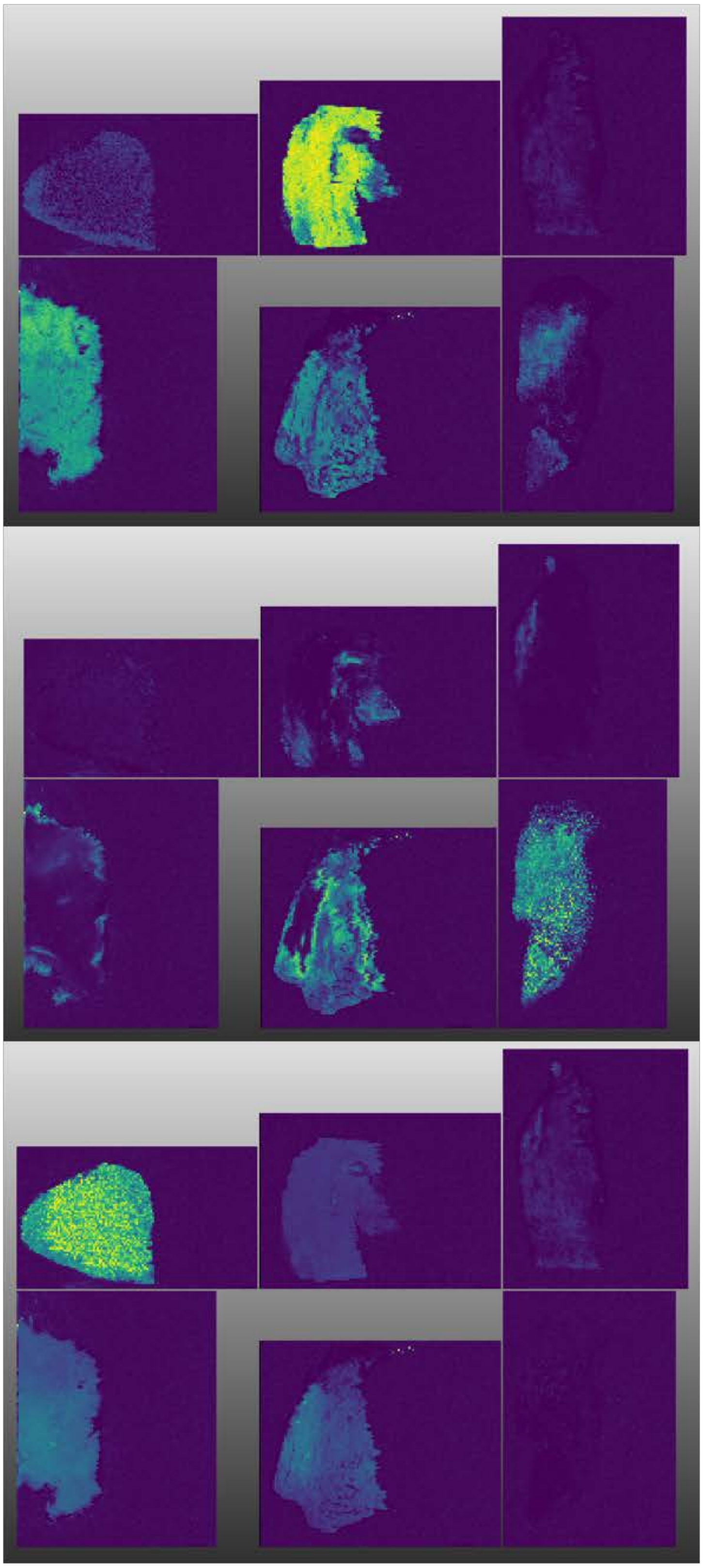

Figure 53 – pLSA analysis of positive ion mode DESI-MS images with components 1, 3 and 4 shown from top to bottom. GBM biopsies clockwise from top left: NP19017T, NP19081T, NP19093 T, NP 19109T, NP19120T and NP19168 T. pLSA components 2 and 5 corresponded to background regions of the samples and as such are not shown

Table 8 – pLSA loadings of components 1, 3 and 4 from positive DESI-MSI of all images in Figure 53. The highest weightest m/z for each componet are listed.

m/z	pLSA component 3 loadings	m/z	pLSA component 1 loadings	m/z	pLSA component 4 loadings
400.335106	0.035154539	782.554693	0.176858773	798.526851	0.063003363
428.369511	0.027682165	760.574344	0.063011134	184.07461	0.056409185
782.554693	0.027523955	184.07461	0.04679381	772.52193	0.032558086
756.538307	0.027405512	756.538307	0.024079322	760.574344	0.027718737
426.351493	0.017457949	810.589098	0.023637693	782.554693	0.019697535
881.747183	0.011317139	784.572711	0.023031418	796.520298	0.019030359
725.54567	0.010194956	804.546508	0.019037959	756.538307	0.01701982
780.54814	0.009217963	798.526851	0.015632526	770.503912	0.016798039
810.589098	0.008944148	832.569447	0.014532004	734.557957	0.016739053
768.566156	0.008635658	806.553061	0.013281841	824.543237	0.014831892
784.572711	0.008502438	808.571079	0.013230794	758.556325	0.014098428

Table 9 – pLSA loadings of component 5 and 4 from the negative ion mode DESI-MSI of NP19120T shown in Figure 42.

m/z	plsa component 5 loadings	m/z	pLSA component 4 loadings
885.57582	0.0726	885.57582	0.0656
303.26077	0.0642	750.56286	0.0474
886.5726	0.0374	766.56107	0.0367
187.03699	0.0291	746.52593	0.0336
834.54102	0.0290	722.55352	0.0292
746.52593	0.0267	187.03699	0.0282
327.23317	0.0240	788.53993	0.0256
281.23208	0.0224	528.28238	0.0249

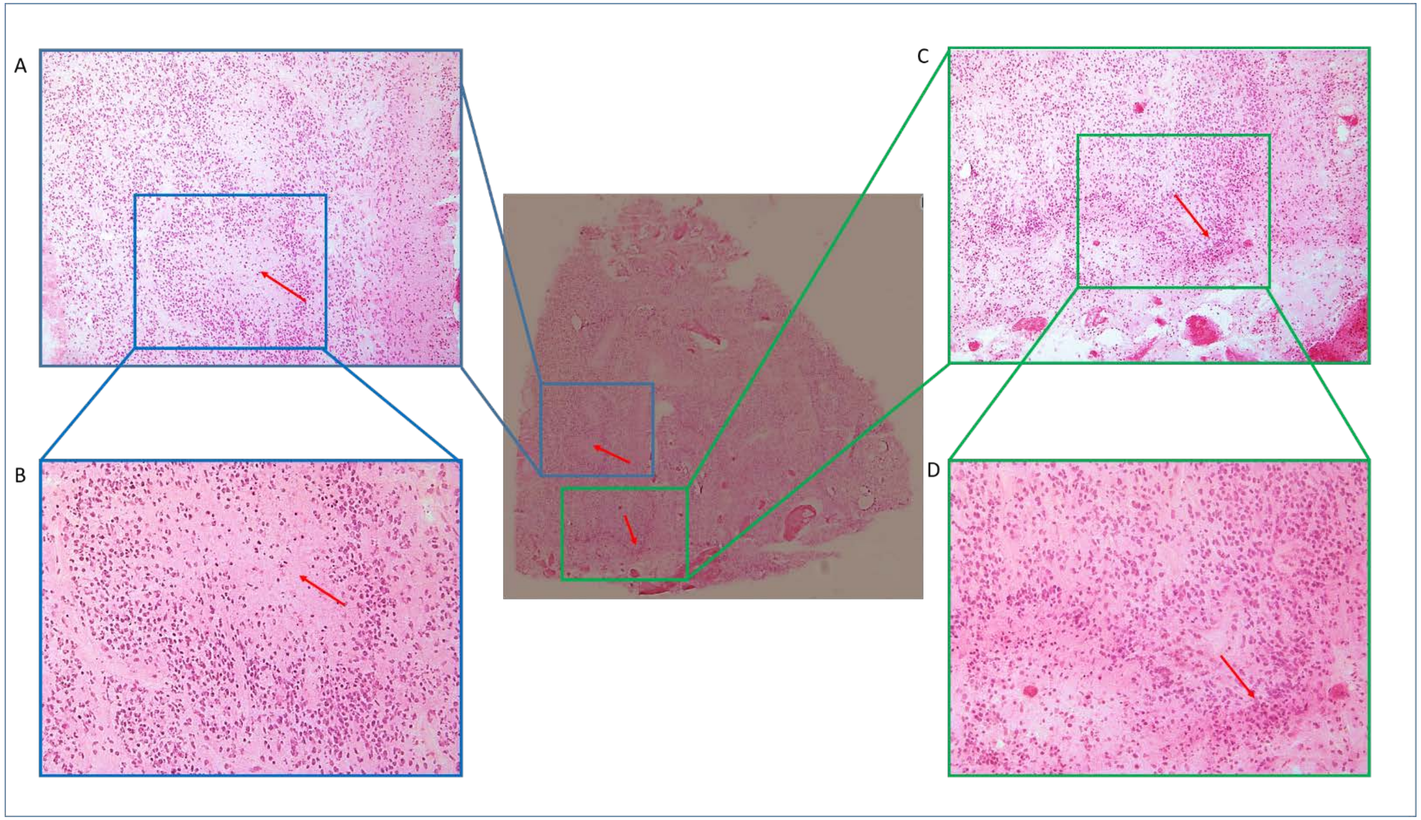

Figure 54 – H&E stained section of NP19120T to highlight histological regions of GBM. A & B shows the hypoxic region with a central necrotic core on the tumour biopsy at 10 X and 20 X magnification respectively. The arrow on A and B points to the necrotic core. C & D show microvascular proliferation which appears to line up to the bands seen in the carnitine and fatty acid distributions

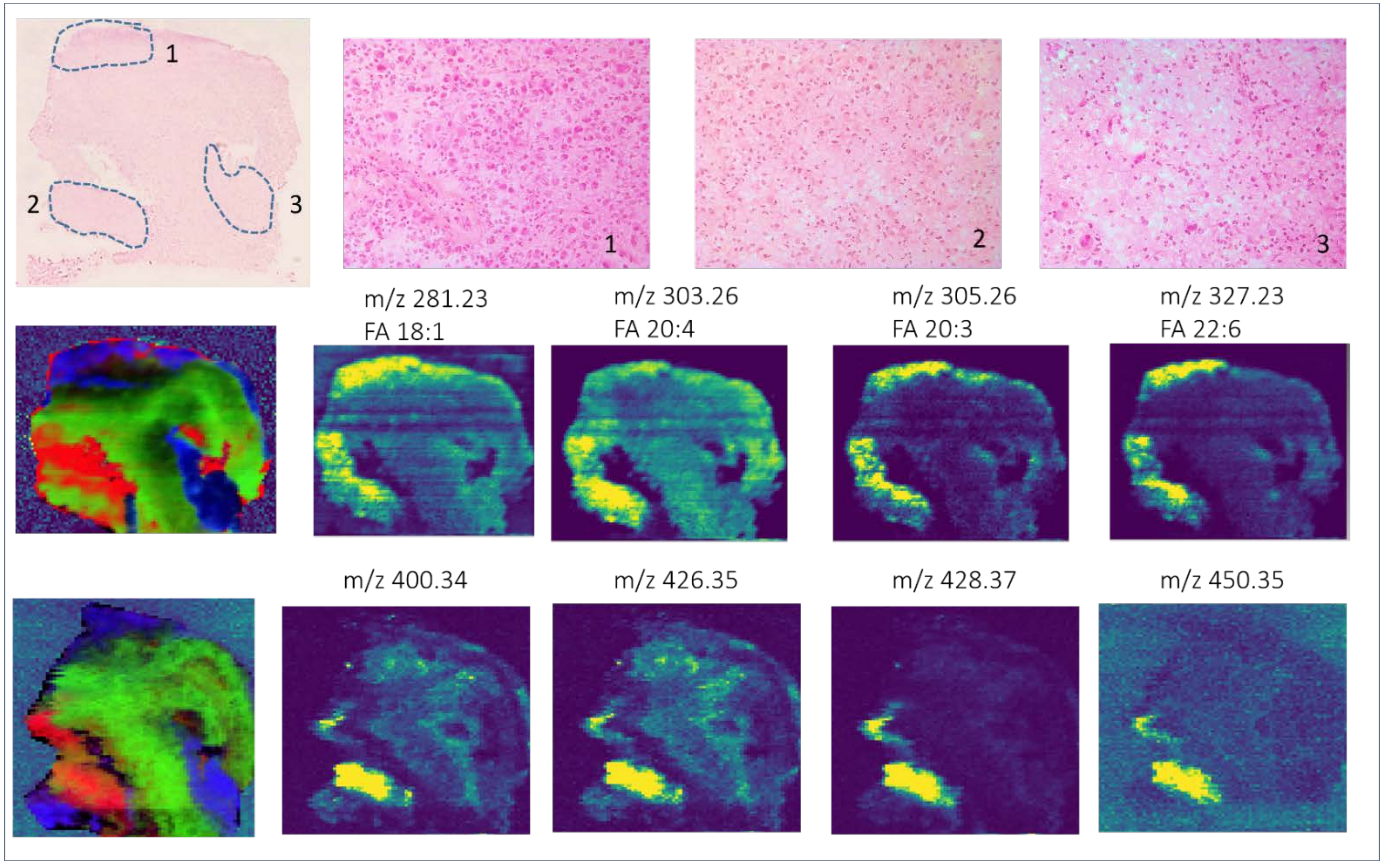

Figure 55 – DESI-MS imaging analysis of biopsy NP19057T. The second row shows the negative ion mode DESI-MS imaging data including pLSA overview of the tissue and fatty acid species detected in the sample. The bottom row shows the positive ion mode DESI-MS imaging data set with a number of carnitines detected in the tumour, matching closely to the component 2 (red) in the pLSA. Fatty acids and carnitines again show corresponding distributions. The H&E image shows three distinct regions as observed from the pLSA and MS imaging data. All regions contain neoplastic cells but ranging in tumour cell density with region 1 containing the highest tumour cell density and region 2 the lowest.

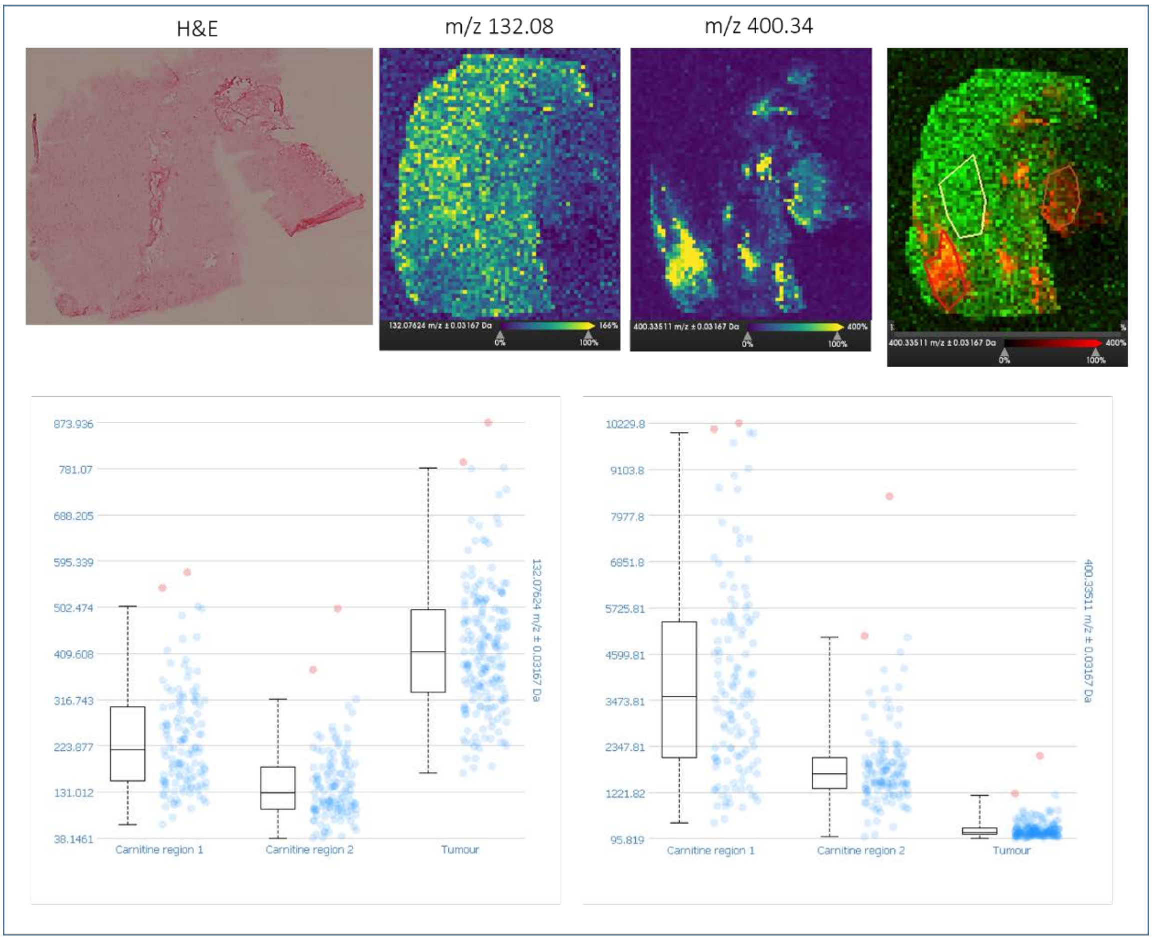

Figure 56 – positive ion mode DESI-MS imaging of NP19081T showing the location of m/z 132.08 and m/z 400.33 tentatively assigned to creatine and palmitoyl carnitine respectively. Single ion images of each ion are shown as well as the overlay of the two molecular species revealing complementary distributions. Ion intensity box and whisker graphs are shown for each ion across three regions on the tissue section, which further corroborate the DESI-MS imaging results.

10. References

1. Thakkar, J.P., et al., *Epidemiologic and Molecular Prognostic Review of Glioblastoma.* Cancer Epidemiology Biomarkers & Prevention, 2014. **23**(10): p. 1985-1996.
2. Liu, A.Z., et al., *Genetics and Epigenetics of Glioblastoma: Applications and Overall Incidence of IDH1 Mutation.* Frontiers in Oncology, 2016. **6**.
3. Li, Q.J., J.Q. Cai, and C.Y. Liu, *Evolving Molecular Genetics of Glioblastoma.* Chinese Medical Journal, 2016. **129**(4): p. 464-471.
4. Stupp, R., et al., *Radiotherapy plus concomitant and adjuvant temozolomide for glioblastoma.* New England Journal of Medicine, 2005. **352**(10): p. 987-996.
5. Kuhnt, D., et al., *Correlation of the extent of tumor volume resection and patient survival in surgery of glioblastoma multiforme with high-field intraoperative MRI guidance.* Neuro-Oncology, 2011. **13**(12): p. 1339-1348.
6. Orringer, D., et al., *Extent of resection in patients with glioblastoma: limiting factors, perception of resectability, and effect on survival Clinical article.* Journal of Neurosurgery, 2012. **117**(5): p. 851-859.

7. Bloch, O., et al., *Impact of extent of resection for recurrent glioblastoma on overall survival Clinical article.* Journal of Neurosurgery, 2012. **117**(6): p. 1032-1038.
8. Morokoff, A., et al., *Molecular subtypes, stem cells and heterogeneity: Implications for personalised therapy in glioma.* Journal of Clinical Neuroscience, 2015. **22**(8): p. 1219-1226.
9. Parker, N.R., et al., *Molecular heterogeneity in glioblastoma: potential clinical implications.* Frontiers in Oncology, 2015. **5**.
10. Vartanian, A., et al., *GBM's multifaceted landscape: highlighting regional and microenvironmental heterogeneity.* Neuro-Oncology, 2014. **16**(9): p. 1167-1175.
11. Louis, D.N., et al., *International Society of Neuropathology-Haarlem Consensus Guidelines for Nervous System Tumor Classification and Grading.* Brain Pathology, 2014. **24**(5): p. 429-435.
12. Warburg, O., *ORIGIN OF CANCER CELLS.* Science, 1956. **123**(3191): p. 309-314.
13. *Biochemistry of Lipids, Lipoproteins and Membranes, 5th Edition*, in *Biochemistry of Lipids, Lipoproteins and Membranes, 5th Edition*, D.E. Vance and J.E. Vance, Editors. 2008. p. 1-640.
14. Henderson, F., et al., *3D DESI-MS lipid imaging in a xenograft model of glioblastoma: a proof of principle.* Scientific Reports, 2020. **10**(1): p. 1-7.
15. Aldape, K., et al., *Glioblastoma: pathology, molecular mechanisms and markers.* Acta Neuropathologica, 2015. **129**(6): p. 829-848.
16. Stummer, W., et al., *Fluorescence-guided surgery with 5-aminolevulinic acid for resection of malignant glioma: a randomised controlled multicentre phase III trial.* Lancet Oncology, 2006. **7**(5): p. 392-401.
17. Regula, J., et al., *PHOTOSENSITIZATION AND PHOTODYNAMIC THERAPY OF ESOPHAGEAL, DUODENAL, AND COLORECTAL RUMORS USING 5-AMINOLEVULINIC ACID-INDUCED PROTOPORPHYRIN-IX - A PILOT-STUDY.* Gut, 1995. **36**(1): p. 67-75.
18. Ennis, S.R., et al., *Transport of 5-aminolevulinic acid between blood and brain.* Brain Research, 2003. **959**(2): p. 226-234.
19. Hadjipanayis, C.G., G. Widhalm, and W. Stummer, *What is the Surgical Benefit of Utilizing 5-Aminolevulinic Acid for Fluorescence-Guided Surgery of Malignant Gliomas?* Neurosurgery, 2015. **77**(5): p. 663-673.
20. Hanselmann, M., et al., *Concise representation of mass spectrometry images by probabilistic latent semantic analysis.* Analytical chemistry, 2008. **80**(24): p. 9649-9658.
21. Brat, D.J. and E.G. Van Meir, *Glomeruloid microvascular proliferation orchestrated by VPF/VEGF: a new world of angiogenesis research.* The American journal of pathology, 2001. **158**(3): p. 789.
22. Rauchová, H., et al., *Hypoxia-induced lipid peroxidation in rat brain and protective effect of carnitine and phosphocreatine.* Neurochemical research, 2002. **27**(9): p. 899-904.
23. Luo, X., et al., *L-carnitine attenuates doxorubicin-induced lipid peroxidation in rats.* Free Radical Biology and Medicine, 1999. **26**(9-10): p. 1158-1165.

24. Fink, M.A., et al., *L-carnitine–mediated tumor cell protection and poor patient survival associated with OCTN2 overexpression in glioblastoma multiforme.* Clinical Cancer Research, 2019. **25**(9): p. 2874-2886.
25. Lin, H., et al., *Fatty acid oxidation is required for the respiration and proliferation of malignant glioma cells.* Neuro-oncology, 2017. **19**(1): p. 43-54.
26. Kant, S., et al., *Enhanced fatty acid oxidation provides glioblastoma cells metabolic plasticity to accommodate to its dynamic nutrient microenvironment.* Cell death & disease, 2020. **11**(4): p. 1-13.
27. Maher, E.A., et al., *Metabolism of [U-13C] glucose in human brain tumors in vivo.* NMR in biomedicine, 2012. **25**(11): p. 1234-1244.
28. Horská, A. and P.B. Barker, *Imaging of brain tumors: MR spectroscopy and metabolic imaging.* Neuroimaging Clinics, 2010. **20**(3): p. 293-310.
29. Grech-Sollars, M., et al., *Imaging and tissue biomarkers of choline metabolism in diffuse adult glioma: 18F-Fluoromethylcholine PET/CT, magnetic resonance spectroscopy, and choline kinase α.* Cancers, 2019. **11**(12): p. 1969.
30. Tamiya, T., et al., *Proton magnetic resonance spectroscopy reflects cellular proliferative activity in astrocytomas.* Neuroradiology, 2000. **42**(5): p. 333-338.
31. Podo, F., *Tumour phospholipid metabolism.* NMR in Biomedicine: An International Journal Devoted to the Development and Application of Magnetic Resonance In Vivo, 1999. **12**(7): p. 413-439.
32. Walke, A., et al., *Protoporphyrin IX Analysis from Blood and Serum in the Context of Neurosurgery of Glioblastoma*, in *Mass Spectrometry*. 2020, IntechOpen.
33. Kröger, S., et al., *Complementary molecular and elemental mass-spectrometric imaging of human brain tumors resected by fluorescence-guided surgery.* Analytical chemistry, 2018. **90**(20): p. 12253-12260.
34. Gledhill, M., *The detection of iron protoporphyrin (heme b) in phytoplankton and marine particulate material by electrospray ionisation mass spectrometry–comparison with diode array detection.* Analytica chimica acta, 2014. **841**: p. 33-43.

Chapter 4: Determining compatible histology stains for DESI-MSI lipidomic analysis

Matthew C. Gentry[1], Emrys A. Jones[2], Nicholas P. Lockyer[3], Adam McMahon[1]

[1]Wolfson Molecular Imaging Centre, Division of Informatics, Imaging and Data Sciences, University of Manchester, United Kingdom

[2]Waters Corporation, Wilmslow, United Kingdom

[3]Photon Science Institute, Depart of Chemistry, University of Manchester, United Kingdom

1. Abstract

Desorption Electrospray Ionisation Mass spectrometry imaging (DESI-MSI) is an ambient ionisation surface analysis technique used predominantly for lipidomic analysis of thin tissue sections. In a conventional mass spectrometry imaging (MSI) workflow, histology analysis is carried out after MSI to accurately link MSI and tissue features visible by histology on the same or adjacent tissue sections. Haematoxylin and Eosin (H&E) staining is the gold standard for histology analysis but renders the tissue unusable for further analysis including proteomic and lipidomic analysis by MSI methods. In instances where it is beneficial to stain tissue sections prior to analysis alternative histology stains are desired. This study investigated alternative histology stains of cresyl violet (CV), toluidine blue (TB), methylene blue (MB) and nuclear fast red (NFR) as DESI compatible stains for negative ion mode analysis tested on control mouse brain sections. These stains were selected as they have previous shown compatibility with MALDI-MS imaging and importantly have a wide range of clinical uses. Profiles of white matter (WM) and grey matter (GM) were analysed by PCA to determine differences between stained and unstained brain sections and DESI-MS

imaging of several lipids was also investigated. The DESI-MS spectra and images show little impact when tissue is stained by CV, MB and TB prior to DESI-MS imaging analysis suggesting these are compatible with DESI-MS imaging. NFR staining altered PCA analysis of WM and GM regions and suggests this is incompatible with DESI-MSI lipidomic analysis.

2. Introduction

Mass spectrometry imaging (MSI) techniques have grown in commonality in the last 20 years as a variety of different ionisation mechanisms have developed. Compared to conventional MS techniques, imaging uses an ionisation source to acquire chemical information at a number of pre-defined locations creating pixels of information, that when combined can form an image for each ion detected [1]. Imaging methods allow the visualisation of hundreds of chemical species simultaneously across a tissue section in 2D.

DESI-MSI is an ambient ionisation technique that uses a high velocity, charged stream of a solvent micro-droplets to extract and ionise biomolecules from the samples surface, with particular focus for lipid analysis [2]. A single DESI-MS imaging experiment can rapidly and simultaneously map hundreds of lipid species across a tissue section at ambient conditions. In combination with other imaging modalities such as optical imaging, histological staining, nuclear medical imaging and fluorescence, can be cross-correlated to further explore the make-up of a tissue section. Correlation of MSI data with histological features is particularly important for investigating diseases of which DESI-MSI is widely used for, particularly in oncology.

In a conventional MSI workflow thin tissue sections are cut from a sample, imaged by MSI and post-analysis histology staining carried out for correlation with the MS imaging data. Histology staining to determine tissue morphology can be carried out on the same tissue section once analysed by DESI-MSI due to its almost non-destructive sampling [3]. Combining DESI-MSI with histology data means that an extremely accurate match of *m/z* distribution to observed histological features can be made. Further histology analysis, such as immunohistochemical (IHC) staining can be incorporated on adjacent tissue sections to illicit biological features of the tissue, which can help to answer key questions raised from MS imaging data.

The gold standard for histopathology staining is the combination of haematoxylin and eoisin (H&E), which is frequently used to accompany mass spectrometry imaging analysis and used by pathologists in the diagnosis of diseased tissue. H&E staining protocols use a series of washes to prepare the sample for staining which include xylene, ethanol, and industrial methylated spirits (IMS). These are all highly non-polar chemicals and would typically be used for lipid extraction methodologies. As such, after H&E staining it is expected that the sample is unusable for further biochemical analysis by DESI-MSI. There are instances where this may be undesirable, particularly if the samples are precious or difficult to prepare for imaging.

Another instance where it would be beneficial to undertake histological analysis prior to MSI is in the analysis of diseased tissue, identifying particular regions of interest (ROIs) for MS analysis. It is also useful where a histological analysis is required for diagnostic purposes, such as in a surgical setting where intra-operative assessment of tumour biopsies is crucial [4]. Recently many mass spectrometry imaging techniques have bridged the gap from benchtop to surgical setting using the “iKnife”[5], DESI-MSI of intrasurgical smears [6] and more recently “SpiderMass”[7] and the mass spec pen [8] for real-time tissue identification. Real-time identification using novel mass spectrometry techniques is gaining momentum, particular in areas where it is difficult but imperative to determine tumour margins and tumourous areas to guide resection. In instances where these techniques are not available, conventional and well-established DESI-MS imaging can rapidly examine tissue sections in less than 10 minutes. Combining this with a rapid, DESI compatible histology stain can provide targeted DESI-MS imaging analysis to aid tissue or tumour identification based on lipid signals.

In this work we investigate the potential for histology stains other than H&E to find compatibility for DESI-MS imaging to probe whether staining can be undertaken prior to mass spectrometry imaging analysis on a single tissue section. Toluidine blue (TB), cresyl violet (CV), methylene blue (MB), nuclear fast red (NFR) and terry polychrome have shown compatibility with MALDI-MS proteomic analysis **[9]** and as such TB, CV, MB and NFR and investigated here for the analysis of lipids by DESI-MS imaging.

3. Methodology

3.1. Materials

All solvents used were purchased from Sigma-Aldrich, UK. Toluidine blue, cresyl violet and methylene blue were all purchased in powder form from Sigma-Aldrich, UK and Nuclear Fast Red was purchased as a solution in 5% aluminium sulfate. Histology stains were all made up in HPLC grade water at the recommended concentration, followed by filtration before using for staining the tissue sections.

3.2. Sample preparation

Sagittal sections were cut from a control CD-1 nude mouse brain on a LEICA CM 3050 S cryostat (Leica, UK) at 12 µm thickness and thaw mounted onto glass slides. Sagittal cut brain sections show large, clear regions of grey and white matter that can be used to extract DESI mass spectrum from. CD-1 nude mice brains were obtained from the ShARM facility at the University of Manchester [10]. Cut sections were stored at -80 ^{o}C in a parafilm sealed container until use. Before staining, tissue sections were thawed to room temperature and stained for analysis on the same day.

To investigate the effect of time on the stained sections, stained sections were analysed by DESI-MSI and placed in slide holders and either wrapped in foil to simulate dark conditions or left uncovered at ambient conditions before further DESI-MSI analysis after 24 hours.

3.3. DESI-MS Imaging

DESI-MS imaging experiments were carried out on a modified 2D DESI stage (Prosolia, Indianapolis USA) mounted onto a Xevo G2-XS quadrupole time of flight (QToF) (Waters, Wilmslow, UK) in negative and positive ion mode. Images were acquired at a spatial resolution of both 400 µm and 200 µm, over a mass range of 50-1500 and 50-1200 respectively, at 8 scans/ second with the aid of a heated collection capillary at 450 ^{o}C (Waters Research Centre, Budapest, Hungary) and a source temperature of

100 ^{o}C. Spray settings used a 98:2% Methanol: Water solvent composition at a flow rate of 1.5 µL/min delivered using a syringe pump (Harvard Apparatus Inc, Holliston, USA) with nebulising gas flow rate of 80 PSI. DESI source geometry positions were optimised prior to all imaging experiments determining maximal lipid signal extraction on control liver sections. Optimised parameter used in this work are 1.5 mm spray tip to sample surface, 6 mm sprayer to heated capillary inlet, 80^{o} sprayer impact angle with a 5^{o} collection capillary angle. Optimised capillary voltages of 1.5 kV and 1 kV were used for negative and positive ion mode respectively, with spectra acquired in sensitivity mode on the Xevo G2-XS. The mass spectrometry images shown in this chapter are from those experiments collected at 200 µm spatial resolution.

3.4. Histology

12 µm thick sections of mouse brain were stained by the methods described below in Table 10. After staining, sections were washed in de-ionised water by dipping 5-10 times until no further stain was washed from the sample. In normal microscopy practice, glass cover slips would be applied to the tissue sections to allow for high resolution images to be obtained. For this work this step was omitted as to obtain chemical information from the sample surface as is the method of analysis using mass spectrometry imaging techniques.

Table 10 - histology staining techniques used throughout this work including the protocol for washing, staining time and common uses for these stains

Stain	Protocol	Stain time	Common uses
Haematoxylin and Eosin (H&E)	Xylene wash, IMS wash (x4), Haematoxylin Stain, Eosin Stain, Xylene wash (x3)	Haematoxylin 3 min, Eosin 1 s	Routine use in histology staining for multiple sample types
Toluidine Blue (TB)	1% Toluidine Blue in aqueous, dH2O wash	5-10 s	Ischemia, renal pathology, carcinoma oral cavity [11, 12]
Methylene Blue (MB)	1% Methylene Blue in aqueous, dH2O wash	5-10 s	Bacteriology, neuronal structures [13]
Cresyl Violet (CV)	0.5% Cresyl Violet in aqueous, dH2O wash	45 s	Neuronal structures in the brain and spinal cord [14]

Nuclear Fast Red (NFR)	0.1% in 5% aqueous aluminium sulfate, dH2O wash	60 s	Rapid nuclear staining

3.5. Data analysis

DESI-MS imaging data was processed and visualised in HDImaging v1.5 (Waters, UK) for the top 1000 peaks, with spectra normalised to the total ion current (TIC). Regions of interest, each of 16 pixels in size, were extracted from the 200 µm spatial resolution DESI-MS imaging results from each tissue section. Regions were selected from both the grey and white matter components, determined by the distribution of *m/z* 834.52 and 888.62 which are known markers for grey and white matter respectively [15, 16] and which show the expected distribution of each component within brain. Each ROI was extracted as an individual MassLynx file that averages the mass spectra from each pixel within the ROI. Spectra extracted as ROIs from the MS images were visualised in MassLynx (Waters, Milford, USA). Principal component analysis (PCA) was carried out using Abstract Model Builder (AMX) (Waters Research Centre, Budapest, Hungary) over the mass range of 100-950 *m/z* with a 0.1 bin width. Spectra were normalised to TIC and lock-massed to *m/z* 885.5499 (PI (38:4)). PCA models were built with 5 principal components.

3.6. Altered MS Imaging workflow

The altered MS imaging workflow is described in Figure 57. Tissue sections are cut and stained, prior to DESI-MS imaging analysis.

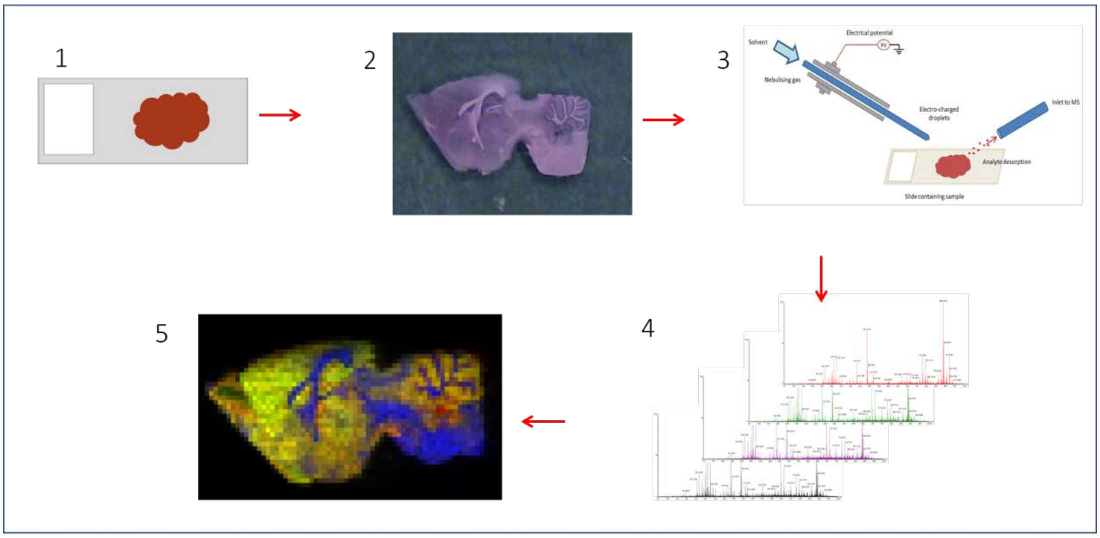

Figure 57 – a schematic of the suggested altered MSI workflow. Histology staining is carried out prior to DESI imaging rather than post-imaging. 1. Sample preparation with tissue section mounted onto glass slides. 2. Histology staining 3. DESI-MS imaging acquisition 4. Mass spectrum generated at hundreds of pre-defined locations on the tissue surface called pixels. 5. DESI-MS imaging distribution of selected m/z values from the overall spectra maps the intensity of this species across the entire tissue section. Multiple MS ion images can be overlaid to provide a comprehensive overview of the tissue section.

4. Results and Discussion

Histology staining of mouse brain sections was undertaken according to the methods in Table 10 followed by DESI-MS imaging of the entire brain section. ROIs were extracted from grey matter (GM) and white matter (WM) regions to investigate any differences in the DESI-MSI spectra between stained and unstained sections. DESI-MS images were further compared to assess the compatibility of these histology stains in the DESI-MSI workflow.

4.1. Lipid imaging by DESI-MS imaging of H&E stained brain section

The spectra obtained by DESI-MS imaging of H&E stained section was compared to that of an unstained brain section, Figure 58 A and C.

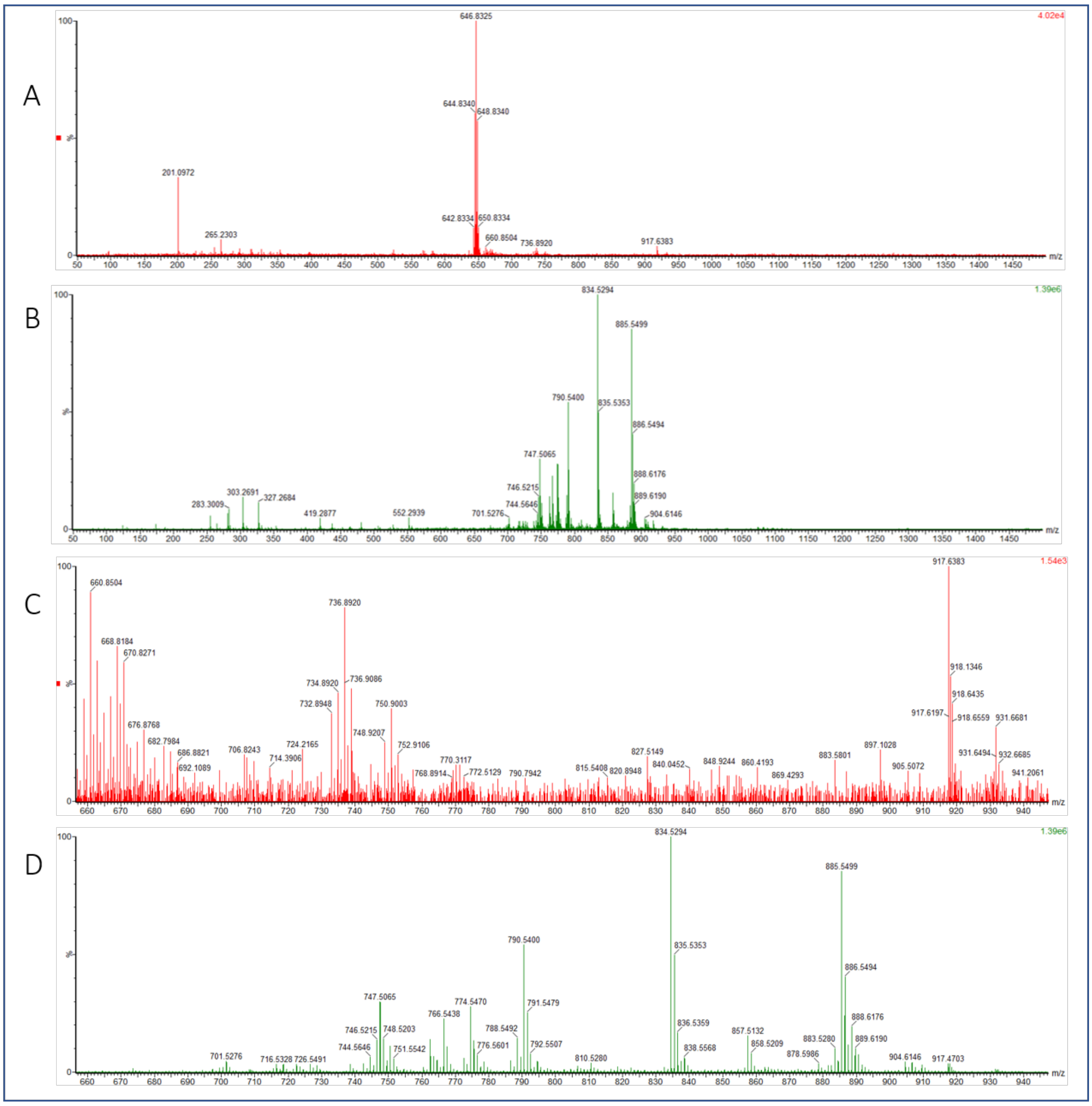

Figure 58 – H&E staining of tissue sections is incompatible with DESI-MS imaging. Extracted DESI-MS spectra from H&E stained brain (A) compared to unstained brain section (B). The H&E spectra is absent of lipid species in the m/z 650 – 900 range (C) which contain highly abundant phospholipids in the spectra of the unstained tissue section (D).

The 600 to 950 mass to charge (*m/z*) range in unstained brain spectra is abundant with phospholipid species observed by DESI-MS which are ionised as singularly charged molecular species. The observed *m/z* values in DESI-MS spectra are therefore equivalent to the molecular ion weight, giving a mass range of 600 to 900 Da where the majority of the DESI-MS species are detected. The unstained brain spectra (Figure 58 B and C) show large numbers of phospholipids in these regions as expected due to the high lipid content of the brain. DESI-MS also favours the analysis of smaller molecular species in the 100 to 400 *m/z* range, covering fatty acid species which ionise in negative ion mode and metabolites which are typically less than 200 Daltons in weight. The spectra obtained from the H&E stained image show none of the corresponding molecules observed in the control brain tissue section, over the full mass range and also in the 600 – 900 *m/z* region. Samples already stained by H&E are unusable for further MS analysis. This is due to multiple wash steps involved in the staining process using organic solvents which strip away surface lipids, and any chemical information obtainable by DESI-MSI, an observation also observed for protein analysis with MALDI MSI [17]. A typical imaging workflow uses adjacent sections that are stained and overlayed with the MS images to obtain spatial resolved *m/z* distributions. However, in instances with precious samples or samples for intra-operative analysis, a compatible stain is desirable for compatibility with DESI-MS lipid imaging.

4.2. Compatibility of alternative histology stains with lipid imaging by DESI-MS

DESI-MS images were acquired in negative ion mode for an unstained brain tissue section, acting as a control, and compared to brain sections stained by toluidine blue (TB), methylene blue (MB), cresyl violet (CV) and nuclear fast red (NFR). Spectra were extracted from each stained tissue section, Figure 59.

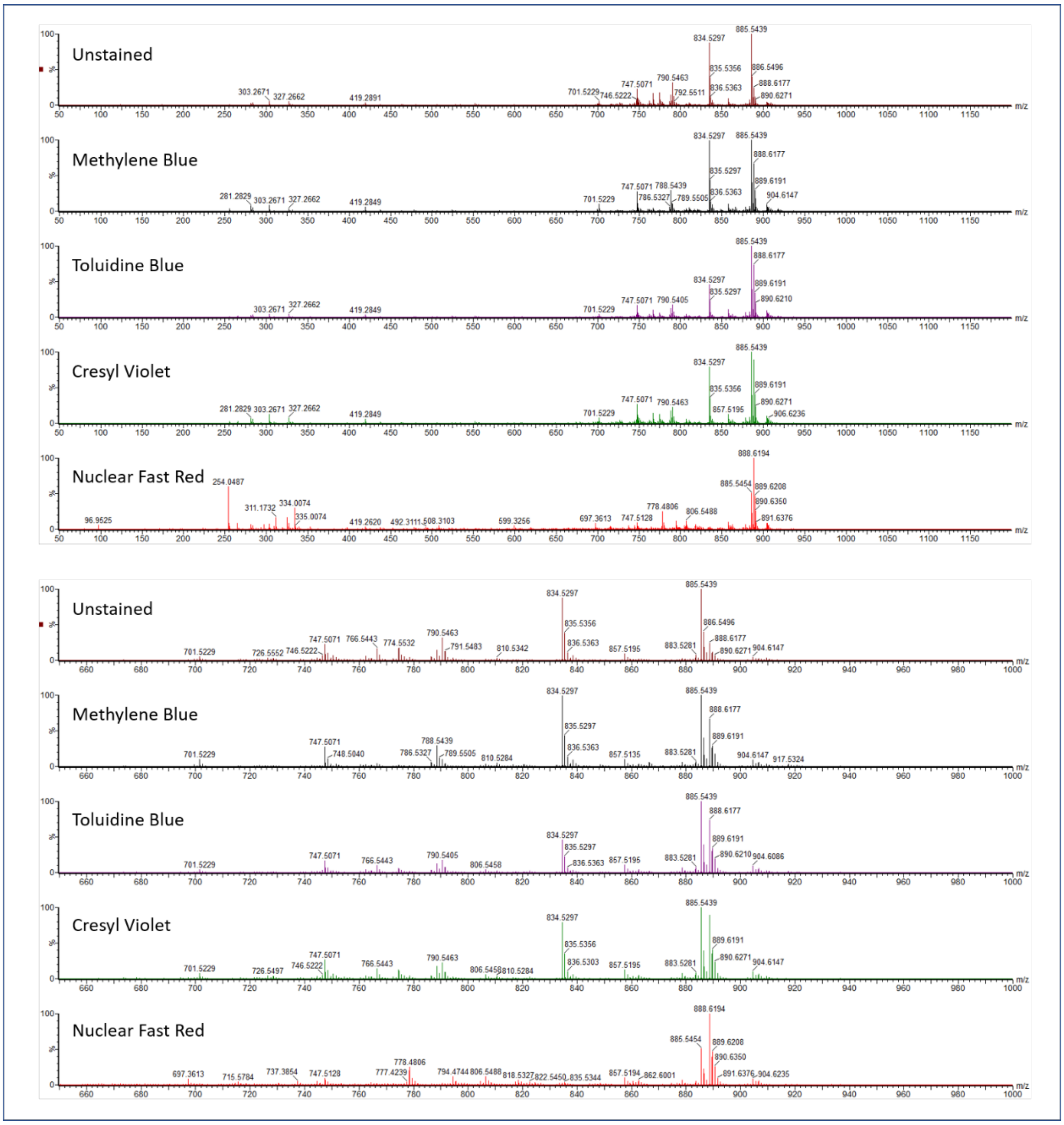

Figure 59 – Negative ion mode DESI-MS spectra from unstained brain section compared to MB, TB, CV and NFR stained brain tissues. Top 5 spectra show the full mass range 50-1500 m/z and the bottom 5 spectra are zoomed into the mass range 650 -1000

The most abundant molecules in the negative ion DESI-MS mice brain spectra are *m/z* 834.53 a known marker of grey matter, *m/z* 888.62 a key lipid species in white matter and *m/z* 885.54 which is highly abundant in mammalian tissues. These species are determined by accurate mass and prior DESI-MS analysis [16] as PS 40:6, Sulfatide 36:1 and PI 38:4 respectively and are highly abundant in all extracted brain spectra. Comparing the average DESI-MS spectra from each stained tissue section, the lipid signals appear unaffected where the tissue section have been stained prior to MS analysis. The full range mass spectra from the tissue of MB, TB and CV all closely match those of the unstained brain section.

To further investigate the compatibility of each stain with DESI-MS imaging analysis, ROIs from the grey matter (GM) and the white matter (WM) were extracted from each section and PCA was undertaken. For each histology stain, GM and WM from the stained sections are shown as red spectra and are compared to the unstained sections shown as green spectra, Figure 60, Figure 62, Figure 65, and Figure 67. The PCA results from the analysis of WM and GM are shown for each stain, Figure 61, Figure 63, Figure 66, and Figure 68. PCA is a multivariate analysis tool routinely adopted for MSI analysis, to determine differences between spectra from different samples as well as different regions within single samples.

Histology stains that are compatible with DESI-MS imaging will have little impact on the overall mass spectra, as well as not significantly altering the interpretation of the data based on PCA.

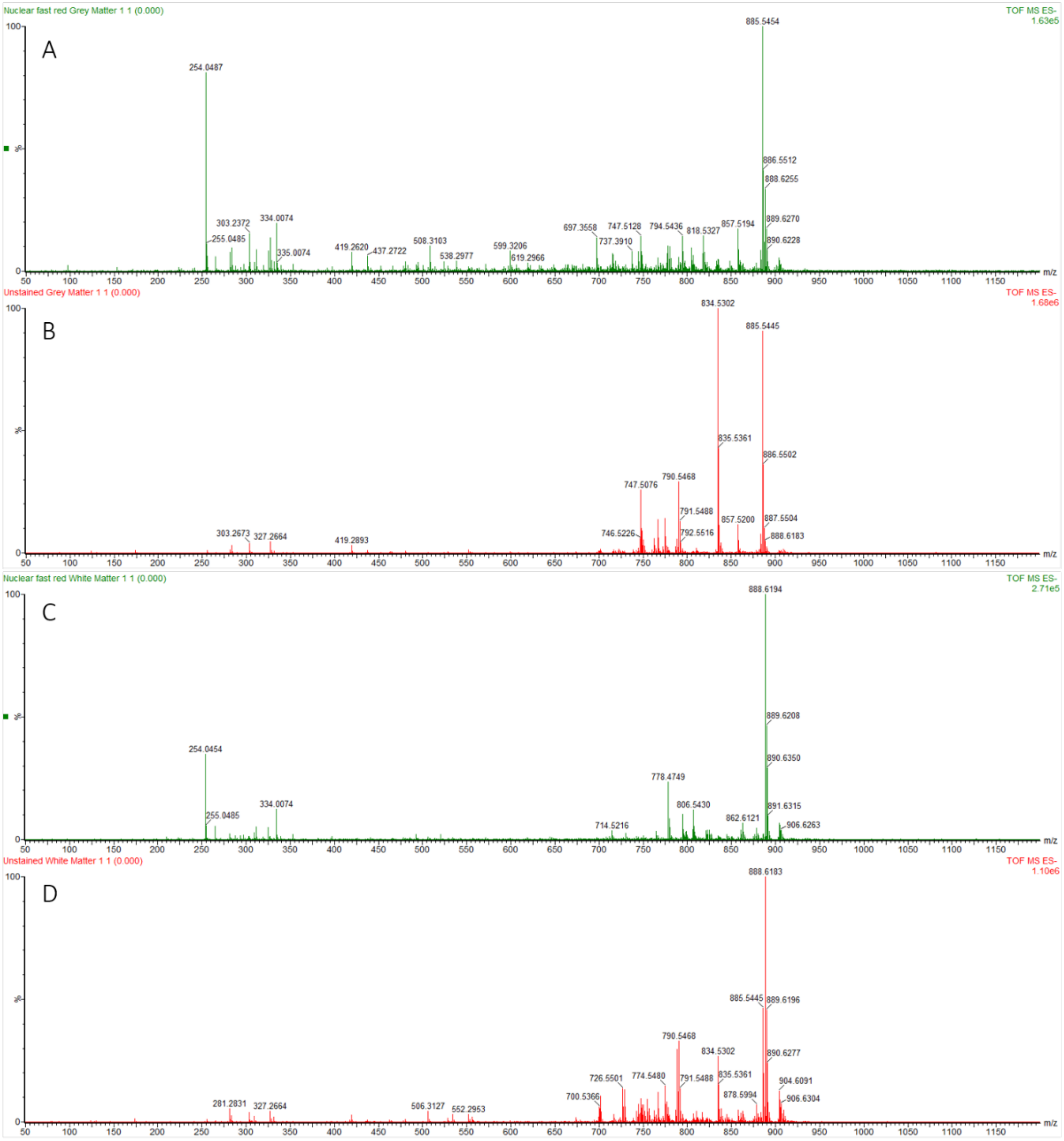

Figure 60 – Effect of nuclear fast red (NFR) tissue staining on the lipid profiles of grey matter and white matter is assessed by DESI-MS negative ion imaging. Mass spectra are the average pixel spectra from a single ROI extracted from the 400 µm DESI-MS imaging data. DESI-MS spectra are extracted and shown for A – NFR grey matter, B – unstained grey matter, C - NFR white matter, D – unstained white matter. Differences in the lipid spectra from NFR stained grey matter to unstained grey matter (spectrum B) can be seen, with m/z 834.52 diminished. Novel molecular species at m/z 254 and 334 are observed in the NFR grey and white matter spectra.

The spectra of NFR show that most of the expected phospholipid's species are detected, but *m/z* 834.52 is diminished. New molecular species at *m/z* 254 and 334 also only appear in the NFR stained brain spectra for both GM and WM.

]

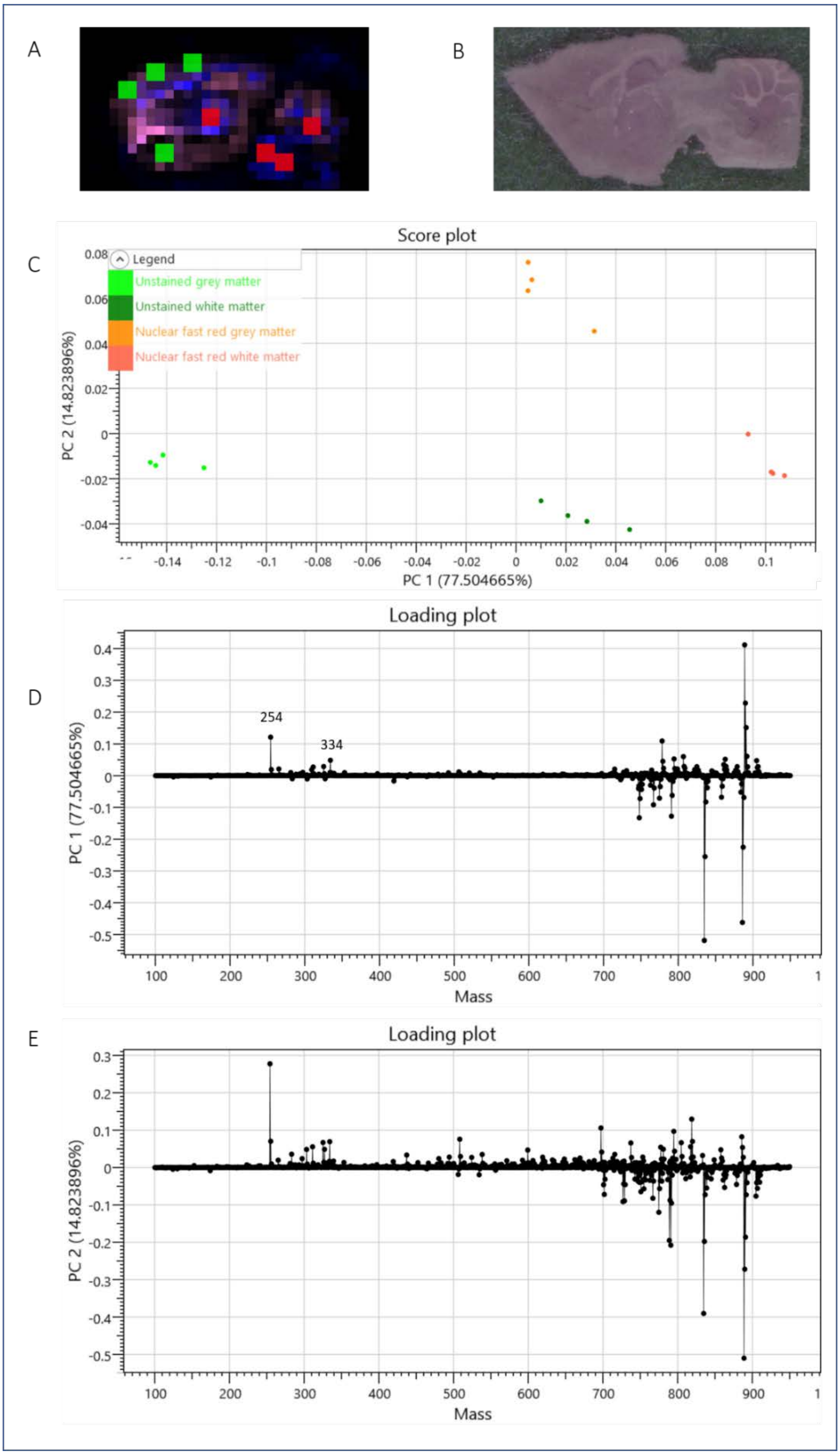

Figure 61 – PCA of DESI-MS data from nuclear fast red (NFR) stained and unstained brain tissue sections. Each dot on the PCA score plot refers to one ROI extracted from the NFR DESI-MS image (A), alongside the stained brain image (B). Overlaying m/z 834.52 and m/z 888.62 allows grey matter (pink) and white matter (blue) regions to be discriminated and DESI-MS spectra of each extracted for PCA analysis. Resultant score plot of principal component 1 v principal component 2 (C) and extracted loading plots of principal component 1 (D) and principal component 2 (E). PCA results separates WM and GM on PC 1 (contribution 77.5%) and PC 2 separates NFR GM from the WM

spectra and GM of unstained brain (contribution of 14.8%) implying that largest variance in the data is between the different brain regions rather than the staining.

The PCA plot for NFR (Figure 61), shows that principal component (PC) 1 describes 77.5% of the variance of the data and PC 2 14.8% of the data. In this analysis, PC 1 separates the unstained WM, NFR WM and NFR GM species from unstained GM, whilst PC 2 separates NFR GM from the rest. The *m/z* species at *m/z* 254 and 334 are positively weighted for PC 1, with *m/z* 254 also having the highest positive weighting in PC 2.

The *m/z* values of 254 and 334 effecting the PC score and loading plots are attributed to the staining molecules of NFR. NFR exists as a sodiated species, with the cation binding to the negatively charged sulfate group of the molecule. When analysed by DESI-MS the molecular species loses the sodium ion and exists as a negatively charged molecule, observed at *m/z* 334, and further the loss of sulfate moiety corresponds to the molecular species observed at *m/z* 254.

The molecular species responsible for CV, MB and TB are positively charged species, and are subsequently detected in the positive ion mode DESI-MS analysis (data not shown). As such it is expected that the negative ion mode spectra extracted from the stained sections should show little difference from the unstained sections.

The MS spectra of CV stained and unstained brains are compared, Figure 62 and Figure 63.

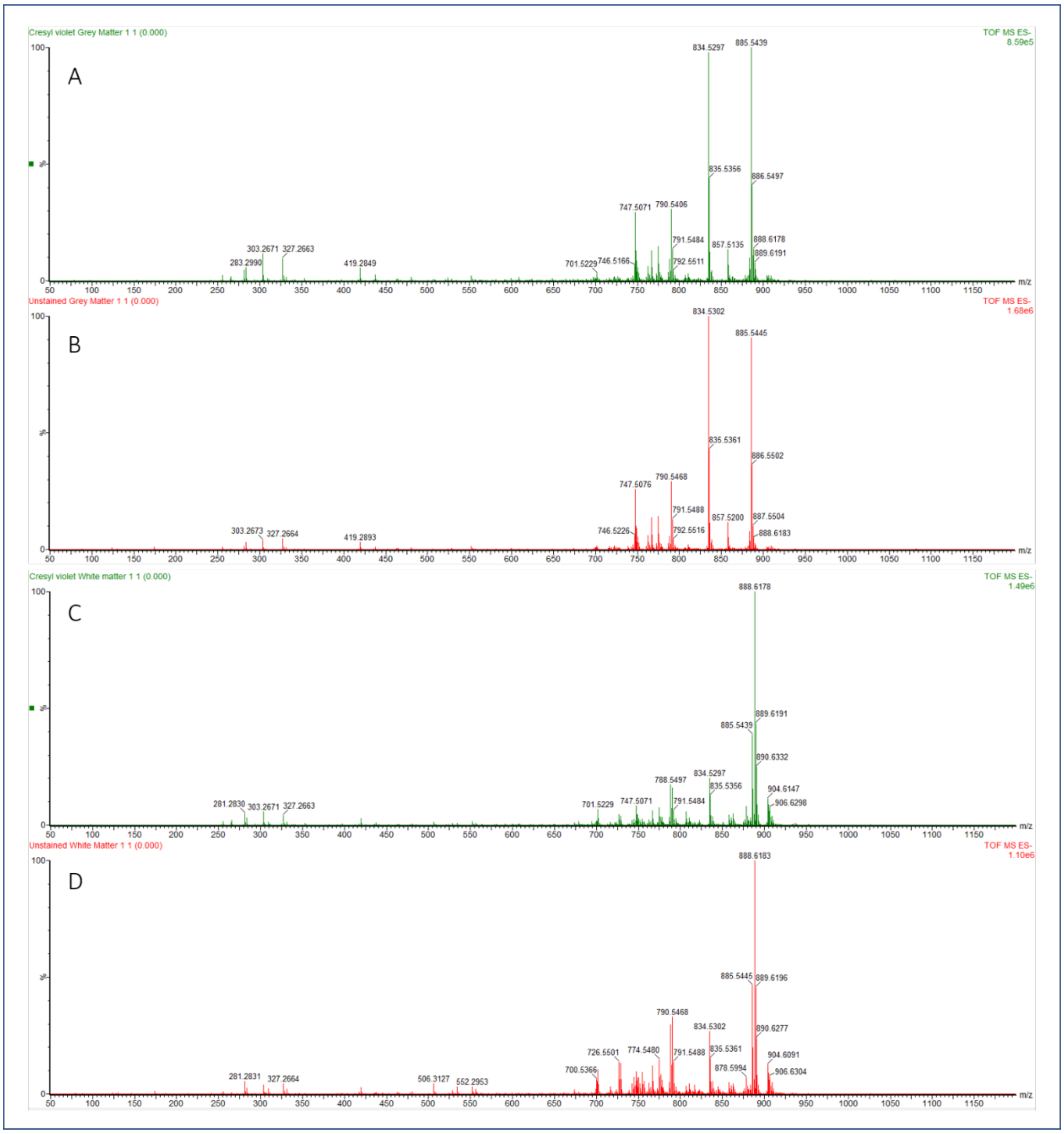

Figure 62 – Effect of cresyl violet (CV) tissue staining on the lipid profiles of grey matter and white matter is assessed by DESI-MS negative ion imaging. Mass spectra are the average pixel spectra from a single ROI extracted from the 400 µm DESI-MS imaging data. DESI-MS spectra are extracted and shown for A – CV grey matter, B – unstained grey matter, C - CV white matter, D – unstained white matter Differences in the lipid spectra from NFR stained grey matter to unstained grey matter (spectrum B) can be seen, with m/z 834.52 diminished. Novel molecular species at m/z 254 and 334 are observed in the NFR grey and white matter spectra

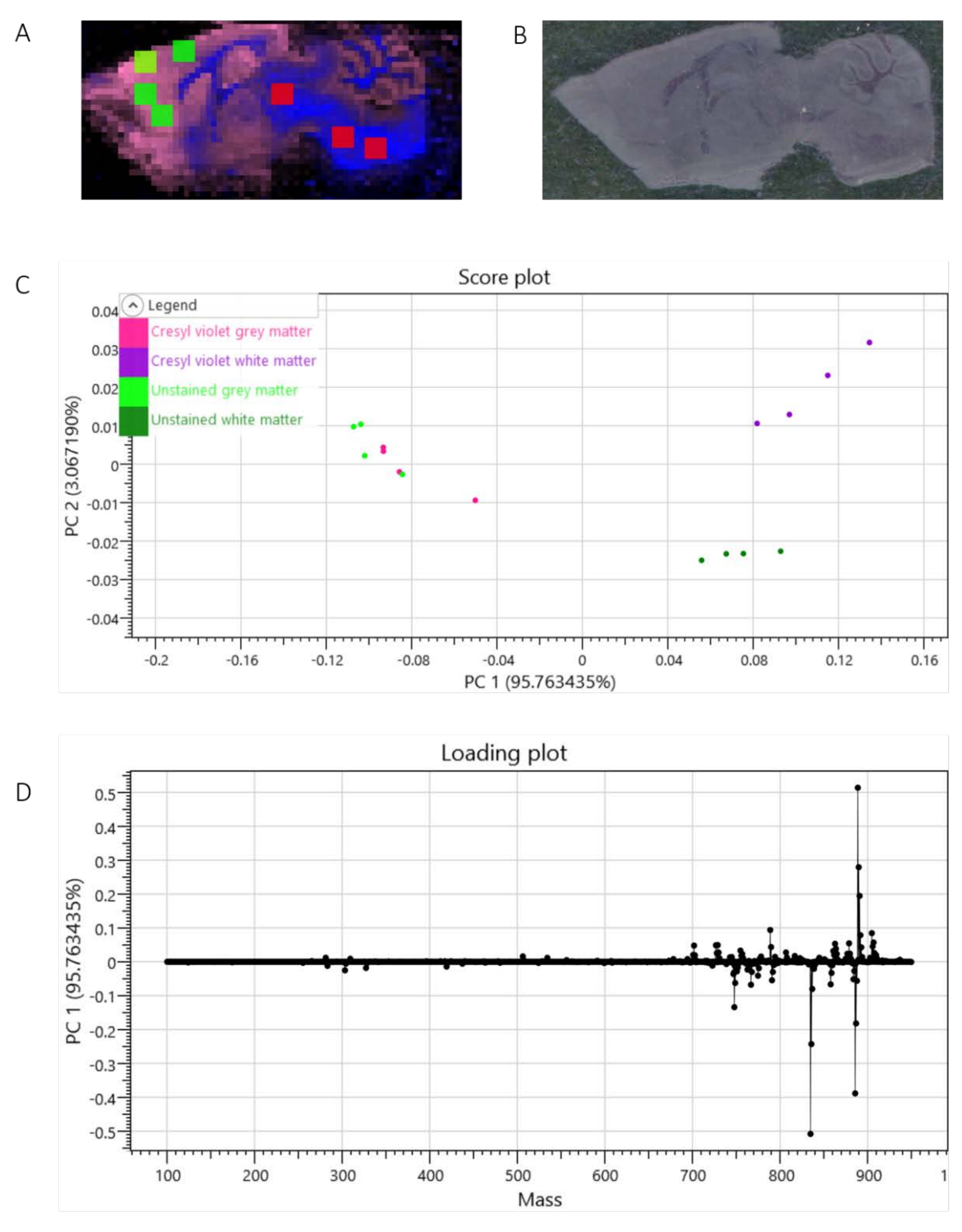

Figure 63 – PCA of DESI-MS data from nuclear fast red (CV) stained and unstained brain tissue sections. Each dot on the PCA score plot refers to one ROI extracted from the NFR DESI-MS image (A), alongside the stained brain image (B). Overlaying m/z 834.52 and m/z 888.62 allows grey matter (pink) and white matter (blue) regions to be discriminated and DESI-MS spectra of each extracted for PCA analysis. Resultant score plot of principal component 1 v principal component 2 (C) and extracted loading plots of principal component 1 (D) and principal component 2 (E). PCA results separates WM and GM on PC 1 (contribution 95.7%) and PC 2 separates the respective GM and WM spectrum from the stained and unstained sections (contribution 3.1%). PCA implies the largest differences are observed between GM and WM, and that staining the tissue has little effect on the spectra produced.

The PCA model built from CV spectra has principal component weightings of 95.76% and 3.07% for PC 1 and PC 2 respectively. The PCA plot in Figure 63 C shows a high similarity between the grey matter spectra of the stained and unstained sections with the spectra barely separated on PC 2, whereas the white matter spectra are separated on this component.

CV is used predominantly by neurobiologists for the staining of Nissl substances within the neurons in the brain and spinal cord [14]. Neurons are the key components of white matter in the brain, where bundles of neurons make up the white matter tracts and key WM features such as the corpus callosum. The preferential staining of white matter using a CV stain, may explain the results shown here. Although there is little difference between the spectra from the stained and unstained WM, as expressed by the weightings of the PCA, this observation may be important if CV staining and DESI-MS imaging is used for the analysis of white matter diseases.

Thus far, ROIs were extracted from the cerebral cortex and the white matter tracts in the midbrain to represent the WM and GM regions, however there are many finer GM and WM structures within the mouse brain. For both grey and white matter, ROIs from 3 distinct regions were selected and shown in a further principal component analysis, Figure 64 A. The grey matter was represented by the cerebral cortex, hypothalamus and cerebellum, whilst the white matter regions covered two regions of white matter tracts, in the midbrain and the cerebellum areas, as well as the corpus callosum.

PCA was run twice; first grouping all samples together as either GM or WM and subsequently, separating GM and WM out into the individual regions mentioned above. The score plots of PC 1 v PC 2 for each model are shown alongside the PC 1 loadings, Figure 64.

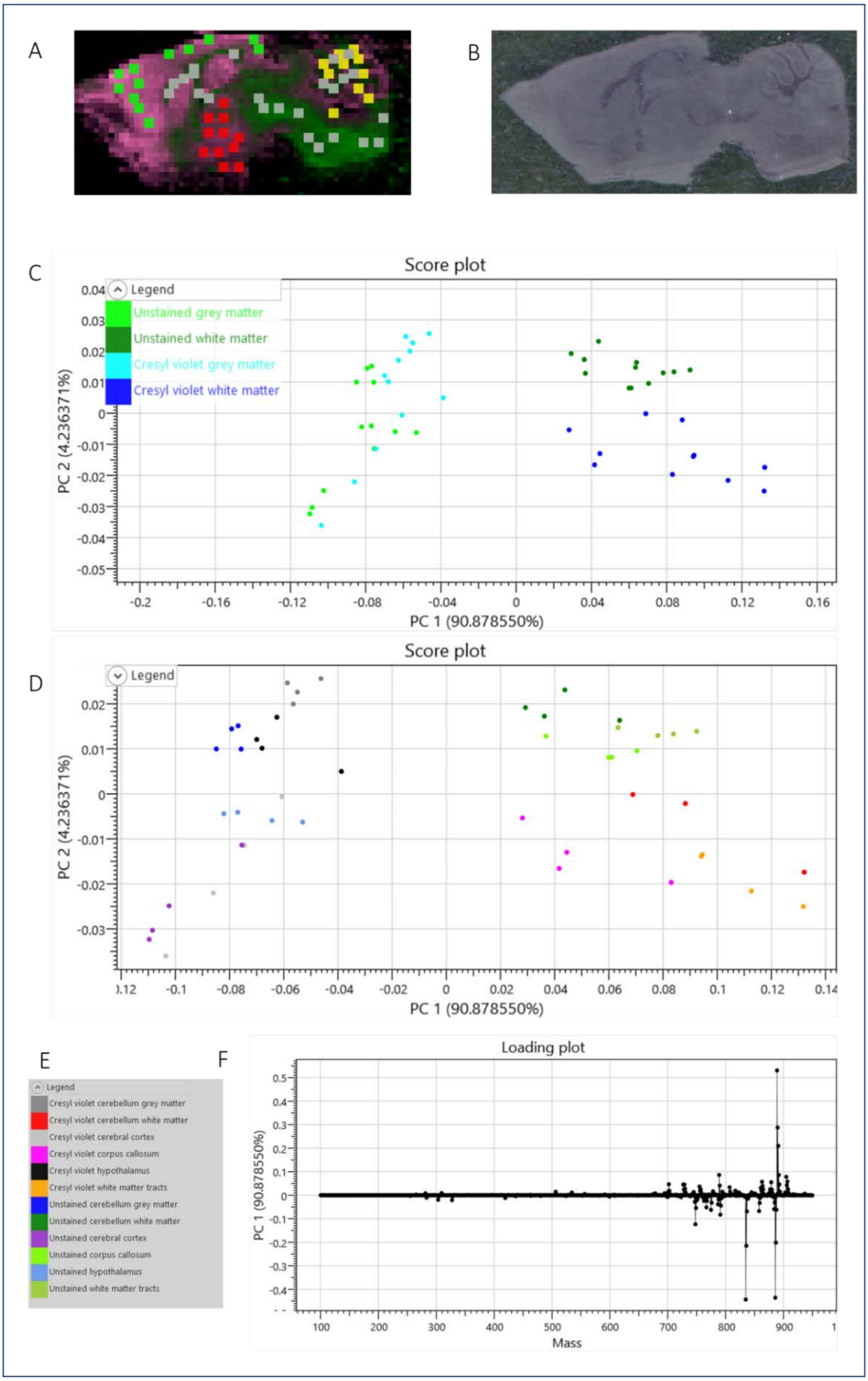

Figure 64 – PCA of DESI-MS data from nuclear fast red (CV) stained and unstained brain tissue sections with increased number of analysed regions. Each dot on the PCA score plot refers to one ROI extracted from the NFR DESI-MS image (A), alongside the stained brain image (B). Overlaying m/z 834.52 and m/z 888.62 allows grey matter (pink) and white matter (blue) regions to be discriminated and DESI-MS spectra extracted from ROIs in; cerebral cortex (green), hypothalamus (red), cerebellum (yellow) and white matter tracts (grey). Resultant score plot of principal component 1 v principal component 2 with; spectra classified as GM or WM (C) and DESI-MS spectra

further segmented to include GM regions (D), with sample identifier (E). Extracted loading plots of principal component 1 (F). Additional GM features and ROIs from more WM areas do not affect the separation and results shown in Figure 59 (add link), with GM and WM spectra separated by PC 1 (contribution 90.9%) and PC 2 separates the respective GM and WM spectrum from the stained and unstained sections (contribution 4.2%).

In the PCA model analysing multiple regions within the grey and white matter classes, PC 1 has a weighting of 90.88%. As previously observed and seen here, PC 1 separates the GM and WM regions preferably over any spectral differences between the stained and unstained brains. Increasing the number of regions has little impact on the PC loading weightings with PC 1 accounting for 90.88% with multiple GM and WM regions, compared to 95.76% with a single GM and WM region.

Distinct grey and white matter regions are known to show greater abundances of *m/z* values and combining multiple *m/z* species from the white and grey matter regions can build up a full understanding of the tissue spectra. Explored later in 4.4.

For the comparison of TB and MB stained brain sections, ROIs from the cerebral cortex and white matter tracts from the midbrain are compared and analysed by PCA, Figure 65 - Figure 68.

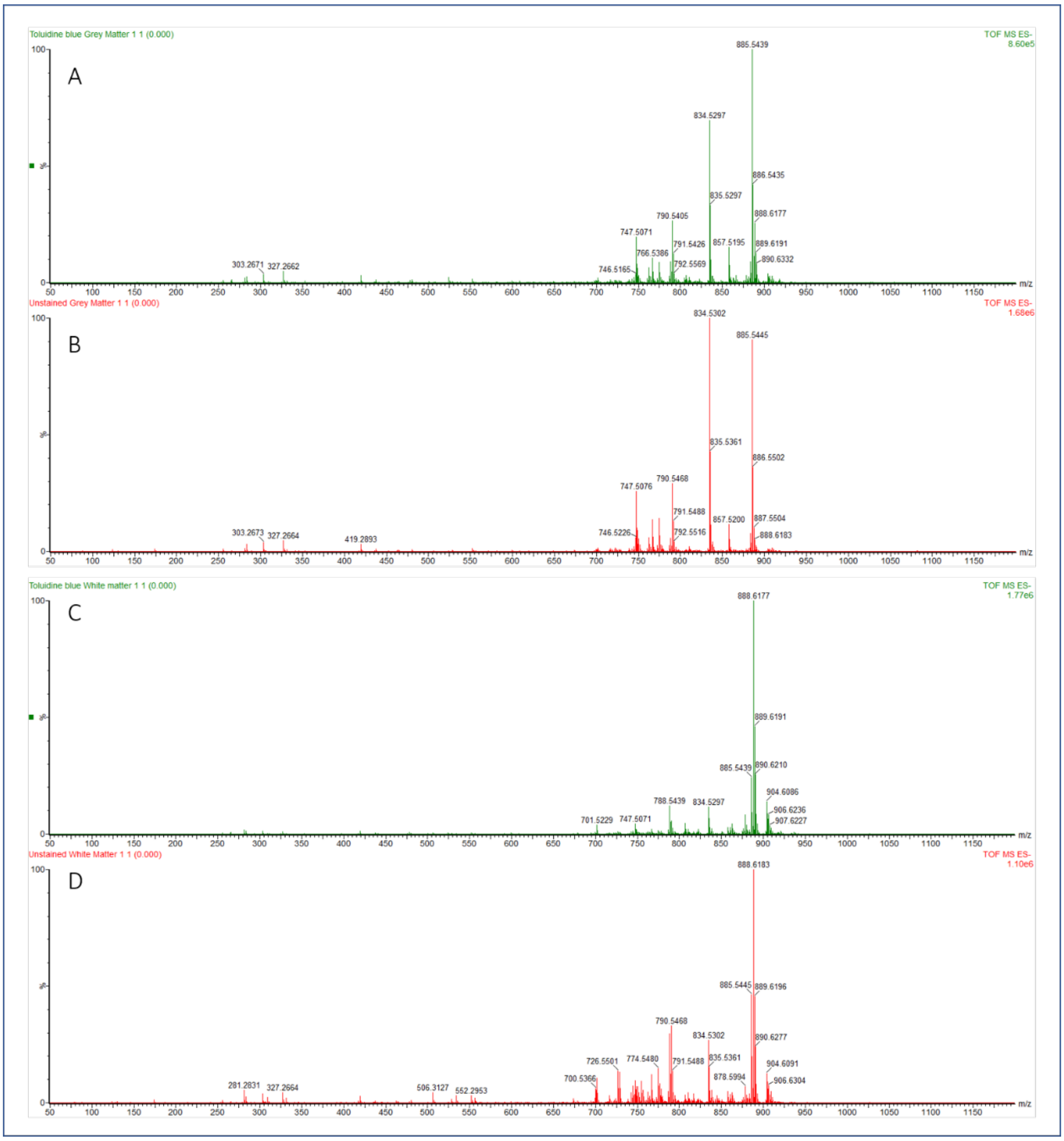

Figure 65 – Effect of toluidine blue (TB) tissue staining on the lipid profiles of grey matter and white matter is assessed by DESI-MS negative ion imaging. Mass spectra are the average pixel spectra from a single ROI extracted from the 400 µm DESI-MS imaging data. DESI-MS spectra are extracted and shown for A – TB grey matter, B – unstained grey matter, C - TB white matter, D – unstained white matter. No observable differences can be seen in the lipid spectra from TB stained to unstained grey or white matter, implying the staining of the tissue sections does not affect the DESI-MS lipid profiles

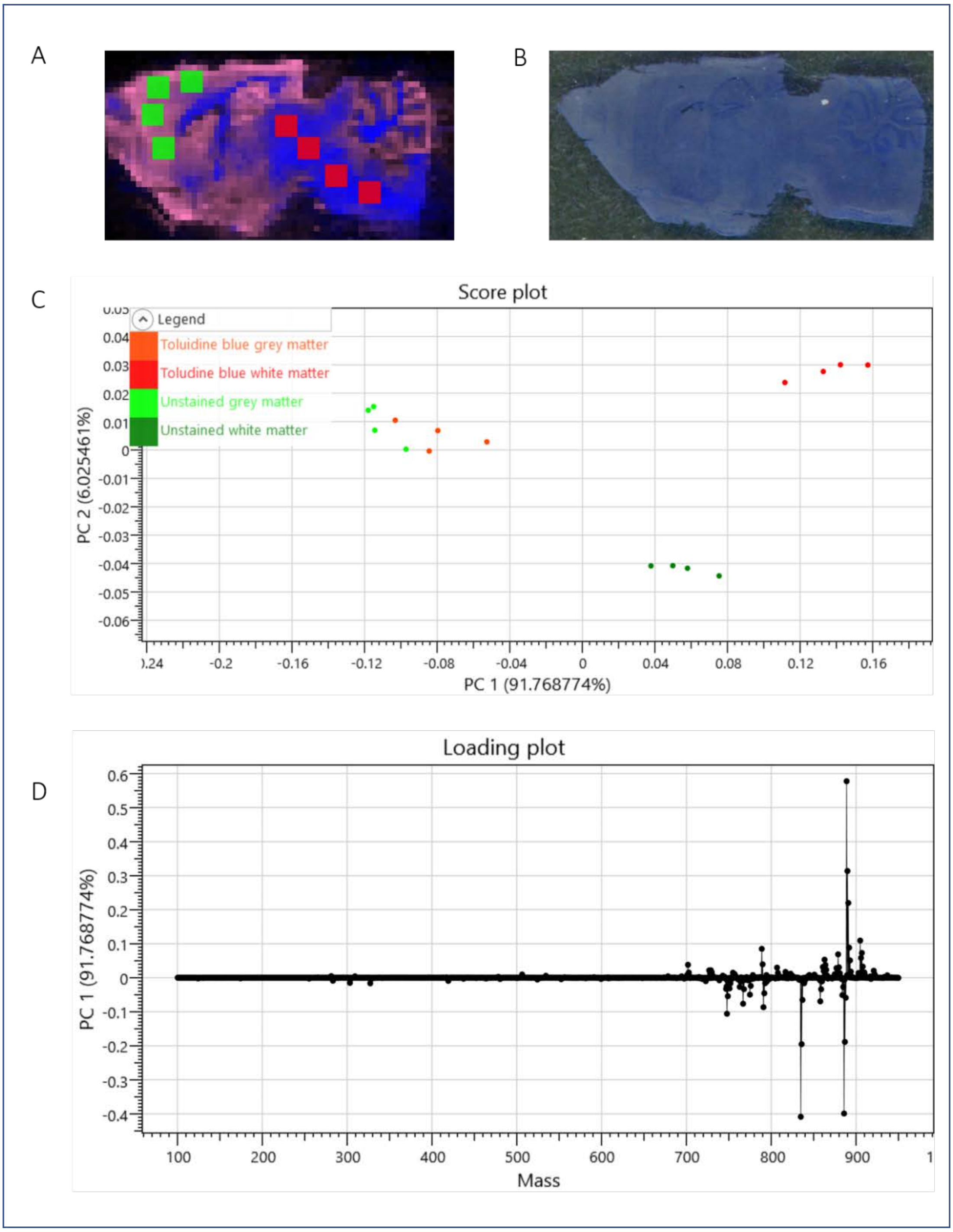

Figure 66 – PCA of DESI-MS data from toluidine blue (TB) stained and unstained brain tissue sections. Each dot on the PCA score plot refers to one ROI extracted from the TB DESI-MS image (A), alongside the stained brain image (B). Overlaying m/z 834.52 and m/z 888.62 allows grey matter (pink) and white matter (blue) regions to be discriminated and DESI-MS spectra of each extracted for PCA analysis. Resultant score plot of principal component 1 v principal component 2 (C) and extracted loading plots of principal component 1 (D). PCA results separates WM and GM on PC 1 (contribution 91.8%) and PC 2 separates the unstained WM spectrum from the stained and unstained sections (contribution 6.0%). PCA implies the largest differences are observed between GM and WM, and that staining the tissue has little effect on the spectra produced

PC 1 and PC 2 of the TB PCA model weight for 91.77% and 6.03% of the variance, respectively. PC 1 separates the WM and GM spectra, whilst PC 2 separates the individual stains from each other. Molecular ions *m/z* 834.5 and 885.5 are negatively weighted in PC 1, representing the GM, whilst *m/z* 888.6 is positively weighted, describing the white matter spectra. Visual comparison of the spectra in Figure 65 representing GM and WM from each region corroborates these results.

A high percentage variance in PC 1 and low percentage variance of PC 2, show the greatest differences in the mass spectra are between the GM and WM regions, rather than between the stained and unstained sections, confirming the minimal effect that staining sections prior to DESI-MS imaging has on the acquired spectra.

PCA of MB stained brain sections match those results observed from the analysis of TB and CV stained brain sections.

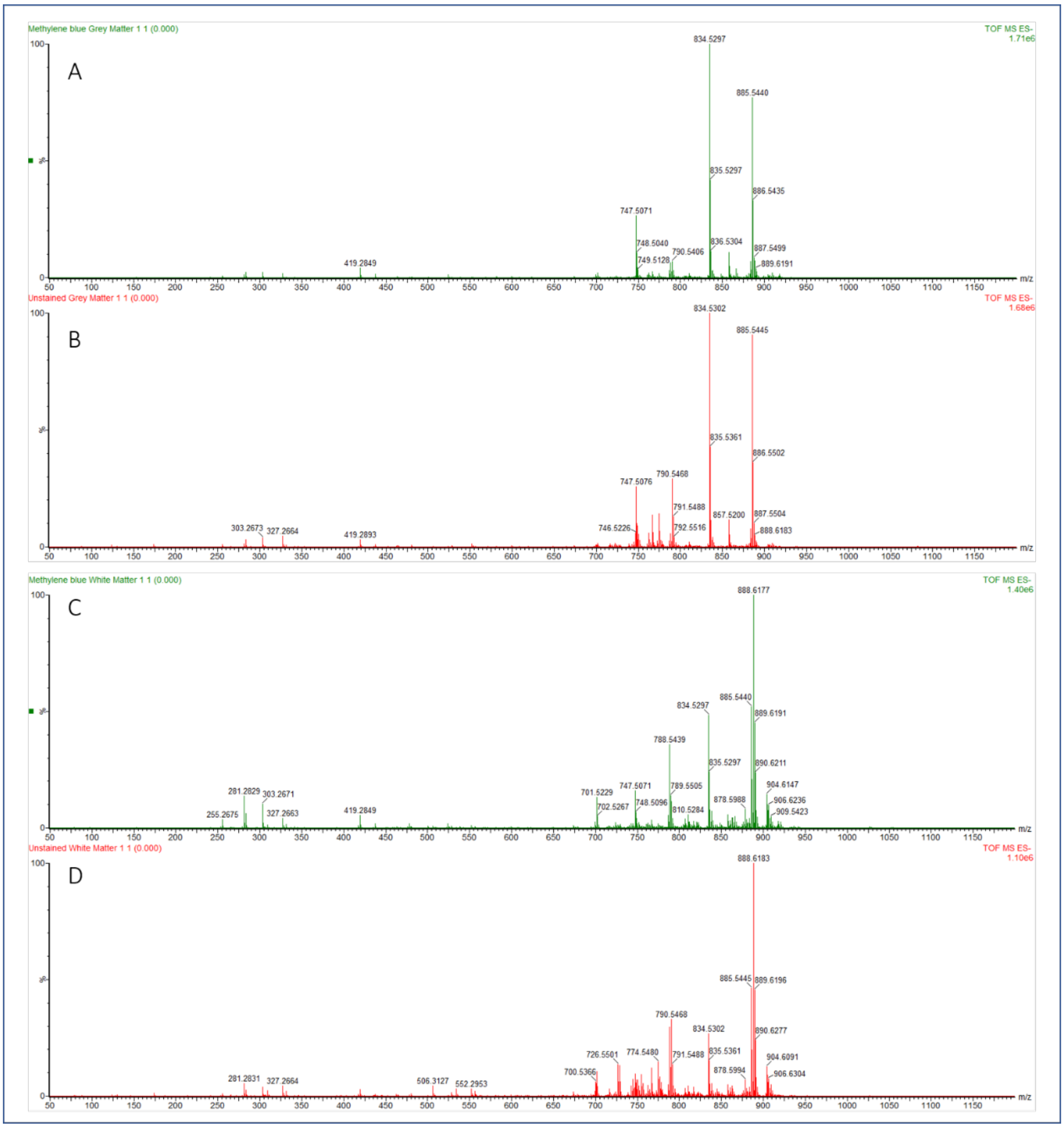

Figure 67 – Effect of methylene blue (MB) tissue staining on the lipid profiles of grey matter and white matter is assessed by DESI-MS negative ion imaging. Mass spectra are the average pixel spectra from a single ROI extracted from the 400 µm DESI-MS imaging data. DESI-MS spectra are extracted and shown for A – MB grey matter, B – unstained grey matter, C - MB white matter, D – unstained white matter. No observable differences can be seen in the lipid spectra from MB stained to unstained grey or white matter, implying the staining of the tissue sections does not affect the DESI-MS lipid profiles

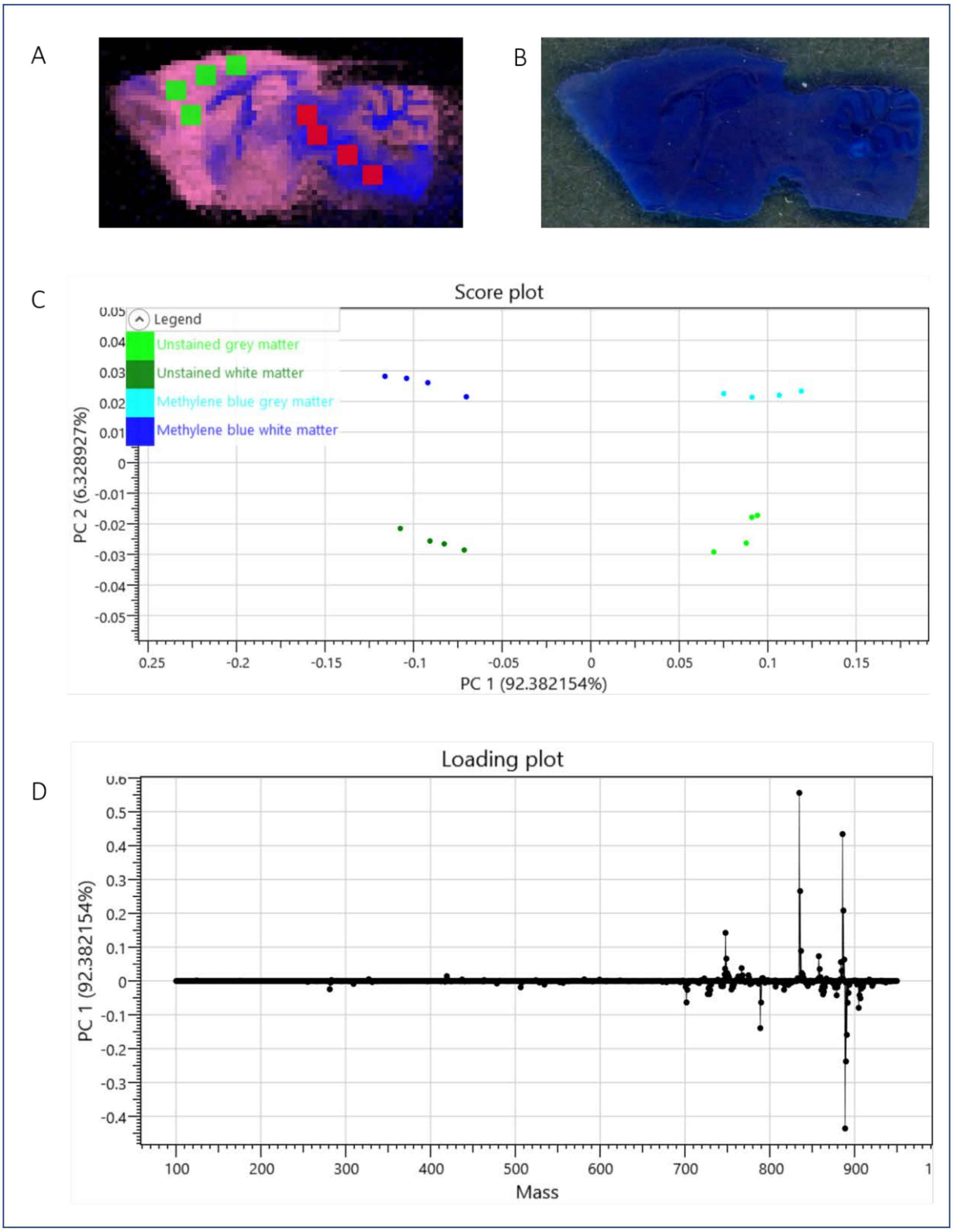

Figure 68 – PCA of DESI-MS data from methylene blue (MB) stained and unstained brain tissue sections. Each dot on the PCA score plot refers to one ROI extracted from the TB DESI-MS image (A), alongside the stained brain image (B). Overlaying m/z 834.52 and m/z 888.62 allows grey matter (pink) and white matter (blue) regions to be discriminated and DESI-MS spectra of each extracted for PCA analysis. Resultant score plot of principal component 1 v principal component 2 (C) and extracted loading plots of principal component 1 (D). PCA results separates WM and GM on PC 1 (contribution 92.4%) and PC 2 separates the unstained WM spectrum from the stained and unstained sections (contribution 6.3%). PCA implies the largest differences are observed between GM and WM, and that staining the tissue has little effect on the spectra produced

PC 1 and PC 2 of the MB PCA model show weightings of 92.38% and 6.33% of the variance, respectively. Positively weighted masses in PC explains the GM, whilst the negative loadings described the WM spectra which is the opposite to the loadings observed for CV and TB. The main molecular identifiers for GM and WM are otherwise unaffected with *m/z* 834.5 and 885.5 heavily positively weighted in PC 1 and *m/z* 888.6 is negatively weighted. As opposed to previous observations, the GM ROIs are fully separated by PC 2, whereas previously for CV and TB these are clustered together.

The PCA results produced above for TB and MB stains reveal similar results to those observed with CV. PC 1 again explains most of the variance in the data, separating the GM and WM spectra, with PC 2 separating out the stained from the unstained data. This further suggests that staining sections with TB and MB prior to DESI-MSI data acquisition does not significantly affect the quality of the spectra produced.

Further PCA was carried out combing all ROIs from grey and white matter regions of the unstained and NFR, CV, MB and TB stained tissue sections, Figure 69.

The number of principal components selected should cover around 70% of the variance in the data, or the PCA would be rejected [18]. In this analysis PC 1 accounts for at least 90% of the variation in the data confirming the validity of the models.

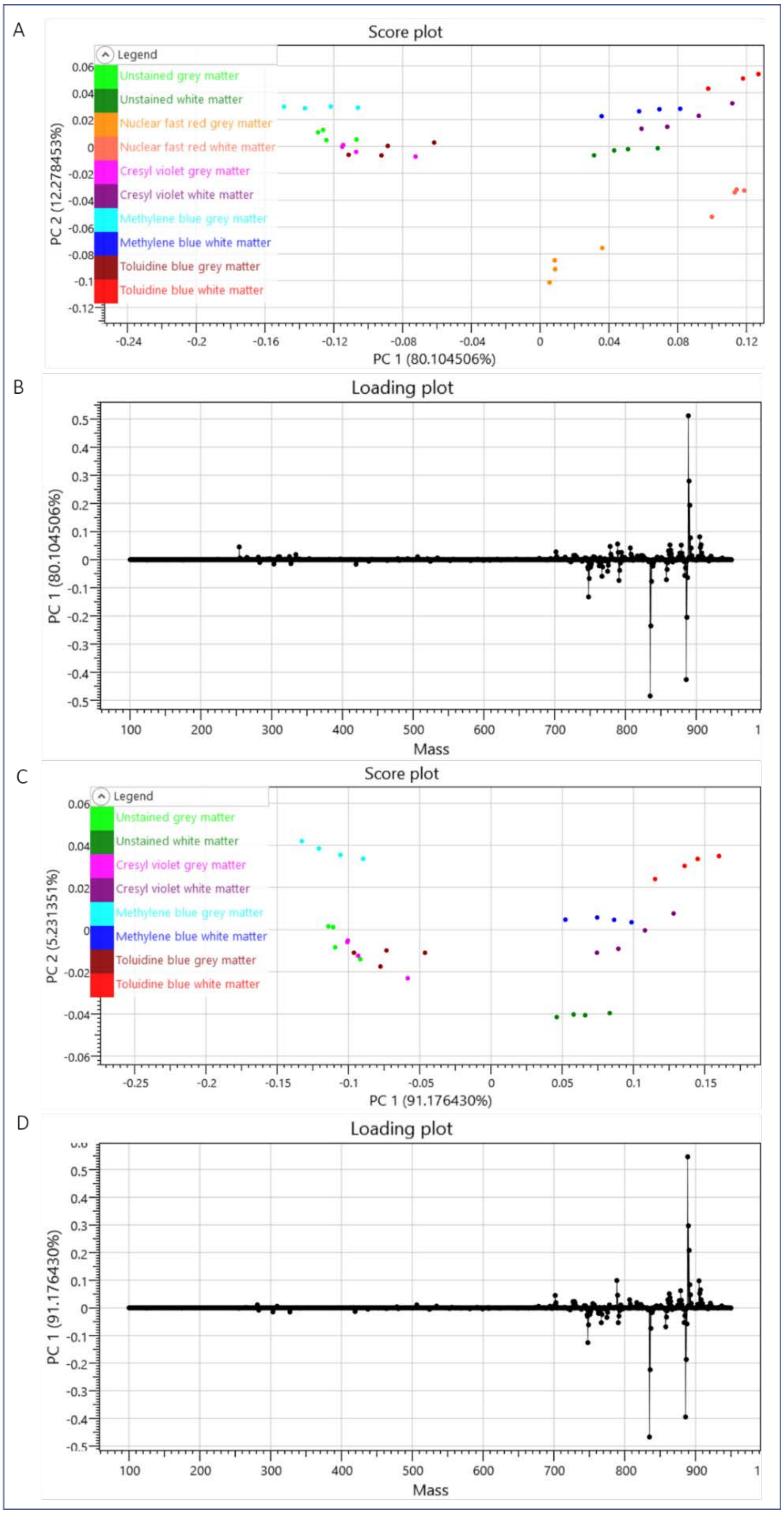

Figure 69 – PCA of DESI-MS data from all stained brain sections with unstained brain tissue sections. Each dot on the PCA score plots refers to one ROI extracted from each of the NFR, TB, MB and CV stained DESI-MS image. Score plot of principal component 1 v principal component 2 PCA analysis of all stained and unstained data (A) and extracted loading plots of principal component 1 (B). Score plot of principal component 1 v principal component 2 of the PCA analysis of stained and unstained data with NFR spectra excluded (C) and extracted loading plots of

principal component 1 (D). Including NFR WM and GM spectra reduces the PCA ability to discriminate between GM and WM with PC 1 separating NFR spectra from the rest

Results of the PCA in include ROIs of NFR stained sections. As observed previously for the individual stain, the PCA score plot shows that NFR ROIs are chemically distinct and separated from all other data points by *m/z* 254 and 334. This further highlights that the detection of the staining molecules is impacting the PCA data. Removing the NFR ROIs from the PCA model again shows that the major differences observed in the model are between GM and WM rather than those differences between the individual stains, Figure 69 C and D. Principal component 1 weights for 91.17% of the variance in the data, compared to 80.10% when NFR ROIs are included. As previously seen the GM spectra are more closely grouped than the WM spectra suggesting less chemical difference between the stained and unstained GM spectra. However, PC 2 only accounts for 5.23% of the variance in the data, suggesting the changes are minimal.

4.3. Assessing the effect of time on DESI-MSI spectra

Intra-operative histopathological analysis is an important tool in neuro-oncology [4], relying on the rapid analysis of tumour biopsies to aid surgical decision making. Stereotaxic biopsies typically followed the smear preparation technique, or in the cases in larger biopsies these will be snap frozen and sectioned. Within an intra-operative setting, DESI-MS has been used for the rapid assessment of brain tumour biopsies through the analysis of surgical smears [6]. Intraoperative assessment is required on a quick time scale and as such tissues should be analysed as soon as possible. In cases where analysis could be delayed, we assessed the impact of time after staining on the DESI-MS spectra produced.

PCA models were built from ROIs extracted from WM and GM regions. Samples were stained, imaged by DESI-MS, left at ambient conditions for 24 hours, before further DESI-MSI analysis on the same tissue section.

ROIs were extracted from corresponding regions on each section from the cerebral cortex and white matter tracts located in the brain stem, representing the GM and WM respectively, followed by PCA of TB stained brain sections, Figure 70. Where light and dark parameters are investigated, two adjacent brain sections on the same slide were analysed by DESI. One brain section was covered to determine if leaving sections in a light or dark setting for 24 hours affected the DESI-MS imaging analysis.

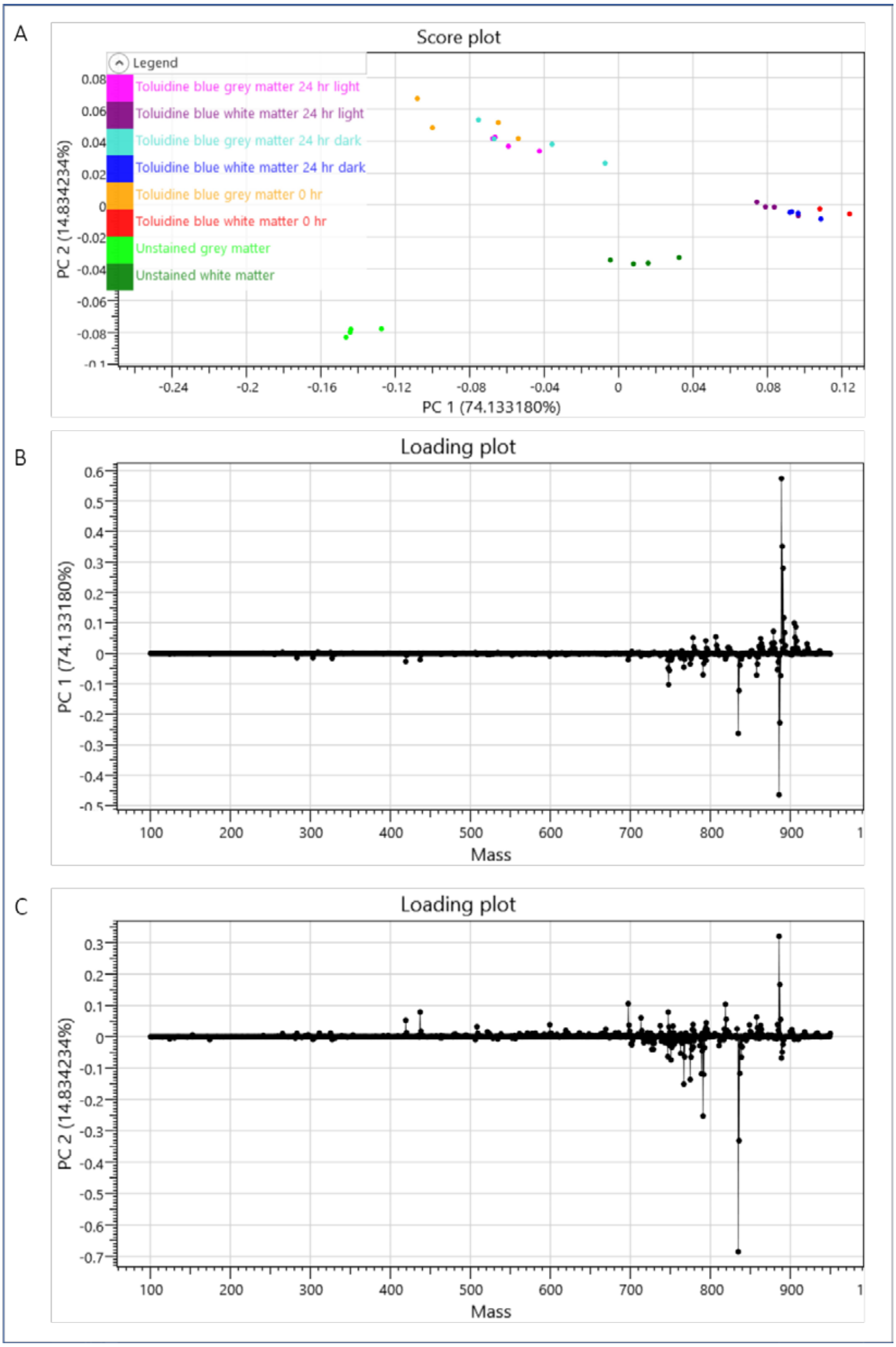

Figure 70 – PCA of DESI-MS data from GM and WM regions of toluidine blue sections analysed 24 hours after initial DESI- MS imaging analysis. DESI-MSI was acquired from brain sections at 0 hours and 24-hour post staining, with two adjacent sections analysed 24 hours later. Adjacent brain sections were left in a dark or light setting to assess

the effect of time and environment on DESI-MS spectra. 4 ROIs from each region were analysed with each dot on the PCA score plot representing one ROI. Resultant score plot of principal component 1 v principal component 2 (A) and extracted loading plots of principal component 1 (B) and principal component 2 (C). PC 1 successful separates WM and GM spectra in each variable (contribution 74.1%) and PC 2 separates TB stained from unstained spectra (contribution 14.8%). Tight cluster of data points on the PC score plot suggest little difference between DESI-MS spectra of sections left in the light or dark locations for 24 hours

The PCA plot of TB stained sections again reveals PC 1 to account for a large proportion of the variation in the data at 74.13%, separating the spectra of white and grey matter regions from each sample. Principal component 2 weights for 14.83% of the variance which is larger than observed when comparing GM and WM spectra of TB stained sections, Figure 66. PC 2 separates the unstained brain spectra from TB stained spectra matched previously shown data. The PC score plot reveals a tight clustering of all corresponding TB-stained regions and little difference between those spectra extracted from the sections left in the dark/ light, Figure 70 A.

No differences were observed in the spectra of the TB stained sections left in the light or the dark for 24 hours compared to those analysed immediately. Subsequently, to assess the effect of time on CV and MB brain sections, the sections imaged by DESI-MS were left in a sealed container, rather than covering with foil to create a dark environment. As observed for TB-stained sections, minimal differences were observed between the CV and MB stained spectra of grey and white matter compared to unstained and those from the same section analysed immediately after staining and drying. In the PCA models for both CV and MB, PC 1 separates WM and GM spectra, weighting for 74.04% and 74.78% of the variance, once more highlighting the major differences are between distinct regions of the brain over the stained and unstained sections, Supplementary Figure 72 and Figure 73.

4.4. DESI-MS imaging of stained brain sections

As well as comparing differences between the mass spectra of chemically distinct regions, direct comparison of the DESI-MS images of unstained and stained sections is important in assessing compatibility of these stains with DESI-MSI. Mass spectrometry imaging experiments produce hundreds of images simultaneously and as such there are many molecular species localised to the GM and WM regions. White matter regions are relatively uniform, composed of glial cells and myelinated neurons, whereas individual GM regions in the brain have more complex biological functions. GM is composed of a variety of neuronal cell bodies. Due to differences in cell types located throughout the brain the abundance and distribution of many *m/z* values varies throughout the section.

Combining and overlaying multiple *m/z* values can build up a complete overview of the tissue sections. The *m/z* values 786.53, 834.52 and 913.54 are abundant in GM structures, whereas *m/z* 888.62 is an abundant WM lipid species. The individual DESI-MS images of these molecular species in an unstained brain section and CV, MB and TB stained sections were compared, Figure 71. The single ion images for each sample were overlayed in HDImaging and represented as a solid colour MS images, supplementary Figure 74 - Figure 77.

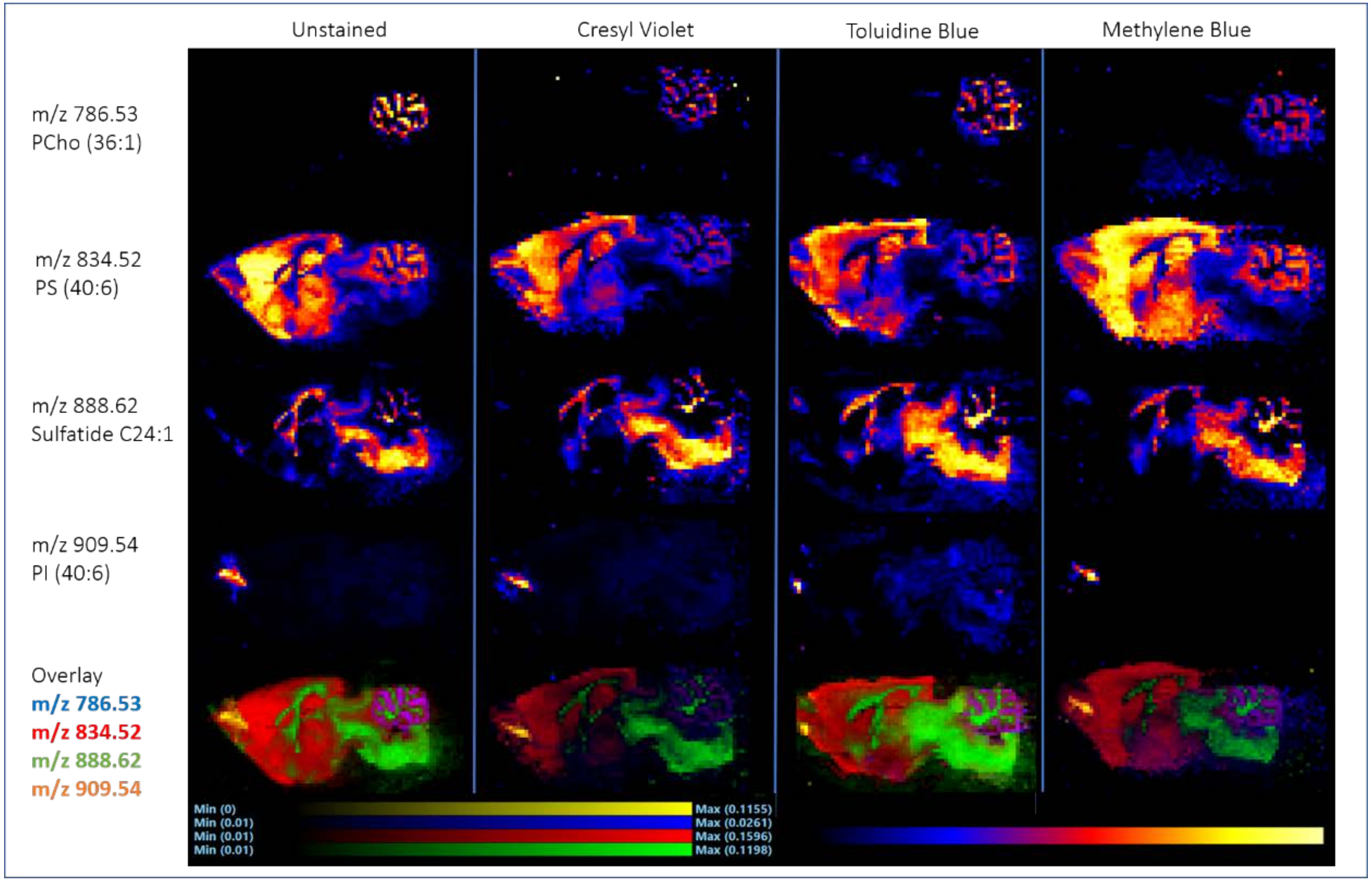

Figure 71 – DESI-MS imaging of unstained brain tissue section compared to the brain sections stained with cresyl violet, toluidine blue and methylene blue. Individual DESI-MS ion images of m/z 786.53, 834.52, 888.62 and 909.54 are shown for each DESI-MS imaging experiment of unstained brain and stain sections of CV, TB and MB. The distribution of each lipid in the stained images matches to the unstained section and overlaying all ions provides a representative makeup of the tissue section.

Each m/z shown above is tentatively assigned using accurate MS and results from literature. *m/z* 786.53 (PS 36:2) and *m/z* 834.52 (PS 40:6) are abundant GM species, located in the cerebellum and throughout the iso-cortex in the GM region respectively. *m/z* 834.52 is a known key component of GM in DESI-MS spectra of human and mammalian brain spectra [15, 16]. In this work *m/z* 834.52 was also the most abundant GM molecular species, observed in all stained and unstained brain sections, Figure 59, and also heavily weighted in the PCA models of each stain Figure 63, 8, 10, 12. *m/z* 913.54, PI (40:6) is another GM marker, observed in a sub structure of the GM in the olfactory bulb. Including *m/z* 913.54 in the overlay, helps build a comprehensive overview of the tissue section. The WM marker of *m/z* 888.62, corresponding to sulfatide C24:1, is an essential component of the myelin sheath found in WM brain regions. This molecule has also been observed previously in DESI-MS analysis of human and mammalian brain [15, 16], located throughout all white matter structures. The m/z value 888.62 is also abundant in the WM spectra of brain, Figure 59, and also heavily weighted in the PCA models.

From visually comparing the individual MS images of CV, MB and TB stained sections, lipid distributions are comparable to those shown in the unstained section. The anatomical features represented by the GM and WM makers show defined boundaries and sharp features. No delocalisation of lipid species was observed in these MS images and the overlaid images of the 4 *m/z* analytes (Figure 71 bottom row) shows an accurate representation of the brain section, particularly when compared to adjacently stained H&E image. The corpus callosum and white matter tracts within the cerebellum are easily observed in the distribution of *m/z* 888.62, including across all stained section. The ability to spatial resolve these regions at 200 µm spatial resolution further highlights the compatibility of the staining protocols with DESI-MSI analysis. Analyte delocalisation is an issue for MSI techniques where spatially resolved analysis is crucial but is not a consideration for histology stains as cellular structures are not damaged during washing and staining.

Analyte delocalisation is an issue for MALDI imaging of peptides following on-tissue digestion (OTD) and can occur when biomolecular species of the tissue are extracted into the solvent washes [19]. The water-based histology stains used here not only provide a rapid and easy stain for the tissue, but also have no observable effect on the lipid distributions.

The overlay images for each DESI-MS imaging dataset show a full mapping of the brain tissue section. The unstained brain shows a sharp contrast between the GM and WM, particularly in the corpus callosum, represented in green in the midbrain of each section. TB overlayed MS images match that of the unstained section extremely closely, whilst those of CV and MB appear less intense, with a weaker contrast to the naked eye between GM and WM features. The cerebellum of the CV-stained section is less visible when overlayed with multiple MS images, which could suggest a suppression effect of CV in this region.

5. Conclusions

This work set out to investigate the compatibility of multiple histology stains in conjunction with DESI-MSI analysis of lipids in an altered mass spectrometry imaging workflow, whereby histological staining occurs prior to MSI analysis, and DESI-MSI is therefore carried out on stained tissue sections. The altered workflow assesses the potential use of histology stains other than H&E which is shown to be incompatible with DESI-MSI and analysis of lipids.

Results from this study conclude that staining sections prior to analysis by DESI-MS imaging using CV, TB and MB does not impact the spectra produced or the quality of the mass spectrometry images acquired, in a way that would limit data interpretation. The results suggest that there is minimal effect of leaving the section for prolonged periods of time after staining up to 24 hours, does not affect the observed lipid species detected by DESI-MSI. This result indicates that stained clinical sections do not have to be analysed immediately and can tolerate the variable timings in a clinical setting.

Of the stains analysed, only the NFR staining molecule is detected in the negative ion spectra. Visualising the lipid region of the NFR spectra show that the lipid species expected from the brain are still present. However, the presence of these staining molecules causes problems when using multivariate statistics to analyse the data, and as such analysing NFR stained sections are not desirable for negative ion mode

DESI-MS analysis. In the PCA model of NFR, PC 1 clearly explains a large percentage of the data variance, however it does not separate white matter from grey matter in PC 1, as is the case with MB, CV and TB. The molecular species associated with the NFR staining molecule, detected at *m/z* 255 and 334 impact the PCA model from separating the WM and GM spectra. Using NFR stained tissue could negatively impact any results observed after analysis particularly in the cases where metabolites and low weight molecular species are of interest for diagnostic purposes, which is particularly important in brain tumour research where NAA and 2-HG are used to determine malignancies in high grade gliomas (HGG) including glioblastoma (GBM) [6, 15, 20].

The histology stains investigated here are all water-based and as such lipid distributions are not affected in the raw spectra, nor is there delocalisation in the MS imaging data obtained from each stained section. Problems may become apparent in the analysis of metabolites that are soluble in water and as such this staining can be used for lipid imaging but would require further testing for metabolite analysis.

Future work would need to determine if the quality of the stain is applicable to those that could be used to differentiate tumour specimens in a clinical setting, as well as characterising the stains in positive ion mode, which may be suited for NFR analysis. The necessary clinical samples were not available for analysis at this time, however the results and compatibility of these stains with control samples should offer further evidence that these stains can be compatible with clinical samples.

To fully assess the compatibility of the DESI compatible stains outlined here with DESI-MS imaging for molecular pathology analysis, a dataset would need to be built and validated based on unstained and stained tissue of the disease tissue of interest.

6. Acknowledgments

The author acknowledges and gives thanks to the MRC and Water’s for funding the studentship.

7. Author Contributions

Matthew Gentry undertook all DESI-MS imaging acquisition and subsequent data analysis.

Matthew Gentry, Emrys Jones and Adam McMahon designed the study.

Adam McMahon, Nicholas Lockyer and Emrys Jones were Matthew Gentry's supervisory team, providing support and guidance throughout this project.

8. Supplementary figures

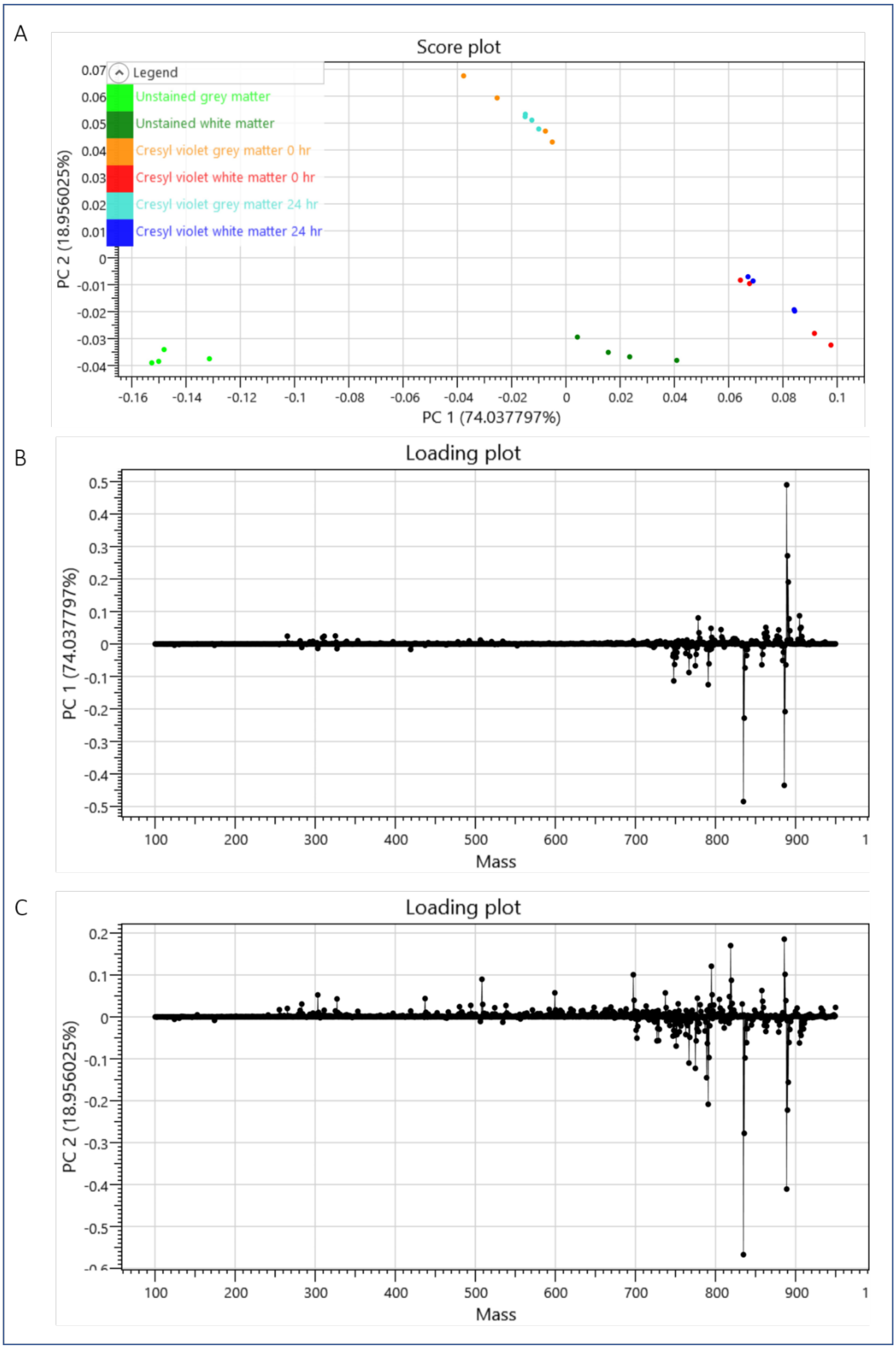

Figure 72 – PCA of DESI-MS data from GM and WM regions of cresyl violet sections analysed 24 hours after initial DESI- MS imaging analysis. DESI-MSI was acquired from brain sections at 0 hours and 24-hour post staining, with two adjacent sections analysed 24 hours later. Adjacent brain sections were left in a dark or light setting to assess the effect of time and environment on DESI-MS spectra. 4 ROIs from each region were analysed with each dot on the PCA score plot representing one ROI. Resultant score plot of principal component 1 v principal component 2 (A) and extracted loading plots of principal component 1 (B) and principal component 2 (C). PC 1 successful separates

WM and GM spectra in each variable (contribution 74.0%) and PC 2 separates CV stained from unstained spectra (contribution 18.9%). Tight cluster of data points on the PC score plot suggest little difference between DESI-MS spectra of sections left in the light or dark locations for 24 hours.

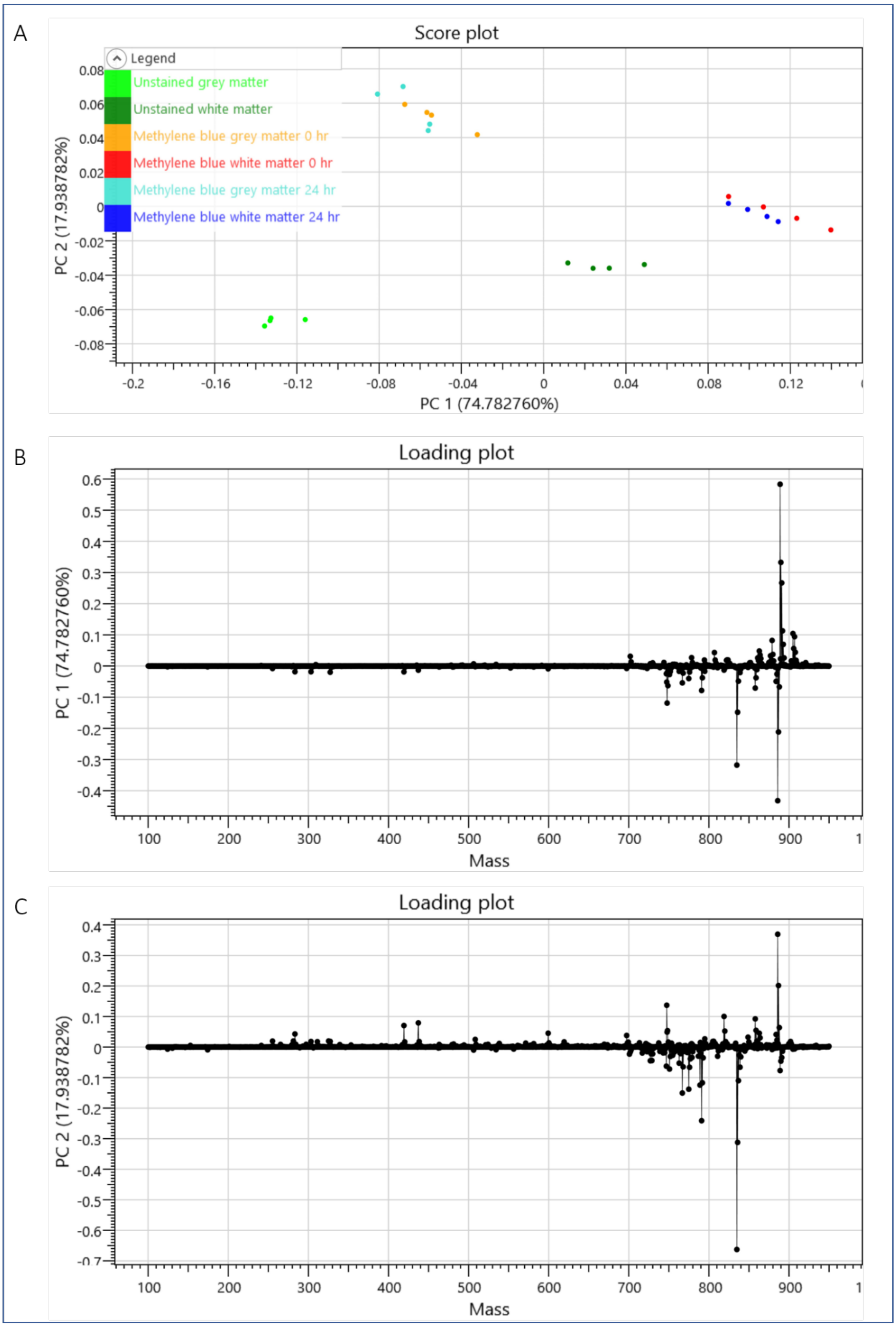

Figure 73 – PCA of DESI-MS data from GM and WM regions of methylene blue sections analysed 24 hours after initial DESI- MS imaging analysis. DESI-MSI was acquired from brain sections at 0 hours and 24-hour post staining, with two adjacent sections analysed 24 hours later. Adjacent brain sections were left in a dark or light setting to

assess the effect of time and environment on DESI-MS spectra. 4 ROIs from each region were analysed with each dot on the PCA score plot representing one ROI. Resultant score plot of principal component 1 v principal component 2 (A) and extracted loading plots of principal component 1 (B) and principal component 2 (C). PC 1 successful separates WM and GM spectra in each variable (contribution 74.8%) and PC 2 separates MB stained from unstained spectra (contribution 17.9%). Tight cluster of data points on the PC score plot suggest little difference between DESI-MS spectra of sections left in the light or dark locations for 24 hours.

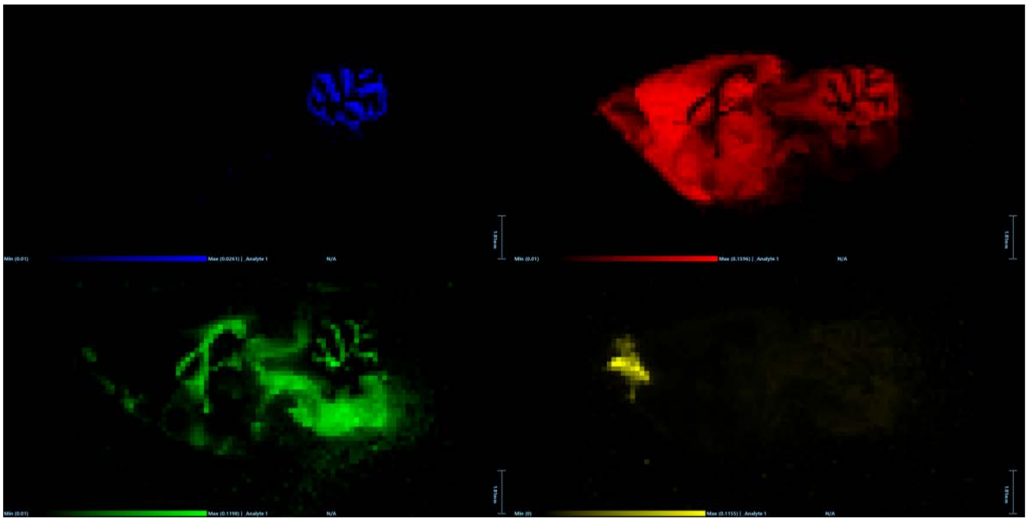

Figure 74 – DESI-MSI of unstained control brain section. Individual MSI extracted for m/z 786.53 (blue), m/z 834.52 (red), m/z 888.62 (green) and m/z 909.54 (yellow) are represented by a single colour and are overlayed in Figure 71to show a complete makeup of the brain section. m/z 786.53 and m/z 834.52 define features of grey matter (cerebellum and isocortex respectively) and m/z 888.62 and 909.54 define features of white matter

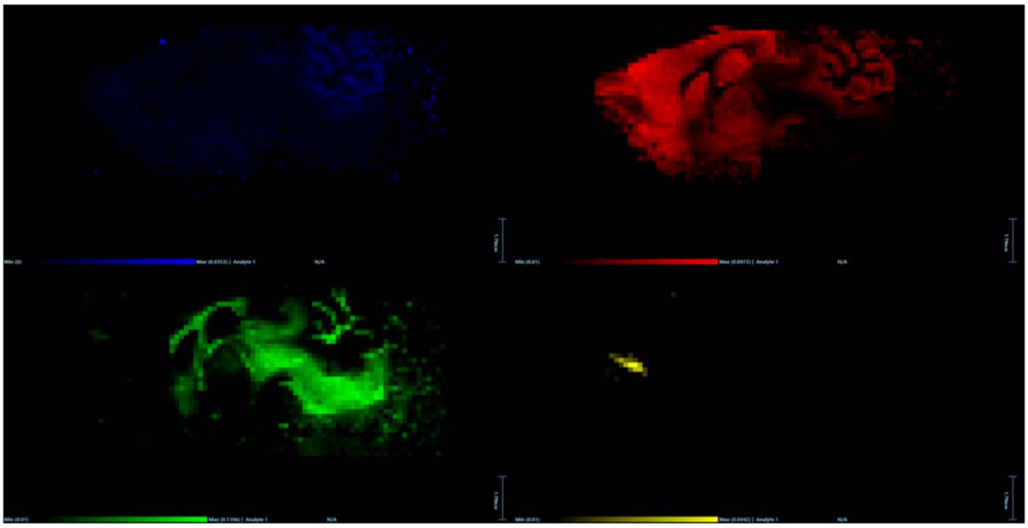

Figure 75 – DESI-MSI of cresyl violet stained brain section. Individual MSI extracted for m/z 786.53 (blue), m/z 834.52 (red), m/z 888.62 (green) and m/z 909.54 (yellow) are represented by a single colour and are overlayed in Figure 71to show a complete makeup of the brain section. m/z 786.53 and m/z 834.52 define features of grey matter (cerebellum and isocortex respectively) and m/z 888.62 and 909.54 define features of white matter

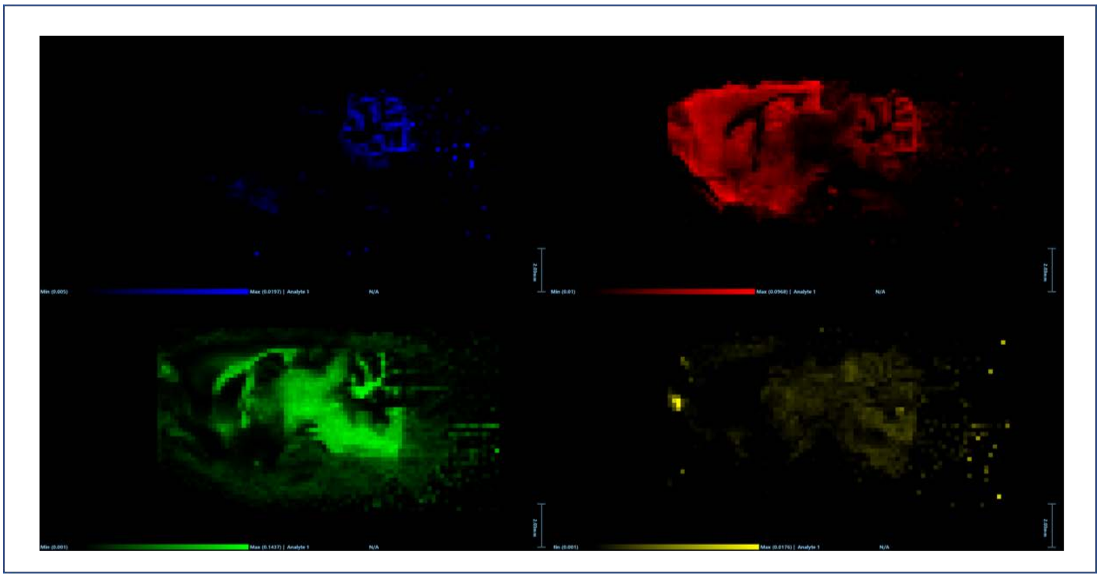

Figure 76 – DESI-MSI of toluidine blue stained brain section. Individual MSI extracted for m/z 786.53 (blue), m/z 834.52 (red), m/z 888.62 (green) and m/z 909.54 (yellow) are represented by a single colour and are overlayed in figure 15 to show a complete makeup of the brain section. m/z 786.53 and m/z 834.52 define features of grey matter (cerebellum and isocortex respectively) and m/z 888.62 and 909.54 define features of white matter

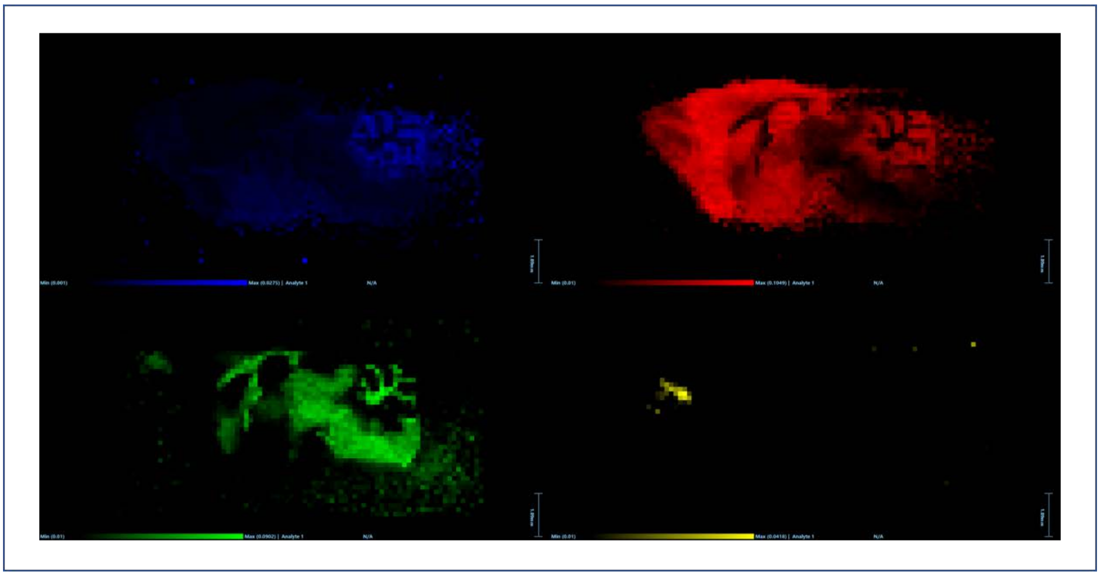

Figure 77 – DESI-MSI of methylene blue stained brain section. Individual MSI extracted for m/z 786.53 (blue), m/z 834.52 (red), m/z 888.62 (green) and m/z 909.54 (yellow) are represented by a single colour and are overlayed in figure 15 to show a complete makeup of the brain section. m/z 786.53 and m/z 834.52 define features of grey matter (cerebellum and isocortex respectively) and m/z 888.62 and 909.54 define features of white matter

9. References

1. Wiseman, J.M., et al., *Mass spectrometric profiling of intact biological tissue by using desorption electrospray ionization.* Angewandte Chemie-International Edition, 2005. **44**(43): p. 7094-7097.
2. Takats, Z., et al., *Mass spectrometry sampling under ambient conditions with desorption electrospray ionization.* Science, 2004. **306**(5695): p. 471-473.
3. Eberlin, L.S., et al., *Nondestructive, Histologically Compatible Tissue Imaging by Desorption Electrospray Ionization Mass Spectrometry.* Chembiochem, 2011. **12**(14): p. 2129-2132.
4. Tilgner, J., et al., *Validation of intraoperative diagnoses using smear preparations from stereotactic brain biopsies: intraoperative versus final diagnosis—influence of clinical factors.* Neurosurgery, 2005. **56**(2): p. 257-265.
5. Balog, J., et al., *Intraoperative Tissue Identification Using Rapid Evaporative Ionization Mass Spectrometry.* Science Translational Medicine, 2013. **5**(194): p. 11.
6. Pirro, V., et al., *Intraoperative assessment of tumor margins during glioma resection by desorption electrospray ionization-mass spectrometry.* Proceedings of the National Academy of Sciences of the United States of America, 2017. **114**(26): p. 6700-6705.
7. Ogrinc, N., et al., *Water-assisted laser desorption/ionization mass spectrometry for minimally invasive in vivo and real-time surface analysis using SpiderMass.* Nature protocols, 2019. **14**(11): p. 3162-3182.
8. Zhang, J., et al., *Nondestructive tissue analysis for ex vivo and in vivo cancer diagnosis using a handheld mass spectrometry system.* Science translational medicine, 2017. **9**(406).
9. Chaurand, P., et al., *Integrating histology and imaging mass spectrometry.* Analytical chemistry, 2004. **76**(4): p. 1145-1155.
10. Duran, A.L., et al., *Shared Ageing Research Models (ShARM): a new facility to support ageing research.* Biogerontology, 2013. **14**(6): p. 789-794.
11. Abou-Bakr, A.A.-E., O.M. Jamali, and L.M. Fathy, *Toluidine blue versus frozen section for assessment of mucosal tumor margins in oral squamous cell carcinoma.* BMC cancer, 2020. **20**(1): p. 1-8.
12. Sridharan, G. and A.A. Shankar, *Toluidine blue: A review of its chemistry and clinical utility.* Journal of oral and maxillofacial pathology: JOMFP, 2012. **16**(2): p. 251.
13. Oz, M., et al., *Cellular and molecular actions of methylene blue in the nervous system.* Medicinal research reviews, 2011. **31**(1): p. 93-117.
14. Alvarez-Buylla, A., C.-Y. Ling, and J.R. Kirn, *Cresyl violet: a red fluorescent Nissl stain.* Journal of neuroscience methods, 1990. **33**(2-3): p. 129-133.
15. Jarmusch, A.K., et al., *Lipid and metabolite profiles of human brain tumors by desorption electrospray ionization-MS.* Proceedings of the National Academy of Sciences of the United States of America, 2016. **113**(6): p. 1486-1491.

16. Eberlin, L.S., et al., *Desorption electrospray ionization mass spectrometry for lipid characterization and biological tissue imaging.* Biochimica Et Biophysica Acta-Molecular and Cell Biology of Lipids, 2011. **1811**(11): p. 946-960.
17. Chaurand, P., et al., *Integrating histology and imaging mass spectrometry.* Analytical Chemistry, 2004. **76**(4): p. 1145-1155.
18. Jolliffe, I.T. and J. Cadima, *Principal component analysis: a review and recent developments.* Philosophical Transactions of the Royal Society A: Mathematical, Physical and Engineering Sciences, 2016. **374**(2065): p. 20150202.
19. Cole, L.M. and M.R. Clench, *Mass spectrometry imaging for the proteomic study of clinical tissue.* PROTEOMICS–Clinical Applications, 2015. **9**(3-4): p. 335-341.
20. Santagata, S., et al., *Intraoperative mass spectrometry mapping of an onco-metabolite to guide brain tumor surgery.* Proceedings of the National Academy of Sciences of the United States of America, 2014. **111**(30): p. 11121-11126.

Chapter 5: Conclusions and future work

Overall, the data shown in this thesis has demonstrated the use of MSI methodology, both as standalone methods, and in support of currently used techniques, in the preclinical and clinical settings. Focussing on the use of DESI-MS imaging for the lipidomic analysis and molecular profiling of glioblastoma in a preclinical model and human tissue biopsies, a variety of imaging modalities were utilised, including LA-ICP-MS and H&E stained tissues , to investigate lipid heterogeneity in glioblastoma samples. These data yield valuable insights into mechanistic and metabolomic pathways of fatty acid oxidation and PI3-K signalling previously reported in preclinical models, and now observed in corresponding human tissue samples. The untargeted analysis of DESI-MS imaging allowed for high spatial resolution distribution of a number of key lipid species to be determined in biological samples. The combination of negative and positive ion mode data has been shown to be crucial, to fully describe the molecular landscape of GBM tissues, demonstrating the importance of DESI-MS imaging as a tool for tissue discrimination, segmentation, and lipid analysis.

Using the G7 preclinical model, analysis with DESI-MSI revealed several lipid classes which differed in intensity between the healthy tissue and the orthotopic tumour areas. Of which, an increase of phosphatidylinositol (PI) lipids were observed, and spatially distributed within the tumour area of the G7 model. Building on what is known in literature, these data add to evidence, suggesting an overexpression of the PI3-K pathway *via* PI signalling lipids. In the negative ion DESI-MS imaging, the PI species detected contained fatty acids with longer chains and increased levels of saturation, compared to PI (18:0/20:4) which makes up the PI lipid backbone of the PI signalling molecules; PIP2 and PIP3. This was contrary to previous findings and may suggest a novel incorporation of fatty acids into PI signalling lipids when there is an overexpression of PI3-K. The mechanism of new PI lipid production is unknown and would be a target for future work. Further, future work will be required to confirm that the PI3-K pathway is in fact altered in the G7 tumour model and corroborate the DESI-MS imaging data and subsequent conclusions drawn. IHC staining to target the downstream changes in the PI3-K pathway would provide evidence of overexpressed PI3-K. Targeting tumour expression of PTEN, using p-PTEN (serine-380/ threonine 382/83) antibody, or phospho-AKT, using p-AKT (serine-473) antibody [1]. Exploration of these altered pathways as potential drug targets may offer an alternative GBM treatment, thus highlighting how MSI data can contribute to future clinical development.

Alteration to the metabolism in GBM tumours has been shown in both preclinical and clinical samples, where fatty acid oxidation can be investigated through the detection of free fatty acids and acyl-carnitines that are central to this mechanism. Both fatty acids and carnitines have been observed in the G7 pre-clinical model as well as in human tissue biopsies through DESI-MSI analysis. Importantly, dual polarity data is required to observe these molecular species with FA only ionising in negative ion mode and carnitines in positive ion mode. Further work to confirm this altered metabolic state by immunohistochemical staining and proteomic analysis of the tissue will be essential to fully quantify the metabolic activity observed in these GBM samples. IHC staining targeting fatty acid synthase (FASN), using anti-FASN monoclonal antibody, and carnitine palmitoyltransferase-1C (CPTC-1C), using anti-CPT1-C antibody, could be used to observe the altered metabolic state in the GBM samples presented [2].

It is known that carnitine and fatty acid intracellular distributions are interlinked. Following analysis with DESI-MSI, these species were shown to have specific spatial distributions. This has been shown for the first time in both the preclinical and clinical samples analysed, locating at the tumour border in the G7 model and appearing heterogeneously in GBM biopsies. Heterogeneity within tumours can cause issues with a standard of care (SOC) treatment and as such more targeted approaches are being made to treat individual cases. The relationship of carnitines and fatty acids was not observed in all clinical samples and as such may suggest heterogeneity between the GBM tumours. If FAO is only observed in some tumours, then using carnitines and fatty acids as biomarkers could drive patient treatment. Additionally, these carnitines and fatty acids were located at the hypoxic boundary of the GBM biopsies, corroborating the data previously shown in U87 pre-clinical models of GBM [3]. Confirming the exact location of carnitines in relation to cell types should be explored through the use of higher spatial resolution imaging by SIMS, with a particular focus on the use of Water cluster beams for intact lipid analysis, which can obtain MS images at the subcellular level and fully probe the tumour boundaries [4]. The relation of carnitines to hypoxia should also be explored using CA-9 IHC staining, a marker of hypoxia, and overlaying this with the observed carnitine distributions. Although MS/MS analysis has been used to determine the structure of lipid species in the G7 model, further MS/MS utilising ion trap MS technology methods such as OzID [5] or data dependant acquisition (DDA) ion trap MS/MS (IT MS/MS) [6] would further confirm these chemical structures, providing additional confidence in the biochemistry proposed.

Examination of the G7 model with LA-ICP-MS, has revealed for the first time that the gadolinium containing MRI contrast agent, was spatially distributed within the tumour tissue areas of the sections. Additionally, zinc is also highly abundant in the tumour tissue region, although the exact reasoning is unconfirmed due to the plethora of roles zinc can play in GBM tumour biology. Accurate fusion of MRI and MS imaging data can further probe the ability of LA-ICP-MS and DESI-MSI to determine tumour boundaries, highlighting the potential of MSI to be used in combination with other methodology, as a way of expanding on the current data and adding a complementary dimension to the results. Future analysis of the G7 model using micro-proteomic approaches can aid in identification of zinc-containing proteins, as well as accurately determining the location of the full MRI contrast agent using alternative MS imaging studies. Determining the origin of zinc can provide downstream information on the proteins upregulated in the GBM tumours analysed, linked proteomic and metallomic data together.

Lipid heterogeneity was revealed in GBM biopsies, obtained following surgical excision guided by the 5-ALA fluorescent marker. The fluorescence marker, PpIX was not detectable by DESI-MS imaging in these tumour sections suggesting that DESI-MSI is not suitable to determine the distribution of PpIX based fluorescence in tissue. As such further analysis using alternative imaging techniques of MALDI-MSI or LDI-MS will be vital in linking fluorescence distribution to lipid signatures to determine the origin and location of fluorescence within GBM tumour cells and further understanding if fluorescence associated with PpIX is homogenous throughout GBM tumours. MALDI-MSI and LDI-MS have different ionisation methods to DESI-MSI, using lasers to ablation material, and MALDI-MSI also incorporates the use of matrices that can be optimised for the extraction of a range of biomolecules. Analysis of PpIX using either of these methods, may provide more favourable ionisation conditions. As such an alternative mass spectrometry imaging modality may be able to extract and analyse PpIX from these tissue samples. MALDI-MSI has previously been used to detect PpIX in GBM biopsies and would be extremely useful to combine this imaging data with lipidomic profiles of key molecular features in GBM [7].

Finally, this study has offered an altered imaging workflow where histology-stained tissue is analysed by DESI-MSI and the compatibility with lipidomic analysis has been discussed. Toluidine blue, cresyl violet and methylene blue stains are compatible with DESI-MSI negative ion mode analysis and have little impact on the lipid profiles and distributions observed in control mouse brain sections. This provides a much-needed alternative to MSI analysis of tissue samples, that is unhindered by tissue amount or resources, as well as proving the option to use directed MSI techniques, where a section of interest prior determined by histology can be analysed specifically. These data may pave a way for histology directed DESI-MS imaging analysis of a single tissue section. Analysis of clinical samples, using histopathology evaluation to guide DESI-MS imaging, would be desired to confirm compatibility of these stains for targeted DESI-MS imaging analysis.

Overall, this thesis provides several methodological advancements and developments, as well as providing insights into applications of MS imaging for lipid analysis, linking molecular profiles to key biochemical pathways altered in GBM, and the benefits of multi-modal analysis. Translational lipidomic results have been observed between G7 GBM pre-clinical models and clinical samples, highlighting the quality of the G7 orthotopic model for GBM pre-clinical research. The molecular species detected by DESI-MSI tissues could be used in the future for detection of GBM and diagnosis purposes; providing key information into pathways mutated, and the metabolic state of GBM tissue without the requirement of other analysis. This work has also demonstrated that DESI-MSI is not suitable for the analysis of PpIX and as such other MS imaging modalities should be explored to map PpIX and link this to lipid species. A multi-modal imaging approach using DESI-MSI for lipidomic analysis and another technique such as MALDI-MSI for PpIX may be beneficial. The results presented, allow for future development as the MSI techniques used in this work generated a plethora of data, and as such further mining or analysis of the data may reveal further links between lipids and GBM tumours.

1. References

1. Jacob, A., et al., *Phosphatidylinositol 3-kinase/AKT pathway activation in human vestibular schwannoma.* Otology & neurotology, 2008. **29**(1): p. 58-68.
2. Wakamiya, T., et al., *Elevated expression of fatty acid synthase and nuclear localization of carnitine palmitoyltransferase 1C are common among human gliomas.* Neuropathology, 2014. **34**(5): p. 465-474.

3. Henderson, F., et al., *3D DESI-MS lipid imaging in a xenograft model of glioblastoma: a proof of principle.* Scientific Reports, 2020. **10**(1): p. 1-7.
4. Sheraz née Rabbani, S., et al., *Enhancing ion yields in time-of-flight-secondary ion mass spectrometry: a comparative study of argon and water cluster primary beams.* Analytical chemistry, 2015. **87**(4): p. 2367-2374.
5. Poad, B.L., et al., *Ozone-induced dissociation on a modified tandem linear ion-trap: observations of different reactivity for isomeric lipids.* Journal of the American Society for Mass Spectrometry, 2010. **21**(12): p. 1989-1999.
6. Ellis, S.R., et al., *Automated, parallel mass spectrometry imaging and structural identification of lipids.* Nature methods, 2018. **15**(7): p. 515-518.
7. Kröger, S., et al., *Complementary molecular and elemental mass-spectrometric imaging of human brain tumors resected by fluorescence-guided surgery.* Analytical chemistry, 2018. **90**(20): p. 12253-12260.